

**AMNIOTIC MEMBRANE
AS A BATTLEFIELD DRESSING
FOR
THE OCULAR SURFACE**



Gerald Arthur Clare

Thesis submitted for the degree of Doctor of Philosophy

University of Nottingham

30th August 2013

This thesis is dedicated to the memory of my beloved father, Arthur George Clare, who fell ill just before the project started and passed away 6 months later, at the age of 63.

To be, or not to be, — that is the question: —
Whether 'tis nobler in the mind to suffer
The slings and arrows of outrageous fortune,
Or to take arms against a sea of troubles,
And by opposing end them? — To die, to sleep, —
No more; and by a sleep to say we end
The heart-ache, and the thousand natural shocks
That flesh is heir to, — 'tis a consummation
Devoutly to be wish'd. To die, to sleep; —
To sleep, perchance to dream: — ay, there's the rub;
For in that sleep of death what dreams may come,
When we have shuffled off this mortal coil,
Must give us pause: there's the respect
That makes calamity of so long life;
For who would bear the whips and scorns of time,
The oppressor's wrong, the proud man's contumely,
The pangs of despis'd love, the law's delay,
The insolence of office, and the spurns
That patient merit of the unworthy takes,
When he himself might his quietus make
With a bare bodkin? who would these fardels bear,
To grunt and sweat under a weary life,
But that the dread of something after death, —
The undiscover'd country, from whose bourn
No traveller returns, — puzzles the will,
And makes us rather bear those ills we have
Than fly to others that we know naught of?
Thus conscience does make cowards of us all;
And thus the native hue of resolution

Is sicklied o'er with the pale cast of thought;
And enterprises of great pith and moment,
With this regard, their currents turn awry,
And lose the name of action.

Hamlet, Act III, scene i

ABSTRACT

The use of amniotic membrane (AM) as a dressing for ocular surface injuries has attracted the interest of the military ophthalmological community. First applied in the 1930s, the tissue is widely used today, although clinical indications for treatment are incompletely defined. While AM is most commonly stored frozen and thawed before use, dried AM is preferred for logistical reasons. Optimal preservation of the tissue is necessary to preserve its quality. The effect of drying on the physical and biological properties of the tissue are unknown.

A systematic review of the evidence of AM treatment of acute chemical injuries was conducted. A framework was proposed for optimising the dried tissue through thermal, moisture sorption and surface analytical techniques. The physical properties of AM preparations were compared by mechanical testing and mathematical modelling, and an attempt was made to cross-link the AM collagen. Inflammatory aspects of the tissue were assessed by immunological techniques, zymography and macrophage assays.

There is a lack of high quality evidence to support the clinical application of AM for acute burns. Complex interactions were demonstrated between the dried tissue, its excipients and moisture, suggesting novel ways of optimising the product. The mechanical properties of the dried membrane indicated that the process adversely affected the tissue, and artificial cross-linking could not be achieved. While the presence of antimicrobial peptides was not clearly established, the elution of collagenolytic enzymes was shown in therapeutic preparations of AM. The production of tumour necrosis factor by macrophages, which adhere to the spongy layer of AM, was suppressed.

This project makes original contributions relevant to the use of dried AM as a biomaterial in ophthalmic surgery. Further refinements of this work, animal model experimentation and clinical trials may support its future acceptance as a clinical application.

ACKNOWLEDGEMENTS

During the 2003 American-led invasion of Iraq, my colleague Lieutenant Colonel Andrew Jacks visited the operating theatres of the US Forces. He found that one of the materials available to the ophthalmic surgeons there was dried amniotic membrane. Some time later, I expressed a desire to conduct research, and it was suggested by the then Defence Consultant Adviser in ophthalmology, Wing Commander Robert Scott that the use of dried amnion in treating battlefield ocular injuries would be a suitable research topic. This was discussed with Professor Harminder Dua, who agreed to take me on as one of his research students. I subsequently applied for approval and funding from the Ministry of Defence and they responded generously - twice. The director of research, Dr Amarjit Samra, and the Medical Director, Surgeon Commodore Alasdair Walker were instrumental in this regard. Dr Andrew Hopkinson became involved, and a full research proposal with costings was hammered out, with a view to manufacturing dried amniotic membrane for clinical use. Dr Claire Allen eventually joined the team as a postdoctoral researcher. My Ph.D. project has run in parallel, but quite separately, to this larger project. I would like to thank all these individuals who have taken part in making this project successful.

For my work, I frequently found that it was necessary to go beyond my department to ask for help in my quest for an understanding of how to approach the topic of dried amniotic membrane. I was never refused help, and some of the people who responded positively became key enablers of my project. The help that I received was given freely, and the only way that I can respond is by vowing to pass it on to whoever should ask it of me.

I would not have been able to conduct a thermal and mechanical analysis of amniotic membrane without the people mentioned here. From the Centre for Biomolecular Sciences, I would like to thank Professor Kevin Shakesheff, Teresa Marshall, Lloyd Hamilton and Melissa Mathers. From the School

of Pharmacy, I wish to thank Professors Morgan Alexander, Clive Davies and Chen Xinyong, as well as Dr Jonathan Burley, Andrew Megarry and Dr David Scurr. From the Faculty of Engineering, I wish to thank Keith Dinsdale.

My understanding of the drying process was greatly helped by my discussions with Professor Sandra Hill at the Division of Food Sciences in Sutton Bonington. Dr Susan Liddell also deserves a special mention here. I would like to single out two individuals who more than anyone else have helped me to understand the difficult concepts I encountered and to apply them to the amniotic membrane. These are Dr Davide de Focatiis, of the Faculty of Engineering, and Dr Bill MacNaughtan at the Division of Food Sciences. My discussions with these men were transformative and profoundly influenced my confidence in my thesis. Jeffrey Glyn van de Velde, who made a special trip to Sutton Bonington to help me with an experiment also has my deep gratitude.

My work on matrix metalloproteases and on macrophages would not have been possible without the expert guidance of Dr Simon Johnson, Dr Imran Haq, Dr Luisa Martinez-Pomares and Sonali Singh. These individuals have been essential to this work, and I simply cannot thank them enough. I am indebted to Trevor Gray and Howard Coleman, and to Dr Emma King, for their help with electron microscopy. For flow cytometry and bead analysis, I'm grateful to Dr Sue Fox, Jane Limer, Jackie Glen and Dr Natalia Dovlatova.

My work on the systematic review was dependent on the insight of Dr Catey Bunce, Dr Richard Wormald and Anupa Shah, whom I wish to thank sincerely. I would also like to thank Dr Hanif Suleman for his input.

In my own department, my thanks go to Elena Lazutina, Naing Lat Tint, Aaron Yeung, Matthew Branch, Khurram Hashmani, Imran Mohammed, Peng Chen, Claire Allen and Megha Verma for their help, and all the others

who helped to make life at Nottingham enjoyable and challenging. Andrew Hopkinson, my co-supervisor, gave me invaluable editorial advice. I must have forgotten some of the contributions made by many individuals over the course of these years spent in Nottingham. For any unintended oversight, I apologise. Finally, thank you, Naruchki.

Contents

Contents	v
List of Figures	xvii
List of Tables	xx
1 INTRODUCTION	1
1.1 Introduction	1
1.1.1 Purpose and objectives	1
1.2 Literature review	2
1.2.1 Ocular surface injuries	2
1.2.1.1 Epidemiology of ocular surface trauma	2
1.2.1.2 Cost of ocular surface injuries	3
1.2.1.3 Ocular surface injuries in military conflict	3
1.2.1.4 Chemical warfare	4
1.2.1.5 Ballistic and blast injuries	4
1.2.1.6 Classification of ocular surface injuries	5
1.2.2 Corneal wound healing	6
1.2.2.1 Epithelial healing	7
1.2.2.2 Stromal healing	7
1.2.3 The amniotic membrane	9
1.2.3.1 Embryological origins	10
1.2.3.2 Anatomy	10

1.2.3.3	Physiology	12
1.2.3.4	Structural composition	12
1.2.4	Therapeutic application	13
1.2.4.1	Historical background	13
1.2.4.2	AM in modern ophthalmic surgery	15
1.2.4.3	AMT in stem cell deficiency	18
1.2.4.4	Mechanism of action of AMT	18
1.2.4.5	Animal models	20
1.2.4.6	Surgical application	21
1.2.4.7	Clinical use of dried AM	22
1.2.4.8	Limitations of treatment	22
1.2.5	AM procurement and preparation	24
1.2.5.1	Procurement	24
1.2.5.2	Preparation	24
1.2.5.3	To denude or not to denude?	25
1.2.5.4	Preservation by freezing	26
1.2.6	Dry preservation	28
1.2.6.1	Commercial preparations	28
1.2.6.2	Sterilisation	29
1.2.7	Biosynthetic alternatives	29

2 AMNIOTIC MEMBRANE TREATMENT OF ACUTE OCULAR BURNS 30

2.1	Introduction	30
2.2	Literature review	31
2.2.1	Epidemiology of ocular burns	31
2.2.2	Pathogenesis of ocular surface burns	32
2.2.2.1	Limbal stem cell failure and stromal ulceration	33
2.2.3	The natural history of ocular surface burns	34
2.2.4	Classification of ocular burns	34

2.2.5	Management of ocular acute surface burns	36
2.2.5.1	Medical management	37
2.2.5.2	Surgical management	38
2.2.6	AM patching of acute ocular surface burns	39
2.2.6.1	Historical background	39
2.2.6.2	Current practice	40
2.2.7	Standardisation of treatment	41
2.3	Materials and Methods	42
2.3.1	Eligibility criteria	42
2.3.2	Outcome measures	43
2.3.2.1	Primary outcomes	43
2.3.2.2	Secondary outcomes	44
2.3.2.3	Follow-up	44
2.3.3	Data extraction	45
2.3.4	Risk of bias assessment	46
2.3.5	Measures of treatment effect	47
2.3.6	Data synthesis	47
2.4	Results	48
2.4.1	Results of the search	48
2.4.2	Excluded studies	50
2.4.3	Included studies	53
2.4.4	Risk of bias in included RCT	55
2.4.4.1	Other causes of bias	56
2.4.5	Effects of interventions	58
2.4.5.1	Quality of the evidence	59
2.5	Discussion	63
2.6	Conclusion	65
3	OPTIMISATION OF DRIED AM	67
3.1	Introduction	67

3.2	Literature review	68
3.2.1	Lyophilisation	68
3.2.2	Stabilisation of biological materials	69
3.2.3	Thermal properties of collagen	70
3.2.4	Moisture sorption	72
3.2.5	Trehalose lyoprotection	73
3.2.5.1	Conformational states of trehalose	74
3.2.5.2	Vitrification of trehalose	76
3.2.6	Trehalose-AM interactions	77
3.3	Materials and methods	80
3.3.1	Tissue procurement and processing	80
3.3.1.1	Harvesting of AM	80
3.3.1.2	AM preparation	80
3.3.1.3	Thermolysin denuding	81
3.3.1.4	Trehalose pre-treatment	82
3.3.1.5	Vacuum-drying	82
3.3.2	Moisture sorption analysis	83
3.3.2.1	Dynamic vapour sorption	83
3.3.3	Thermal analysis	86
3.3.3.1	Thermogravimetric analysis	86
3.3.3.2	Differential scanning calorimetry	88
3.3.4	Dynamic mechanical analysis	90
3.3.4.1	Frequency sweep	93
3.3.4.2	Humidity sweep	94
3.3.4.3	Temperature sweep	94
3.3.5	Surface analysis	95
3.3.5.1	Wide-angle X-ray diffraction	95
3.3.5.2	Infrared spectroscopy	96
3.3.5.3	Mass spectrometry	97

3.3.5.4	Data analysis	98
3.4	Results	100
3.4.1	Moisture analysis	100
3.4.1.1	Drying curves	100
3.4.1.2	Water vapour sorption	102
3.4.1.3	Isotherm plots	104
3.4.1.4	Young and Nelson plots	104
3.4.2	Thermal analysis	107
3.4.2.1	Open pan	107
3.4.2.2	Closed pan	111
3.4.2.3	Differential scanning calorimetry	112
3.4.3	Dynamic mechanical analysis	116
3.4.3.1	Frequency sweep	116
3.4.3.2	Humidity sweep	118
3.4.3.3	Temperature sweep	121
3.4.4	Surface analysis	125
3.4.4.1	X-ray diffraction	125
3.4.4.2	Infrared spectroscopy	129
3.4.4.3	Mass spectrometry	129
3.5	Discussion	136
3.5.1	Moisture sorption analysis	136
3.5.2	Thermal analysis	139
3.5.3	Dynamic mechanical analysis	142
3.5.4	Surface analysis	145
3.6	Conclusion	147
4	PHYSICAL CHARACTERISATION OF AM	148
4.1	Introduction	148
4.2	Literature review	149
4.2.1	Physical properties of natural AM	149

4.2.1.1	Structural components	150
4.2.1.2	Therapeutic preparations	152
4.2.2	Mechanical characterisation	153
4.2.2.1	Uniaxial testing	153
4.2.2.2	Stress-strain analysis	154
4.2.2.3	Stress-strain characteristics	155
4.2.2.4	Mathematical modelling of AM behaviour	156
4.2.3	Accelerated degradation	157
4.2.4	Non-destructive tests	158
4.2.4.1	High frequency rheology	158
4.2.4.2	Atomic force microscopy	159
4.2.5	Cross-linking of AM	162
4.2.5.1	Assessment of cross-linking	164
4.3	Materials and methods	165
4.3.1	Imaging studies	165
4.3.1.1	Transparency assay	165
4.3.1.2	Electron microscopy	165
4.3.1.3	Sample processing	166
4.3.1.4	Scanning electron microscopy	166
4.3.1.5	Degradation assay	168
4.3.1.6	Transmission electron microscopy	168
4.3.1.7	Atomic force microscopy	169
4.3.2	Optical microscopy	170
4.3.2.1	Embedding of AM samples	170
4.3.2.2	Slide preparation	170
4.3.2.3	Cryostat sectioning	171
4.3.2.4	Thickness measurement	171
4.3.2.5	Haematoxylin and Eosin staining	171
4.3.3	Uniaxial testing	172

4.3.3.1	Data synthesis	174
4.3.3.2	Data filtering	175
4.3.3.3	Mathematical modelling	176
4.3.3.4	Statistical analysis	180
4.3.4	Non-destructive tests	181
4.3.4.1	Acoustic impedance	181
4.3.4.2	Nanoindentation	182
4.3.5	Cross-linking study	182
4.3.5.1	Ultraviolet irradiation	183
4.3.6	Analysis of cross-linking	183
4.3.6.1	Extraction of type I collagen	183
4.3.6.2	Protein purification	184
4.3.6.3	Protein quantification	184
4.3.6.4	Gel electrophoresis	185
4.3.7	Mass spectrometry	185
4.3.8	Western blotting	188
4.3.8.1	Preparation of samples	188
4.3.8.2	Protein electrophoresis	188
4.3.8.3	Protein transfer	189
4.3.8.4	Incubation with primary antibody	189
4.3.8.5	Detection of protein bands	189
4.3.9	Analysis of cross-linking by other methods	190
4.3.9.1	Interfibrillar measurement	190
4.3.9.2	Uniaxial tensile tests	191
4.3.9.3	Ninhydrin assay	191
4.4	Results	191
4.4.1	Transparency assay	191
4.4.2	Scanning electron microscopy	192
4.4.2.1	Degradation assay	196

4.4.3	Transmission electron microscopy	197
4.4.4	Atomic force microscopy	200
4.4.5	Optical microscopy	202
4.4.5.1	Optical microscopy	202
4.4.6	Uniaxial testing	203
4.4.6.1	AM micrometry	203
4.4.6.2	Data filtration	203
4.4.6.3	Force-distance analysis	204
4.4.6.4	Stress-strain analysis	206
4.4.6.5	Model fitting	208
4.4.7	Non-destructive tests	209
4.4.7.1	Acoustic wave impedance	209
4.4.7.2	Nanoindentation	209
4.4.8	Cross-linking	211
4.4.8.1	Gel electrophoresis	211
4.4.8.2	Western blotting	212
4.4.8.3	Mass spectrometry	212
4.4.8.4	Inter-fibrillar measurement	214
4.4.8.5	Uniaxial tests of irradiated AM	214
4.4.8.6	Ninhydrin assay	215
4.5	Discussion	215
4.5.1	Physical properties of dried AM	216
4.5.2	Cross-linking	226
4.6	Conclusion	228

5 BIOLOGICAL ACTIVITY OF THERAPEUTIC AM₂₃₀

5.1	Introduction	230
5.2	Literature review	231
5.2.1	Antimicrobial peptides	233
5.2.1.1	Foetal immunity	234

5.2.1.2	Ocular surface immunity	235
5.2.2	Matrix metalloproteases	236
5.2.2.1	Collagenolysis in AM	236
5.2.2.2	Ocular surface metalloproteases	237
5.2.3	Modulation of inflammation	239
5.2.3.1	Soluble factors	239
5.2.3.2	Direct contact	240
5.2.3.3	Suppression of neovascularisation	241
5.3	Materials and methods	242
5.3.1	SDS-PAGE/western blotting	243
5.3.1.1	Sample preparation	243
5.3.1.2	Protein quantification	245
5.3.1.3	Protein extraction	245
5.3.1.4	Sample loading	246
5.3.1.5	Protein electrophoresis	246
5.3.1.6	Protein transfer	247
5.3.1.7	Incubation with primary antibody	247
5.3.1.8	Detection of protein bands	247
5.3.1.9	Minigel staining	248
5.3.1.10	Gel drying	248
5.3.2	Mass spectrometry	249
5.3.3	Cytometric Bead Analysis	249
5.3.3.1	Labelling of detection antibody	250
5.3.3.2	Bead preparation	250
5.3.3.3	Capture antibody modification	251
5.3.3.4	Buffer exchange	251
5.3.3.5	Protein Conjugation	251
5.3.3.6	Confirmation of conjugation of beads	252
5.3.3.7	Cytometric analysis	252

5.3.3.8	Protein extraction	253
5.3.3.9	Detection of antigen in samples	253
5.3.4	Flow cytometry	254
5.3.4.1	Preparation of single cell suspension	254
5.3.4.2	Optimisation of permeabilisation and fixation	255
5.3.4.3	Antibody staining	255
5.3.4.4	Flow cytometry	256
5.3.4.5	Data analysis	257
5.3.5	Antimicrobial assays	257
5.3.6	Protein microarray	258
5.3.6.1	Sample preparation	259
5.3.6.2	Data analysis	259
5.3.7	Zymography	259
5.3.7.1	Sample preparation	260
5.3.7.2	MMP markers	261
5.3.7.3	Gel electrophoresis	262
5.3.7.4	Band intensity measurement	262
5.3.7.5	Statistical analysis	262
5.3.8	Macrophage assays	263
5.3.8.1	Macrophage culture	263
5.3.8.2	Extraction of peripheral blood mononuclear cells	264
5.3.8.3	Cell counting	265
5.3.8.4	Labelling of monocytes	266
5.3.8.5	Magnetic cell separation	266
5.3.8.6	Monocyte culture	266
5.3.8.7	Harvesting of macrophages	267
5.3.8.8	Confirmation of phenotype	267
5.3.8.9	Inflammation assays	268
5.3.8.10	Preparation of stimulants	269

5.3.8.11	Stimulation of macrophages	270
5.3.8.12	Cytometric bead preparation	270
5.3.8.13	Flow cytometry	271
5.3.9	Scanning electron microscopy	272
5.4	Results	272
5.4.1	Antimicrobial peptide detection	272
5.4.1.1	Western blotting	272
5.4.1.2	Cytometric bead analysis	276
5.4.1.3	Flow cytometry	278
5.4.2	Antimicrobial assays	281
5.4.3	Protein microarray	281
5.4.3.1	Matrix metalloprotease elution	285
5.4.4	Macrophage assays	288
5.4.5	Scanning electron microscopy	299
5.5	Discussion	300
5.5.1	Antimicrobial activity	300
5.5.2	The elution of metalloproteases	303
5.5.3	Macrophage suppression	306
5.6	Conclusion	310

6 CONCLUSION 311

6.1	Discussion	311
6.1.1	Significance of this study	311
6.1.1.1	Clinical trials	311
6.1.1.2	Optimisation of AM	312
6.1.1.3	Cross-linking of AM	313
6.1.1.4	Biological activity of AM	313
6.1.2	Further work	314
6.1.2.1	Future RCTs	314
6.1.2.2	Animal model	316

6.1.2.3 Tissue engineering	318
6.2 Conclusion	318
References	320
Appendix A	380

List of Figures

1.1	Blast injury to face and eyes	5
1.2	Birmingham Eye Trauma Terminology	6
1.3	Corneal repair mechanisms	8
1.4	Human amnion and chorion	11
2.1	Study selection	49
2.2	Included patients	54
2.3	Survival analysis of epithelial defects	59
3.1	Trehalose forms	75
3.2	Preparation of AM	81
3.3	DVS instrument	84
3.4	Multifrequency moduli and $\tan \delta$ of PMMA	91
3.5	DMA of v-d AM sample	92
3.6	XRD instrument	95
3.7	Drying curves of 0% and 10% v-d AM	101
3.8	Water vapour sorption	103
3.9	Sorption-desorption isotherms	105
3.10	Young and Nelson plots of 0% and 10% v-d AM	106
3.11	TGA plots of v-d AM and trehalose	108
3.12	First derivatives	109
3.13	Comparison of drying methods	110
3.14	Closed pan TGA	111

3.15 Ramp mode DSC	113
3.16 Cyclic DSC of trehalose:PBS	114
3.17 Cyclic DSC of 0%, 5% and 10% v-d AM	115
3.18 Frequency sweep DMA	117
3.19 Humidity-sweep DMA	119
3.20 Humidity sweep DMA (2)	120
3.21 Temperature sweep DMA of 0% v-d AM (1)	122
3.22 Temperature sweep DMA (2)	123
3.23 Temperature-sweep DMA of 5% v-d AM	124
3.24 Temperature sweep DMA of 5% and 10% v-d AM	126
3.25 Moduli and $\tan \delta$ of 0%, 5% and 10% v-d AM	127
3.26 XRD of v-d AM	128
3.27 FTIR absorbance spectra	130
3.28 FTIR of v-d AM	131
3.29 Scores and loadings plots	133
3.30 Chemical species	135
4.1 Phases of stress-strain behaviour in soft tissue	155
4.2 Force-displacement nanoindentation plot	160
4.3 Cross-linking mechanism	162
4.4 Uniaxial testing of AM strips	173
4.5 Uniaxial test data filtration	175
4.6 Nominal stress versus stretch ratio	177
4.7 Experimental and model curves	179
4.8 Transparency assay	192
4.9 SEM of fresh and v-d AM epithelium	193
4.10 SEM of collagenous layers	194
4.11 SEM images of 10% v-d AM	195
4.12 Accelerated degradation assay	196
4.13 Cross-section of v-d AM	197

4.14	TEM images of fresh and v-d AEC	198
4.15	TEM of denuded v-d AM	199
4.16	IFD measurements	200
4.17	AFM images of v-d AM	201
4.18	Optical microscopy (× 40)	202
4.19	Acoustic impedance tests	211
4.20	AM collagen extract	212
4.21	Mass spectrometry bands	213
5.1	Western blots of hBD3	274
5.2	Western blots of hBD1 and LL-37	275
5.3	CBA assay for LL-37	277
5.4	Flow cytometry optimisation	279
5.5	Flow cytometry for AMPs (1)	280
5.6	Flow cytometry (2)	282
5.7	MMPs and TIMPs in fresh AM	283
5.8	Protein microarrays of MMPs and TIMPs	284
5.9	MMP-2 and MMP-9 zymography markers	285
5.10	Zymography of fresh, v-d and f-t AM	286
5.11	Elution of MMP-2 and MMP-9	287
5.12	MMP-2 band intensity	288
5.13	Activated macrophage markers	289
5.14	Macrophage Assay 2	290
5.15	Macrophage Assay 3	292
5.16	Macrophage Assay 4	294
5.17	Macrophage Assay 6	296
5.18	Macrophage Assay 7	298
5.19	Macrophage adherence	299
5.20	Suppression of inflammation by AM	309

List of Tables

1.1	Composition of human AM	13
1.2	Applications of AM in ophthalmic surgery	17
2.1	Roper-Hall classification	35
2.2	Dua classification	35
2.3	Prospective studies/RCTs	51
2.4	Retrospective series	52
2.5	Risk of bias summary figure	55
2.6	AMT versus medical therapy	58
2.7	Summary of findings, moderate burns	60
2.8	Summary of findings, severe burns	61
3.1	Drying curve parameters	101
3.2	Water vapour sorption of v-d AM	102
3.3	Young and Nelson parameters, v-d AM	104
3.4	TGA events at 10°C min ⁻¹	107
3.5	TGA events at 5°C min ⁻¹	110
3.6	Thermal reversal temperatures by closed pan TGA	112
3.7	Enthalpy values of DSC endotherms	116
3.8	Moduli of v-d AM	118
3.9	T_g events of 0%, 5% 10% v-d AM	125
3.10	Chemical species identified by PCA	132
3.11	Summary of findings	136

4.1	Non-collagenous AM matrix proteins	151
4.2	Mascot Peptide Summary Report data	187
4.3	UTS and ΔL of AM	205
4.4	Stress-strain measurements by AM category	207
4.5	Modelling data by AM category	208
4.6	Modulus, contact hardness and plasticity	210
4.7	Mascot Peptide Summary Report	213
4.8	Uniaxial tests of riboflavin/UVA-treated AM	215
5.1	AMP antibodies	242
5.2	Western blotting of AMPs	243
5.3	Primary antibodies, flow cytometry	256
5.4	Culture medium	263
5.5	Markers of activated macrophages	268
5.6	Macrophage assays	269
5.7	Mascot Peptide Summary Report	275
5.8	LL-37 levels in AM	276
5.9	AMP fluorescence per AM	278
5.10	Median levels of MMPs and TIMPs	283
5.11	Intensity values, MMP-2	287
5.12	Cytokine levels, Assay 2	291
5.13	Cytokine levels, Assay 3	292
5.14	Cytokine levels, Assay 4	293
5.15	Cytokine levels, Assay 6	295
5.16	Cytokine levels, Assay 7	297
5.17	Mean cytokine levels, Assay 7	297

ABBREVIATIONS

Δ Np63	N-terminal truncated isoform of p63
ABCG2	Adenosine triphosphate-binding cassette sub-family G member 2
AEC	Amniotic epithelial cells
AFM	Atomic force microscopy
AM	Amniotic membrane
AMP	Antimicrobial peptide
ANOVA	Analysis of variance
AMT	Amniotic membrane transplantation
AP	Alkaline phosphatase
APC	Allophycocyanin
APES	3-aminopropyltriethoxysilane
ARRIVE	Animal Research: Reporting of In Vivo Experiments
ATR	Attenuated total reflectance
A_w	Water activity
BCIP	5-Bromo-4-chloro-3-indolyl phosphate
BDNF	Brain-derived neurotrophic factor
BET	Brunauer, Emmet and Teller
Bis-Tris	2-[Bis(2-hydroxyethyl)amino]-2-(hydroxymethyl)-1,3-propanediol
BM	Basement membrane
BSA	Bovine serum albumin

BSS	Balanced salt solution
CBA	Cytometric bead analysis
CD	Cluster of designation
CEC	Corneal epithelial cells
C_p	Heat capacity
DAPI	4', 6-diamidino-2-phenylindole
DI	De-ionised
DMA	Dynamic mechanical analysis
DMEM	Dulbecco's modified Eagle medium
DMSO	Dimethylsulfoxide
DMT	Derjaguin-Müller-Toporov
DSC	Differential scanning calorimetry
DTT	Dithiothreitol
DVS	Dynamic vapour sorption
E'	Modulus
E''	Loss modulus
ECM	Extracellular matrix
EDC	1-Ethyl-3-(3-dimethylaminopropyl) carbodiimide hydrochloride
EDTA	Ethylenediaminetetraacetic acid
EGF	Epidermal growth factor
FA	Formaldehyde
FasL	Fas ligand

FBS	Fetal bovine serum
FCS	Fetal calf serum
FITC	Fluorescein isothiocyanate
FPL	French press lysate (<i>Pseudomonas</i> antigen)
F-t	Freeze-thawed
FTIR	Fourier transform infrared spectroscopy
Gly	Glycine
GM-CSF	Granulocyte-macrophage colony-stimulating factor
GRADE	Grading of Recommendations Assessment, Development and Evaluation
H&E	Haematoxylin and eosin
hBD	Human beta defensin
hCAP-18	Human cathelicidin
HEPES	4-(2-hydroxyethyl)-1-piperazineethanesulfonic acid
HGF	Hepatocyte growth factor
HLA	Human leukocyte antigen
HPLC	High performance liquid chromatography
HUGO	Human Genome Organisation
Hyp	4-Hydroxyproline
IED	Improvised explosive device
IFD	Inter-fibrillar distance
IFN γ	Interferon-gamma

Ig	Immunoglobulin
IL-1	Interleukin 1
ISO	International Organization for Standardization
KGF	Keratinocyte growth factor
LB	Lysogeny broth
LC-MS	Liquid chromatography - mass spectrometry
LDS	Lithium dodecyl sulfate
LEAP	Liver expressed antimicrobial peptide
LESC	Limbal epithelial stem cell
LPS	Lipopolysacharide
LSC	Limbal stem cell
LSCD	Limbal stem cell deficiency
M Φ	Macrophages
MACS	Magnetic-Activated Cell Separation
MANOVA	Multivariate analysis of variance
MCP	Monocyte chemotactic protein
Md	Median
MD	Mean difference
MES	2-(N-morpholino) ethanesulfonic acid
MFI	Mean (or median) fluorescence intensity
MIF	Macrophage migration inhibitory factor
MIP	Macrophage inflammatory protein

MMP	Matrix metalloprotease
MOWSE	Molecular weight search
mRNA	Messenger RNA
MS	Mass spectrometry
MT1-MMP	Membrane-tethered MMP
MVA	Multivariate analysis
MWCO	Molecular weight cut-off
NBT	Nitro blue tetrazolium chloride
NCBR	National Centre for Biotechnology Information
NEM	N-Ethylmaleimide
NGF	Nerve growth factor
NGS	Normal goat serum
NNTB	Number needed to treat for 1 patient to benefit
NNTH	Number needed to treat for 1 patient to suffer harm
NT-3	Neurotrophin-3
OCT	Optimal cutting temperature
OSR	Ocular surface reconstruction
PAA	Peracetic acid
PAGE	Polyacrylamide gel electrophoresis
PBMC	Peripheral blood mononuclear cells
PBS	Phosphate-buffered saline
PCA	Principal component analysis

PCR	Polymerase chain reaction
PCy5	Phycoerythrin-coupled cyanin 5
PDGF	Platelet-derived growth factor
PDF	Powder diffraction files
PED	Persistent epithelial defect
PEDF	Pigment epithelium-derived factor
PEG	Polyethylene glycol
PGE ₂	Prostaglandin E ₂
PLGA	Polylactic co-glycolic acid
PMN	Polymorphonuclear cells
PRK	Photorefractive keratectomy
Pro	Proline
PROM	Premature rupture of the membranes
PTFE	Polytetrafluoroethylene
PE	Phycoerythrin
pHEMA	Poly-hydroxy ethyl methacrylate
PMMA	Polymethyl methacrylate
PP/EVOH	Polypropylene/ethylene alcohol vinyl
PVDF	Polyvinylidene fluoride
Q-Tof	Quadrupole-Time of flight
RA	Receptor antagonist
RANTES	Regulated upon activation, normal T-cell expressed and secreted

Rbf	Riboflavin-A
RCF	Relative centrifugal force
RH	Relative humidity
RMS	Root-mean-squared error
RNase	Ribonuclease
R-PE	R-Phycoerythrin
RPMI	Roswell Park Memorial Institute
RT	Room temperature
<i>SD</i>	Standard deviation
SDS	Sodium dodecyl sulfate
SJS	Stevens-Johnson syndrome
SLPI	Secretory leukocyte protease inhibitor
SL	Spongy layer
SMCC	Succinimidyl-4-(N-maleimidomethyl) cyclohexane-1-carboxylate
Smad3	Small mothers against decapentaplegic homolog 3
TBS	Tris Buffered saline
TBST	Tris-buffered saline containing 0.1% Tween 20
TBS-TM	5% non-fat dry milk in TBST
TBST _x	Tris-buffered saline containing 1% Triton X-100
TEN	Toxic epidermal necrolysis
<i>T_g</i>	Glass transition
TG	Transglutaminase

TGA	Thermogravimetric analysis
TGF	Transforming growth factor
TIMP	Tissue inhibitor of MMP
TLR	Toll-like receptor
TNF	Tumour necrosis factor
ToF-SIMS	Time-of-flight secondary ion mass spectrometry
tPA	Tissue plasminogen activator
TRAIL	TNF-related apoptosis-inducing ligand
TT-AM	Thermolysin-treated AM
UTS	Ultimate tensile strength
V-d	Vacuum-dried
VEGF	Vascular endothelial growth factor
XRD	X-ray diffraction

GLOSSARY OF SPECIALISED TERMS¹

Enthalpy (H): A thermodynamic quantity used to express energy change, enthalpy is the energy required to heat a material to a given temperature.

Tensile stress (σ): The failure strength of a material is measured in Newtons (N) and can be described as the ultimate tensile strength (UTS). Nominal tensile stress measure of the force pulling a material divided by the cross-sectional area, expressed as

$$\sigma^N = \frac{F}{A_0} = \frac{F}{w_0 t_0} \quad (1)$$

where F is force, and A_0 is the initial area (initial width, w_0 , multiplied by initial thickness, t_0). Stress is measured in Pascals (Pa, equal to Nm^{-2}). The ultimate stress, σ_f , represents the stress at failure. For measurements of true stress, σ^T , the instantaneous cross-sectional area A must be known. In the special case of incompressible materials, σ^T is calculated as

$$\sigma^T = \lambda_1 \sigma^N \quad (2)$$

where λ_1 is the ratio of final length to original length. Thus, A_0 measurements can be used to convert force-distance curves into true stress-strain curves.

Tensile strain (ε): ε is a measure of the amount of lengthening of a material (ΔL) in response to tensile stress divided by its original length, L

$$\varepsilon = \frac{\Delta L}{L} = \lambda_1 - 1 \quad (3)$$

As a ratio, ε does not take a unit, and it may be expressed as a percentage. Failure strain, ε_f , represents the limit of deformation. The area under the true stress-strain curve can be integrated to give a value of toughness,

¹Adapted from Ashby and Jones, 2012, Gabbott, 2008 and Adams, 2007.

measured in Joules (J) mm⁻³.

Poisson's ratio (ν): When a compliant material is stressed longitudinally, it gets thinner. The amount by which it narrows is defined by Poisson's ratio, the negative of the ratio of lateral strain to tensile strain. Perfectly incompressible elastic materials have a nominal ν of 0.5.

Shear modulus (G^*): This defines a material's response to shearing strains. It is defined as the ratio of shearing stress to shearing strain. G^* consists of the storage modulus, G' , related to the elastic part of the response, and the loss modulus, G'' , which corresponds to viscous behaviour.

Elastic modulus (E): The application of tensile force to a unit area (stress, σ) of a material results in a degree of deformation (strain, ϵ). The resistance encountered is an inherent feature of the material known as its modulus. For a purely elastic substance, σ is in phase with ϵ . E (stress divided by strain) takes the same unit as the numerator and is derived by measuring the gradient of a stress-strain curve. A higher E equates with increased stiffness. Elastic moduli for linearly elastic materials are defined through Hooke's law, which states that strain is proportional to stress:

$$\sigma = E\epsilon \quad (4)$$

or, at any given time point, t , the instantaneous derivative is represented by

$$E = \left. \frac{d\sigma}{d\epsilon} \right|_{\epsilon,t} \quad (5)$$

where E is known as Young's modulus, measured in Pa, and ϵ is strain. In a perfect, Hookean relationship between stress and strain, E does not change, and is related to G and ν by the equation

$$E = 2G(1 + \nu) \quad (6)$$

or, for an incompressible material,

$$E = 3G \quad (7)$$

The modulus of an elastic polymer (elastomer) such as rubber is between 10^7 and 10^8 Pa. Polycarbonate has a modulus of 2.6×10^9 Pa, whereas ice (H_2O) has a modulus of 9.1×10^9 Pa.

Viscoelasticity: Viscoelastic materials exhibit hysteresis, a dissipation of energy which manifests in varying degrees under cyclic loading at different deformation rates. Strain increases as a constant stress is applied (creep). Stress decreases as a constant strain is applied (stress relaxation). For a viscoelastic material, there is a phase lag between σ and ε . The in-phase tensile storage modulus, E' , represents the sample elasticity, whereas the out-of-phase loss modulus, E'' , represents the viscous portion. The phase lag between σ and ε is expressed as a phase angle, defined by the equation

$$\tan \delta = \frac{E''}{E'} \quad (8)$$

$\tan \delta$ is a measure of damping.

Glass transition (T_g): T_g , is a complex event that occurs over a range of temperatures and depends on many factors, e.g, the method of measurement. The vitrified (glassy) state is a characteristic of amorphous materials (having no crystalline structure, or long-range molecular order). In this state, molecules in amorphous materials (or in the amorphous portion of semi-crystalline materials) are disordered and immobile, and the material can be rigid and brittle. At the T_g temperature, the molecular relaxation time shortens. In amorphous and semi-crystalline polymers, this is manifest as an increase in malleability, and is known as a rubbery state. Other amorphous materials, such as sugars, may undergo a T_g from a highly viscous, immobilised state to a less viscous state. Plasticisation can occur as a

result of moisture absorption, resulting in reduction of the T_g temperature. In addition to the T_g , smaller thermal transitions characteristically occur in relation to events such as covalent cross-linking of molecules.

Water activity (A_w): A_w describes the extent to which water is available in a sample at equilibrium, and is dependent on temperature. The A_w of a sample can be described by the equation

$$A_w = \frac{p}{p_0} \quad (9)$$

where p is the vapor pressure of water in the sample, and p_0 is the vapor pressure of pure water at the same temperature, and it therefore has a value of between 0 and 1. When temperature equilibrium is observed between a sample and ambient air, the A_w equilibrates with ambient RH. Thus, the RH of a sample at equilibrium can be calculated simply by expressing A_w as a percentage:

$$RH = A_w \times 100\% \quad (10)$$

A_w directly influences organism growth and chemical reactions in the sample, thus affecting quality indicators such as physical appearance and shelf life. Most moulds normally require an A_w of at least 0.80 to grow.

Triple point: At subatmospheric pressures, the three states of water (ice, liquid and vapour) can co-exist at a certain temperature known as the triple point. Below this point, ice becomes converted directly into a gaseous state, a process called sublimation. For pure water, the triple point occurs at exactly 273.16 K (0.01°C) and a partial vapour pressure of 6.1173 millibars. However, the addition of sodium chloride results in a mixture that depresses the freezing point. This is known as a eutectic system, the eutectic point of a saturated solution of sodium chloride in water being -21.12°C.

Chapter 1

INTRODUCTION

1.1 Introduction

Human amniotic membrane (AM) is widely used in modern ophthalmic surgery. Although it is most commonly used in chronic eye conditions, it also has a place in the treatment of certain acute eye injuries, including burns. In military conflicts, eye injuries can be very serious, frequently resulting in the repatriation of combat troops. For logistical reasons of transport and storage, dried AM is more suitable for field use than frozen AM, which is the current standard in modern hospital settings. While treatment with AM may be useful, the parameters of treatment are incompletely defined. In addition, there are no clear guidelines for the preparation of dried AM for therapeutic use. If it is to be accepted by the surgical community, the quality of dried AM must be comparable with that of the more widely available frozen version, the biological properties of which are not fully understood.

1.1.1 Purpose and objectives

The purpose of this study is to investigate the potential of dried AM in the treatment of acute eye injuries in a military setting. The project objectives are as follows:

1. To conduct a systematic review of studies of the treatment of acute ocular surface burns with AM and to examine the quality of the evidence supporting its use.
2. To construct a framework for optimising dried AM with excipients, using moisture sorption, thermal, dynamic mechanical and surface analytical techniques.
3. To conduct a comparative study of the mechanical properties of therapeutic AM and to cross-link the collagenous matrix.
4. To investigate biological aspects of AM, including its antimicrobial properties and its effects on inflammation.

1.2 Literature review

1.2.1 Ocular surface injuries

Ocular surface injuries form a disparate group of injuries ranging from mild to severe.

1.2.1.1 Epidemiology of ocular surface trauma

In 1998, ocular surface injuries were estimated to be responsible for approximately 1.6 million cases of blindness, 2.3 million cases of bilateral low vision and 19 million cases of unilateral blindness or low vision worldwide (Négrel and Thylefors, 1998). The global annual incidence of monocular blindness, as a result of trauma and corneal ulceration, has been calculated to reach approximately two million (Whitcher et al., 2001). In a survey from rural India, the majority of victims of ocular trauma were young and male (Sinha, 2008).

1.2.1.2 Cost of ocular surface injuries

Visual impairment from any cause has profound psychological, economic and social consequences for patients (Wong et al., 2008), and the steep costs of avoidable visual loss makes it a highly important public health concern worldwide (Chiang et al., 2006). The burden of severe eye injuries is highest in developing countries, where chemical assaults give rise to least one third of all cases of ocular burns (Merle et al., 2008) and hospitals are ill-equipped to treat them (Adepoju et al., 2007). Even in developed countries, the economic burden of visual impairment is comparable to that of cancer, arthritis and dementia (Frick et al., 2007; Keeffe et al., 2009). Treatment can make a difference in the quantity and quality of vision, and can influence future quality of life and dependence on care services (Vu et al., 2005).

1.2.1.3 Ocular surface injuries in military conflict

In the case of military personnel, ocular surface burns are significant concerns for their employers and society at large. The frequency of battlefield ocular injuries is out of proportion to the surface area of the eye, and is common even in modern conflicts despite mandatory eye protection (Blanch and Scott, 2009). Anterior segment closed-globe injuries accounted for 103 out of 523 cases of globe and adnexal trauma sustained in combat by American troops during Operations Iraqi and Enduring Freedom between March 2003 and October 2006 (Weichel et al., 2008). Between July 2004 and May 2008, of 630 British soldiers surviving major trauma in hostile operations, 48 had significant eye injuries, including a number of blast injuries and burns to the ocular surface (Blanch et al., 2011). Moreover, corneal injuries are the commonest non-battle ocular injuries in recent conflicts in Iraq and Afghanistan (Ari, 2006), although most are treated in the theatre of operations and only infrequently require repatriation (Psolka et al., 2007).

1.2.1.4 Chemical warfare

Mustard agents, which cause cell death by alkylation of DNA, remain a threat to armed forces and civilians. Out of over 5000 soldiers and civilians treated for exposure to 2,2'-dichlorethyl sulphide (mustard gas) during the eight-year war between Iran and Iraq, 10% suffered ocular surface damage including persistent epithelial defects (Safarinejad et al., 2001). Two per cent progressed to corneal ulceration, neovascularisation, scarring and visual loss. The clinical picture of late complications from exposure to vesicant agents is identical to the presentation of limbal stem cell deficiency caused by chemical burns (Kadar et al., 2009).

1.2.1.5 Ballistic and blast injuries

Two distinct patterns of ocular injury occur in conflict, including direct ballistic trauma and burns. In military action, the gross effects of both these mechanisms can be observed in blast injuries from explosions (Abbotts et al., 2007). During an explosive blast, a primary pressure wave is followed by secondary fragmentation, tertiary physical displacement and quaternary thermal effects, leading to multiple injuries (Champion et al., 2009). The improvised explosive device (IED), seen in roadside mines and suicide bombings, was the main threat to troops in recent operations in Afghanistan (Ramasamy et al., 2009). IEDs cause high-pressure, superheated gaseous detonation products to eject at supersonic speed, together with fragments and ejecta from soil and clothing. Examples of IED injuries to the face and eyes are shown in figure 1.1. Fragmentation effects cause the majority of severe eye injuries (Morley et al., 2010). These are frequently bilateral, and may have a thermal component and may cause foreign material to be retained in the ocular surface (Weichel et al., 2008). Although superheated metallic fragments are sterile, the clothing and soil ejecta which frequently accompany blasts are not. In recent warfare in Afghanistan and Iraq, the

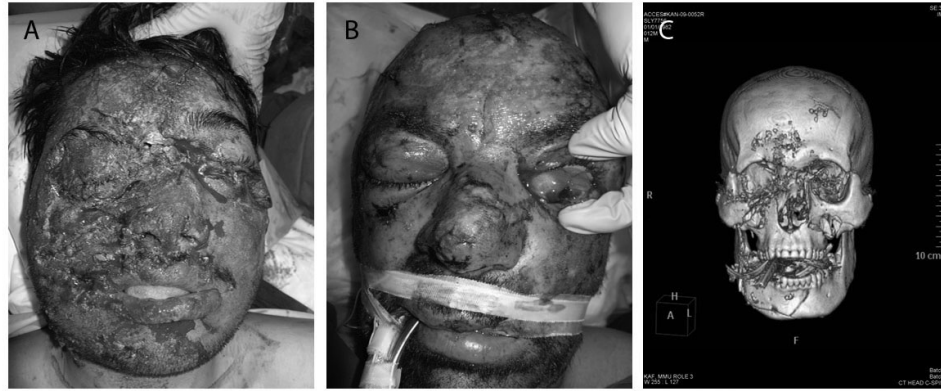


Figure 1.1: Blast injury to face and eyes

Images of blast injury patients from the conflict in Afghanistan (2001 - present) are shown. The injuries resulted from nearby detonation of an improvised explosive device. Gross effects of complex thermal and mechanical damage are visible in image A. The left eye has been sliced open by a projectile fragment in a second patient (image B). Image C shows a spiral computer-assisted tomography scan demonstrating multiple fragmentation injuries through bones of skull and orbits (courtesy of Lieutenant Colonel Neil McKenzie RAMC).

proportion of evacuated US personnel with significant ocular injuries was 13%, of whom 79% suffered blast injury with fragmentary munitions (Weichel and Colyer, 2008). The most common cause of severe ocular injury among troops during the Iraq Insurgency was the IED, occasionally augmented with gasoline jelly, producing complex trauma and thermal damage to the ocular surface (Mader et al., 2006).

1.2.1.6 Classification of ocular surface injuries

Assessing complex eye trauma produced by secondary blast injuries requires an understanding of the different mechanisms involved, including both mechanical and thermal components. These disparate mechanisms of wounding have different classifications. The Birmingham Eye Trauma Terminology (BETT) system, developed by Kuhn et al. (2002), is used to classify mechanical globe injuries (figure 1.2). The ocular trauma score (OTS) works in synchrony with this system to prognosticate visual outcome (Kuhn et al., 2002). In complex injuries in which the ocular surface is burned, this classification may be used in conjunction with a burns classification, discussed

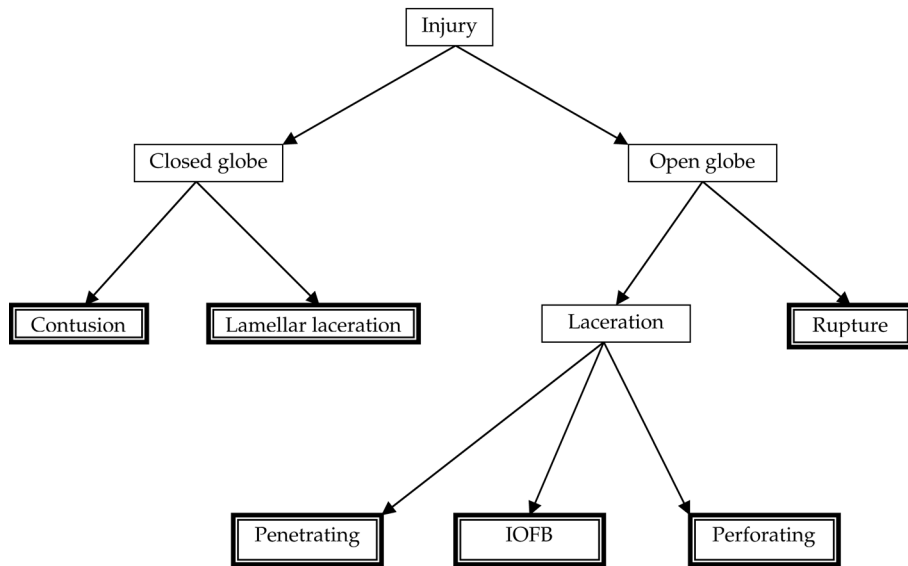


Figure 1.2: Birmingham Eye Trauma Terminology

The Birmingham Eye Trauma Terminology (BETT) system is used to classify mechanical globe injuries. IOFB, intra-ocular foreign body. Reproduced from Kuhn et al., 2002 with kind permission.

in detail in Chapter 2. Acute ocular injuries, including burns, mechanical trauma and mixed injuries are a complex group of pathologies without a single, unifying course of treatment.

1.2.2 Corneal wound healing

Corneal healing mechanisms are a useful platform from which to assess the therapeutic potential of AM. Regardless of the aetiology, corneal injuries have common motifs potentially amenable to manipulation by adjunct treatments. An immediate tissue response occurs following ocular surface injuries, mediated by local signalling mechanisms (Lim et al., 2003) and systemic signals which attract bone marrow-derived cells to the cornea, at least in animal models (Nakamura et al., 2005). Multiple pathways are activated, leading to a complex healing response which may result in further tissue destruction, fibrotic repair, or, potentially, regeneration of healthy corneal tissue (Fini, 1999).

1.2.2.1 Epithelial healing

Corneal epithelial healing is a highly regulated process requiring the coordination of multiple humoral and neural signalling pathways, involving lacrimal gland cells, keratocytes, epithelium and extracellular matrix (ECM) (Lu et al., 2001). Superficial cells initially slide towards the denuded surface. Presumed stem cell-derived cells in the central and peripheral cornea proliferate and migrate towards the injury, differentiating into stratified squamous epithelial layers until integrity is restored (Chang et al., 2008). Mammalian corneal epithelial cells (CECs) are thought to originate from slowly-dividing epithelial stem cells resident in specialised crypts at the corneal limbus (Dua et al., 2005), and possibly from cells retaining stem-like qualities ('stemness') in the limbal basal epithelium and distributed throughout the mammalian ocular surface (Majo et al., 2008).

1.2.2.2 Stromal healing

Renewed attention to the pathways governing fibrotic repair, remodelling and regeneration and has come from the refractive surgery community (Salomao and Wilson, 2009). The healing response involves communication between the epithelium and the stroma, a process in which interleukin (IL) 1α is a key player (Wilson et al., 1999). If the injury is limited to the epithelial layer, without damage to the underlying BM, apoptosis of the underlying stromal cells occurs following autocrine production of the Fas ligand (Wilson et al., 2003). This may be an evolutionary response protecting the cornea from inflammation and scarring (West-Mays and Dwivedi, 2006).

Evidence from wound-healing studies suggests that the stromal scarring response is switched on by injury to the basement membrane (BM) and driven by epithelial factors, of which the transforming growth factor (TGF) β isoform appears to be pivotal. In an animal model, blockage of TGF- β was shown to abrogate the myofibroblast response, reducing stromal fibro-

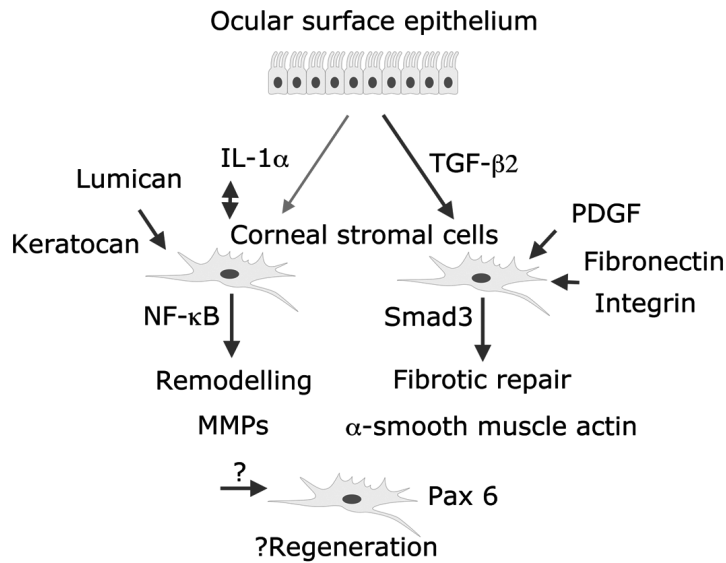


Figure 1.3: Corneal repair mechanisms

A schema of corneal repair mechanisms is shown. An injury that breaches the basement membrane stimulates fibrotic repair. After the initial response, remodelling is mediated by matrix metalloprotease enzymes. A regenerative response may also occur. *Smad3*, small mothers against decapentaplegic homolog 3; *NF-κB*, nuclear factor κ B; *Pax 6*, paired box protein 6; *IL-1*, interleukin-1; *TGF-β2*, transforming growth factor β2.

sis (Moller-Pedersen et al., 1998). The extent of the response depends on the size and irregularity of the injury. If the BM is breached, the epithelial cells communicate with stromal cells via cytokines and growth factors to trigger multiple pathways (Fini and Stramer, 2005). Some of these interactions are summarised in figure 1.3. A subpopulation of stromal keratocytes becomes activated following interaction with epithelial cell-derived *TGF-β2* (in a murine model), transforming into myofibroblasts via activation of the so-called small mothers against decapentaplegic homolog (*Smad*) 3 intracellular pathway (Fini and Stramer, 2005). Myofibroblast activation is characterised by expression of the α isoform of smooth muscle actin stress fibres, as well as suppression of cluster of designation molecule (CD) 34, proteoglycans and MMPs (Barbaro et al., 2006). Myofibroblast induction may require synergistic platelet-derived growth factor (PDGF) and fibronectin/integrin signalling (Jester et al., 2002).

Following the initial fibrotic response, there is a gradual shift towards remodelling. Animal gene targeting and knock-out models have shown that

keratocytes interact with ECM proteoglycans such as lumican and keratan activating intracellular signalling pathways (Kao, 2006). Autocrine secretion of IL-1 α may occur in keratocyte-derived fibroblasts, a mechanism that appears to involve transcription factor nuclear factor κ B (NF- κ B) (Fini and Stramer, 2005). This is a central transcription factor that regulates numerous biological processes on the ocular surface, including wound healing and angiogenesis (Lan et al., 2012). This up-regulates MMPs, which participate in remodelling the cornea after the BM has undergone repair (West-Mays et al., 1995).

Stromal cells expressing stem cell markers may retain stem cell characteristics capable of activating regenerative gene expression pathways (Du et al., 2005, 2007, 2009). Keratocyte progenitors are thought to express mesenchymal markers such as the paired box protein (Pax) 6 gene, and could contribute to stromal regeneration by secreting organised collagen and ECM (Funderburgh et al., 2005). Moreover, cultured keratocytes can express markers of relatively undifferentiated putative haematopoietic stem cells (Perrella et al., 2007). In a rabbit model, a rapid bone marrow reaction occurs after a corneal alkali injury, releasing progenitor cells into the circulation (Ye et al., 2008). This suggests that corneal wound-healing is the product of a co-ordinated system which simultaneously elicits repair, remodelling and regeneration.

1.2.3 The amniotic membrane

The precise role of AM in the complex process of corneal wound healing is unclear. In attempting to address the question of how AM might interact with with the ocular surface, it is necessary first to understand the basic development, structure and function of AM.

1.2.3.1 Embryological origins

AM is the avascular internal lining of the amniotic sac in which foetal growth occurs. Its embryological origins are reflected in its mature structure and function, since AM is genetically foetal tissue consisting of layers derived from both ectoderm (epithelium) and mesoderm (mesenchyme or stroma) (Bryant-Greenwood, 1998). The membrane origins lie in the formation of the blastocyst, an embryonic collection of cells which cavitates internally to form a space, the blastocoel, on the 5th day after fertilisation in primates (Enders et al., 1986). A mass of cells inside the blastocyst forms the bilaminar disc of primary ectoderm and endoderm, the precursors of the amniotic sac and the yolk sac (the developmental circulatory system) respectively. The external blastocyst layer differentiates into the trophoblast, the precursor of foetally-derived chorion and placenta. The bilaminar disc acquires an intermediate third layer, the mesoderm, by day 12. Mesoderm migrates to invest every structure in the blastocoel, including the yolk sac, the amniotic sac and the internal wall of the trophoblast, by day 18. Thus, the ectodermally-derived epithelial layer of AM becomes fused with a stromal layer of mesodermal origin. By day 23, the amniotic sac begins to envelop the formative foetus, which, in turn, internalises the yolk sac. The ectoderm of the fluid-filled amniotic sac is contiguous with the foetal skin and the future umbilical cord. The mesodermal outer layer of the amniotic sac eventually fuses with the mesodermal layer lining the trophoblast, obliterating the blastocoel. The obliterated blastocoel is filled with the spongy layer (see below).

1.2.3.2 Anatomy

Basic AM structures can be visualised by light and electron microscopy. It is composed of 5 layers, the innermost of which is composed of a single layer of cuboidal to columnar amniotic epithelial cells (AEC) (Bourne, 1960). Figure

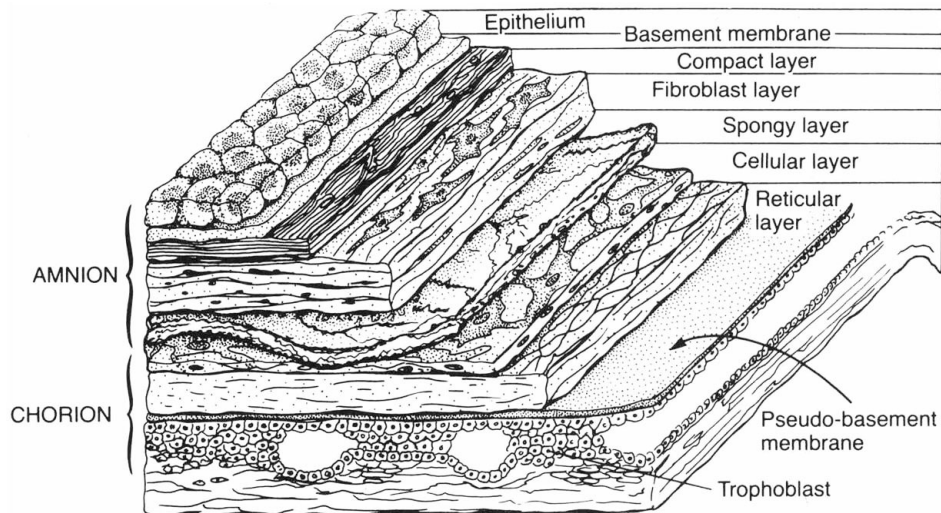


Figure 1.4: Human amnion and chorion

A diagram of a section through amnion and chorion is shown, highlighting the various layers. Reproduced from Bourne, 1960 by kind permission.

1.4 shows the general organisation of the multilayered amnion and chorion. The epithelial cells secrete collagen (Types III and IV) and non-collagenous proteins (laminin, entactin and proteoglycans) forming the basement membrane (BM) (Parry and Strauss, 1998). The BM overlies a compact and mechanically resistant reticular third layer containing interstitial collagens (types I and III), small amounts of minor fibrillar collagens (V, VI and VII) (Malak et al., 1993) and non-collagenous proteins including laminin, elastin, fibronectin, plasminogen and others. The third layer varies in thickness and provides the bulk of tensile strength (Bryant-Greenwood, 1998), and is secreted by mesenchymal cells (fibroblasts). These reside in a fourth layer of loose connective tissue (Parry and Strauss, 1998). AEC and stromal fibroblasts have different profiles of gene expression and protein translation, each contributing to the overall AM structure (Bryant-Greenwood, 1998). The final layer is the spongy layer (SL), which consists of jelly-like hyaluronan-rich mucopolysaccharide (Meinert et al., 2001) and permits a sliding movement between the AM and the chorion (Fawthrop and Ockleford, 1994). AM varies in thickness from 20 or so microns in the apical zone to a few hundred microns in the zone overlying the placenta, and contains no blood vessels. It

comprises a mechanically strong and biologically complex collagenous and elastin-rich interstitium designed to accommodate growth and eventually rupture.

1.2.3.3 Physiology

AM is an aneural membrane whose functions include homeostasis of the amniotic fluid (see review by Dua et al., 2004). It obtains nutrients from the surrounding fluid and the maternal decidua via a complex intercellular canalicular network (Bourne, 1966). A wide array of enzymes, such as prostaglandin synthase (Smieja et al., 1993), growth factors such as epidermal growth factor (EGF) and TGF- β 2 (Koizumi et al., 2000b), and cytokines such as IL-6 and IL-8 (Keelan et al., 1997) are associated with the membrane. Human AEC and mesenchymal cells both appear to release prostaglandins (Whittle et al., 2000), an occurrence associated with apoptosis prior to membrane rupture (Moore et al., 2003). The amniotic ECM is a complex biological medium, hosting a variety of autocrine and paracrine cascades (Bryant-Greenwood, 1998). These include the activation of MMPs and their inhibitors, which are thought have a critical function in the eventual rupture of the membrane (Arechavaleta-Velasco et al., 2002). Antimicrobial peptide mRNA has been found in AEC (King et al., 2007b; Stock et al., 2007), suggesting that the membrane can mediate an antimicrobial response. Amnion-derived mesenchymal cells may have progenitor characteristics, although it is not clear at present why this should be the case in a tissue predisposed eventually to be discarded (Dobrevva et al., 2010).

1.2.3.4 Structural composition

As a complex biological material, AM is a composite of structural, matriceal and biological components, and has a high water content (table 1.1). The composition of dry amnion from healthy donors has been calculated by var-

Table 1.1: Composition of human AM

Component	Composition	Reference
Total collagen	382 $\mu\text{g}/\text{mg}$ (<i>SD</i> 23)	Meinert et al. (2001)
Total collagen	419 $\mu\text{g}/\text{mg}$ (<i>SD</i> 73)	Prévost (2006)
Total collagen	357 $\mu\text{g}/\text{mg}$ (<i>SD</i> 68)	MacDermott and Landon (2000)
Glycosaminoglycans	213 $\mu\text{g}/\text{mg}$ (<i>SD</i> 31)	Prévost (2006)
Small proteoglycans	Approx. 2%	Meinert et al. (2001)
Hyaluronic acid	Approx. 2%	Meinert et al. (2001)
Elastin	Approx. 10 - 20%	Jabareen et al. (2009)
Glycoproteins	< 1%	Bhatia et al. (2007)
Water	86%	Prévost (2006)
Water	87.5% (<i>SD</i> 2.6)	Halaburt et al. (1989)
Water	87% (<i>SD</i> 4.2)	Prévost (2006)

SD, standard deviation. Composition given as dry weight.

ious authors. The total collagen content in the studies cited was calculated using the hydroxyproline assay described by Stegeman and Stalder (1967), which stipulates the hydroxyproline to collagen ratio to be 7.64:1. The extracellular matrix consists (in dry weight) of approximately 35-45% collagen, 10-20% sulphated glycosaminoglycans such as dermatan and chondroitin sulphate, 10-20% elastin, and smaller quantities of small proteoglycans (biglycan, decorin), hyaluronic acid, large proteoglycans and glycoproteins such as fibronectin. 10-15% of the dry weight is accounted for by bound water. There is less collagen but more elastin than other collagen-rich tissues such as skin (Park and Lakes, 1992).

1.2.4 Therapeutic application

1.2.4.1 Historical background

The idea of using AM therapeutically emerged nearly a century ago. The amniotic sac lining was first grafted to the skin by a pioneering plastic surgeon at the Johns Hopkins Hospital in Baltimore following a suggestion

from a medical student, but it had limited success (Davis, 1910). Two reports emerged in 1913 highlighting the potential of AM as a skin graft for burns (Sabella, 1913; Stern, 1913). The first documented use of foetal membranes in ophthalmic surgery was in 1938 by de Rötth, of Budapest, who used amnion still attached to chorion as a conjunctival substitute to treat 5 cases of symblepharon (de Rötth, 1940). Of these cases, one was deemed a partial success.

Wider applications for AM were found in diverse surgical specialities (Trelford and Trelford-Sauder, 1979). In neurosurgery, AM separated from chorion and stored in 70% ethanol, termed ‘amnioplastin’, was used to fill in defects of the dura mater (Chao et al., 1940). Reports of a case of lime burn (Lavery, 1946) and of a series of 56 chemical and 2 firework injuries (Sorsby and Symons, 1946; Sorsby et al., 1947) treated with amnioplastin patching within one or two days of injury suggested favourable outcomes. The tissue, prepared in salt solutions rather than ethanol, appeared to function as a splint for proliferating tissue. It was recognised that AM might be a suitable biomaterial for treating ophthalmic injuries on the battlefield (Dansey-Browning, 1949), and it was thought to improve comfort and prevent symblepharon (Shafto, 1950).

For unclear reasons, the documented use of AM in ophthalmic surgery almost completely disappeared from English language scientific literature for a period of almost forty-five years thereafter. A study on the treatment of corneal ulcers with AM emerged from India during this period (Shukla, 1962). In contrast to the dearth of reports in English after 1950, a number of publications on the ophthalmological applications of AM appeared in Eastern bloc countries (Zankiewicz, 1960; Wolsztyn, 1951; Stoenchev, 1953; Makeeva, 1983).

Samples of this ‘allotransplant’ were obtained by Dr Horacio Serrano following a visit to Russia, and used in Venezuela in 1988 without knowledge

of its true biological identity (Dua et al., 2004). Following its histological identification, AM was again promoted as a conjunctival substitute (Batlle and Perdomo, 1993), and its use in ophthalmic surgery was further conceptualised by Scheffer Tseng and his colleagues at the Bascom Palmer Eye Institute in Miami. Following experiments on rabbit eyes, it was suggested that AM had a possible role in promoting transformation of conjunctival epithelium to a corneal phenotype, thus significantly enhancing ocular surface reconstruction (OSR) and preventing neovascularisation of the stem cell-deficient ocular surface (Kim and Tseng, 1995b,a). Soon afterwards, reports emerged of the treatment of corneal PEDs and pterygium with AM (Lee and Tseng, 1997; Prabhasawat et al., 1997). Over the next few years, AM became more and more accepted into mainstream ophthalmic surgical practice.

1.2.4.2 AM in modern ophthalmic surgery

Since its re-introduction into modern ophthalmic surgery, the number of therapeutic indications for AM treatment has risen steadily (Dua et al., 2004). Its versatility is perhaps best illustrated by an example of its potential use over the course of an ocular burn. In the acute and early phases of a burn, AM can be sutured over the entire ocular surface as a surgical dressing (Meller et al., 2000). Alternatively, it can be wrapped around a conformer and inserted between inflamed forniceal tissues. In later phases, the scarred and contracted conjunctival fornices can be managed by transplanting AM to restore the gross anatomy (Solomon et al., 2003). However, mucous membrane, buccal and basal turbinate mucosae are considered more robust (De Sousa et al., 2009). Multilayered AMT can be performed for refractory corneal melts and deep ulcers in danger of imminent perforation (Kruse et al., 1999; Hanada et al., 2001), and small perforations can be managed with AMT in conjunction with cyanoacrylate (Su and Lin,

2000) and fibrin glues (Hick et al., 2005). The AM scaffold becomes incorporated into the host tissue, adding bulk to the stroma and supporting fibrotic change (Nubile et al., 2011). Furthermore, AM can be used to augment the treatment of bacterial keratitis, an effect of prolonging the action of topically applied antibiotics (Gicquel et al., 2007). Inflammatory cells stick to the stromal aspect of AM, which may promote anti-inflammatory activity (Shimmura et al., 2001). The size of the AM transplant can be customised according to need. Thus, it can be applied as a limited corneal inlay graft - 1 or 2 mm in diameter - to treat a persistent epithelial defect (PED), or as a 5 cm diameter dressing for the entire ocular surface. Several different modalities of AM treatment can be applied simultaneously (Letko et al., 2001). Besides being widely used to treat the human ocular surface, AM has an established role in the treatment of veterinary eye injuries (e.g., Kim et al., 2009).

The evolution of AM use in ophthalmic surgery is illustrated by the 12 applications listed in chronological order in table 1.2. It can be seen that the majority of these applications make use of the physical properties of AM, and do not require additional biological functions. Biological factors are invoked in the treatment of acute burns, but this is speculative. A survey of the first 233 cases of AMT in the United Kingdom, carried out between June 1998 and December 2002, showed that the most common indications for treatment were PEDs (37.8%) followed by OSR (28.8%), treatment of painful bullous keratopathy (18.0%) and acute chemical injuries (18.0%) (Saw et al., 2007). These functions rely primarily on the properties of AM as a membrane, with any additional biological functions being suggested rather than demonstrated.

Table 1.2: Applications of AM in ophthalmic surgery

Function	Surgical application	Examples of pathology	Primary reference
Substitute for conjunctiva	Conjunctival graft	Conjunctival defect	de Rötth (1940)
Surgical dressing	Ocular surface patch (stroma down)	Acute burn	Sorsby and Symons (1946)
Spacer to prevent symblepharon	Forniceal patch	Acute burn	Sorsby and Symons (1946)
Corneal patch	Multilayered overlay	Corneal ulcer	Shukla (1962)
Substrate for epithelial growth	Corneal inlay	PED	Lee and Tseng (1997)
Scaffold for stromal matrix growth	Multilayered graft	Reconstruction of ulcers	Kruse et al. (1999)
Patch to prevent leak	Scleral patch	Leaking bleb	Budenz et al. (2000)
Substrate for stem cell expansion	Ocular surface reconstruction	Diffuse LSCD	Tsai et al. (2000)
Plug for corneal perforations	Corneal underlay	Acute perforation	Su and Lin (2000)
Source of soluble factors	Ocular surface patch (stroma up)	Acute burn	Meller et al. (2000)
Trap for inflammatory cells	Bilayered patch (stroma up)	Inflammation	Shimmura et al. (2001)
Reservoir for topical antibiotics	Multilayered corneal inlay	Infectious keratitis	Gicquel et al. (2007)

PED, persistent epithelial defect; LSCD, limbal stem cell deficiency.

1.2.4.3 AMT in stem cell deficiency

AM is commonly used as an adjunct in the rehabilitation of eyes with limbal stem cell deficiency (LSCD) (Cauchi et al., 2008). In partial LSCD, AM can be applied as an inlay within a PED (Anderson et al., 2001). When applied with the epithelial side up, it facilitates the migration and adhesion of epithelial cells (Lee and Tseng, 1997). In many cases, however, it is difficult to identify a treatment effect because the extent of LSC loss at the outset may be unclear (Shimmura and Tsubota, 2008). In total LSCD, AM can be applied as a protective patch overlying limbal tissue grafts (Tsubota et al., 1996). Alternatively, autologous LSCs can be expanded directly onto AM prior to transplantation (Tsai et al., 2000). AM can be denuded to facilitate the expansion of *ex vivo* LSC colonies (Koizumi et al., 2000b), producing a stratified corneal epithelium Koizumi et al. (2001a). Cultivated autologous oral mucosal epithelial sheets on denuded AM substrates are a more recent development (Nakamura and Kinoshita, 2003; Kinoshita and Nakamura, 2004; Inatomi et al., 2006). Patients with ocular surface disorders such as Stevens-Johnson syndrome (SJS) and chemical injuries have been treated with epithelial sheets cultivated on AM both from corneal LSCs (Koizumi et al., 2001b; Shimazaki et al., 2002) and autologous oral mucosal stem cells (Nakamura et al., 2004; Ma et al., 2009). AM is not an obligatory carrier, and methods of expanding LSC on fibrin have been developed (Rama et al., 2010).

1.2.4.4 Mechanism of action of AMT

The putative mechanisms of action of AM on the ocular surface broadly fall into two categories: those that can be explained by directly observable physical interactions between the membrane and the eye, and those that are implied by presumed biological properties of AM. In the first of these categories, AM functions as a biocompatible membrane with empirically ob-

servable benefits, such as sealing a perforation (Duchesne et al., 2001) or preventing a leak from a surgical procedure (Budenz et al., 2000). In the second category, a biological property is attributed to AM over and above its self-evident value as a biomaterial, such as promotion of epithelial healing and suppression of inflammation (Tseng et al., 2004).

Many of the useful effects of AM are due to its gross physical properties as a thin membrane. Placing an AM bandage on denuded cornea appears to reduce pain (Dua et al., 2004). This effect may occur by reducing eyelid friction over the injured surface whilst allowing oxygen transfer to take place (Baum, 2002).

In addition, AM may function as a physical barrier to inflammatory cells and as a source of anti-inflammatory and pro-epithelial mediators, such as fibronectin and epidermal growth factor. These constitute the properties of a 'biological dressing' (Talmi et al., 1990; Tseng et al., 2004). AM is known to express biological factors, such as anti-inflammatory and anti-angiogenic proteins (Hao et al., 2000). Preserved AM contains mRNA for numerous growth factors (e.g., EGF, TGF- α and - β isoforms) and their protein products in both the stroma and the epithelium (Koizumi et al., 2000b). Soluble AM-derived factors appear to be capable of suppressing the immune response *in vitro* (Li et al., 2005). Conditioned supernatants from AM cultures suppress alloreactive T lymphocytes in mice, an action attributed to soluble inhibitory factors (Ueta et al., 2002).

However, the putative role of biological factors in therapeutic AM is controversial. Since AM epithelial and stromal cells are not considered viable following preparation (Dua et al., 2004), the contribution of biological factors is limited to those produced before preservation. AEC undergo a process of programmed cell death before the onset of labour, suggesting that these cells may be declining by the time of harvesting of AM for therapeutic application (Lei et al., 1996). Some of the factors have opposing effects, not

all of which can be expected to be positive (Dua et al., 2004). For example, regulatory proteins retained in therapeutic AM include TGF- β 1 (Hopkinson et al., 2006b), which may cause scarring. Similarly, anti-angiogenic factors such as TIMP-1 (Hao et al., 2000) may promote ischaemia. Furthermore, the concentration of biological factors in therapeutic AM is variable, both due to its heterogeneity (Gicquel et al., 2009) and as a result of processing (Hopkinson et al., 2006b). The lack of evidence surrounding the pharmaceutical use of AM indicates that the benefits of AMT in some conditions are as yet unproven, and suggest an important need for clinical research into this treatment to continue. Since the promotion of AMT may be driven by commercial interests, it is particularly important to clarify its true potential.

1.2.4.5 Animal models

Experimental animal models have been used to explore the potential of AM as a dressing for a range of ocular injuries with diverse causes. These have produced variable results. A study of alcohol-induced epithelial injuries in a canine model reported faster healing in eyes treated with AMT (Kim et al., 2009), while there was no difference in the healing rate of mechanical corneal wounds in rabbit eyes treated with AM (Libera et al., 2008). In another study, *ex vivo* rabbit corneas were placed in an air-interface organ culture and treated with 20 μ l of amniotic fluid every eight hours, showed significantly faster rates of re-epithelialisation compared to controls (Castro-Combs et al., 2008). Conditioned culture medium from human AEC suppressed corneal neovascularisation in experimental mice (Kamiya et al., 2005). In a rabbit model of alkali corneal burns, AMT produced faster epithelial healing (Kim et al., 2000). In addition, AM acted as a barrier to neutrophils, reducing levels of proteinase activity. In similar experiments, AMT was more effective at promoting epithelialisation than autologous serum or preservative-free artificial tears (Shahriari et al., 2008). Another study doc-

umented fewer α -SMA cells and reduced expression of MMPs 14 days after an alkali burn in rabbit eyes treated with AMT (Takahashi et al., 2007). Laser-induced corneal wound models have been helpful in understanding the effects of AM on stromal injuries. In a rabbit model, AM patching for 48 hours after excimer laser to the corneas resulted in significantly reduced numbers of keratocytes infiltrating the anterior stroma (Choi et al., 1998). Similar studies reported significantly faster epithelial healing (Woo et al., 2001) and reduced corneal haze (Wang et al., 2001). In one series, rabbit eyes with induced total LSCD recovered a corneal epithelial phenotype following treatment with AMT, suggesting LSC recovery (Kim and Tseng, 1995a,b). In contrast, in similar experiments by Koizumi et al. (2000b), all the rabbit eyes had persistent total epithelial defects. While many of these studies suggest a benefit of AMT, the risk of bias is sometimes ignored.

1.2.4.6 Surgical application

There are different methods of applying AM to the ocular surface, whether as a temporary patch or as a graft. As a temporary patch, AM is frequently sutured onto the ocular surface, although it can also be applied wrapped around a symblepharon ring conformer. There are reports of difficulty in keeping AM fixated to the ocular surface (Gris et al., 2002), which has led to the use of adhesives such as fibrin glue (Sekiyama et al., 2007; Kheirkhah et al., 2008), chemical bioadhesives (Takaoka et al., 2008) and medical grade glues such 2-octyl-cyanoacrylate (Kitagawa et al., 2009) to keep it in place. AM coated with 2-octyl-cyanoacrylate has been used effectively as a primary treatment for corneal perforations up to 3 mm in diameter (Kitagawa et al., 2011). When AM is applied as a graft, the corneal epithelium grows over the AM, which slowly disintegrates, obviating the need for an additional procedure to remove sutures. The integration of an AM allograft into corneal tissue is an active process which results in the formation of adhesion struc-

tures, desmosomes and hemidesmosomes (Resch et al., 2006). Besides promoting CEC migration, AM appears to have an important effect on corneal stromal cells, providing them with a collagenous AM scaffold into which they migrate and proliferate (Said et al., 2009). This may have important implications for repair of stromal damage.

1.2.4.7 Clinical use of dried AM

A dried AM product, known as 'hyper-dry-amnion' was developed for clinical use in Japan as a non-immunogenic alternative to frozen AM (Toda et al., 2007). It had the advantage of being easy to handle by ophthalmic surgeons, and could be stored indefinitely at room temperature. It was applied clinically as a conjunctival replacement. Since then, clinical publications on the application of dried AM have been few, restricted to reports of corneal perforations and wound leaks (e.g., Kitagawa et al., 2009, 2011). Other centres have considered the potential of dried AM as an ocular biomaterial through the *in vitro* studies and animal models (e.g., Sekiyama et al., 2007; Nakamura et al., 2008; Libera et al., 2008). Lyophilised AM has also been used as a biological dressing in the treatment of skin burns, with apparently favourable results (Gajiwala and Gajiwala, 2004).

1.2.4.8 Limitations of treatment

While there are now numerous common indications for AM treatment, AM has been used in excess of its true potential Dua et al. (2004). Because of its early promise, the usefulness of AM has sometimes been overstated in the search for novel applications, often without evidence of benefit and despite the lack of RCTs (Bouchard and John, 2004). Even for its most common indications, AM treatment by no means guarantees success. When stringent outcome criteria were applied to a large series of cases, the success rate of AM treatments was less favourable than had been previously reported, with

many cases of treatment failure (Saw et al., 2007). Similarly, Maharajan et al. (2007) analysed 74 AMT procedures retrospectively, clearly defining objectives for AM treatment. High failure rates were found, especially where there was associated stem cell deficiency.

Significant heterogeneity between AM samples in terms of both physical attributes such as thickness and transparency (von Versen-Höynck et al., 2004; Cannon et al., 2007; von Versen-Hoeynck et al., 2008; Cannon et al., 2010) and biochemical components such as growth factors (Hopkinson et al., 2006b; Gicquel et al., 2009). These differences exist between donors and also between therapeutic samples obtained from a single donor, and the preparation process itself results in the depletion of factors. Although AM is widely used, there is no standard method of preparation and storage (Dua et al., 2010). The variability in AM, its preservation and its application constitute significant limitations of AM treatment.

The clinical use of AM has to be weighed against its potential risks and limitations (Rahman et al., 2009). With proper testing, the risk of donor transmission of infectious disease is negligible, but cannot be discounted entirely. Fungal and other corneal infections can occur after AMT, and must therefore be considered as a risk factor (Das et al., 2009). AM has the advantage of low immunogenicity (Wang et al., 2006), but the host can become sensitised to the donor AM epithelium major histocompatibility complex (MHC) class I antigens and reject future transplants (Hori et al., 2006). The possibility of sensitisation is indicated by a report of a steroid-responsive hypopyon in a patient who received sequential AM grafts from the same donor (Gabler and Lohmann, 2000). Serious adverse outcome of AM treatment have included corneal melting (Schechter et al., 2005).

1.2.5 AM procurement and preparation

1.2.5.1 Procurement

The use of AM is not risk-free, and carries an important risk of maternal disease transmission Rahman et al. (2009). To minimise this risk, potential AM donors undergo a formal consenting process in which social risk factors for communicable diseases are identified, and these patients are usually excluded from donation. Mandatory screening is carried out for a number of contagious diseases, including HIV, Hepatitis B and C and syphilis. Infection screening can be done by serological testing. This requires repeat testing after six months' quarantine to exclude the transmission of recently acquired, undiagnosed infections in seronegative mothers (Addis et al., 2001b). An alternative method is by polymerase chain reaction (PCR) of the donor tissue, along with tissue culture, which yields results within two weeks of birth. In developing countries in particular, this risk assessment is not as strict, and unpreserved tissue has been used to reconstruct the ocular surface (Mejía et al., 2000) and to treat acute burns (Uçakhan et al., 2002).

1.2.5.2 Preparation

After harvesting, therapeutic AM must be sterilised and preserved. The risk of bacterial contamination of donor AM is present in samples obtained by Caesarean section, and is increased in membranes obtained by vaginal delivery (Addis et al., 2001a). In most countries, donor AM is normally harvested in strict aseptic conditions after a caesarean section (Dua et al., 2004). Once it has been separated from the chorion and placenta, AM is typically washed several times in saline solution containing a cocktail of broad-spectrum antibiotics and antimycotics, and is then ready to be processed by freezing or drying for clinical use.

1.2.5.3 To denude or not to denude?

Cell viability is not considered necessary for AM to function as a biomaterial. In order to circumvent any allogeneic effects, researchers have developed cell-free AM matrices for tissue engineering purposes (Wilshaw et al., 2006; Portmann-Lanz et al., 2007). They used detergents to ensure the complete removal of cellular material from AM. Human AEC are rendered non-viable by glycerol preservation, by washing in water, by freezing and lyophilisation and by γ -irradiation (Hennerbichler et al., 2007). A number of leaders in the field of ocular surface reconstruction routinely remove the amniotic epithelium (Nakamura et al., 2003; Sangwan et al., 2003). Epithelial cell attachment and stratification may occur preferentially on denuded membrane, the cells forming significantly more desmosomes and junctional attachments than those cultured on intact AM (Koizumi et al., 2007). Limbal epithelial stem cell progeny may lose their stemness and become differentiated early on denuded AM, evidenced by the expression of markers of corneal basal epithelium (Grueterich and Tseng, 2002). Conversely, the limbal phenotype may persist longer on intact AM, giving rise to the conceptualisation of intact membrane as a 'surrogate niche' for stem cells (Grueterich et al., 2003; Li et al., 2006b; Dietrich-Ntoukas et al., 2012). Nonetheless, cell outgrowths of limbal explants cultured on intact membrane appear to lose staining for putative stem cell markers ABCG2 and Δ Np63 (Kolli et al., 2008). Shortt et al. (2009) did not find any difference in the expression of putative stem cell markers between cells cultured on intact and denuded membrane. Currently, the weight of evidence suggests that the clinical differences between intact and denuded AM are not significant, and therefore the debate concerning the retention of biological factors of AM is less relevant than is commonly supposed. AM epithelium can be removed using a variety of methods involving trypsin, dispase, ethylenediaminetetraacetic acid (EDTA), urea or ethanol in combination with mechanical scraping (see

review by Riau et al., 2010). One method uses thermolysin, which cleaves the epithelium away from the BM at the level of hemidesmosome complexes (Hopkinson et al., 2008).

1.2.5.4 Preservation by freezing

At present, the most common method of preserving AM is by freezing. The freezing of tissue for long-term storage - cryopreservation - is an area of expertise in the domain of mammalian reproductive technology, where gametes and embryos can be frozen in the presence of cryoprotectants and stored at -196°C (reviewed by Woods et al., 2004). Cryoprotectants are low-toxicity, highly soluble compounds that cause a profound drop in the intracellular freezing temperature, and include glycerol, dimethyl sulfoxide (DMSO), ethanediol and propanediol (Pegg, 2007). Each cell type requires a carefully optimised protocol of cryoprotectant selection and concentration, as well as cooling, freezing and thawing rates to maintain cell viability. Human ovarian tissue preservation, for example, is made possible either by staging programmed reductions of temperature, allowing water to diffuse out of the cell without ice crystallisation, or by a process known as vitrification, in which freezing is prevented by appropriate cryoprotectants (Keros et al., 2009). Without adequate cryoprotection, freezing of tissues results in irreversible cell damage. During chilling, cell membrane micro-domains aggregate together, leading to inappropriate signalling and ion leakage and rendering the cells non-viable (Crowe et al., 2003). As the temperature drops to below 0°C , uncontrolled freezing causes major damage to the cells due to the formation of ice crystals and the harmful concentration of solutes.

AM does not require vascular support for its function, making it an excellent candidate for cryobiological preservation. It is typically frozen in a 1:1 Dulbecco's Modified Eagle Medium (DMEM)/glycerol mixture at -80°C and thawed immediately before surgical application, although it can be refrig-

erated at 4°C for shorter periods (Hennerbichler et al., 2007). Glycerol does not protect the epithelium or prevent osmotic damage to the AM-derived cells (Woods et al., 2004). In contrast to reproductive cells, therefore, the cells do not usually retain any viability after cryopreservation in glycerol, and mitochondrial activity is abolished (Hennerbichler et al., 2007; Kruse et al., 2000). Under electron microscopy, the devitalised AEC have grossly altered morphology, detach from the BM and form vacuoles (Rejzek et al., 2001). Glycerol preservation may adversely affect the ability of AM to serve as a substrate for limbal stem cell expansion (Shortt et al., 2009). Nonetheless, useful factors may be retained within the damaged cell membrane, eventually becoming released on the ocular surface (Kruse et al., 2000). In keeping with Lee and Tseng's original method of cryopreservation (Lee and Tseng, 1997), both experimental and commercial methods of cryopreserving AM have continued to use 50% glycerol (Grueterich et al., 2002; Tsai et al., 2000). The most widely available commercial preparations of glycerol-cryopreserved AM include AmnioGraft® and ProKera®, both from Bio-Tissue, Inc. (Miami, USA), founded by Tseng in 1997. In the United Kingdom, AM is cryopreserved in tissue banks in a similar way, and supplied to the National Health Service following a period of quarantine.

DMSO is an alternative cryoprotectant used by some researchers and clinicians (e.g., Shimazaki et al., 1997). The viability of AEC following cryopreservation in DMSO has been estimated at 13-18% (Hennerbichler et al., 2007), $21.9 \pm 23.3\%$ (Wolbank et al., 2009), 40% (Rama et al., 2001) and over 50% (Kubo et al., 2001). DMSO-preserved AM was found to secrete significant quantities of factors such as IL-8, whereas factor release from glycerol-preserved AM was negligible (Wolbank et al., 2009). Although DMSO-preserved AM is often used to treated ocular surface conditions (Azua-Blanco et al., 1999; Daya et al., 2005; Shimazaki et al., 2002), the clinical effects of DMSO in comparison to glycerol are not fully understood, and it

may have toxic side effects. Thus, whether glycerol or DMSO can improve clinical aspects of AM is unknown. For most purposes, simple freezing of the intact AM in buffered saline at -80°C may be adequate for clinical use.

1.2.6 Dry preservation

Although therapeutic AM is most commonly frozen, dried preparations have distinct advantages, eliminating the need for a cold chain and permitting storage at room temperature (RT), thus reducing transportation and storage costs. In contrast to frozen tissue, dried AM can be deployed for field use. However, experience with this preparation is limited, and the impact of drying on the properties of AM is unclear. While dried AM can be reconstituted for use, rehydration is not mandatory, as the tissue can also be used in its dry form. Whether undertaken in the laboratory or on a commercial level, the principles of preservation are the same. Preserved biological tissues undergo degradation as a result of endogenous enzyme activation and exposure to exogenous (microbial or host) enzymes. These processes can be slowed by exposure to temperatures below the standard physiological range (freezing), or by removing the water medium in which enzymatic reactions take place (drying).

1.2.6.1 Commercial preparations

As a thin film, AM presents a large surface area for evaporation and can be dried quickly and efficiently by a variety of methods. Commercial preparations of dried AM include heat-dried products such as Acelagraft™ from Celgene Cellular Therapeutics (Cedar Knolls, NJ, USA), and AmbioDry™ (formerly made by Okto-Ophtho, Costa Mesa, California, US) (Chuck et al., 2004). Others include AmniSite-Cornea® (Bioland, Korea), which is reported to be lyophilised (Koh et al., 2007). One method of preparation makes use of far-infrared rays and microwaves to produce a hyper-dry tis-

sue (Kitagawa et al., 2009), whereas laboratory-based preparations of AM are typically air-dried (Singh et al., 2003; von Versen-Hoeynck et al., 2008).

1.2.6.2 Sterilisation

Dried preparations can be sterilised by exposure to 25 kGy of γ -irradiation, which gives the tissue a high sterility assurance level (Singh et al., 2007b). There is evidence that γ -irradiation can weaken the collagen fibres in AM (Fujisato et al., 1999), although this may not be functionally significant (Nakamura et al., 2004; Singh et al., 2007). Low-dose electron beam irradiation can also be used, but may significantly weaken the tissue (Chuck et al., 2004). Irradiation can be performed after vacuum-packaging the product. An alternative method of sterilisation involves pre-soaking the membrane in peracetic acid (PAA)/ethanol solution (Wilshaw et al., 2006).

1.2.7 Biosynthetic alternatives

Although AM has proven to be a useful surgical biomaterial, it has clear disadvantages, such as variability and imperfect transparency. A number of biosynthetic alternatives to AMT have recently emerged, offering improvements in hygiene and consistency (Yiu et al., 2007). These have included a thermosensitive hydrogel bandage developed from polyethylene glycol and polylactic co-glycolic acid (PEG/PLGA) (Pratoomsoot et al., 2008). Stored cold, it undergoes gelation upon contact with the ocular surface. Hydrogels and collagen shields have been used to treat surgically induced wounds following cataract surgery (Dell et al., 2011). Recombinant human collagen-phosphorylcholine hydrogels implanted onto rabbit eyes that had received severe alkali burns two months earlier were found to promote nerve and cell regeneration and to delay neovascularisation (Hackett et al., 2011).

Chapter 2

AMNIOTIC MEMBRANE TREATMENT OF ACUTE

OCULAR BURNS

2.1 Introduction

Ocular surface burns can constitute true ophthalmic emergencies involving the eyelids and both external and internal ocular structures. They can be devastating injuries causing permanent visual loss, blindness and cosmetic deformity, and include injuries caused most commonly by chemical agents, but also by thermal insults, munitions and explosive blasts. The common feature is compromised regeneration of the ocular surface, leading to unwanted sequelae. The acute stage of the injury represents a window of opportunity in which treatment can maximise recovery and prevent complications. Although AM has found widespread use in ophthalmic surgery, the specific parameters of treatment for acute ocular surface burns remain undefined. Questions remain about which grade of burn to treat, the timing and dose of treatment, the recommended surgical method and the expected outcome. The enthusiasm of a number of retrospective studies have not translated into reliable evidence for AM treatment of burns. A Cochrane systematic review was performed.

2.2 Literature review

2.2.1 Epidemiology of ocular burns

Between 11.5% (Wong et al., 2000) and 22.1% (Loon et al., 2009) of traumatic eye injuries are caused by chemical burns. The commonest causes of exposure to alkali or acid are from occupational hazards in industry and agriculture, domestic accidents and assault (Wagoner, 1997). The most severe ocular surface injuries typically result from alkali burns. Chemicals used in agriculture, chemical engineering and other industries are most commonly implicated (Wagoner, 1997). These include alkalis like ammonia (NH_3), used in fertilisers, refrigerants and cleaning agents, and lime ($\text{Ca}(\text{OH})_2$), used in plaster, cement and whitewash. Common acids causing ocular burns include sulphuric acid (H_2SO_4), found in battery acid and industrial cleaners. Some chemicals, like magnesium hydroxide ($\text{Mg}(\text{OH})_2$), which is present in fireworks, produce marked thermal damage to the eye. Industrial accidents involving alkalis such as ammonia remains a serious consideration (Bhattacharya et al., 2007). The prevalence of facial attacks with acids or alkalis can be marked in developing nations, especially the Middle East (Afghanistan and Pakistan), South East Asia (Cambodia), West Africa and the Caribbean (Merle et al., 2008). Industrial accidents may cause ocular surface burns on a mass scale, a notable example being the Bhopal disaster of 1984, when methyl isocyanate was released into the atmosphere causing thousands of eye injuries (Dwivedi et al., 1985). Thermal burns are usually prevented by the protective reflex of the eyelids and are comparatively rare (Malhotra et al., 2009). In civilian ophthalmic practice, munitions injuries are commonly seen in firework accidents, which combine heat and mechanical trauma (Knox et al., 2008). Damage ranges from minor and self-limiting, involving the most superficial layers, to severe, involving the stem cell population and leading to sight loss if left untreated

(Shimazaki et al., 2006). Thermal eye injuries can result from a variety of agents including hot liquids in homes (Vajpayee et al., 1991), molten metals in industrial workplaces (Schrage et al., 2000) and direct contact with an open flame (Boone et al., 1998). Infrequent causes of corneal burns include steam and molten metals (Schrage et al., 2000). Radiation and electrical burns also occur rarely (Borderie, 2004).

2.2.2 Pathogenesis of ocular surface burns

The depth of penetration, duration of exposure and area of involvement determine the severity of an ocular burn (Wagoner, 1997). In the case of chemical injuries, the relative toxicity of the substance is another determinant of severity. Alkalis cause saponification of cell membrane fatty acids, rapidly penetrating the anterior chamber of the eye to cause extensive cell and tissue damage. Acids tend to cause protein coagulation, thus limiting penetration. Hydrofluoric acid is an exception, the free fluoride ions being able to produce deep penetration and severe toxic effects (McCulley et al., 1983). It may not be possible to distinguish alkali from acid burns by clinical examination. The immediate effects of a burn can include irreversible damage to multiple ocular tissues, including the cornea and conjunctiva. The epithelial layers are denuded, and protein denaturation occurs. In the cornea, destruction of Bowman's layer exposes the stroma, where orthogonally arranged collagen bundles become subject to enzymatic degradation (Fini et al., 1998). Particulate matter may become lodged in the stroma, perpetuating severe damage (Schrage et al., 1990). Occlusion of blood vessels causes ischaemia to the corneal limbus, the presumed source of limbal stem cells (LSC) necessary for regeneration of the ocular surface epithelium. Limbal ischaemia stimulates inflammation and new vessel formation, leading to long-term complications and visual loss. In severe cases, deep ischaemia leads to necrosis (Pfister and Koski, 1982). Deep corneal structures, such as

the endothelium, and intraocular structures such as the lens and trabecular meshwork are damaged by severe burn injuries, causing corneal opacification, cataract and a rise in intraocular pressure. This, in turn, leads to glaucoma.

2.2.2.1 Limbal stem cell failure and stromal ulceration

For all kinds of ocular burn injuries, the extent of limbal involvement is of special significance, as it can be used to estimate the likelihood of failure of re-epithelialisation (Dua et al., 2001). This is a critical determinant of future complications, as there is evidence that human corneal epithelial stem cells originate in crypts located in the subconjunctival space adjacent to the limbus (Dua et al., 2005). Extensive damage to the conjunctiva causes conjunctival stem cell loss in the fornices, and the loss of goblet cells and accessory lacrimal glands, essential for surface wetting. The compromised ocular surface is vulnerable to sight-threatening infections. In the absence of an intact epithelium, stromal proteoglycans and collagens become exposed to hydrolysis, a process mediated by latent collagenases such as MMPs (Fini et al., 1998). Immunoregulatory cells are recruited from the tear film and the blood vessels contributing to the inflammatory reaction. Polymorphonuclear cells degrade exposed collagen fibres via enzymes and reactive oxygen species (Hayashi et al., 1997). There is loss of keratocytes and endothelial cells, resulting in impairment of collagen regeneration and water regulation (Pfister and Koski, 1982). Ascorbate levels in the eye become depleted, compromising vitamin C-dependent collagen synthesis (Levinson et al., 1976). Stromal ulceration stops once epithelialisation is complete, which explains the primacy of directing treatment towards epithelial regeneration. Viable conjunctiva grows over corneal zones with insufficient limbal stem cell reserves, and fibrosis of the damaged structures occurs over weeks and months.

2.2.3 The natural history of ocular surface burns

The clinical course of chemical injuries was divided into four distinct phases by McCulley (1987): immediate, acute (day 0-7), early repair (day 7-21) and late repair (after day 21) phases. This classification may also apply to non-chemical burns. The eye rapidly becomes inflamed in the acute phase. For mild injuries, there is a rapid recovery of the epithelial surface. In the case of severe chemical injuries, delayed epithelialisation becomes apparent in the early repair phase. At this point, the initial clinical suspicion of the grading of the injury may be confirmed, and corneal ulceration can begin. The late repair phase, lasting many months, is characterised by marked scarring, including between the ocular surface and eyelids (symblepharon). Progressive conjunctival fibrovascular tissue ('pannus') may have extended across the denuded cornea, protecting it against further melting. This has been called a Type III healing pattern, resulting in a tectonically stable, but optically compromised, eye (Wagoner, 1997). In contrast, Type I and II healing patterns are associated with total or sub-total recovery of the ocular surface. In severe injuries, if the cornea remains denuded of either corneal or conjunctival epithelium, corneal melting will develop in the weeks after the burn injury (Type IV healing), leading to perforation unless the appropriate surgical intervention is performed. In these eyes, the entire anterior segment may be severely damaged, including intraocular structures. The outcome in the long term depends on the severity of the initial injury, stem cell survival and the healing response (Shimmura and Tsubota, 2008). Severe burns carry an extremely poor prognosis (Kuckelkorn et al., 1995b).

2.2.4 Classification of ocular burns

The extent of damage at initial assessment can help to predict the final visual outcome (prognosis) of chemical injuries. The 1965 Roper-Hall classification of ocular burns (Roper-Hall, 1965) concentrated on corneal involve-

Table 2.1: Roper-Hall classification

Grade	Prognosis	Cornea	Conjunctiva
I	Good	Corneal epithelial damage	No limbal ischaemia
II	Good	Corneal haze, iris details visible	< 33% limbal ischaemia
III	Guarded	Total epithelial loss, stromal haze, iris details obscured	33% to 50% limbal ischaemia
IV	Poor	Cornea opaque, iris and pupil obscured	> 50% limbal ischaemia

Table 2.2: Dua classification

Grade	Prognosis	Limbal involvement	Conjunctival involvement	Analogue scale
I	Very good	0 clock hours	0%	0/0%
II	Good	< 3 clock hours	< 30%	0.1–3/1 to 29.9%
III	Good	3 to 6 clock hours	> 30% to 50%	3.1–6/31 to 50%
IV	Good/ guarded	6 to 9 clock hours	> 50% to 75%	6.1–9/51 to 75%
V	Guarded/ poor	9 to <12 clock hours	> 75% to < 100%	9.1–11.9/75.1 to 99.9%
VI	Very poor	12 clock hours	100%	12/100%

ment and limbal ischaemia to predict the anatomical and visual outcomes from the initial clinical presentation (table 2.1). Burns were graded from I (mild) to IV (severe). This benchmark classification for chemical burns takes into account the degree of corneal opacity, limbal ischaemia (a marker of presumed stem cell loss) and epithelial involvement at presentation. The Roper-Hall (1965) classification was a modified version of earlier systems of classification by Ballen (1964) and by Hughes (1946), who recognised the relationship between the initial appearance and the final visual outcome.

A modern understanding of ocular surface stem cell distribution and ocular surface surgery underscores the Dua classification of thermal and chemical ocular burns, which further subdivides Roper-Hall grade IV burns into grades IV, V and VI (Dua et al., 2001). The Dua classification is based on an estimate of limbal involvement (in clock hours) and the percentage of conjunctival damage (table 2.2). The prognosis is considered in the light of recent advances in the surgical rehabilitation of burned eyes, which have

greatly improved outcomes. The Dua classification has been found to be superior to the Roper-Hall classification in predicting the outcome of an ocular burn (Gupta et al., 2011). However, the initial clinical appearance can be misleading, and can result in the misclassification of clinical injuries, leading to unexpected outcomes (Shimmura and Tsubota, 2008).

Another classification, from the International Life Sciences Institute, includes two clinical parameters requiring specialised equipment for diagnosis (Bagley et al., 2006). These parameters are the depth of corneal injury, which can be assessed by confocal microscopy, and the extent of corneal endothelial cell loss, which can be assessed by specular microscopy. Classifications of ocular surface burns have not been validated in animal models or in prospective human trials. They do not allow the prognosis to be modified on account of the causative agent or the extent (depth) of exposure, but are a useful clinical guide to the healing potential of the damaged ocular surface. The prognosis of ocular surface burns is affected by damage to associated adnexal structures (Malhotra et al., 2009). If the external environment of the ocular surface is compromised by damage to the eyelids, healing will be delayed or impossible.

2.2.5 Management of ocular acute surface burns

The immediate management of burns is directed at removing any noxious agent from the ocular surface. In the case of chemical injury, this may include irrigation for several hours until pH returns to normal. In the case of firework, munition and blast injuries, debris is carefully removed under a microscope and penetrating injuries are managed surgically. A careful assessment of the injury will reveal the extent of the burn and the likelihood of further complications. Subsequent medical and surgical treatment measures are directed at promoting epithelialisation, augmenting corneal repair and controlling inflammation (Wagoner, 1997). Aggressive treatment in the

acute phase is necessary to prevent a type IV healing pattern. The survival of conjunctival and corneal stem cells is critical to a recovery with few complications. Treatment goals in the acute phase include pain relief. Promotion of epithelialisation, prevention of infection and dampening of inflammation constitute early phase goals. Long-term aims include prevention of conjunctivalisation, of neovascularisation and of fibrotic sequelae including symblepharon.

2.2.5.1 Medical management

Acute ocular surface burns are conventionally treated with emergency irrigation and removal of particulate matter within minutes of presentation. Irrigation is carried out with phosphate-free solutions to limit calcification (Daly et al., 2005). Medical therapy is instilled as soon as possible in the 7-10 day 'window of opportunity' to limit damage (Wagoner, 1997). Treatment is directed at assisting re-epithelialisation and preventing ulceration, for which the reduction of inflammation is a priority. Tear substitutes and antibiotic eye drops are administered to prevent infection. Ocular surface inflammation is maximally controlled by topical corticosteroids in the first 10-14 days after the injury. However, one of the unwanted effects of the steroids is to inhibit keratocyte migration and collagen synthesis, precipitating melting. Thus, steroids are used minimally in cases where the epithelium has not healed after 14-21 days. Further measures are directed at reducing the risk of corneal melting and perforation by promoting collagen regeneration. Corneal repair is helped by orally administered doxycycline, which appears to inhibit the induction of corneal MMP-9 by TGF- β 1 (Kim et al., 2005). It also inhibits the activity of MMP-2 in the cornea by chelating essential metal ions (Smith and Cook, 2004). Topical and orally-administered ascorbate may assist healing by replenishing vitamin C supplies essential for collagen synthesis (Levinson et al., 1976). Topical sodium citrate drops

are given to chelate calcium required by inflammatory polymorphonuclear cells (PMN), which release harmful MMPs. Citrate therapy may reduce the incidence of corneal ulceration (Pfister et al., 1997). Control of eye pressure may require topical and/or systemic medications. Pain control can be helped with cycloplegic eye drops, and adequate lubrication is given for comfort.

2.2.5.2 Surgical management

Surgical treatment during the acute phase is rarely necessary as long-term measures, which include LSC transplants, are usually only successful once the eye inflammation has subsided (Tsai and Tseng, 1995). If lid closure is not possible, a bandage contact lens may be placed on the eye (Tuft and Shortt, 2009) or surgical appositioning of the lids (tarsorrhaphy) may be performed (Malhotra et al., 2009). In severe alkaline injuries, fluid paracentesis of the anterior chamber can help reduce the pH. Acute measures are directed at providing a vascular supply to ischaemic tissues and an epithelial covering to prevent corneal melting (Wagoner, 1997). All necrotic tissue is excised. Following excision of necrotic tissue, healthy conjunctiva and the subconjunctival Tenon's layer may be advanced over the burned tissue to the limbus (Tenon-plasty), allowing the conjunctiva to grow onto the cornea to provide temporary protection and nourishment (Reim et al., 1992). Tenon-plasty can only be carried out if there is sufficient residual vascularised tissue. Alternatively, a conjunctival autograft from the uninjured fellow eye may be placed directly onto the burned areas of the ocular surface (Thoft, 1977). Autologous conjunctival grafting requires healthy residual conjunctiva and an adequate blood supply to the damaged ocular surface. Oral and nasal mucosal transplants are possible alternatives, and are carried out in some centres (Kuckelkorn et al., 1996). Conjunctival and mucosal grafts may fail to vascularise and become necrotic, limiting their use (Kuckelkorn et al., 1995). In contrast to autologous conjunctiva and

mucosa, AM is avascular and generally easily available, and has acquired a more widely accepted role in the treatment of acute ocular burns.

2.2.6 AM patching of acute ocular surface burns

2.2.6.1 Historical background

Before the First World War, ocular burns were treated with autologous oral mucous membrane (Denig, 1912). The procedure Denig advocated was the excision of necrotic conjunctiva and its replacement with the membrane. An alternative dressing was subsequently proposed in the form of rabbit peritoneum (Brown, 1941). Rather than applying the membrane over excised tissue, Brown invested the entire ocular surface, anchoring the membrane in the forniceal recesses with external bolsters and reflecting the membrane to the lid margin. Rabbit peritoneum, however, was not well tolerated. A few years after the de Rötth (1940) series on AMT as a conjunctival replacement, AMT was used as a patch for the whole ocular surface to treat acute burns (Sorsby and Symons, 1946; Sorsby et al., 1947; Lavery, 1946; Shafto, 1950). These early studies affirmed that AMT relieved pain, promoted healing and prevented symblepharon. AM treatment for burns soon became widespread, and a method of suturing AM into the inferior fornix was described as a means of preventing symblepharon after chemical injuries (Shafto, 1950). Alternatives, such as egg membrane, were proposed around this time (Croll and Croll, 1952). Roper-Hall's 1965 address to the Ophthalmological Society of the United Kingdom cited AM as one of a number of membranes used in the immediate surgical management of ocular burns, along with mucous membrane, cadaveric conjunctiva, egg membrane and peritoneum (Roper-Hall, 1965). At the same meeting, the use of a stainless steel ring wrapped in AM was advocated to prevent symblepharon and pain by keeping the inflamed bulbar and tarsal surfaces apart. AM was also in use in Eastern bloc countries as a treatment for ocular burns (Uglova and

Goleminova, 1957; Alberth and Kettesy, 1971; Batmanov et al., 1990).

2.2.6.2 Current practice

In recent years, attention has turned back to AMT as a treatment for burns during the acute and early repair phases. Since the introduction of cryopreserved AM by Scheffer Tseng, of the Ocular Surface Center in Miami, it has again been suggested that AMT applied therapeutically during the acute phase of a burn could promote healing (Meller et al., 2000). Tseng and co-authors have claimed that AMT can dampen inflammation, promote epithelialisation and prevent scarring and neovascularisation through a variety of biological factors (Tseng et al., 2004). In keeping with this concept, autologous serum drops and umbilical cord serum have recently been tried as therapeutic modalities in acute ocular surface chemical injuries (Sharma et al., 2011), with some degree of success reported. Moreover, patching with AMT has been tried for a subset of inflammatory eye diseases that are similar to acute burns. These are acute Stevens-Johnson syndrome (SJS) (Gregory, 2008) and toxic epidermal necrolysis (TEN) (Shay et al., 2010), which are commonly regarded as being part of the same disease of hypersensitivity. In common with acute burns, the syndromes cause acute epithelial loss, eventually leading to neovascularisation, chronic inflammation and conjunctival ingrowth. Conclusive evidence of the benefits of AMT in these conditions has not been established in clinical trials, yet the treatment is not risk-free. Although there are no common adverse effects reported from using AM, rare reports of serious complications of AMT can be found in the literature including fungal keratitis (Das et al., 2009), uveitis (Srinivasan et al., 2007) and corneal melt (Schechter et al., 2005). A steroid-responsive hypopyon (a collection of inflammatory cells in the eye) may appear after repeated exposure to AM from the same donor, suggesting sensitisation (Gabler and Lohmann, 2000).

2.2.7 Standardisation of treatment

The application of AM for burns is not standardised (Dua et al., 2010). The tissue is heterogeneous, with both biochemical (Hopkinson et al., 2006b; Gicquel et al., 2009) and physical (von Versen-Höynck et al., 2004; Connon et al., 2007; von Versen-Hoeyneck et al., 2008; Connon et al., 2010) variations between donors and even between areas of one donor membrane. These variations may be increased by tissue handling during processing. Variability may be accentuated by different methods of preserving AM. The timing, surgical application and extent of treatment vary. AM can be applied from a few hours (Kobayashi et al., 2003) to weeks (Sridhar et al., 2000) after an ocular surface burn. AM is usually placed with the stromal side in direct contact with the ocular surface, but it may be placed epithelial side down (Meller et al., 2000). Suturing of AM patches to the lids can be performed with interrupted sutures or with running sutures for easy removal (Arora et al., 2005; Kobayashi et al., 2003). Alternative methods of application include fitting a purpose-made plastic ring conformer (symblepharon ring) wrapped in AM (Arora et al., 2005; Kheirkhah et al., 2008; Tamhane et al., 2005) and gluing with fibrin-based adhesives (Sekiyama et al., 2007). Although AM is typically applied as a removable patch (Kobayashi et al., 2003; Kheirkhah et al., 2008), the tissue can be grafted onto the damaged ocular surface and left until it degrades (Meller et al., 2000). The burns treated have ranged from mild (Kheirkhah et al., 2008) to severe (da Silva Ricardo et al., 2009; Joseph et al., 2001; Sridhar et al., 2000). Together with unclearly defined criteria for success and failure, this has led to confusion regarding the purpose and objectives of treatment (Maharajan et al., 2007).

Because of its early promise, AM has been used in spite of a lack of RCTs (Bouchard and John, 2004). On one hand, it has been argued that AM has been used in excess of its true potential (Dua et al., 2004). Conversely, AM may be underused, with only 35% of American Burn Association facilities

admitting to using it for acute ocular burns in a recent survey (Son et al., 2011). Ophthalmic surgeons need to know which grades of burns to treat and when, which products and techniques to use and what outcomes may be expected (Panda et al., 2002). High quality evidence of the benefits of this treatment has thus far been lacking, suggesting a pressing need for a systematic review to highlight which characteristics are needed for future RCTs. This in turn will encourage high quality trials to be conducted. Systematic reviews are becoming increasingly powerful tools for assessing the quality of evidence, since studies may lack methodological quality and contain multiple sources of bias (Jüni et al., 2001).

2.3 Materials and Methods

2.3.1 Eligibility criteria

The objectives of this systematic review were to assess RCTs of amniotic membrane patching of moderate and severe ocular burns in the acute phase (day 0 to 7).¹ The minimum length of patient follow-up was 6 months. Participants of all ages were eligible and included those presenting for emergency eye care with chemical ocular surface burns of grade II or worse or ocular surface thermal injuries of similar severity. Exclusion criteria included pre-existing ocular surface disease or visual loss. Participants who received AM treatment after day 7 and those who received secondary procedures such as limbal transplants were not considered eligible. Two subgroup populations were considered:

- moderate burns - patients who had ocular burns of grade II and III (Roper-Hall and Dua classifications).
- severe burns - patients who had ocular burns of grade IV (Roper-Hall)/

¹This systematic review was undertaken in collaboration with Dr Catey Bunce, statistician, Dr Hanif Suleman and Professor Harminder Dua, content expert.

grades IV to VI (Dua).

RCTs were included in which amniotic membrane patching of whole or part of the ocular surface (including the fornices but not the external lids) was performed within seven days of injury, combined with all types of medical therapy together. Studies in which AM extracts or suspensions were applied as drops were not eligible. As Tenon-plasty and autologous conjunctival patching are not commonly reported, a comparison between surgical treatments could not be performed. The control patients received all types of medical therapy together, with no surgical intervention other than manual lysis of mechanical adhesions between the eyelids and the globe during the repair phases. The medical therapy used was defined for each included study. Relevant studies that were excluded from the analysis were tabulated with details of study characteristics and comments from the study conclusions.

2.3.2 Outcome measures

Outcome measures included primary and secondary outcomes for each included RCT. An explanation of the significance of each outcome to the study is provided with each outcome measure. These included dichotomous, continuous, time-to-event and ordinal measures.

2.3.2.1 Primary outcomes

1. The proportion of eyes with complete corneal epithelialisation 21 days after the burn injury. A persistent epithelial defect (PED) after 21 days of an ocular surface burn carries an increased risk of corneal stromal melting, and is therefore clinically meaningful.
2. Visual outcomes at final follow-up.

2.3.2.2 Secondary outcomes

1. The proportion of eyes with symblepharon. Symblepharon limits normal movement, is an index of severity.
2. The proportion of eyes with new vessels in the cornea (corneal neovascularisation). The extent of new vessels is an index of oxygen deprivation to the tissues. The number of quadrants of neovascularisation was expressed as an ordinal outcome from 0 to 4.
3. The proportion of eyes with adverse events, including rare incidences of corneal infections and immune reactions to AM.
4. The time-to-complete corneal epithelialisation.
5. The proportion of eyes with vascularised scarring on the cornea (fibrovascular pannus), a cause of disfigurement and visual loss.
6. The proportion of patients who report pain reduction after AMT.

2.3.2.3 Follow-up

For the primary outcome of epithelial healing, the critical point for follow-up was 21 days after the injury, because in the absence of an intact epithelium at the end of the early repair phase, the chances of requiring later ocular surface reconstruction are significant. Therefore, any difference between treatment and control groups at this stage can be considered to be clinically significant, and it is more likely to reflect a difference in treatment in the acute phase than would be the case after several more weeks. By 21 days, attrition rates of follow-up appointments would not be high, and secondary surgeries would not yet have been performed. For most secondary outcomes (except pain reduction, which would be immediate), measurement time points reflected the healing process during the late repair phase. The

exact time points were less critical, and could be multiple (e.g., 6 and 12 months), depending on outcome reporting.

2.3.3 Data extraction

Multiple sources were used to conduct a comprehensive review, including electronic databases and reference lists. Starting with the highest yield source, the Cochrane Central Register of Controlled Trials (CENTRAL, containing the Cochrane Eyes and Vision Group Trials Register) (*The Cochrane Library*, Issue 8, 2011), MEDLINE (January 1966 to August 2011), EMBASE (January 1980 to August 2011), Latin American and Caribbean Health Sciences Literature Database (LILACS), the *meta*Register of Controlled Trials (*mRCT*) (www.controlled-trials.com) and the www.clinicaltrials.gov website were searched electronically. There were no date or language restrictions in the electronic searches for trials. Medical subject headings were finalised after review by the Cochrane Eye and Vision Group. Details of search strategies are available in Appendix A. References cited in studies identified as relevant were also assessed, and the authors of included studies were contacted to find out about ongoing trials.

The search results were screened to assess relevant titles and abstracts. These were categorized as included, excluded or unclear. Published articles were retrieved to identify and link multiple publications from the same study and to review the study characteristics of all included and unclear studies. A screening form containing eligibility criteria was used to justify inclusion or otherwise. This included details on study type, grade of burn, intervention and control characteristics and outcome reporting.

Data from included studies was then entered into a data extraction form to obtain details of methodology and outcomes. General information entered included demographic details of the participants and trial characteristics. The diagnostic criteria, grades and causative agents of the injuries,

timing and method of application of AMT and primary and secondary outcome data of interest were also recorded. The form was used to confirm eligibility for review. In the event of missing data, the trial authors were contacted for more details. The data was entered into RevMan software (version 5.1), which is standard software for preparing Cochrane reviews. For dichotomous and stratified ordinal data, the proportion of patients in each intervention arm having the outcomes of interest was recorded. Continuous data were recorded with relevant statistical data. Time-to-event data was processed separately in GraphPad Prism statistical software (La Jolla, California). The curves were attached as additional figures.

2.3.4 Risk of bias assessment

A domain-based evaluation of the risk of bias was conducted within each included study, using an assessment tool provided in the Cochrane Handbook for Systematic Reviews of Interventions (Higgins and Green, 2011). The following domains were considered:

- Specification of sequence generation method
- Implementation of allocation concealment
- Masking of participants and personnel
- Masking of outcome assessment
- Completeness of outcome data
- Selective outcome reporting
- Other biases related to particular clinical setting

The risk of bias in each domain was assessed as low, serious or very serious.

2.3.5 Measures of treatment effect

The relative risk (RR) of incomplete epithelialisation was calculated by dividing the number of incompletely epithelialised eyes (treatment failures) by the total number of eyes (successes and failures) in each group, and then dividing the risk of failure in the experimental group by the risk of failure in the control group. This was reported with the 95% confidence interval (CI) and the p value. The number-needed-to treat (NNT) for one additional patient to benefit (NNTB) or suffer harm (NNTH) was calculated with its 95% CI using the Newcombe-Wilson hybrid score without a continuity correction (Newcombe, 1998). In cases of non-significance (i.e., where the CI of the difference between the control event rate and the experimental event rate does not exclude 0), the estimated confidence intervals for NNT were quoted using the method described by Altman (1998). Visual acuity measurements were converted to a logarithmic scale to calculate the difference in the mean visual acuities between the experimental and control groups. Treatment effects on dichotomous outcomes were evaluated by calculating RR. The number of quadrants of neovascularisation was expressed as an ordinal outcome from 0 to 4 and then dichotomised at a clinically meaningful cut-off point (0 versus 1-2 or 0 versus 3-4), allowing the calculation of a clinically informative RR. Time-to-complete epithelialisation data were analysed with survival curves to express the findings as a hazard ratio (HR). Additional sensitivity analyses could not be conducted at different cut-off points because of the small sample size.

2.3.6 Data synthesis

The primary outcomes were eye-related rather than patient-related. Analyses based on a single eye per individual conveniently allow standard statistical methods to be employed, although information for the fellow eye is lost (Murdoch et al., 1998). If one eye was chosen for bilateral patients,

the method of selection was documented. Studies which included bilateral injuries were not excluded, as long as treatment to one eye in no way determined treatment to the second eye. In the event of fellow eyes having different treatments, the treatment to one eye might determine treatment to the other eye, introducing a bias. On the other hand, if both eyes were treated similarly the likely correlation between fellow eyes might induce a cluster effect. These issues would be assessed for each study individually.

The heterogeneity of outcomes was analysed by considering the grades of burns severity (i.e., moderate versus severe) as separate subgroups, as these have different natural histories. In the absence of evidence of a different treatment effect of AM on burns caused by different causative agents, these were considered as single categories rather than subgroups.

Guidelines developed by the GRADE Working Group were used to assess the quality of the evidence (GRADE Working Group, 2004) with GRADEprofiler software (GRADEpro). The GRADEprofiler software allowed a downgrading of the quality of the evidence based on the risk of bias, inconsistency, indirectness, imprecision and publication bias. These were identified as absent, serious or very serious, which resulted in a grading of the quality of evidence for each outcome from high to very low. Tables summarising the findings of the included study were constructed with reference to two outcomes of interest: the proportion of eyes with complete epithelial closure by the 21st day after the injury and visual acuity at final follow-up (table 2.7). Moderate and severe burns were addressed separately.

2.4 Results

2.4.1 Results of the search

The studies identified by the original electronic search included patients of a wide range of ages with alkaline, acid and thermal injuries. Besides

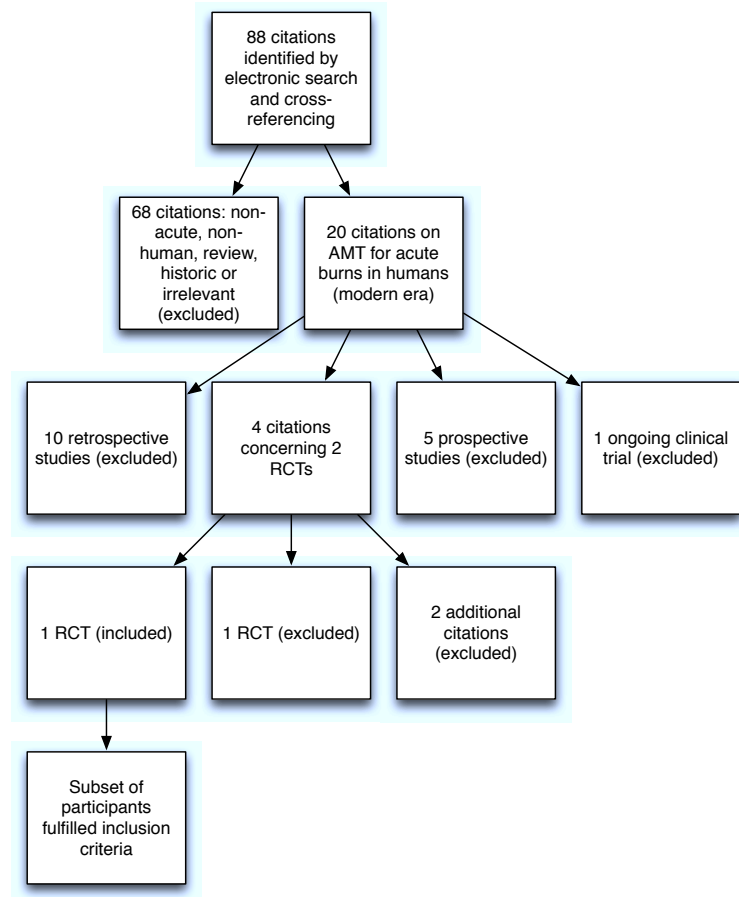


Figure 2.1: Study selection

An electronic search for studies on the treatment of acute ocular burns with AMT produced a subset of eligible participants from one RCT.

RCTs, retrospective and uncontrolled or non-randomised prospective studies, review articles, animal models and studies which did not directly deal with AMT or acute ocular burns were found by this strategy. A number of historical and non-English language studies were identified by extensive cross-referencing of known recent studies and more general articles about AM, and not by the electronic search. There were 88 citations identified in total (2.1). Seventy-eight studies were excluded after reading the title or abstract. Of these, 10 were recent retrospective case series of ocular burns Chen et al. (2000); Sridhar et al. (2000); Joseph et al. (2001); Uçakhan et al. (2002); Kobayashi et al. (2003); Zhou et al. (2004); Tejwani et al. (2007); Prabhasawat et al. (2007); Kheirkhah et al. (2008); da Silva Ricardo et al. (2009). One citation (Baradaran-Raffiee, 2008) concerned a clinical trial of

AMT for acute chemical burns for which no results have yet been published. Repeated efforts to contact the principal investigator proved unsuccessful, which led to a classification of the study as ongoing. Five citations concerned non-randomised prospective studies (Arora et al., 2005; López-García et al., 2006, 2007; Meller et al., 2000; Muraine et al., 2001). These were definitively excluded after checking the full report against the eligibility criteria (full-text assessment). Four citations concerned two relevant RCTs carried out by the same group in New Delhi, India ((Tamhane et al., 2005; Tandon et al., 2011; Gupta et al., 2011; Chew, 2011)). Of these, two were excluded after reading the abstract (Chew, 2011; Gupta et al., 2011). Of the two RCTs, one was excluded after contacting the authors for further details (Tamhane et al., 2005). One RCT contained a subset of participants that fulfilled the inclusion criteria for this review (Tandon et al., 2011).

2.4.2 Excluded studies

The studies on AMT for ocular burns that were excluded from the analysis are shown in tables 2.4 and 2.3. These fall into four main groups shown below. Additional study characteristics and reasons for exclusion are provided. A number of case series comment on the limitations of AMT in severe burns, and a small number of series have dealt exclusively with AMT for severe ocular burns (Joseph et al., 2001; Sridhar et al., 2000; da Silva Ricardo et al., 2009).

1. Non-randomised prospective case series (table 2.3): The non-randomised prospective studies either lacked controls (Meller et al., 2000; Arora et al., 2005) or reported outcomes that were not directly clinically relevant, such as histological findings (López-García et al., 2006) and impression cytology (López-García et al., 2007).
2. Retrospective case series (table 2.4): Similarly lacking in controls, most

Table 2.3: Prospective studies/RCTs

Reference	n	Grade	Controls	Timing (days)	Comments
Meller et al. (2000)	13	II-IV (R-H)	-	Mean 9.4 (<i>SD</i> 4.5)	'AMT alone rapidly restores both corneal and conjunctival surfaces'
Muraine et al. (2001)	9	Severe	-	1 month to 5 years	'preferable to conjunctival advancement'
Arora et al. (2005)	15	II-IV (R-H)	-	Mean 9.9 (<i>SD</i> 3.8)	'AMT increases patient comfort and reduces inflammation'
López-García et al. (2006)	12	Moderate	12	4-6	'Corneal epithelialisation occurred earlier in patients treated with AMT' (Impression cytology study)
López-García et al. (2007)	5	III-IV (Dua)	4	4-6	'AMT improved limbal stromal and epithelial regeneration' (Histopathological study)
Tamhane et al. (2005)	20	II-IV (R-H)	24	Range 1 to 14	'Reduces pain and promotes epithelialisation'

R-H: Roper-Hall classification, n: number of treatment eyes

Table 2.4: Retrospective series

Reference	n	Grade	Controls	Timing (days)	Comments
Chen et al. (2000)	6	-	-	-	'...can effectively reduce neovascularization, fibrosis and inflammation'
Uçakhan et al. (2002)	5	II-IV (R-H)	-	<i>M</i> 14.2 (<i>SD</i> 12.3)	'...decreased the extent and severity of vascularization'
Kobayashi et al. (2003)	5	II-III (R-H)	-	<i>Md</i> 4 (0 to 6)	'...facilitating rapid epithelialisation and pain relief'
Zhou et al. (2004)	20	III	-	-	'...can prevent corneal ulcer'
Tejwani et al. (2007)	24	II-IV (Dua)	-	<i>Md</i> 2 (1 to 20)	'...partially restores limbal stem cell function'
Prabhasawat et al. (2007)	13	II-IV (R-H)	8	1-10	'...promoted rapid epithelial healing and reduced corneal complication'
Kheirkhah et al. (2008)	5	I-III (R-H)	-	<i>M</i> 3.7 ± 3.1	'...may help preserve remaining limbal stem cells'
Sridhar et al. (2000)	2	Severe	-	'Within weeks'	'Long-term studies are warranted'
Joseph et al. (2001)	4	Severe	-	14 - 21	'..AMT did not help to restore ocular surface'
da Silva Ricardo et al. (2009)	5	Severe	-	10 - 30	'...not possible to avoid the limbic deficiency'

R-H: Roper-Hall classification, n: number of treatment eyes; Md, Median, M, Mean.

retrospective studies had fewer than 10 participants (Chen et al., 2000; Kheirkhah et al., 2008; Kobayashi et al., 2003; Uçakhan et al., 2002). Two uncontrolled studies of more than 20 participants have been reported (Tejwani et al., 2007; Zhou et al., 2004). One retrospective series from Thailand compared the treatment group to a set of matched controls (Prabhasawat et al., 2007).

3. Non-comparative case series of severe ocular burns (tables 2.4 and 2.3): For these, AMT was performed during the early to late reparative phases (table 2.4).
4. RCTs (table 2.3): The RCT conducted by Tamhane et al. (2005) did not present sufficient evidence of adequate randomisation, and patients were treated outside the 7-day period. The authors were contacted and could not supply the necessary data to stratify the treatment. Therefore, the Tamhane et al. (2005) RCT was excluded from the systematic review.

2.4.3 Included studies

One RCT (Tandon et al., 2011) contained a subset of patients that met the inclusion criteria for this review, and additional data were provided by the authors. AMT was carried out within two days of presentation by draping the stromal side over the entire ocular surface up to the lid margins and securing it in place with vicryl sutures. As there was no stratification of treatment into acute versus early repair phases, the authors were contacted for further information. The original data reported outcomes for 100 patients. Of the original 100 participants, 68 were treated in the first 7 days and have been included in this review (figure 2.1). In the event of bilateral injuries, only the right eye was entered into the study. The length of follow-up of the included patients was 6 to 24 months. The 68 participants

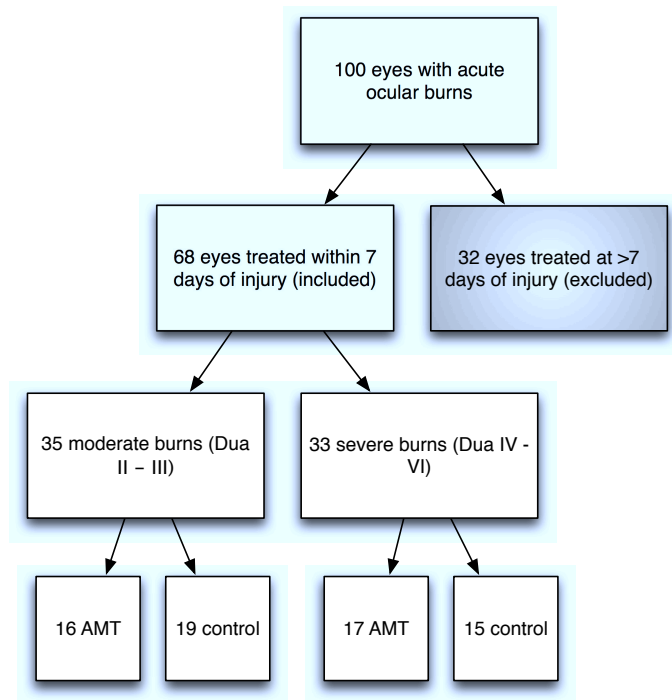


Figure 2.2: Included patients

Flow chart showing the subset of patients selected from an RCT by Tandon et al. (2011) for analysis as part of a systematic review.

included 36 with moderate and 32 with severe ocular burns. In the moderate burns group, there were 34 males and two females, with a mean age of 22.3 years (SD 10.1). The burns were caused by alkali in 22 cases, acid in 10 and direct heat in four. The severe category consisted of 24 males and 8 females with ocular burns, 23 caused by alkali, seven by acid and two by heat. The mean age was 19.3 years (SD 15.8). All patients were randomised to receive AMT and medical therapy or medical therapy alone. This consisted of topical prednisolone acetate (1%) every six hours, ofloxacin (0.3%) every six hours, sodium ascorbate (10%) every four hours, sodium citrate (10%) every four hours, preservative-free tear substitutes every two hours, homatropine drops (2%) twice daily and oral vitamin C (500 mg) every six hours for two to four weeks. Anti-glaucoma therapy included timolol maleate drops (0.5%) and/or oral acetazolamide if required.

Table 2.5: Risk of bias summary figure

Domain	Risk
Random sequence generation	Low
Allocation concealment	Low
Masking of participants and personnel	High
Masking of outcome assessors	High
Incomplete outcome data	Low
Selective reporting	Low
Other bias	High

2.4.4 Risk of bias in included RCT

A summary of the Cochrane Collaboration's tool for assessing the risk of bias of the included study (Tandon et al., 2011) is shown in figure 2.5. The risk of bias is summarised across domains for both study-level entries, such as allocation, and outcome-specific entries such as masking. The patients were randomised to a treatment assignment list prepared from a random numbers table. Serial numbers were given to the cases, and the randomly allocated treatment decision was concealed by using sealed envelopes. This suggests that adequate measures were taken to prevent foresight of treatment at the point of enrolment. The overall risk of allocation (selection) bias was therefore classified as low. For practical reasons, it was not possible to mask study participants and personnel from knowing which treatment was received, indicating a high risk of performance bias. Although digital photographs were used for assessment of outcomes by masked observers, the outcome assessors would have known whether AMT had been allocated since the AM persists for several weeks. This indicates a high risk of detection bias (Higgins and Green, 2011). Since no patients in the study were lost to follow-up, the overall risk of attrition bias was classified as low. The possibility of a selective reporting bias in the study was considered to be low, i.e. the outcomes reported are not a subset of those included in the protocol and they have not been chosen because they were significant.

2.4.4.1 Other causes of bias

The risk of bias from other causes in the included study was considered to be high. Several potential sources of bias are identified below. For each reason, the risk of bias is shown in brackets. Cases in which the direction of bias favoured a treatment effect were graded as having a high risk of bias.

1. The data presented concerns a subset of the patients recruited in the included RCT. This may have introduced a bias, since the patients treated within 7 days of injury may have had different characteristics to the remaining patients (unclear).
2. Of the 68 patients included in the study, 24 went on to have secondary procedures, such as limbal transplantation, in the months following the initial injury. The confounding effects of the secondary procedures on the measured outcomes (e.g., vision) are not clear. These eyes are likely to have suffered more serious injuries, and any treatment effect of AM is therefore likely to be smaller (unclear).
3. There was a significant difference in baseline visual acuity between treatment and control groups in the moderate burns category. The mean LogMAR visual acuity at presentation was 0.45 in the treatment group (*SD* 0.29) and 0.92 in the controls (*SD* 0.88) (independent samples *t* test, $p = .047$, equal variances assumed). This could have skewed the final visual outcomes in favour of a treatment effect (high).
4. Although final visual acuities were better in the AMT group (0.06, *SD* 0.10 versus 0.38, *SD* 0.52), the mean difference (MD) in visual acuity before and after treatment was greater in the control eyes (AMT -0.39, 95% CI -0.23 to -0.55, $p = .001$ vs controls -0.54, 95% CI -0.08 to -1.00, $p < .001$). The implication that final visual acuity was improved by AMT is therefore misleading (high).

5. The poor outcomes in the control eyes are not fully explained. In the moderate category, three control eyes had a time-to-epithelial closure of 90 days, while in the treatment group only one eye took longer than 18 days for the epithelium to heal. Five control eyes had a final visual acuity of less than 0.50. In contrast, no participant in the AMT treatment group had a final visual acuity of less than 0.30. While a treatment effect cannot be excluded, moderately burned eyes typically have a good prognosis. This raises the possibility that some injuries in the control group were misclassified at presentation. The randomisation process would not normally result in differential misclassification, which raises the possibility of a flawed process (high).
6. There was a significantly longer follow-up for treated eyes (*Med* 14.5 months, range 10 to 24 versus *Med* 12 months, range 6 to 24; Mann-Whitney $U = 94$, $z = -2.31$, $p = .021$). Since there was no common time-point for reporting visual acuity, this constitutes a potential source of bias. In the severe group, length of follow-up (12 months) was not significantly different between the groups (unclear).
7. The methodology of measurement of epithelial healing may be a source of bias. The study authors state that in some AMT cases, the margins of the epithelial defect could not be made out beneath the amniotic membrane. There is no indication that any data were missing or excluded, yet it is not explained in the report how the problem was circumvented. The unit of measurement of the healing rate (mm^2/day) implies that the eyes were seen every day until complete healing, which was not the case. This suggests that the precise timing of epithelial closure was a best guess between appointments or the appointment day itself. This may have led to imputation of data (unclear).

Table 2.6: AMT versus medical therapy

Outcome/subgroup	AMT	Controls	Stat. Method	Effect Estimate	<i>p</i> value
PED at 21 days					
Moderate burns	1/16	7/20	RR (95% CI)	0.18 [0.02, 1.31]	.09
			NNTB	3.5 [NNTB 2 to 104.5]	
Severe burns	16/17	14/15	RR (95% CI)	1.01 [0.84, 1.21]	.93
			NNTH	127.5 [NNTH 4 to ∞ to NNTB 5]	
Corneal nv					
Moderate burns (1-2 quadrants)	4/16	8/20	RR (95% CI)	0.63 [0.23, 1.71]	.36
Moderate burns (3-4 quadrants)	0/16	1/20	RR (95% CI)	0.41 [0.02, 9.48]	.58
Severe burns (1-2 quadrants)	4/17	4/15	RR (95% CI)	0.88 [0.27, 2.93]	.84
Severe burns (3-4 quadrants)	12/17	10/15	RR (95% CI)	1.06 [0.66, 1.70]	.81
Symblepharon					
Moderate burns	0/16	0/20	-	-	-
Severe burns	2/17	2/15	RR (95% CI)	0.88 [0.14, 5.52]	.89
Mean final VA (SD)					
Moderate burns	0.06 (0.10)	0.38 (0.52)	MD (95% CI)	-0.32 [-0.09, -0.55]	.007
Severe burns	1.77 (1.31)	1.64 (1.48)	MD (95% CI)	0.13 [-0.84, 1.10]	.79

RR, risk ratio; MD, mean difference; CI, confidence interval; nv, new vessels.

2.4.5 Effects of interventions

The median follow-up of both moderate and severe burns in the included study was 12 months (range 6 to 24). A summary of the treatment effects is shown in table 2.6. All treatment effects are represented as a RR with the exception of final LogMAR visual acuities, which were calculated as means at final follow-up. For failure of epithelialisation, the treatment effect is also shown as the NNTB/NNTH. 95% CI were used throughout. No information was available about the effects on pain or the presence of fibrovascular pannus. The study reported that no complications were encountered during the

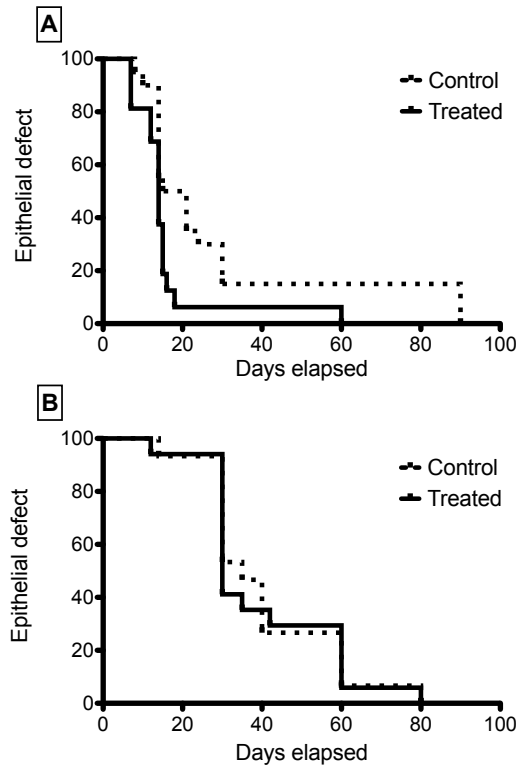


Figure 2.3: Survival analysis of epithelial defects

Survival curves of epithelial defects of moderate (A) and severe (B) ocular burns treated with AMT and medical therapy versus medical therapy alone.

study period. Survival curves representing the time-to-epithelialisation for the treatment and control arms of the moderate and severe burns groups are shown (figure 2.3 A and B respectively). Since the lines cross, the proportional hazards assumption and a HR are not valid with these data.

2.4.5.1 Quality of the evidence

Summaries of the findings of the systematic review are shown in tables 2.7 and 2.8 for moderate and severe burns respectively.

Based on the GRADE assessment, the quality of the evidence is shown to be low or very low for two outcomes (the relative risk of failure of epithelialisation and visual acuity) in both subgroups. The quality of the evidence was downgraded due to the risk of bias (assessed to be serious) and to imprecision in outcome reporting (assessed to be serious). In the moderate category, the risk of bias assessment reflected the imbalance between the control and

Table 2.7: Summary of findings, moderate burns

Outcomes	Illustrative comparative risks* (95% CI)		Relative effect (95% CI)	No of participants	Quality of the evidence
	Assumed risk (control)	Corresponding risk (AMT)			
Epithelial non-healing (Day 21)	350 per 1000	63 per 1000 (7 to 458)	RR 0.18 (0.02 to 1.31)	36	Low ¹
Mean visual acuity (final follow-up)	0.38**	MID -0.32 (0.09 lower to 0.55 higher)		36	Very low ^{2, 3, 4}

Patient or population: patients with acute ocular burns (moderate severity). Settings: ophthalmology secondary care for emergencies.
Intervention: amniotic membrane transplantation.

*The basis for the assumed risk (e.g. the median control group risk across studies) is provided in footnotes. The corresponding risk (and its 95% confidence interval) is based on the assumed risk in the comparison group and the relative effect of the intervention (and its 95% CI).
CI: Confidence interval; RR: Risk ratio; AMT: Amniotic membrane transplant. **LogMAR visual acuity range 0 -3 (lower is better).

GRADE Working Group grades of evidence High quality: Further research is very unlikely to change our confidence in the estimate of effect. Moderate quality: Further research is likely to have an important impact on our confidence in the estimate of effect and may change the estimate. Low quality: Further research is very likely to have an important impact on our confidence in the estimate of effect and is likely to change the estimate. Very low quality: We are very uncertain about the estimate.

¹ Epithelial defect assessed on day of clinic review, not daily. Defect was assessed under partially opaque membrane. This suggests possible imputation of data; ² High risk of performance and detection biases, as not possible to mask personnel and outcome assessors; ³ Mean visual acuity in control eyes significantly worse than treatment eyes at presentation. Improvement in visual acuity was greater in control group. Follow-up was significantly longer in treatment group. In a number of control eyes, outcome was very poor, suggesting possible misclassification. These factors could have skewed findings in favour of treatment; ⁴ Visual acuity measured at final follow-up rather than at a fixed interval.

Table 2.8: Summary of findings, severe burns

Outcomes	Illustrative comparative risks* (95% CI)		Relative effect (95% CI)	No of participants	Quality of evidence
	Assumed risk (control)	Corresponding risk (AMT)			
Epithelial non-healing (Day 21)	933 per 1000	943 per 1000 (784 to 1000)	RR 1.01 (0.84 to 1.21)	32	Low 1, 2
Mean visual acuity (final follow-up)	1.64**	MD 0.13 (0.84 lower to 1.10 higher)		32	Low 1, 3

Patient or population: patients with acute ocular burns (moderate severity). Settings: ophthalmology secondary care for emergencies.
Intervention: amniotic membrane transplantation.

*The basis for the assumed risk (e.g. the median control group risk across studies) is provided in footnotes. The corresponding risk (and its 95% confidence interval) is based on the assumed risk in the comparison group and the relative effect of the intervention (and its 95% CI).
CI: Confidence interval; RR: Risk ratio; AMT: Amniotic membrane transplant. **LogMAR visual acuity range 0 -3 (lower is better).

GRADE Working Group grades of evidence High quality: Further research is very unlikely to change our confidence in the estimate of effect. Moderate quality: Further research is likely to have an important impact on our confidence in the estimate of effect and may change the estimate. Low quality: Further research is very likely to have an important impact on our confidence in the estimate of effect and is likely to change the estimate. Very low quality: We are very uncertain about the estimate.

¹ High risk of detection and performance biases related to difficulties in masking personnel and outcome assessors; ² Possible imputation of data due to non-daily clinic attendance of patients and assessment of defect under partially opaque membrane; ³ Visual acuity measured at final follow-up rather than at a fixed interval

treatment groups, as well as the performance and detection biases. The imprecision of outcome reporting related to data gathering for both epithelial healing (measured in mm^2/day despite there being no daily reviews) and visual outcomes (measured to final follow-up rather than a fixed interval).

2.5 Discussion

Systemic reviews and meta-analyses are an integral part of evidence-based medicine, and recent years have seen a vast increase in their publication for ophthalmic interventions (Chen and Jhanji, 2012). The value of this systematic review will be to highlight the lack of evidence supporting the use of AMT in acute ocular burns and to provide a protocol for future RCTs (Clare et al., 2011).

Several non-randomised, uncontrolled studies have affirmed that AMT accelerates corneal epithelialisation and suppresses inflammation, neovascularisation and scarring (tables 2.3 and 2.4). According to these studies, AM prevents symblepharon (Meller et al., 2000), scarring (Chen et al., 2000), perforation (Zhou et al., 2004) and melting (Arora et al., 2005). In addition, impression cytological and histopathological studies of the corneal limbus of eyes with moderate burns have indicated that epithelial and stromal regeneration are more complete in eyes treated with AMT than in eyes treated with medical therapy alone (López-García et al., 2006, 2007). Intact AM has been postulated to act as a microenvironmental niche for stem cells (Grueterich and Tseng, 2002), and some researchers have suggested that this reduces the need for a limbal stem cell transplant in burned eyes (Kheirkhah et al., 2008; da Silva Ricardo et al., 2009). However, the strength of the claims is limited by the study designs. The burns treated were of varying severity and aetiology, and the timing of application of AM ranged from a few hours (Kobayashi et al., 2003) to several days (Tejwani et al., 2007) after the initial injury. These limitations reduce confidence in the study conclusions, since different grades of burn carry different prognoses, and the variability in the timing and duration of AMT further obfuscates any treatment benefits. Many non-comparative studies fail to define the purpose and objectives of AM treatment and criteria for treatment success and failure (Maharajan et al., 2007). The outcome measures are often un-

clear, with inadequate grading systems of the outcomes. In this context, the need for an RCT had been pressing.

Two RCTs from the same centre have addressed AMT patching for acute burns (Tamhane et al., 2005; Tandon et al., 2011). In the first RCT (Tamhane et al., 2005), 20 eyes with ocular burns were treated with AMT, with 24 controls. Participants with grades II-IV (Roper-Hall classification) were included, and treatment was carried out between one and fourteen days after the injury. The study found that AMT reduced pain and promoted early epithelialisation. The latter finding was determined by comparing the logarithm of the mean percentage reduction of the epithelial defect size at various time points. Although the study found some statistically significant difference in the healing rates, the treatment and control groups did not differ in clinical parameters such as final visual outcome. There was also a high participant dropout rate, further weakening the study. Moreover, there was significant baseline imbalance, with the treatment group having more severe injuries, and this was attributed to the small sample size and the randomisation strategy. This was reported as a 'fallacy' in a subsequent RCT, conducted to redress this bias by increasing the sample size and improving the randomisation process (Tandon et al., 2011). A total of 100 participants were recruited. The authors found epithelial healing to be significantly faster in the treatment arm of the moderate burns group. While the later study addressed some of the limitations of the former, it has been considered underpowered (Chew, 2011).

Both RCTs (Tamhane et al., 2005; Tandon et al., 2011) considered the rate of corneal epithelial healing as a primary outcome measure. While the speed of epithelial healing is important, it is not considered a 'patient-centred' outcome. Outcomes that are important to patients can be investigated through direct interview with eye-injured patients, and include quality of life measures and a return to normal function (Pager et al., 2004).

Moreover, the rate of epithelial healing may reflect variables other than a treatment effect, including timing of presentation, size of epithelial defect, severity of injury and patient factors. Besides being technically difficult to achieve, accurate and precise measurements of the rate of corneal epithelial healing following burns are limited by the number of time-points of patient attendance and by treatment with semi-opaque AM patches. For these reasons, the first of two primary outcome measures addressed in the current systematic review was not the epithelial healing rate, but the proportion of eyes with a PED at the end of the early reparative phase as designated by (McCulley, 1987). A further primary outcome measure was final visual acuity. In patients with moderate burns treated with AMT within the first 7 days of injury in the Tandon et al. (2011) study, there was a RR of a PED at day 21 of 0.18 compared to controls, which was non-significant. Although visual outcomes were better in the treatment group (M 0.06 versus 0.38), there was a high risk of bias from a baseline imbalance. As a result, the quality of the evidence of the two main outcomes was found to be low, indicating a need for further research.

2.6 Conclusion

The systematic review demonstrates the lack of conclusive evidence supporting the use of AMT in acute ocular burns, and reveals the lack of clarity that surrounds the use of AMT. Nonetheless, AM remains a useful biomaterial in ophthalmic surgery. Its biocompatibility and versatility enable it to be used empirically when the benefits of its application outweigh the risks. For military use, dried versions of the product may be a useful substitute for frozen or unpreserved tissue, and may in fact be advantageous in some clinical scenarios. Technical considerations of drying AM for therapeutic use are far from straightforward, yet are critical to its optimisation, and are

explored in the next chapter.

Chapter 3

OPTIMISATION OF DRIED AM

3.1 Introduction

The preservation of a biological material, whether by drying or any by other method, has as its primary goal the retention of maximal product quality for as long as possible. Excipients, such as trehalose, can be used to achieve this. For AM that is dried for therapeutic use, quality attributes include a long shelf life and sterility. These are determined by two related concepts: water activity (A_w) and glass transition (T_g). The determination of these variables falls within the related domains of moisture sorption and thermal analysis. The lines of investigation available for optimisation include dynamic vapour sorption (DVS), which can be used to correlate moisture content to A_w for a particular material. The T_g temperature can be localised by thermal methods, such as differential scanning calorimetry (DSC) and mechanical methods, such as dynamic mechanical analysis (DMA). In addition, thermogravimetric analysis (TGA) can be used to determine end moisture content. Surface analytical techniques, which include X-ray diffraction (XRD), attenuated total reflectance-Fourier transform infrared spectroscopy (ATR-FTIR) and time-of-flight secondary ion mass spectrometry (ToF-SIMS), can provide useful supplementary information about the inter-

actions between the excipient and the product. The objective of this chapter was to employ these techniques to create a framework for the optimisation of therapeutic dried AM, with trehalose as an excipient. The A_w and the T_g temperature both of trehalose-treated and untreated AM were investigated.

3.2 Literature review

3.2.1 Lyophilisation

Lyophilisation, or freeze-drying, is a complex and specialised drying technique and is the preferred method of drying biological tissues (Adams, 2007). The initial step in freeze-drying is freezing. Freezing complex biological materials below a critical point produces a mixture of crystallised solutes and an amorphous matrix associated with unfrozen moisture. The frozen tissue can then be placed on a temperature-controlled shelf in a sealed vacuum chamber. As pressure in the chamber falls (to a few millibars), a vapour pressure gradient is set up between the tissue and an ice condenser, which is typically programmed to reach at a temperature of $\sim -55^\circ\text{C}$. At temperatures below the triple point, frozen water undergoes sublimation into vapour. Simultaneously, moisture from the amorphous matrix evaporates. The resulting water vapour freezes onto the ice condenser. Together, sublimation and evaporation constitute a primary drying phase, which can proceed for several days. A secondary phase, in which the pressure is lowered further (to the level of microbars), then removes residual unfrozen moisture by desorption. The vacuum may be broken by an inert gas, and the product sealed within the chamber to avoid equilibration with ambient humidity. Lyophilisation minimises tissue shrinkage, deformation, solute concentration effects and thermal inactivation of proteins and enzymes that occur during drying by alternative heat-based methods. Because it operates within a closed system, particulate contamination is minimised. Lyophilisation can achieve

very low levels of moisture, typically between 1 to 4%. However, if the initial freezing step is uncontrolled, cellular structures can be damaged by the formation of ice crystals (Fuller and Paynter, 2007). Avoiding ice crystal formation during cryopreservation is a complex task, requiring controlled cooling and cryoprotectants. The extent to which this process is controlled will ultimately depend on the cost to benefit ratio.

The initial freezing step is omitted in drying protocols of certain biological tissues, a process more correctly referred to as vacuum-drying (Tindall, 2007). This may occur in freeze-drying systems without temperature-controlled shelves. It is not clear from the published protocols whether AM has been lyophilised or vacuum-dried in a freeze-drier (Nakamura et al., 2004; Libera et al., 2008). As a thin film, frozen AM may thaw during the process of freeze-drying, invalidating the benefits of the initial freezing step. Vacuum-drying can protect proteins against the effects of thermal inactivation, but not from harmful solute concentration effects. While AEC become devitalised during both drying and conventional cryopreservation (Hennerbichler et al., 2007), cellular damage can be reduced by preserving the tissue in isotonic media such as phosphate buffered saline (PBS) (Acker et al., 2002) and by adding lyoprotectant excipients such as trehalose, a naturally occurring osmolyte widely used in the food and pharmaceutical industries (reviewed by Kaushik and Bhat, 2003).

3.2.2 Stabilisation of biological materials

Preservation invariably causes quality modifications to tissues, manifest as phenomena such as shrinkage and discolouration (Quirijns, 2006). The T_g is a key determinant of the quality of amorphous (non-crystalline) materials, such as foods and pharmaceuticals (MacNaughtan and Farhat, 2008; Saunders, 2008). This is a thermal transition between long and short molecular relaxation times. Amorphous polymers undergo a T_g from a glassy, or vitri-

fied, state to a more malleable, rubbery state. Amorphous sugars, such as trehalose, undergo a T_g from a highly viscous to a less viscous state. Below the T_g temperature, the molecules of biological materials and pharmaceuticals are immobilised, which directly influences their shelf life and stability (Patist and Zoerb, 2005). Increasing the moisture content directly lowers the T_g temperature, an effect known as plasticisation. The moisture content also determines the A_w . This is an index of the water available for biological processes to take place. A_w determines the susceptibility of the tissue to contamination by micro-organisms (Adams, 1995) and to enzymatic degradation (Huis in 't Veld, 1996). A_w is equivalent to sample relative humidity (RH), which is expressed as a percentage. Excipients such as trehalose are widely used in the pharmaceutical and food industries to preserve quality, and have a useful role in the preservation of biomaterials (Crowe et al., 1996). Moisture content in excipients is a key determinant of protein stability, and can affect the stability and mechanical behaviour of pharmaceutical products (Khankari and Grant, 1995). Trehalose can exist in a variety of conformational states, including amorphous and crystalline forms, depending on the preparation method (Surana et al., 2004b). Some, but not all, of the crystalline forms are protective during drying. The preserved material and trehalose-PBS are immiscible, forming a heterogeneous mixture with distinct thermodynamic profiles. Therefore, it is important that both the material and the excipient are stored in glassy phases.

3.2.3 Thermal properties of collagen

As a collagen and elastin-rich tissue with abundant ECM, AM can be conceived of as a composite polymer consisting of crystalline and amorphous fractions (Li, 2000). Individual collagen molecules consist of ordered polyproline-like triple-helical chains with regularly arranged amino acid motifs rich in glycine (Gly), proline (Pro) and hydroxyproline (Hyp) (most commonly Gly-

Pro-X and Gly-Hyp-X). The chains form weak associations as a result of Van der Waal's forces and hydrogen bonds, which may cause viscoelasticity (Sasaki and Odajima, 1996). Peptide-bound aldehyde groups form covalent cross-links between the molecules, giving rise to polymeric fibrils (Eyre et al., 2008). Type I and III collagen molecules form heterotypic fibrils, interacting with other fibrils, proteoglycans and water to provide the bulk of mechanical strength (Cameron et al., 2002). The long-range crystalline order of the helical ultrastructure of the fibrils is suggested from X-ray diffraction patterns (Cameron et al., 2002). The polypeptides consist of ordered chains flanked by disordered fringes, analogous to semi-crystalline polymers (Morawetz, 1985). Collagenous tissue exhibits a T_g at about 40°C and a denaturation of the crystalline collagen fibrils at about 56°C (Li, 2000). This is contingent upon moisture content, which lowers the stiffness of purified collagen (Ntim et al., 2006). Bound water molecules are intrinsic to the collagen structure, forming an extensive network of bridges within and between the collagen molecules and fibrils (Zhang et al., 2011). When collagen is dehydrated, neighbouring peptides develop weak associations, causing stiffness to increase (Pashley et al., 2003). The collagen fibres are enmeshed in an amorphous matrix consisting of non-collagenous glycosaminoglycans, glycoproteins and elastin (Kaplan et al., 1987). The mechanical behaviour of elastin is similar to that of an amorphous polymer (Lillie and Gosline, 1990).

DSC is the most widely used thermal analytical technique, providing a wealth of information about the thermal properties of a material (Gabbott, 2008). It is especially effective in the analysis of semicrystalline polymers, where it can be used to determine events such as melting and crystallisation, to characterise T_g and to quantify corresponding enthalpy changes (Schick, 2009). In one study, DSC was used together with TGA to investigate the thermodynamic properties of air-dried AM-derived collagen membranes

cross-linked with chitosan (Kumar et al., 2003). The authors showed a single DSC plot for AM-derived collagen, identifying endotherms at 86.21°C and 218.90°C as being due to water loss and melting respectively. The initial weight loss tapered off at around 100°C, and was followed by a gradual thermal decomposition at temperatures upwards of 175°C. The cross-linked membrane decomposed more gradually than a non-cross-linked control, which was taken as evidence of improved thermal stability. The study failed to identify a T_g temperature. DMA is an even more sensitive method of investigating thermal transitions than DSC, and is especially useful in characterising the viscoelastic properties of amorphous and semi-crystalline polymers (Duncan, 2008), including purified collagen (Ntim et al., 2006) and elastin (Lillie and Gosline, 1990).

3.2.4 Moisture sorption

An understanding of a biomaterial's moisture sorption characteristics is fundamental to its characterisation (Gabbott, 2008), since a high A_w increases the risk of spoilage (Adams, 1995). In many foods, the A_w above which fungal growth can occur is approximately 0.65 (Abdullah et al., 2000). In common with foodstuffs, biological soft tissues are at risk of contamination from psychrotrophic bacteria, yeasts and moulds. Vacuum-packing, sterilisation and a low A_w extend the shelf-life (Gould, 1996). The non-linear relationship between equilibrium moisture content and A_w is given by the moisture sorption isotherm, which must be determined experimentally by DVS. Moisture can either be adsorbed onto the surface of type I collagen or absorbed into the bulk of the tissue (Zhang et al., 2011), and the same may be true for AM. Adsorption can occur as a monolayer, by interaction with polar groups on the surface, or as a multilayer, through hydrogen bonding. The data from DVS analysis can be used in mathematical models to distinguish between the different types of adsorption and absorption (Young and

Nelson, 1967). The equilibrium moisture content can be obtained by TGA, which measures weight changes as a function of temperature in a controlled atmosphere (Bottom, 2008).

3.2.5 Trehalose lyoprotection

In nature, the accumulation of trehalose by certain organisms enables them to survive drying (see Møbjerg et al., 2011). This discovery led to its use as a cryoprotectant for eukaryotic cells (Wolkers et al., 2002). Trehalose is a non-reducing disaccharide with a hydrolysis-resistant glycosidic bond between two α -glucose units (α -D-glucopyranosyl-(1 \rightarrow 1)- α -D-glucopyranoside). It does not cause non-enzymatic discolouration of organic materials, caused by the reaction between amino acids and reducing sugars (Maillard reaction), making it particularly suitable as an excipient for biomaterials (Schebor et al., 1999). Trehalose can enable mammalian platelets to survive freeze-drying (Wolkers et al., 2001) and can preserve the function of mammalian pancreatic cells after long-term storage (Beattie et al., 1997). It is widely thought to be an exceptional stabiliser of proteins and enzymes (Crowe et al., 1998). The molecular mechanisms by which trehalose stabilises cellular proteins are not fully understood (see review by Jain and Roy, 2009). Crowe et al. (1998) have suggested that it achieves this effect both by vitrification and by direct interactions with proteins. When amorphous trehalose undergoes vitrification (T_g), it encases cell membranes and proteins in a protective glassy matrix, stabilising cell membrane integrity (Chen et al., 2001). By maintaining the separation of micro-domains, it keeps the lipid bilayer in its liquid crystalline phase as it becomes dehydrated (Wolkers et al., 2010). Moreover, trehalose can have intracellular effects. In solution, trehalose can cross the cell membranes of platelets and red blood cells by endocytosis (Crowe et al., 2003). Intracellular vitrification prevents the fusion of organelles and the formation of large ice crystals.

Trehalose may also protect proteins from unfolding during drying by entrapping water at the interface with the molecule (Crowe, 2007). By disrupting the tetrahedral hydrogen bond network of water, it reduces the amount of water available for freezing (Patist and Zoerb, 2005). This mechanism has been termed water sequestration. In addition, it interacts directly with polar residues via hydrogen bonding, replacing water molecules (Crowe et al., 1984). Known as water replacement, this is thought by some researchers to be necessary for lyoprotection (Christensen et al., 2008). However, this does not fully explain its functions, which are related to its structural polymorphism (Nagase et al., 2002).

3.2.5.1 Conformational states of trehalose

Trehalose exists in various polymorphic structural conformations that differ in their molecular interactions and hygroscopic properties (Gil et al., 1996). The forms are summarised in figure 3.1. They include ordered crystalline and amorphous forms. Other conformations are also possible (e.g., liquid). The most common form is the dihydrate crystal, which is formed from solution in water (Sussich et al., 2001). Gil et al. (1996) identified an anhydrous form with unique properties. Formed by evaporation of moisture from the dihydrate crystal, anhydrous trehalose is able to readily absorb moisture (Sussich et al., 2001). ‘Fast’ evaporation from the dihydrate crystal molecule gives rise to an amorphous form in preference to the crystalline alternatives (Sussich et al., 2001). At least two other crystalline forms (e.g., anhydrate) can be formed from the dihydrate and the amorphous sugar. As these do not easily interact with moisture and do not vitrify, they are not protective (Hancock and Zografi, 1997). The crystallisation of trehalose from dihydrate, amorphous and glassy forms releases water to the material, which profoundly reduces its performance as a protectant (Costantino et al., 1998a; Hunter et al., 2010). The ability of trehalose to bind water

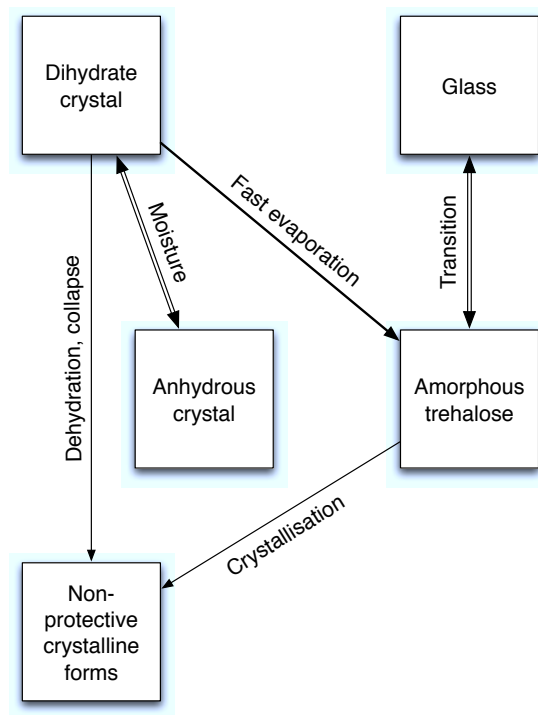


Figure 3.1: Trehalose forms

Schema of trehalose conformational states, adapted from Sussich et al. (2001). The dihydrate crystal, formed from solution in water, can reversibly release moisture to produce an anhydrous form which can act as a desiccant. Under certain conditions, amorphous trehalose can be produced, which can undergo vitrification. The dihydrate and the amorphous form can also produce two other crystalline forms which are not protective. Only relevant transitions have been included.

is determined by the torsional angles around the C-O-C glycosidic linkage (Akao et al., 2001). The anhydrous form is characterised as having an ‘open’ conformation, and can bind water stoichiometrically. Conversely, the non-protective anhydrate form is densely packed. The causes of crystallisation of trehalose on preserved products are incompletely understood. In experimental conditions, crystallisation can be induced by altering the humidity and temperature of the dihydrate and amorphous forms for periods of time lasting several hours (Akao et al., 2001; Surana et al., 2004b).

3.2.5.2 Vitrification of trehalose

Amorphous and anhydrous conformations can be formed simultaneously (Nagase et al., 2002). The anhydrous crystal acts as a desiccant, preventing devitrification and recrystallisation of the amorphous sugar (Akao et al., 2001). This effectively enables the sugar to remain glassy despite the sorption of moisture. When completely dry, amorphous trehalose possesses a T_g temperature of 120°C (Chen et al., 2000). Moisture acts as a plasticiser, reducing the T_g temperature down to even less than -100°C. As the T_g temperature approaches ambient temperature, crystallisation of the amorphous sugar causes its protective effect to be lost (Costantino et al., 1998b). This occurs at a RH of approximately 50%, suggesting that, in order to maintain the protective effects of trehalose, the A_w should be kept below at least 0.5 (Costantino et al., 1998b). Sitaula and Bhowmick (2006) have reported that a dry basis trehalose-PBS ratio of 10:1 provides the optimal trehalose concentration for the storage of cells as long as A_w is kept below 0.23 to maintain the glassy state. The trehalose effect is complicated by the addition of other excipients. While the T_g may be decreased by increasing the mass fraction of buffered saline in the medium (Sitaula and Bhowmick, 2006), certain divalent cations are reported to act synergistically with amorphous sugars to stabilise proteins by inhibiting crystallisation (Carpenter et al.,

1992).

3.2.6 Trehalose-AM interactions

Despite the interactions of trehalose and cell membranes, the disaccharide is excluded from the lipid bilayer of most intact cells (Satpathy et al., 2004), yet may have important effects on the whole tissue. It has been suggested that trehalose can preserve the ultrastructure of lyophilised, denuded AM (Nakamura et al., 2008). As different methods of drying strongly influence the pharmaceutically relevant forms and properties of trehalose (Surana et al., 2004b), they can substantially alter the preservation of AM. Drying methods that produce more amorphous and anhydrous forms of trehalose would favour its role in preserving both the gross physical properties of AM and its more subtle properties such as cell morphology and protein content.

The precise interactions between AM, moisture and excipients are unknown, and can be explored by ancillary techniques commonly used in thermal analysis, including XRD, ATR-FTIR and ToF-SIMS/PCA. These techniques have the advantage of being able to sample biological tissues without much further preparation, providing information on molecular changes at or near the surface.

The extent to which substances can be characterised as amorphous or crystalline can be estimated from XRD spectra by a method described by Hermans and Weidinger (1948). XRD is performed by irradiating a sample through a range of angles at a known wavelength. The angle of deflection (angle 2θ) corresponds to the characteristic spacings of planes within crystal structures (d-spacings). This produces a series of diffraction peaks, which can be identified by comparing the data to tabulated PDFs, available from the International Centre for Diffraction Data®. The various polymorphic crystalline forms of trehalose have XRD profiles with characteristic peaks Nagase et al. (2002). Trehalose dihydrate can be identified from a character-

istic diffraction peak with an angle 2θ of 23.9° , whereas the anhydrous form has a characteristic peak at 16.1° . These are absent in the non-protective crystalline forms, while the amorphous phase is smooth and featureless.

The principal parameter that can be obtained from FTIR spectra is the band position of molecular group vibrations (Movasaghi et al., 2008). As a collagenous material, AM demonstrates characteristic amide absorption bands at 1655 cm^{-1} (C=O stretching, amide I), 1551 cm^{-1} (N-H bending, amide II) and 1239 cm^{-1} (N-H bending, amide III) (Singh et al., 2007). Ma et al. (2010) found additional peaks at 3315 cm^{-1} (N-H stretching) and 2929 cm^{-1} (C-H stretching). The FTIR spectra of trehalose polymorphs were initially reported by Gil et al. (1996). The dihydrate crystal exhibits a characteristic sharp peak at 3500 cm^{-1} , corresponding to the stretch vibration of two crystal water molecules (O-H stretching), and another at 1680 cm^{-1} (H-O-H bending). Additional FTIR peaks occurring at 994 and 954 cm^{-1} correspond to asymmetric and symmetric stretching of the trehalose α -(1 \leftrightarrow 1)-glycosidic bond. The sharp peak at 3500 cm^{-1} disappears in the anhydrous and amorphous forms, while altered conformation of the glycosidic linkage causes the 994 and 954 cm^{-1} peaks to shift in a characteristic way that is specific for the various forms (Akao et al., 2001). The spectrum of amorphous trehalose is similar to that in solution and markedly different from the crystalline form, suggesting that hydrogen bonding in the dried state is comparable to the dissolved state (Wolkers et al., 2004). Hydrogen bonding between the trehalose hydroxyl groups and surface polar groups shifts the FTIR bands to frequencies typical of hydrated proteins (Crowe et al., 1984). As a result, the surface proteins of freeze-dried platelets retain a similarity to proteins in fresh platelets when treated with trehalose (Wolkers et al., 2001). Conversely, the addition of large amounts of PBS to trehalose has been shown to reduce the hydrogen bonding capacity of trehalose (Sitaula and Bhowmick, 2006). FTIR studies have demonstrated that at high RH,

trehalose undergoes crystallisation, losing its protective ability (Costantino et al., 1998b).

The investigative technique of ToF-SIMS uses a primary ion beam is used to generate secondary ions from the uppermost surface monolayer of a material (a depth of approximately 10 Å). This highly energetic process fragments the molecules into smaller ions which can be analysed by their time-of-flight to produce a mass spectrum (Gross, 2004). This can generate a vast repository of information, so multivariate analysis (MVA) is usually necessary to extract the information required from the ToF-SIMS spectral data in a meaningful way (Wagner et al., 2004). Principal component analysis (PCA) is a powerful method of MVA of spectra from different samples, providing statistically robust transformations of large data sets into more manageable ones (Yang et al., 2005). A thorough understanding of PCA assumes a knowledge of vector and matrix algebra. A comprehensive explanation is given by Lee and Gilmore (2009). Since the spectral peaks of the amino acid fragment ions are known, ToF-SIMS/PCA can be used to characterise adsorbed protein films on biomaterial surfaces (Wagner and Castner, 2001). Using ToF-SIMS and PCA, Xia et al. (2002) found that proteins treated with trehalose retained hydrophilic or polar amino acids, analogous to their state in aqueous solution, whereas untreated proteins had high concentrations of hydrophobic amino acids typically found in the interior of the protein molecule.

3.3 Materials and methods

3.3.1 Tissue procurement and processing

3.3.1.1 Harvesting of AM

AM was obtained from healthy volunteers following ethics committee approval of this project. A formal consenting procedure was observed requiring the patient's signature. Women with a history of intravenous drug abuse and multiple sexual partners were not invited to participate. The medical notes were checked for infectious diseases, such as Hepatitis B and C, HIV, syphilis and tuberculosis. Gestational diabetes was considered a contraindication, as were other rarer medical conditions. Tissue was only procured if the healthy pregnant mother understood the explanation and was satisfied. A maternal age over 40 was considered a bar to donation. The operating theatres were informed of all mothers wishing to participate. The midwives who were responsible for checking the placenta were asked to isolate the placenta in a sterile plastic bag with the umbilical cord clamped at its two ends. It was collected immediately after birth had occurred and transported to the laboratory for processing.

3.3.1.2 AM preparation

Processing was carried out in a fume hood, following departmental protocols described by Hopkinson et al. (2006b). The mid-zone and apical AM was cut with scissors to leave a 2 cm skirt of tissue around the placenta (figure 3.2 A). The tissue was immediately placed in normal saline solution. The AM was separated from the chorion by peeling (B) and placed into a flask containing 300 mL of cold normal saline. It was washed by placing the flask on a rocker and replacing the saline every 30 mins \times 3. After the final 30 min wash, the hydrated spongy layer was then peeled off by pushing it away in a single layer with the back of a surgical blade (C), and any

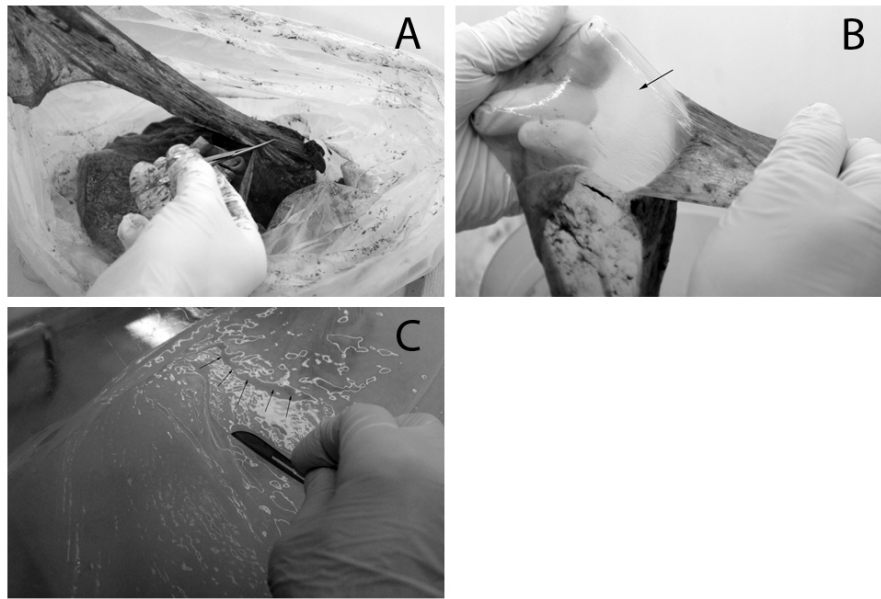


Figure 3.2: Preparation of AM

This sequence shows cutting of amniochorion from placenta (A), peeling of chorion from AM (black arrow, B) and removal of spongy layer (black arrows, C)

areas of blood contamination were removed before a further quick wash. The AM was carefully checked for blood and then cut into sections. This was initially carried out with a surgical blade. To achieve a more consistent size and shape, stainless steel templates were designed for the purpose. The templates were round, to allow circular cutting movements, and were available in 2.5 cm or 5.0 cm diameter sizes. Fresh AM was placed in a solution of modified, sterile-filtered 1 × Dulbecco's PBS without magnesium chloride (Sigma-Aldrich, UK) and kept at 4°C. For freezing, the AM pieces were placed in polypropylene universal tubes (Sarstedt, Germany) containing PBS. These were labelled and placed in a freezer at -80°C. Alternatively, AM pieces were vacuum-dried. AM preserved by freezing and then thawed for experimentation is referred to as 'freeze-thawed', abbreviated to 'f-t AM'.

3.3.1.3 Thermolysin denuding

When required, the thermolysin method was used to denude the epithelium as described by Hopkinson et al. (2008) and modified by Gicquel et al. (2009). The bacterial protease thermolysin (from *Bacillus thermoproteolyti-*

cus rokkō) was obtained from Sigma-Aldrich (St. Louis, MO, USA). Sections of fresh AM (5 cm × 5 cm) were placed in flasks containing a solution of thermolysin in 1 × PBS (125 µg/mL). The flasks were agitated for 9 mins at 37°C or for 20 mins at room temperature. The thermolysin-treated membranes were then washed in PBS in a flask until it turned cloudy, and then washed twice more until the cloudiness disappeared. Next, the AM sections were washed on a rocker for 20 mins in PBS.

3.3.1.4 Trehalose pre-treatment

When required, AM was pre-treated in trehalose solution in PBS. A 5% or 10% weight to volume solution of trehalose dihydrate (FW = 378.34) was prepared by dissolving the desired weight of trehalose in 1 × PBS. For a 10% solution, 4 g of trehalose dihydrate powder (molar mass 378.33 g mol⁻¹) was dissolved in 40 mL 1 × PBS, containing 0.32 g NaCl, 0.008 g potassium phosphate (monobasic), 0.046 g sodium phosphate (dibasic) and 0.008 g potassium chloride. Sections of AM were incubated in 0%, 5% or 10% trehalose solution and agitated in an orbital shaker at 37°C for 2 hrs prior to vacuum-drying. This produced AM pieces covered with a mixture of trehalose and PBS with an approximate dry weight ratio of sugar to salt of 10.5:1 (100 g sugar per 9.55 g salt).

3.3.1.5 Vacuum-drying

As a thin film, AM could be dried very rapidly without pre-freezing. In order to minimise processing steps, the cut AM discs were placed stromal side down into open smooth thermoplastic pouches (Orved SpA, Musile di Piave, Italy), made of a transparent polyamide air-impenetrable exterior and a polyethylene interior, before vacuum-drying. These were placed into a vacuum drying chamber (ALPHA 1-4 LSC Advanced Freeze Dryer, Christ®, Osterode, Germany). The time and pressure settings during main and final

drying were programmed manually. The main drying phase settings used included a time of 2 hrs, ice condenser temperature of -55°C and chamber pressure of 1.030 mbar. The final drying phase was 60 mins, with a pressure of 0.0010 mbar. This was sufficient to produce a dry tissue which could be rehydrated in a few drops of sterile water. Once the vacuum-drying cycle was completed, the thermoplastic pockets containing the samples were vacuum-sealed in a VM12 vacuum chamber (Orved SpA). Samples were stored at room temperature. Vacuum-dried AM was tested either as a dry tissue or in its reconstituted state. Vacuum-dried AM is referred to as 'v-d AM'. The samples which were incubated in PBS with no trehalose are referred to as '0% v-d AM' or 'untreated v-d AM'. The addition of 5% or 10% w/v trehalose is referred to as 5% or 10% trehalose treatment, and the samples are referred to as '5% v-d AM' or '10% v-d AM'.

3.3.2 Moisture sorption analysis

3.3.2.1 Dynamic vapour sorption¹

DVS was performed on three pairs of 0% and 10% v-d AM samples. Two pairs (A and B) were prepared with 2 hrs main drying time and 1 hr final drying. One pair (C) was prepared with 1 hr main drying and 30 mins final drying. The 10% v-d AM sample from this pair was given a final wash in PBS prior to drying. The 0% v-d AM sample was exposed to the atmosphere for 7 days prior to testing. AM samples were chopped into 5 mm squares with a blade. These were weighed and placed in a glass basket in a temperature-controlled chamber in the DVS instrument (model DVS-1, Surface Measurement Systems Ltd, Wembley, UK) (figure 3.3). The glass basket was cleaned with ethanol prior to use and dryness assured by repeat gravimetric checking. The DVS phases consisted of a drying phase, lasting 500 mins, and a sorption-desorption phase lasting 167 hrs.

¹The DVS was operated by Dr Bill MacNaughtan at the School of Pharmacy.

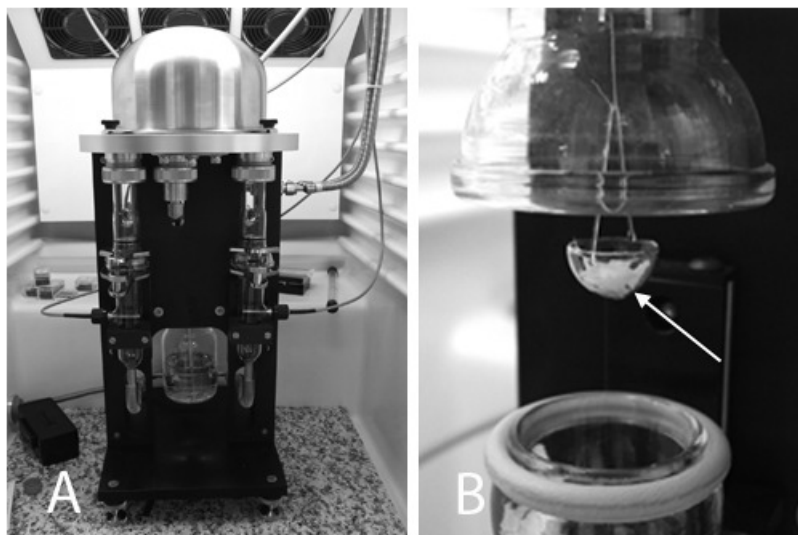


Figure 3.3: DVS instrument

The DVS-1 instrument is shown in A, with a chopped AM sample (arrow) in a glass basket in the temperature-controlled chamber before closure (B).

Drying phase In preparation for the sorption isotherms, drying curves were obtained for the three pairs of v-d AM samples (A, B and C). During the drying phase, the samples were exposed to a dry stream of N_2 gas at a constant temperature for 500 mins. The temperature was kept at 20.3°C throughout. The percentage mass lost due to drying was calculated from an initial normalised mass of 100%. The slopes of the final 10% of the drying curves were calculated by using simple linear regression analysis software (Sigmaplot® for Windows, Systat Software, Inc., CA, USA). The data was fit to the following polynomial linear equation:

$$y = y_0 + ax$$

where x is time, y is mass and a is the returned value for the slope.

Sorption isotherms At the end of the drying phase, the dry weight was set at 100%. The samples were exposed to a series of step changes in target RH, while the change in mass was monitored continuously. This instrument was programmed to allow the dry gas to mix with gas of a known water

vapour saturation, producing the desired target RH. This was increased from 0% to 95% in nine steps lasting 500 mins: 10%, 20%, 30%, 40%, 50%, 60%, 70%, 80% and 95%. The sample RH was measured continuously by an electronic humidity probe in the chamber. At the end of the last step, the target RH was decreased back to 0% in equal steps. A number of plots were produced from the data:

1. Target RH and equilibrium RH were plotted against time, comparing the equilibration of 0% and 10% v-d AM.
2. Water vapour sorption kinetic graphs were plotted. This plots the change in percent dry mass (moisture content) alongside the measured sample RH (A_w) and is useful for comparing the sorption characteristics of 0% and 10% v-d AM. These variables were tabulated at a series of RH values (10%, 60%, 70%, 80% and 95%) to compare v-d AM samples.
3. Moisture content (change in mass) was plotted against the A_w of the 0% and 10% v-d AM samples to produce isotherm graphs. The two components of each isotherm include a sorption phase (increasing humidity) and a desorption phase (decreasing humidity). The hysteresis was calculated as the maximum difference in mass between the sorption and desorption phases at any one target RH. From these curves, the A_w was extrapolated from moisture contents of 10% and 20% as examples. Conversely, the moisture content was extrapolated from the target RH at 70%.
4. The DVS software automatically generated Young and Nelson plots. These fit the sorption and desorption data to a mathematical equation which estimates differences in the monolayer and multilayer adsorption and bulk absorption of 0% and 10% v-d AM. The Young and Nelson parameters are generated as positive changes in mass for adsorption

and negative changes for internal absorption by the software.

Statistical comparisons between samples of 0% and 10% v-d AM (A and B) were made using the paired *t* test.

3.3.3 Thermal analysis

3.3.3.1 Thermogravimetric analysis

TGA was performed by open and closed pan methods to compare their suitability for measurement of thermal events in v-d AM. Baseline adjustment experiments were performed for both methods by conducting TGA runs on empty pans. The change in pan mass over the course of the experiment was then subtracted from the sample runs to determine the actual gravimetric change in sample mass.

Open pan method TGA was initially performed in open platinum pans to determine the moisture content of four sets of 0%, 5% and 10% v-d AM samples. A Q600 SDT simultaneous thermogravimetric analyser/differential scanning calorimeter (TA Instruments, Delaware, USA) was used. Vacuum-sealed AM samples were cut into squares of approximately 10 mm × 10 mm immediately prior to testing and weighed. The platinum pans used as sample holders were heated with a small blowtorch to burn off any residual organic material. AM samples approximately identical in weight (2 - 3 mg) were placed inside open platinum pans. Trehalose dihydrate powder was analysed for comparison. The pans were placed side by side on transducers. These were then sealed in a chamber which was filled with N_2 gas. The instrument was started at room temperature, and heating was ramped up by either 5°C or 10°C min⁻¹. At the end of each cycle, the instrument was air-cooled to a temperature close to room temperature in preparation for a further sample. Trace of mass versus temperature were recorded by TA

Universal Analysis software. The data were analysed at a cut-off start temperature in order to zero the TGA curves from the different runs. Two sets of 0%, 5% and 10% v-d AM samples was analysed with a cut-off temperature of 25.2°C and a heating rate of 10°C min⁻¹. For two further sets, the cut-off temperature was 19.5°C and the heating rate was 5°C min⁻¹. The TGA curves obtained were analysed using Universal Analysis 2000 software (TA Instruments) and by plotting first derivative curves (below). The decomposition gradients were measured from the TGA curves and expressed as % mass loss per °C.

First derivatives The first derivatives of the TGA curves were plotted, enabling key points of flux to be identified. This useful function is available as a macro within Sigmaplot® software. The point at which total evaporation occurred and decomposition started was identified as the point at which the initial slope of water loss became completely flat (complete evaporation of bound water). The maximal rate of decomposition was identified as a point on the decomposition gradient at which a reversal in the first derivative curve occurred. The gradient of decomposition and moisture content were obtained for each sample. The moisture content was obtained by subtracting the sample weight at the point of maximal water loss from the mass at the cut-off temperature. The curves were normalised by express mass as a percentage. A locally weighted smoothing function (loess algorithm), available in Sigmaplot®, was applied to the first derivative curves with a sampling proportion of data of 0.1 and a polynomial degree of 1.

Alternative drying methods To assess the effectiveness of vacuum drying AM, samples were dried by alternative methods. AM samples were laid on PTFE sheets and placed in a standard laboratory drying cupboard heated to 70°C for 24 and 48 hrs. Further samples were placed in glass vials in a vacuum oven (Heraeus® Vacutherm® Oven, Fisher Scientific UK, Ltd) at

50°C and 50 mbar for 48 hrs. For comparison, TGA was performed on single samples dried by each method (three in total). The moisture content was measured by subtracting the mass at the point of maximum water loss from the mass at the cut-off temperature (25.2°C).

Closed pan method Further TGA experiments were performed in hermetically sealed aluminium pans to determine the moisture content of quadruplicate 0%, 5% and 10% v-d AM samples. The SDTA 851e (Mettler Toledo, Leicester, UK) was used for the closed pan experiments. This instrument uses a TSO801RO sample robot to pierce the pans a few milliseconds before heating starts. Thermogravimetric data is fed to a STARe software interface for analysis. Whole dried discs of AM were cut from the same template to a diameter of 5 cm and placed into the sealable aluminium pans, which were then capped shut and placed in the instrument. In this set of experiments, the cut-off temperature was 25.0°C and the heating rate was 5°C min⁻¹. Moisture content calculations were performed from the curves. This method enabled the identification of the maximal rate of water loss ('peak loss') as an additional variable. This was calculated along with evaporation and decomposition.

3.3.3.2 Differential scanning calorimetry

DSC was initially conducted by increasing the temperature at a constant rate until a desired end point is reached (ramp mode). This, however, did not permit visualisation of any thermal transitions that may occur beneath the main endotherms. An alternative method was employed by ramping the temperature up to an intermediate, reversible level and then repeating the cycle (cyclic DSC). Cyclic DSC permits the unmasking of hidden reversible changes, for example by those masked by water, as the flatter curves reveal additional hidden transitions. The main property that DSC measures is

heat flow in watts (W). Thermal transitions are characterised by changes in heat flow, known as endotherms (or exotherms if the direction of heat flow is outward). T_g temperature can be localised as an endothermic step on a DSC trace. By subtracting a baseline from the heat flow curve, the specific heat capacity (C_p) of a material may be determined. Enthalpy is then calculated by integrating the area under the C_p curve.

Ramp mode DSC was performed in triplicate on 0% v-d AM samples and in duplicate on 10% v-d AM samples from different donors. A DSC Q2000 (TA Instruments, Delaware, USA) was used in ramp mode at a heating rate of 5°C min^{-1} from -40°C to 300°C . V-d AM samples were carefully weighed and loaded into aluminium pans which were also weighed and then sealed with a crimper. A separate pan was weighed as a reference for the sample pans. The samples were loaded by a robot arm, and the pre-set heating rate was applied at 5°C min^{-1} as a single ramp. The data was recorded in Universal Analysis 2000 (TA Instruments) software files. Baseline measurements were subtracted.

Cyclic DSC Cyclic DSC runs were performed on the TGA/SDTA851 instrument (Mettler-Toledo). Whole v-d AM discs were weighed and placed in stainless steel pans which were then hermetically sealed and loaded in the automated instrument. Duplicate samples of 0%, 5% and 10% v-d AM were analysed. A sample of vacuum-dried 10% w/v trehalose dihydrate powder in PBS was analysed alongside the v-d AM samples. This was prepared under the same conditions as 10% v-d AM to keep the same fractions. For all the samples, the cycle temperature ranged from -50°C to 180°C , rising at a rate of $10^\circ\text{C min}^{-1}$. The onset, peak and end points of the endotherms and the enthalpies of the curves were obtained by automated STARe software. Baseline measurements were subtracted automatically. For T_g temperatures, the inflection point of the sigmoidal step was calculated by extrapolating the

tangents of the curves and finding the midpoint of a line joining the tangents. The onset and end point of the transition were obtained from the crossing points of the extrapolated tangents.

3.3.4 Dynamic mechanical analysis²

DMA testing of vacuum-dried AM was carried out using a Triton Technology Dynamic Mechanical Analyser (PerkinElmer, Inc., MA, USA) equipped with humidity and temperature control. The instrument applies a sinusoidal displacement (strain) to samples under tension and measures the material response (stress) with a linear variable differential transducer. In automatic tension mode, it adjusts the static displacement via a feedback mechanism, attempting to maintain the static force at a set percentage above the dynamic force required to drive the sample. As the sample slackens or tightens, the static displacement is automatically adjusted to keep the sample under tension and maintain the oscillatory amplitude. The oscillatory amplitude is typically within the linear viscoelastic region of the material (Turi, 1997). Parameters generated by DMA include the storage modulus E' , the loss modulus E'' and the ratio between the loss and storage moduli, $\tan \delta$. These undergo characteristic changes at the T_g , which occurs over a temperature range. The instrument has a E' resolution of 0.0001 Pa and a force resolution of 0.0025 N. Only once the sum influences of the static and dynamic forces are correct will the initial E' measurements appear credible.

The T_g of an amorphous viscoelastic polymer is illustrated by an example of a DMA trace obtained from data for a strip of PMMA of geographic dimensions of 12.44 mm \times 7.10 mm \times 2.36 mm (figure 3.4).³ Frequencies of 1 and 10 Hz and an oscillatory amplitude of 0.5% were used to obtain the trace. As the material undergoes a transition between its glassy and

²This was performed with the help of Dr Jeffrey Glyn van de Velde, formerly of Triton Technology.

³Data kindly provided by Dr Bill MacNaughtan

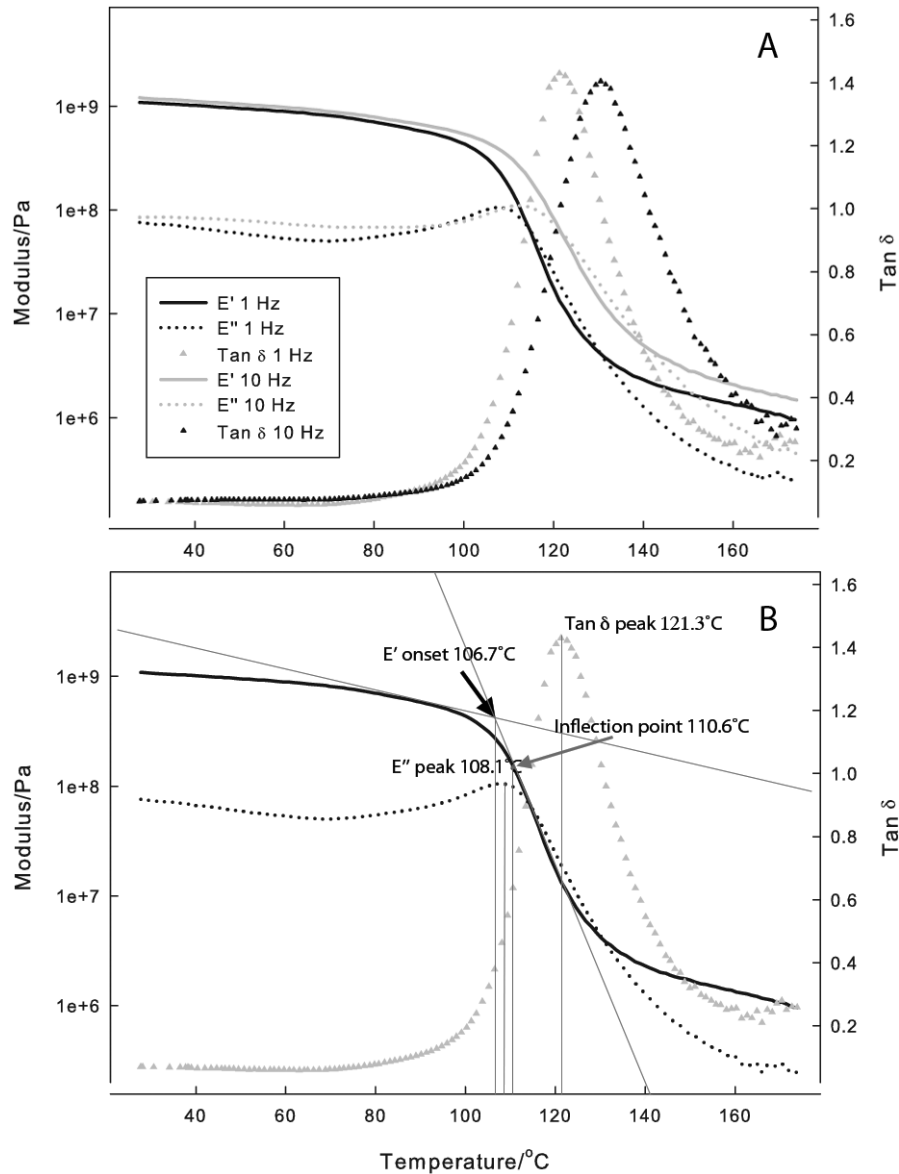


Figure 3.4: Multifrequency moduli and $\tan \delta$ of PMMA

An example of a DMA trace obtained for PMMA is shown. The storage modulus E' begins to decrease more steeply above $\sim 100^{\circ}\text{C}$, whereas both E'' and $\tan \delta$ exhibit peaks. T_g is frequency dependent, occurring at higher temperatures with higher oscillatory frequencies (A; 1 Hz and 10 Hz). The measurement of T_g from a DMA trace can include different methods (B), including the onset of the steep decrease in E' (black arrow), the inflection point of E' (gray arrow) and the maximum values of E'' and $\tan \delta$ (1 Hz).

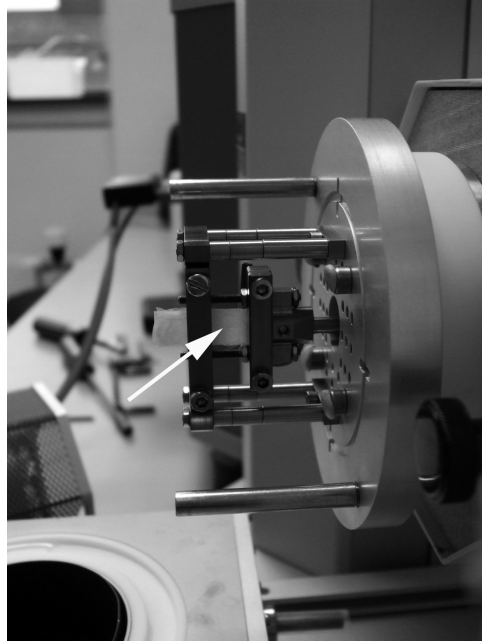


Figure 3.5: DMA of v-d AM sample

A 10 mm wide multiplex strip of AM (white arrow) is clamped for DMA. The free length is 10 mm.

rubbery states, E' begins to fall, while E'' and $\tan \delta$ exhibit peaks. The T_g values undergo shifts in temperature at different oscillatory frequencies, demonstrating strain-rate dependency. A number of measurements are possible, including the onset of the fall in E' , the peak of E'' and the peak of $\tan \delta$ at each frequency. The inflection point of E' has been obtained from the first derivative of the data, and represents the maximum flux of the slope. ISO 6721-11 part 11 stipulates that this measurement should be quoted as the T_g temperature of plastics. Measurements can be complicated by overlapping processes, such as smaller thermal relaxations and the effects of moisture and excipients, which can be variable and broad. Accurate and precise measurement of the sample geometry is essential in obtaining credible data.

V-d AM specimens (mid-zone of AM, random orientation) were cut into longitudinal strips 10 mm wide and 30 mm long (figure 3.5). The geometry of the strips was measured by using a digital micrometer and a digital caliper (Mitutoyo UK, Andover). The strips were mounted lengthways in

tension clamps, with a free length of 1 mm, 5 mm or 10 mm between the clamps. The dimensions of the sample were entered into the instrument software. Exploratory frequency sweep DMA runs were conducted across a variety of ranges of humidity and temperature. These were performed with automatic tension mode off. The longitudinal oscillatory displacement amplitude was set at 0.05% of the free length of the sample. An additional static force of between 0.01 and 0.5 N was then applied. Applying a small force ensured that residual slack from the clamping procedure was taken up, placing the sample under tension.

Following the initial frequency sweep tests, temperature sweep and humidity sweep modes were used to obtain information on the T_g temperature and the effects of moisture. The ratio of static to dynamic force was controlled by applying an automatic tension setting of 150% for the humidity and temperature sweep modes. A DMA run was considered successful if the static force remained higher than the dynamic force during the glassy phase. To increase the amount of tensile force applied to the sample, DMA runs were also conducted with multiple layers of v-d AM sandwiched together. On checking the data, a decision was made to proceed or halt the experiment. DMA runs were abandoned if the sample broke or if the dynamic force exceeded the static force in the initial part of the run, giving lower than expected values of E' . The ratio of sample to total stiffness (instrument + sample) was used as an additional guide. Typically, this ratio is high (above ~80%) in the glassy phase of the run. An unusually low ratio suggested slackness of the sample. Runs that ended in sample breakage were halted and repeated until successful traces were obtained if possible.

3.3.4.1 Frequency sweep

DMA measurements were performed on 12 strips of 0% v-d AM and six strips of 10% v-d AM in ambient temperature. The DMA was started in

frequency sweep mode to determine the kinetic parameters at which the moduli E' and E'' and $\tan \delta$ could be measured. The exposed area of AM between the clamps was $10 \text{ mm} \times 10 \text{ mm}$. A positive total applied static force of 0.02 N was applied, and the displacement amplitude was set at $50 \mu\text{m}$. DMA runs were performed in triplicate at 15 intervals of increasing frequency ranging from 0.10 to 100 Hz . The frequencies were set at increments of between 0.1 and 100 Hz . E' , E'' and $\tan \delta$ were plotted against the oscillatory frequency of the DM analyser for a representative strip of 0% v-d AM.

3.3.4.2 Humidity sweep

Humidity sweep DMA runs were carried out in triplicate on strips of 0% , 5% and 10% v-d AM. V-d AM strips of different dimensions (10 mm and 1 mm) were used to assess the influence of RH on T_g . The oscillatory frequencies were set at 1 and 10 Hz . A moisture control system was attached to a sealable chamber on the DMA instrument. The samples were enclosed within the chamber before testing. The system was capable of varying the RH between 10% and 90% . The humidity sweep tests were conducted at room temperature or at a constant temperature. RH was increased either as a series of stages or in a single ramp. E' , E'' and $\tan \delta$ were plotted against RH to localise the T_g .

3.3.4.3 Temperature sweep

Temperature sweep DMA runs were performed at ambient RH on triplicate samples of 0% and 10% v-d AM samples. Samples with free lengths of 10 mm , 5 mm and 1 mm were tested to assess the relationship between temperature and T_g . The oscillatory frequencies were set at 1 and 10 Hz . A liquid nitrogen-based cryogenic cooling system and a radiant oven were attached to a sealable chamber that enclosed the DMA clamps. Each sample

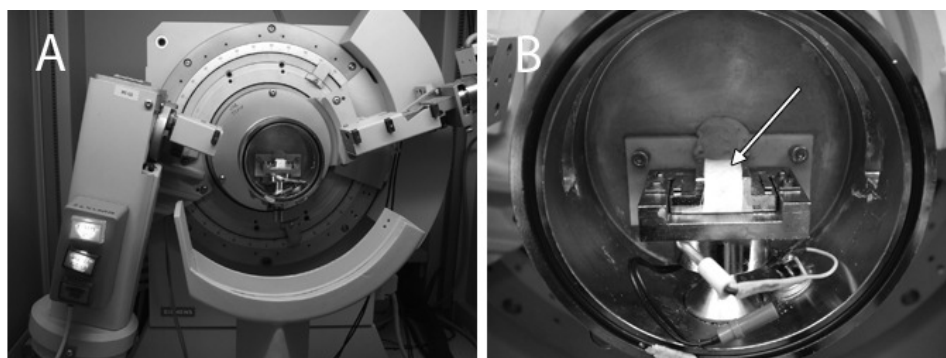


Figure 3.6: XRD instrument

The Bruker-AXS D5005 XRD diffractometer is shown (A), with a close-up view of the AM sample (B, arrow).

was carefully mounted before the temperature-control chamber was placed on the instrument. The heating ramp rate was $2 - 4^{\circ}\text{C min}^{-1}$. The moduli E' , E'' and $\tan \delta$ were plotted with RH to localise the T_g . The temperature sweep tests were performed at ambient humidity, which was not recorded.

3.3.5 Surface analysis

3.3.5.1 Wide-angle X-ray diffraction

The X-ray patterns of duplicate 0% and 10% v-d AM samples were obtained using a Bruker-AXS D5005 diffractometer (Siemens, Erlanger, Germany). AM samples were folded twice into a strip, which was mounted horizontally on a stainless steel sample holder and secured with tape. The steel holder was placed in the X-ray diffractometer (figure 3.6). An X-ray beam was shone from a 2.2 kW sealed copper anode (K-alpha emission wavelength λ 1.5418 Å) at a current of 40 mA and a voltage of 40 kV. The scanning region of the diffraction angle (ϑ) ranged from 2° to 45° with a step size of 0.05° and a time per step of 1.5 secs. The sample rotation speed was 60 rpm. The intensity of the peaks was plotted against the angle of deflection, 2ϑ . The AM traces were aligned and normalised to a peak from the sample holder that was common to all traces. Background emission from the empty steel holder was then subtracted from the AM traces. The proportion of crystallinity of

the samples was estimated visually by dividing the area under the peaks only (crystalline regions) by the area under the entire diffraction pattern (crystalline plus amorphous regions).

3.3.5.2 Infrared spectroscopy

For ATR-FTIR, a beam of infrared light is passed into a crystal with a tissue sample apposed to the optically denser crystal surface. The light is reflected, although a small amount of light also penetrates the sample to a depth of a few μm . The vibrating molecular bonds within the sample absorb specific infrared frequencies, attenuating the propagating wave. A mathematical algorithm (Fourier transform) then converts the attenuated wave into a spectrum. The sample absorbance can be plotted against the wavelengths (wavenumbers, measured in cm^{-1}) to give characteristic patterns relating to specific chemical bond vibrations, such as carboxyl stretching or amide bending.

Initial ATR-FTIR runs were carried out on 0%, 5% and 10% v-d AM samples using a Bio-Rad FTS-6000 spectrometer (now made by Digilab) equipped with a thallium bromoiodide crystal (KRS-5). The penetration depth of a sample with a refractive index of 1.4 at $1,000\text{ cm}^{-1}$ is 1-2 μm , depending on the angle of incident infrared light. The instrument was calibrated by running a background scan with no sample. This was then set as a baseline for subsequent samples. Each sample was pressed directly onto the crystal to maximize optical contact. The incident light was set at an angle of 45° . The AM samples were folded in two or three layers in order to allow the instrument to obtain a reading. Trehalose dihydrate powder was examined by covering the crystal with powder and pressing it down. The AM spectra were normalised with respect to the peak absorbance of C=O stretching, a characteristic absorption band which formed a prominent peak at 1652 cm^{-1} in v-d AM, but which was negligible in trehalose dihydrate and

of equal wavenumber across treated and untreated samples. The various spectral bands were identified from studies on AM by Ma et al. (2010) and on trehalose by Akao et al. (2001). The spectra were annotated for comparison.

ATR-FTIR was then conducted on triplicate 0% and 10% v-d AM samples on a Bruker TENSOR™ 27 FT-IR spectrometer (Bruker Optik GmbH, Ettlingen, Germany), which is equipped with a diamond crystal. A background scan was performed prior to sample testing. The spectra were normalised automatically by OPUS 5.5 spectroscopic software. In contrast to the previous method, this involved automated vector normalisation of the entire FTIR spectra. The spectra were not compared quantitatively. The fingerprint regions of trehalose were examined to identify the polymorphs present.

3.3.5.3 Mass spectrometry

Samples of 0%, 5% and 10% AM were prepared and cut in two to assess both surfaces, designated a and b, separately. Each sample was secured onto a sample holder for loading into the spectrometer and placed in an airlock overnight which was pumped down to ultra-high vacuum conditions. The samples were placed in the main chamber of the mass spectrometer for analysis. ToF-SIMS analysis of the samples was conducted using a TOF-SIMS IV time-of-flight secondary ion mass spectrometer (ION-TOF GmbH, Münster, Germany) using a 25 KeV Bi₃⁺ primary ion source and a single-stage reflectron analyser. Positive and negative secondary ion ToF-SIMS spectra were acquired from a mass-to-charge ratio of 0 to 800 m/z over a rastered area of 100 μm × 100 μm at a resolution of 256 × 256 pixels, while maintaining a primary ion dose less than 10¹² ions/cm² to ensure static conditions. The data was integrated by the instrumentation software and exported as for further pre-processing. The area selected was as flat as possible, since

topographical variation could give rise to small changes in recorded data. Each sample was analysed in two different areas for both positive and negative spectra. A pulsed low-energy electron flood gun was used for charge neutralization for all the samples used in this study. Positive and negative ion ToF-SIMS spectra were calibrated prior to further analysis.

3.3.5.4 Data analysis⁴

The ToF-SIMS data were initially analysed using SurfaceLab 6 (ION-TOF GmbH) software. The peak intensities were corrected by the software to account for differences in dead time, which arises from the detection of only one secondary ion count per primary ion pulse, regardless of the number of secondary ions arriving at the detector at any time interval. A data set was designed as a spreadsheet matrix, consisting of 12 columns for each of both sides of three duplicate v-d AM preparations (0%, 5% and 10%) and n rows for each spectral peak. The corrected peak intensities for each secondary ion were normalised to the total intensity produced by each sample. This corrected for the differences in total secondary ion yield between spectra that can result from instrumental drift. The data was mean-centred by subtracting the mean intensity in each column from the samples, generating a new data set with the data mean at the origin.

The ToF-SIMS data sets were then analysed by PCA using PLS_Toolbox (version 5.2, eigenvector Research, Manson, WA) for MATLAB (Mathworks, Inc., Natick, MA). For PCA, each peak intensity value in a mass spectrum is considered as a unique variable in a multidimensional coordinate system. Each sample produces a mass spectrum with different intensity values, recorded as a data set. The data set is used to generate a covariance matrix that measures the extent to which the data points vary from the mean with respect to each other. Thus, the maximal variation across the various spec-

⁴Performed with the kind help of Dr David Scurr.

tra can be captured and plotted on a new axis, known as a principal component (PC). Each PC is ranked so that the axis that captures the largest fraction of the variation is denoted PC1. PC2, which must be uncorrelated to PC1, captures the next largest variation, and so on for the remaining PCs. The dimensionality of each new axis in the multidimensional space is termed eigenvector. Each eigenvector is associated with a numerical value that represents the amount of variance it contains, termed an eigenvalue (PC1 has the largest eigenvalue). The individual numbers in an eigenvector are called ‘loadings’. Linear combinations of the original variables and their loadings generate new data values called ‘scores’ for each sample on each PC, producing a scores matrix (\mathbf{T}). The correlation between the original *variables* and the PC axes is calculated as a loadings matrix (\mathbf{P}). The scores enable discrimination between the samples, whereas loadings plots identify the positive and negative peaks exhibiting most variation. An analytical model is used to reduce the data matrix \mathbf{X} to the sum of a cross-product of a transposed loadings matrix (\mathbf{P}') and the scores matrix \mathbf{T} , with a residual matrix, \mathbf{E} , representing ‘noise’:

$$X = TP' + E$$

\mathbf{TP}' is a reproduced data matrix, representing the bulk of the original variance in \mathbf{X} . Thus, PCs are linear, uncorrelated combinations of the original data sets. Transformation of data into uncorrelated eigenvalues and eigenvectors is a straightforward procedure with appropriate software. A small number of PCs is required to capture the salient information in a particular data set, making the detection of patterns in the differences between samples relatively straightforward.

PCA was performed by software algorithm to determine the eigenvalues and eigenvectors of the covariance matrix of the data set. Hotelling’s T^2 statistic, a multivariate generalisation of the student’s t distribution,

was used to detect outliers. The scores of respective PCs (e.g., PC1 and PC2) were plotted against each other to identify variations between samples. Loadings plots were used to identify the individual chemical species exhibiting the most variance by their mass-to-charge (m/z) ratio. The m/z ratios were matched to their chemical species. The average normalised corrected peak intensities of the chemical species identified were then plotted against the different v-d AM preparations.

3.4 Results

3.4.1 Moisture analysis

Moisture analysis was performed on a total of six v-d AM samples. Two pairs of samples (A and B) were prepared by drying for a 2 hr main phase and a 1 hr final phase. One pair of samples (C) had a main drying phase of 1 hr and a final drying phase of 30 mins. 10% v-d AM sample C was given a final wash in PBS before vacuum drying. 0% sample C was left exposed to the atmosphere for 7 days prior to DVS.

3.4.1.1 Drying curves

The drying curves are recorded as mass versus time plots and normalised by expressing the sample mass as a percentage (figure 3.7). The results are shown in table 3.1. The mean percentage loss in mass of 10% v-d AM samples A and B is 6.84% (SD 1.67%), whereas 0% v-d samples A and B, it is 9.95% (SD 1.03%) ($p = .157$). The means of the slopes of the final 10% of the drying curves, in % mass per minute, are significantly steeper for 10% v-d AM samples A and B ($-2.33E-03$, SD $9.69E-05$) than for 0% v-d AM samples A and B ($-4.67E-04$, SD $6.12E-05$) ($p = .002$). Subsequent statistical analyses concern samples A and B.

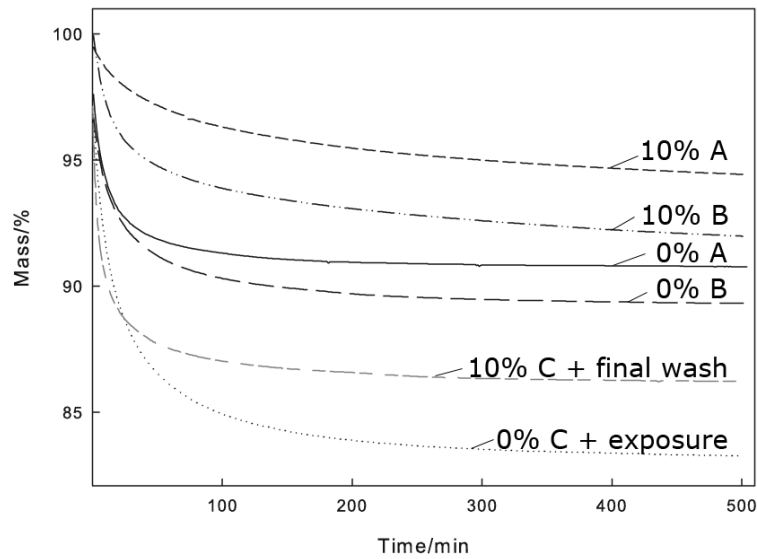


Figure 3.7: Drying curves of 0% and 10% v-d AM

Drying curves of three pairs of 0% and 10% v-d AM samples are shown. Samples A and B were prepared by drying for 2h (main phase) and 1 h (final phase). Samples C were prepared by drying for 1h and 30 mins. The 10 % C sample was washed in PBS prior to drying. The 0% C sample was left exposed to air for 7 days prior to DVS. DVS, dynamic vapour sorption.

Table 3.1: Drying curve parameters

V-d AM	% mass loss	Final 10% slope
0% A	10.68	-5.09E-04
0% B	9.22	-4.23E-04
0% C	16.72	-7.01E-04
10% A	5.58	-2.26E-03
10% B	8.02	-2.40E-03
10% C	13.76	-2.51E-04

The means of the slopes of the final 10% of the drying curves were measured in % mass per minute.

Table 3.2: Water vapour sorption of v-d AM

AM	Data (SD)	Target RH				
		10%	60%	70%	80%	95%
0% v-d AM	% dry mass	104.43	116.88	126.29	169.58	243.48
	SD	0.35	0.11	1.45	2.39	3.12
	Sample RH	12.7	60.8	70.1	78.7	92.7
	SD	0	0	0.35	0.14	0.35
10% v-d AM	% dry mass	101.69	111.08	116.93	126.36	161.29
	SD	0.76	1.38	1.69	1.14	1.23
	Sample RH	12.5	60.1	69.3	78.3	92.1
	SD	0.07	0	0.42	0.57	0.49

Values shown were recorded at the ends of the 10%, 60%, 70%, 80% and 95% RH stages. RH, relative humidity.

3.4.1.2 Water vapour sorption

Following drying, the samples were equilibrated in steps of increasing target RH for 500 mins each, followed by decreasing steps of equal duration. The target RH was plotted alongside sample RH (A_w) against time. To illustrate this relationship, one example (sample A, 0% and 10% v-d AM) is shown in figure 3.8 A. Data shown are means for samples A and B. In 10% v-d AM, equilibrium between target RH and sample RH occurs during the 60% RH stage, whereas in 0% v-d AM, it occurs at the 70% RH stage (table 3.2). Water vapour sorption kinetic plots were used to assess the changes in moisture content (% mass; serrated curves) with step changes in sample RH (figure 3.8 B). The end of the 60% RH stage is indicated with a black arrow for orientation. The mean corresponding changes in mass at the ends of five stages of RH (10%, 60%, 70%, 80% and 95%) are shown with the mean sample RH in table 3.2 for 0% and 10% v-d AM. By the end of the 80% RH stage, the percentage change in mass is significantly higher for 0% v-d AM (169.6%) than for 10% v-d AM (126.4%) ($p = .013$).

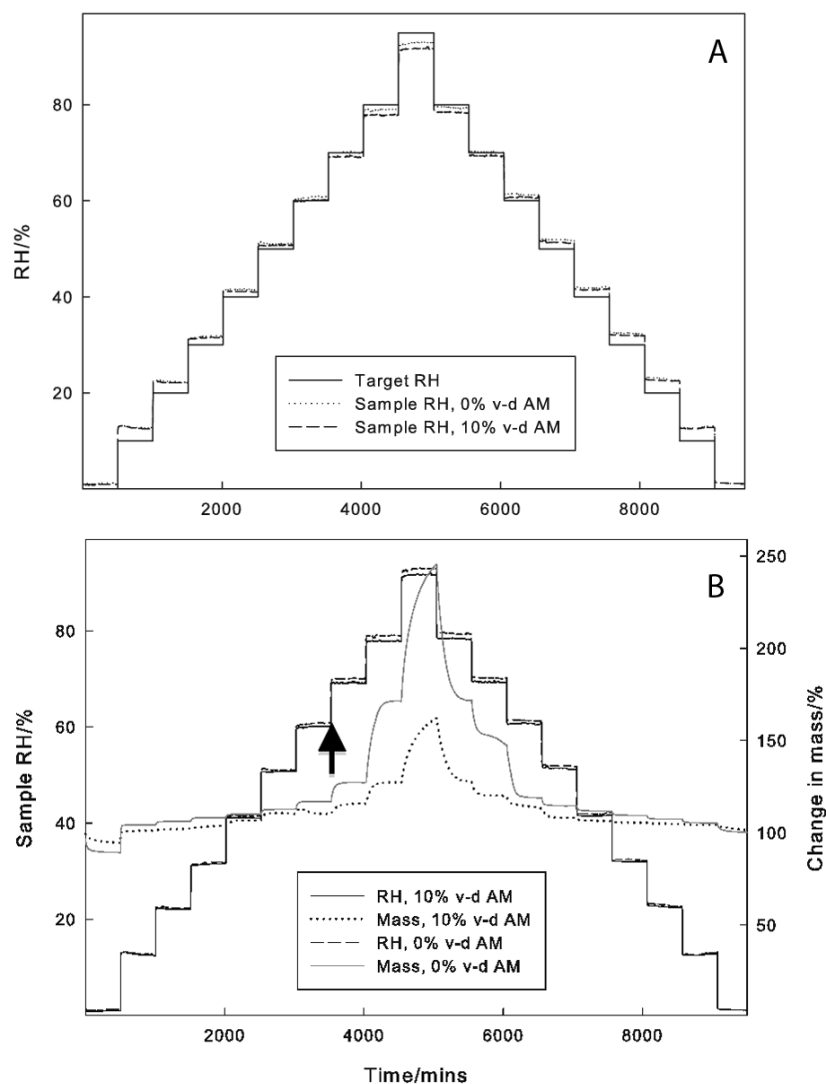


Figure 3.8: Water vapour sorption

From the DVS data, target RH and sample RH were plotted against time (A). This plot represents one pair of 0% and 10% v-d AM samples (A). The 10% v-d AM equilibrated at 60% RH, whereas the 0% v-d AM equilibrated at 70% RH. A water vapour sorption plot demonstrates changes in the % mass of the v-d AM samples (moisture content) with step changes in sample RH (A_w) (B). A black arrow indicates the end of the 60% RH stage. RH, relative humidity.

Table 3.3: Young and Nelson parameters, v-d AM

Sample	A parameter	B parameter	R ²
0%	0.24 (<i>SD</i> 0.02)	-0.50 (<i>SD</i> 0.11)	92.0%
10%	0.11 (<i>SD</i> 0.01)	-0.22 (<i>SD</i> 0.04)	94.6%
<i>p</i> value	.013	.075	

3.4.1.3 Isotherm plots

Plots of dry basis moisture content versus A_w (isothermal sorption-desorption plots) are shown for 0% and 10% v-d AM (sample A) in figure 3.9. From the desorption curves, at a dry basis moisture content of 10%, the mean A_w of 0% v-d AM is 0.35 (*SD* 0), and that of 10% v-d AM is 0.54 (*SD* 0.01) ($p = 0.003$) (black arrows). At a dry basis moisture content of 20%, the mean A_w of 0% v-d AM is 0.61 (*SD* 0), and that of 10% v-d AM is 0.70 (*SD* 0.01) ($p = .014$) (gray arrows). The mean hysteresis for 0% v-d AM was 22.8% (*SD* 3.3), whereas for 10% v-d AM it was 2.8% (*SD* 2.0) ($p = .018$). At a target RH of 70%, 10% v-d AM has a moisture content of 19.33% (*SD* 0.80) on the desorption curve, whereas 0% v-d AM has a moisture content of 49.01% (*SD* 1.88) ($p = .002$).

3.4.1.4 Young and Nelson plots

Young and Nelson plots were generated automatically from the DVS data for 0% and 10% v-d AM samples, of which one (sample A) is shown below (figure 3.10). The A and B parameters respectively indicate the magnitude of combined (monolayer and multilayer) adsorption and absorption. These parameters are larger for 0% than 10% v-d AM (table 3.3). The R-squared values of the plots indicate a good fit to the model.

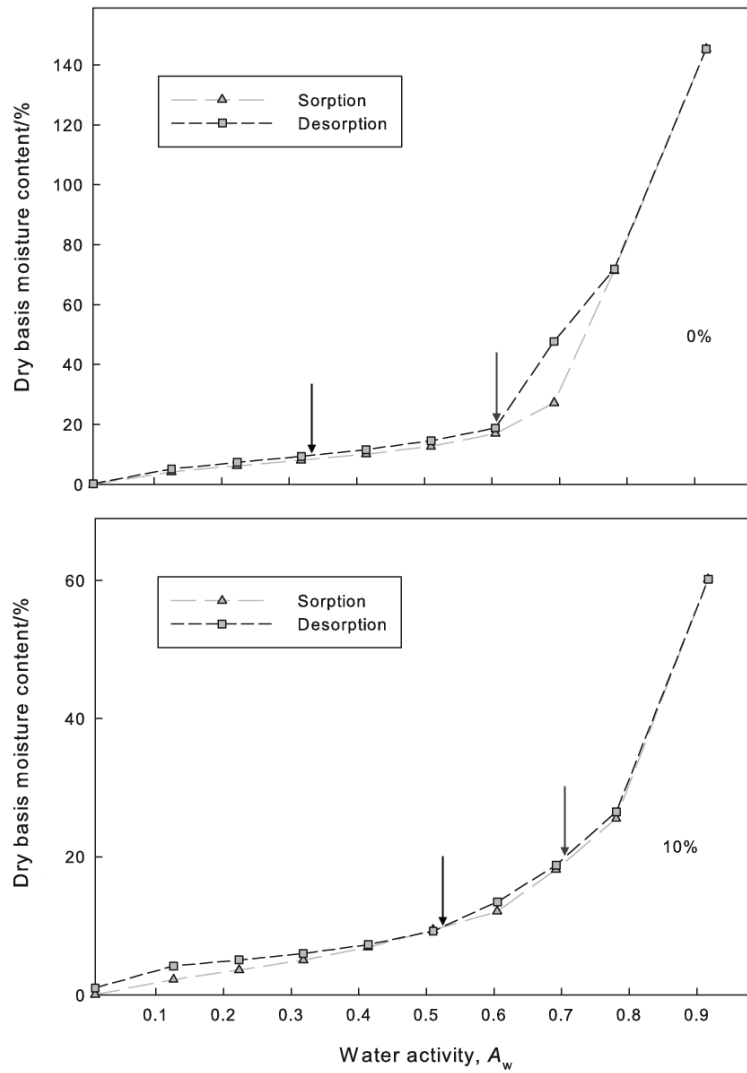


Figure 3.9: Sorption-desorption isotherms

Sorption-desorption plots of moisture content versus A_w for representative 0% and 10% v-d AM samples are shown (of two). At a moisture content of 10%, the A_w of 0% v-d AM is 0.35 and the A_w of 10% v-d AM is 0.53 (black arrows), while at a moisture content of 20%, the A_w of 0% v-d AM is 0.61 and the A_w of 10% v-d AM is 0.71 (gray arrows). There is increased hysteresis in the 0% v-d AM sample. A_w , water activity.

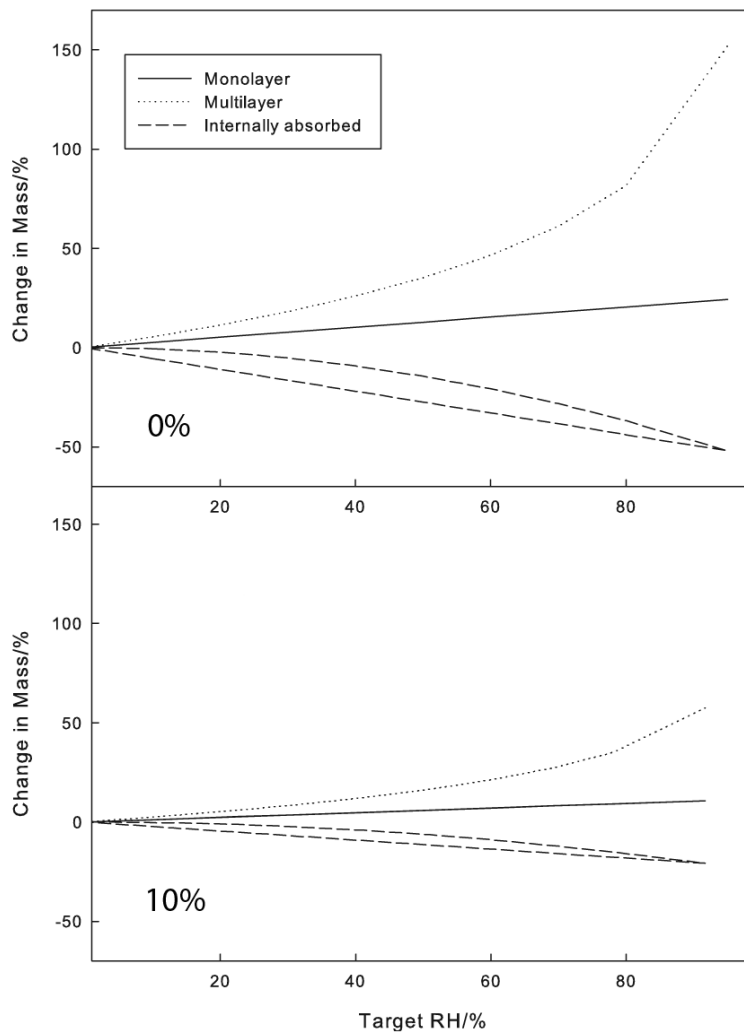


Figure 3.10: Young and Nelson plots of 0% and 10% v-d AM

Young and Nelson plots were generated for the 0% and 10% v-d AM samples from the DVS data (one of two shown). There is increased adsorption (in both monolayer and multi-layer systems) and absorption in 0% v-d AM compared to 10% v-d AM.

Table 3.4: TGA events at 10°C min⁻¹

Trehalose	Evaporation	Decomposition	Gradient	Moisture
0%	138.5°C (0.1)	311.7°C (2.1)	-0.45%/°C (0.03)	6.9% (0.1)
5%	165.0°C (5.1)	296.1°C (1.9)	-0.79%/°C (0.17)	8.2% (1.8)
10%	175.6°C (0.3)	295.1°C (0.7)	-1.06%/°C (0.04)	8.9% (1.5)

Each value represents the mean of two measurements (SD).

3.4.2 Thermal analysis

3.4.2.1 Open pan

The baseline correction determined for a representative sample of v-d AM affected the results negligibly and was therefore omitted from further analyses. The TGA curves of a representative group of three samples (0%, 5% and 10% v-d AM) are shown in figure 3.11 A. The analysis cut-off was set at 25.2°C to capture the starting temperature of all the curves. The initial loss in mass, caused by evaporation of water, appears as a linear slope (black arrow). The rate of decomposition increases at temperatures above ~250°C. A TGA curve of pure trehalose dihydrate powder demonstrates initial water loss upon heating and a steep decomposition curve beginning at ~250°C (figure 3.11 B).

First derivative curves First derivative curves were plotted from the TGA curves for duplicate 0%, 5% and 10% v-d AM samples. These are shown for a representative v-d AM sample in figure 3.12 A. From the derivatives, the maximal points of flux of these were identified at 138°C (black arrow) and 313°C (gray arrow) respectively. The derivative curves of 0% and 10% v-d AM samples are shown in figure 3.12 B. The maximal evaporation and decomposition points, decomposition gradients and moisture contents were measured for 0%, 5% and 10% v-d AM samples. Mean results for the two sets of AM samples are shown in table 3.4. The analysis was performed on two further sets of AM samples with a cut-off start temperature of 19.5°C

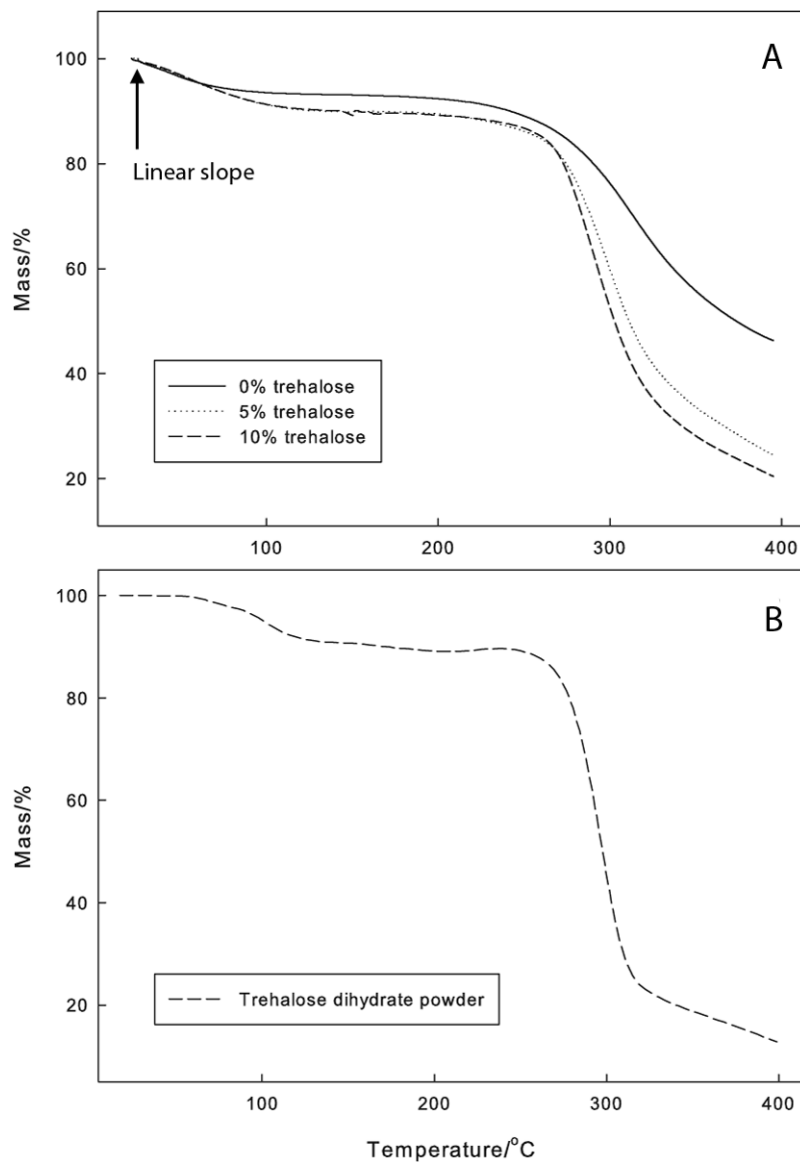


Figure 3.11: TGA plots of v-d AM and trehalose

TGA curves were obtained for 0%, 5% and 10% v-d AM. A representative set of traces is shown above (A). There is an initial linear slope (black arrow). Above ~250°C, the curve shows a steep decline, with different gradients for treated and untreated samples. A TGA trace of a sample of pure trehalose dihydrate powder (B) is shown for comparison.

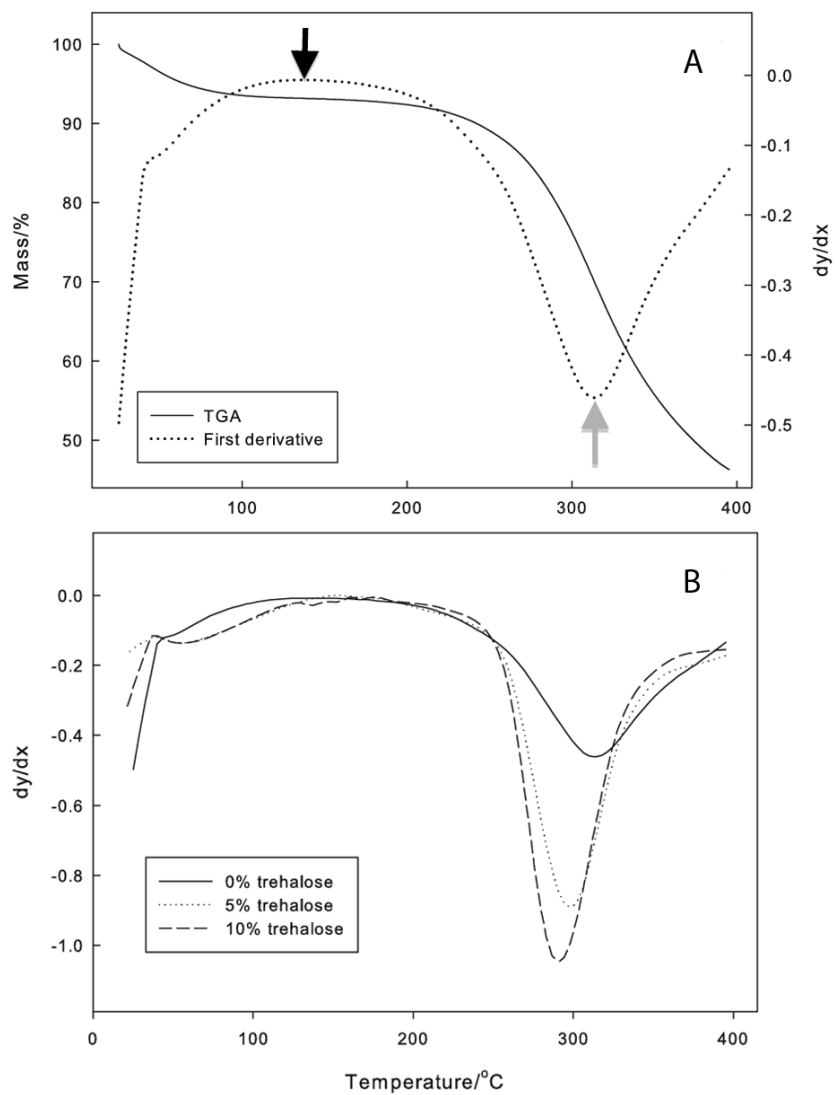


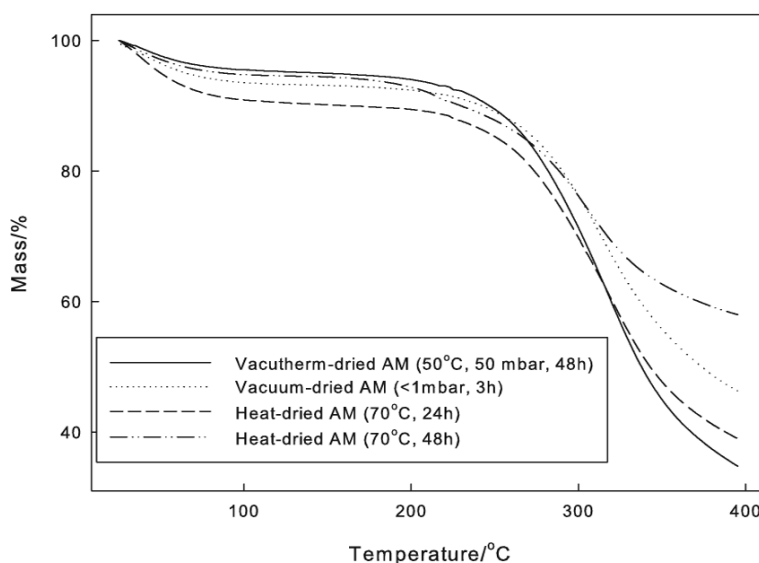
Figure 3.12: First derivatives

The first derivative of the TGA plot for a representative a v-d AM sample is shown (A). It enables identification of points of maximal flux (black arrow and gray arrow) . TGA was performed on 0%, 5% and 10% v-d AM samples from two donors. Derivative curves for a representative set of samples are shown (B), indicating marked differences in the TGA profiles of treated and untreated AM preparations.

Table 3.5: TGA events at 5°C min⁻¹

Trehalose	Evaporation	Decomposition	Gradient	Moisture
0%	128.4°C (2.1)	301.0°C (0.1)	-0.49%/°C (0.1)	10.0% (0.4)
5%	144.6°C (0.6)	289.9°C (1.1)	-0.74%/°C (0.2)	10.2% (1.5)
10%	167.8°C (0.3)	288.0°C (0.1)	-0.98%/°C (0.2)	10.8% (1.1)

Each value represents the mean of two measurements (SD).

**Figure 3.13:** Comparison of drying methods

Four different methods were used to dry AM samples, including vacuum-drying, heat-drying for 24 and 28 hrs and heat-drying with vacuum (Vacuotherm) for 48 hrs. TGA curves were obtained using the open pan method, and moisture content was calculated as the difference between the mass at the cut-off and the point of maximal moisture loss.

and a slower heating rate of 5°C min⁻¹(table 3.5).

Alternative drying methods TGA curves for four samples dried by different techniques, including Vacuotherm® oven, vacuum-drying and heat-drying for 24 and 48 hrs are shown in figure 3.13. The AM moisture contents were as follows: Vacuotherm® oven, 4.9%, drying cupboard 48 hrs, 5.2%, vacuum-dried, 6.8%, drying cupboard 24 hrs, 9.8%.

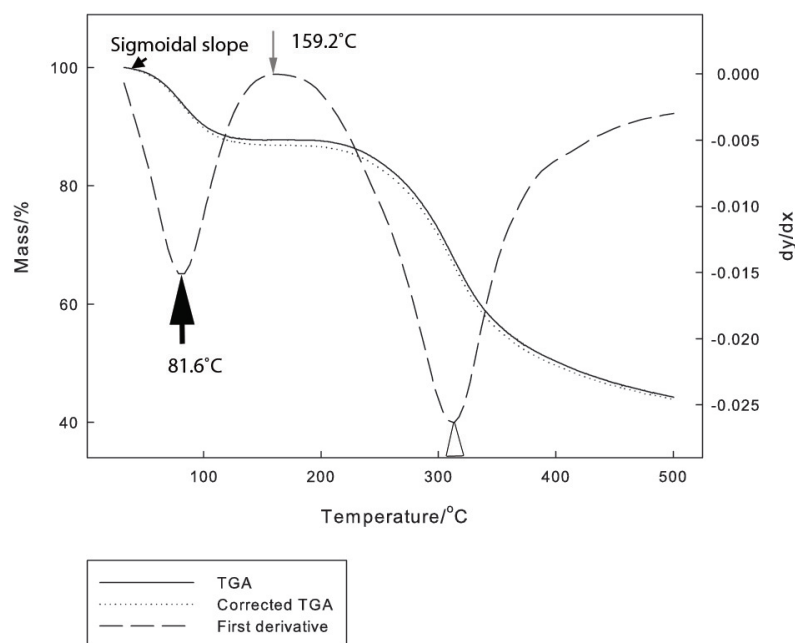


Figure 3.14: Closed pan TGA

The TGA curve of a representative v-d AM sample is shown with a baseline-corrected curve. The baseline correction changes the moisture content from 12.3% to 13.2% in this example, and was applied to all subsequent analyses. The cut-off temperature was 25.0°C. The initial slope is sigmoidal (small black arrow). The smoothed first derivative shows an initial negative peak at 81.6°C (large black arrow), a positive peak at 159.2°C (gray arrow), and a second negative peak at 310.0°C (white arrowhead).

3.4.2.2 Closed pan

Since the initial sample mass was found to be highly sensitive to temperature change using the open pan method of TGA, hermetically sealed pans were used next. TGA was performed on quadruplicate 0%, 5% and 10% v-d AM samples. Moisture content calculations were found to be significantly different when the baseline adjustment for an empty pan was applied, as shown for a representative v-d AM sample (figure 3.14). Therefore, a weighted baseline correction was applied to subsequent analyses. The initial curve is sigmoidal (small black arrow). The first derivative curves have an initial negative peak at the point of maximal moisture loss (black arrow). The points of maximal rate of water loss, completion of evaporation

Table 3.6: Thermal reversal temperatures by closed pan TGA

Trehalose	Peak loss	Evaporation	Decomposition	Moisture
0%	80.5°C (0.4)	161.1°C (1.3)	309.4°C (3.4)	12.8% (2.2)
5%	95.5°C (1.1)	166.6°C (0.4)	285.6°C (1.4)	13.2% (3.9)
10%	100.4°C (9.9)	183.4°C (22.1)	279.0°C (3.9)	12.7% (2.3)

Each value represents the mean of four measurements (SD).

and maximal decomposition are shown in table 3.6. A cut-off temperature of 25.0°C was applied to the curves.

3.4.2.3 Differential scanning calorimetry

Ramp mode DSC was performed in closed pans in on three 0% v-d AM samples at temperatures between -50°C and 300°C. The curves are shown in figure 3.15 (top). These show a small step with a midpoint at 5°C (gray arrow), an endotherm with a peak at 73 - 79°C (black arrow) and a second peak at 219°C. Ramp mode DSC runs were conducted on two 10% v-d AM samples. Two DSC runs are shown in figure 3.15 (bottom). The principal endotherm peaks occur at between 84 and 88°C and at 171°C.

Cyclic DSC Cyclic DSC was performed on 20.4 g of a 10:1 vacuum-dried trehalose:PBS mixture. The DSC curves for the trehalose-PBS mixture are shown in figure 3.16. During the initial run, an endotherm occurs between 39°C and 93°C (arrowheads). This does not reappear during the reheat. Both the initial run and the reheat are characterised by a sigmoidal step in heat flow. On the reheat curve, the T_g onset occurs at 6.8°C, the inflection point at 14.9°C and the endpoint at 21.3°C. Cyclic DSC runs were performed in duplicate on samples of 0%, 5% and 10% v-d AM at temperatures from -50°C to 180°C. These showed two principal endotherms (figure 3.17). In 10% v-d AM, the two endotherms merge. Values for the onset, peak and end point (in °C) and normalised enthalpy (in Jg^{-1}) were obtained for both peaks from automated software. The mean values for each pair of samples

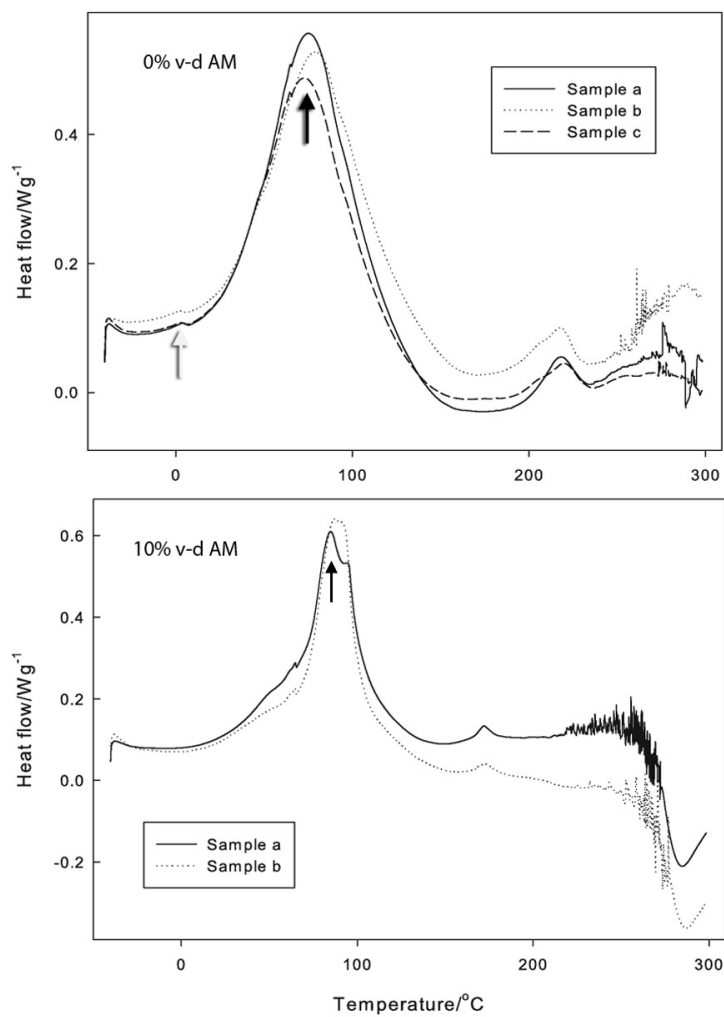


Figure 3.15: Ramp mode DSC

DSC was performed on triplicate samples of 0% v-d AM (top) and duplicate samples of 10% v-d AM (bottom). Two main endotherms are seen, the first peaking at 73 - 79°C (black arrow) and the second peaking at 219°C in 0% v-d AM. A small step was seen at 5°C (gray arrow). The two endotherms peak at 84 - 88°C (black arrow) and at 171°C in 10% v-d AM.

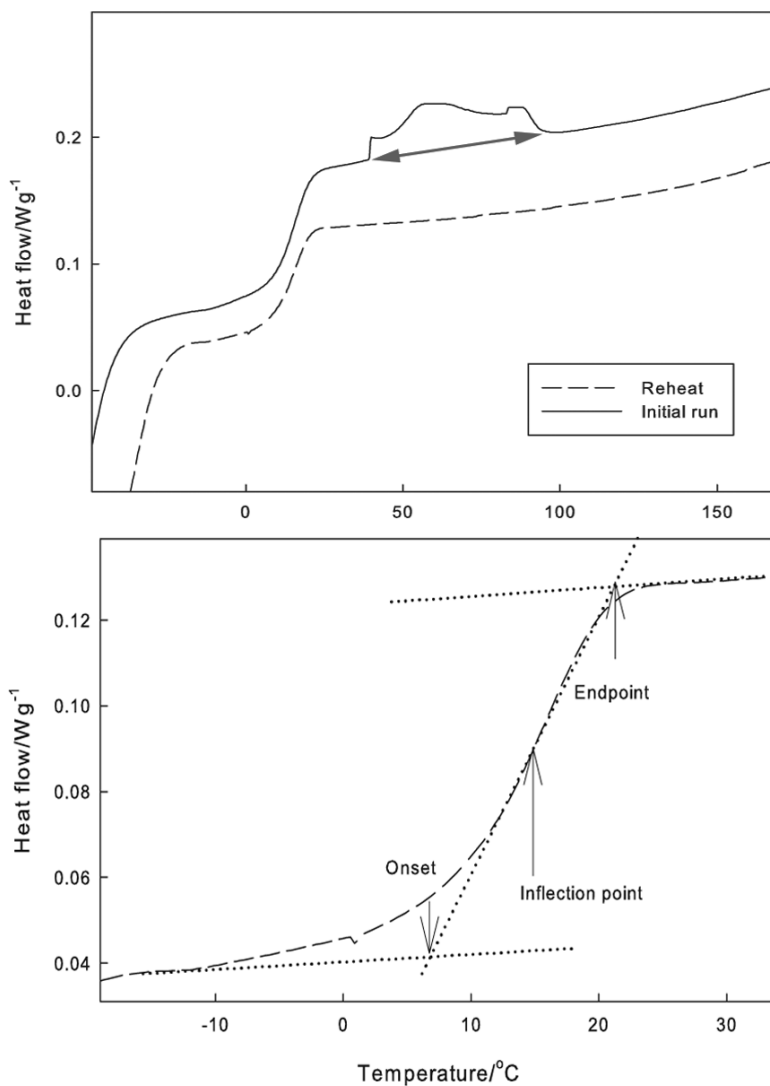


Figure 3.16: Cyclic DSC of trehalose:PBS

A DSC run was conducted on a vacuum-dried mixture of trehalose dihydrate and PBS in a 10:1 ratio (top). The trace shows an endotherm on the initial run (arrowheads). The sigmoidal curve on both the initial run and the reheat curve indicates a T_g . From the magnified curve (below), the T_g has an onset at 6.8°C, an inflection point at 14.9°C and an endpoint at 21.3°C.

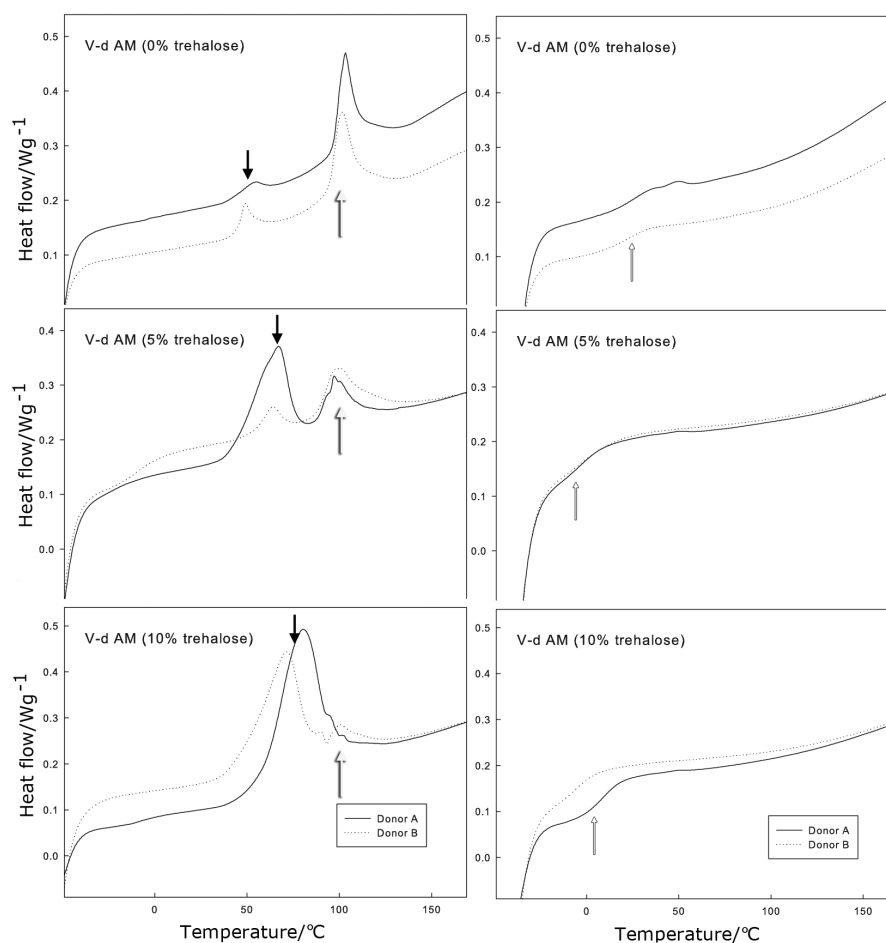


Figure 3.17: Cyclic DSC of 0%, 5% and 10% v-d AM

Cyclic DSC runs were performed on duplicate 0%, 5% and 10% v-d AM samples (left). The curves show two endotherms, one occurring between 50°C and 80°C (black arrows) and a second at ~100°C. Reheat curves are shown on the right. Small sigmoidal steps are visible (white arrows).

Table 3.7: Enthalpy values of DSC endotherms

Peak	Measurement points	V-d AM		
		0%	5%	10%
1	Onset (°C)	42.9	48.8	52.5
	Peak (°C)	51.6	65.3	75.7
	End point (°C)	58.9	74.6	90.7
	Integral (Jg ⁻¹)	1.9	11.3	~40.0
2	Onset (°C)	95.2	86.7	-
	Peak (°C)	102.3	97.4	-
	End point (°C)	112.0	128.9	-
	Integral (Jg ⁻¹)	13.6	9.2	7.6

were calculated (table 3.7). The normalised enthalpy for the first isotherm 10% v-d AM was estimated from the total value of the two endotherms (47.6 Jg⁻¹). The reheat curves of the DSC runs are shown separately in figure 3.17. The traces show small sigmoidal steps (white arrows). The mean inflection points for these transitions was calculated as 26.6°C for 0% v-d AM (*SD* 0.9), -4.6°C for 5% v-d AM (*SD* 0.1) and 3.8°C for 10% v-d AM (*SD* 8.8) (white arrows).

3.4.3 Dynamic mechanical analysis

3.4.3.1 Frequency sweep

Frequency sweep DMA was conducted on single ply v-d AM strips with a free length of 10 mm and a width of 10 mm. Multiple samples were lost due to breakage. Measurements were performed in triplicate on 12 different strips of 0% v-d AM and six strips of 10% v-d AM at room temperature (24.0 - 24.4°C). The average thicknesses of the 0% v-d AM and 10% v-d AM samples were 18.67 μm (*SD* 4.42) and 25.50 μm (*SD* 7.99) respectively. The DMA trace for a representative sample of v-d AM is shown in figure 3.18. At frequencies between 0.1 and 10 Hz, E', E'' and tan δ measurements are

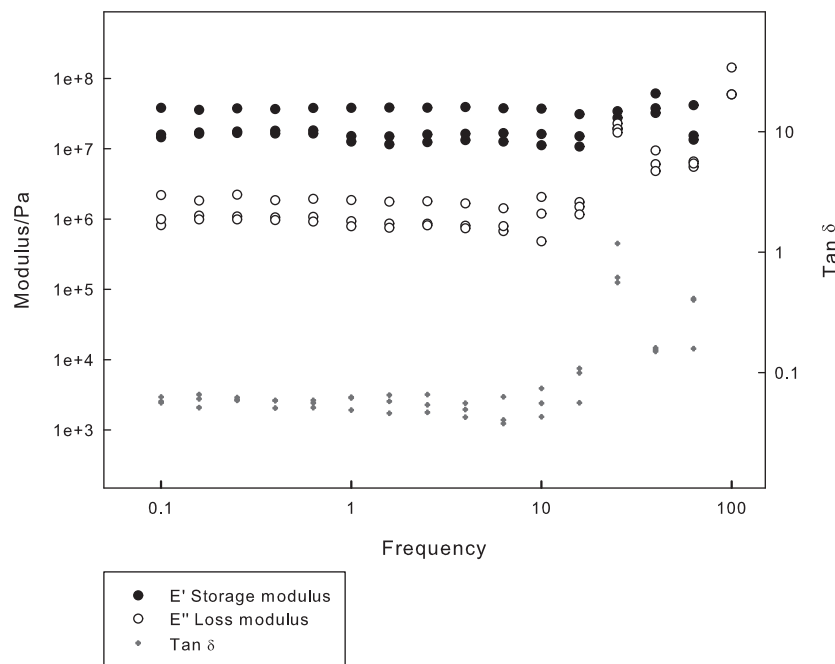


Figure 3.18: Frequency sweep DMA

This DMA plot is from a representative 0% v-d AM strip. It was performed at room temperature on a 10 mm \times 10 mm sample, at oscillatory frequencies between 0.1 and 100 Hz. Triplicate measurements were obtained. The trace shows a modulus E' value of $\sim 10^7$, E'' of $\sim 10^6$ and a tan δ of ~ 0.1 at frequencies between 0.1 and 10 Hz.

Table 3.8: Moduli of v-d AM

	0% v-d AM	10% v-d AM	p value
E' (SD)	1.95×10^7 Pa (1.34×10^7)	1.40×10^7 Pa (8.37×10^6)	.30
E'' (SD)	1.95×10^6 Pa (1.84×10^6)	2.61×10^6 Pa (2.40×10^6)	.57
Tan δ (SD)	0.12 (0.07)	0.20 (0.07)	.06

relatively constant. The average values of E' , E'' and $\tan \delta$ measured were calculated over this frequency range, and are shown in table 3.8. There was no significant difference between the two preparations.

3.4.3.2 Humidity sweep

Multifrequency humidity sweep DMA runs were performed on triplicate samples of 0%, 5% and 10% v-d AM. It was not possible to obtain results for 5% and 10% v-d AM because of early rupture of the samples. Five successful DMA runs were obtained from 0% v-d AM samples of different dimensions (free lengths of 1 mm and 10 mm), for which two representative traces are shown below. DMA runs are presented individually to illustrate the salient points from the experiment.

A humidity sweep trace is shown in figure 3.19 (top). It was performed on a single strip of 0% v-d AM ($1.1 \text{ mm} \times 5.2 \text{ mm} \times 7 \text{ }\mu\text{m}$) at a constant temperature of 30°C . The RH was ramped up from 20% to 60% over a period of ~ 45 mins, maintained at 60% for 60 mins and then reduced to 20%. The modulus E' is seen to follow an inverse pattern to RH. As RH rises, E' falls from 9.4×10^8 to 3.2×10^8 Pa. E' then rises to 1.0×10^9 Pa as RH falls below 20%. Simultaneous measurements of static and dynamic force and static displacement are shown in figure 3.19 (bottom). Automatic adjustments are made in the static displacement to retrieve the tension on the sample. Eventually, the loss in static force cannot be fully compensated by the displacement.

A second humidity trace obtained from a 3-ply strip of 0% v-d AM (9.9

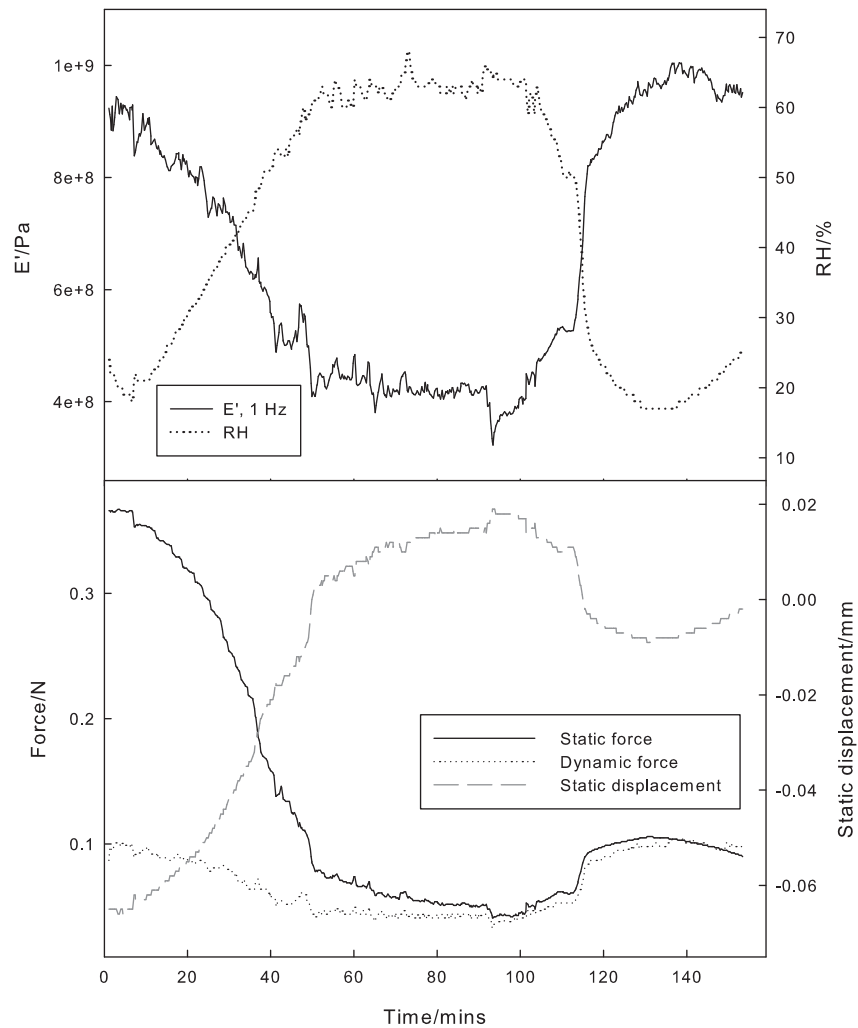


Figure 3.19: Humidity-sweep DMA

DMA was carried out on a 1 mm strip of 0% v-d AM at constant temperature (30°C) (1 trace). Increasing the RH reduced E' in a reversible way. A trace of static and dynamic force and static displacement for this sample is shown below.

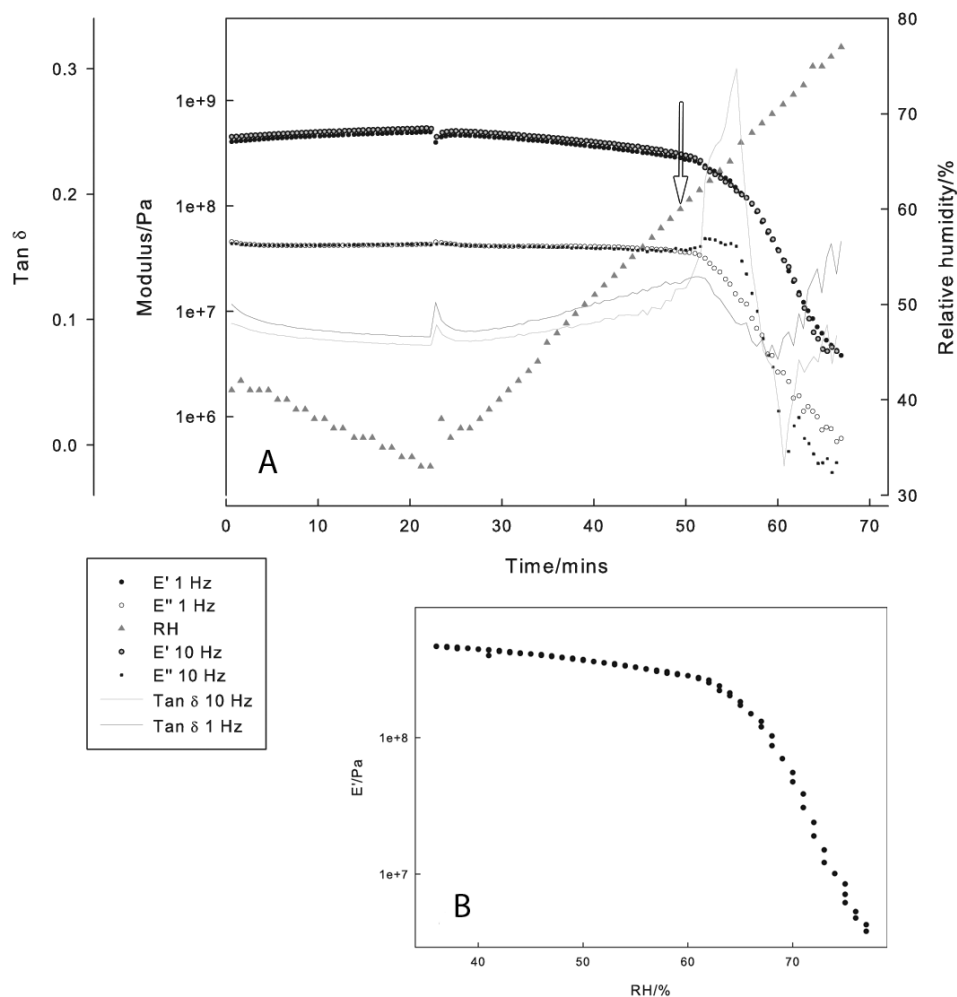


Figure 3.20: Humidity sweep DMA (2)

A humidity sweep DMA was performed at room temperature on 0% v-d AM, demonstrating a T_g at a RH of ~60% (arrow) (A). E' (at 1 Hz) is plotted against RH between 30 and 80% (B).

mm \times 10.0 mm \times 34 μ m) is shown in figure 3.20. The ambient temperature recorded by the instrument was between 26.0 and 28.5°C. The RH was ramped down from 40% to 30% and then ramped up to 80%. The initial values of E' are 4.1×10^8 Pa (1 Hz) and 4.5×10^8 Pa (10 Hz), while those of E'' are 4.6×10^7 Pa (1 Hz) and 4.4×10^7 Pa (10 Hz), making tan δ ~0.1. As RH rises to ~60% (arrow), a T_g begins to occur, evidenced by a drop in E' and peaks in the traces of E'' and tan δ (10 Hz). There is a separation of the E'' and tan δ values by frequency, indicating strain-rate dependence. E' (1 Hz) has been plotted against RH (figure 3.20 B). These findings are

representative of the three remaining humidity sweep traces.

3.4.3.3 Temperature sweep

Multifrequency temperature sweep DMA was performed on triplicate samples of 0%, 5% and 10% v-d AM samples. The samples had varying geometries, with free lengths of 5 mm and 10 mm. Successful traces were obtained for 6 samples of 0% v-d AM (4 shown), three samples of 5% and one sample of 10% v-d AM (all shown). In all cases, RH was not controlled.

Untreated v-d AM Two representative temperature sweep DMA traces of 10 mm strips of 0% v-d AM are shown in figure 3.21. They were each performed on performed on 3-ply strips of 0% v-d AM. Sample A (9.8 mm \times 10.0 mm \times 48 μ m) underwent DMA over a temperature range of -56°C to 80°C. Initial values of E' and E'' were 3.5×10^8 Pa and 4.0×10^7 Pa respectively. The E' starts to decrease at -17.5°C, followed by a $\tan \delta$ peak at -11.5°C, indicating a T_g . The moduli continue to decrease until 18.9°C. The sample stiffness then increases again between 20°C and 50°C. The $\tan \delta$ reaches a second peak at 19.8°C. The $\tan \delta$ traces are noisy at low stiffness. The moduli regain a plateau formation at 50°C, with E' and E'' values of 1.6×10^8 Pa and 1.8×10^7 Pa respectively. Sample B (9.80 mm \times 10.0 mm \times 30 μ m) underwent DMA between -6.5°C and 120.0°C. The trace demonstrates a T_g occurring at the start of the run, with a clear reversal occurring between 20°C and 50°C. These traces indicate that the 0% v-d AM samples were in a rubbery state at room temperature, and they returned to the glassy state as the temperature climbed.

Three DMA traces were obtained for 5 mm \times 5 mm 0% v-d AM strips, of which two are shown in figure 3.22. Sample A (single ply; 5.0 mm \times 4.9 mm \times 16 μ m) had an initial E' of 1.6×10^9 Pa, while sample B (single ply; 5.0 mm \times 5.1 mm \times 18 μ m) had an initial E' of 1.4×10^9 Pa. In contrast

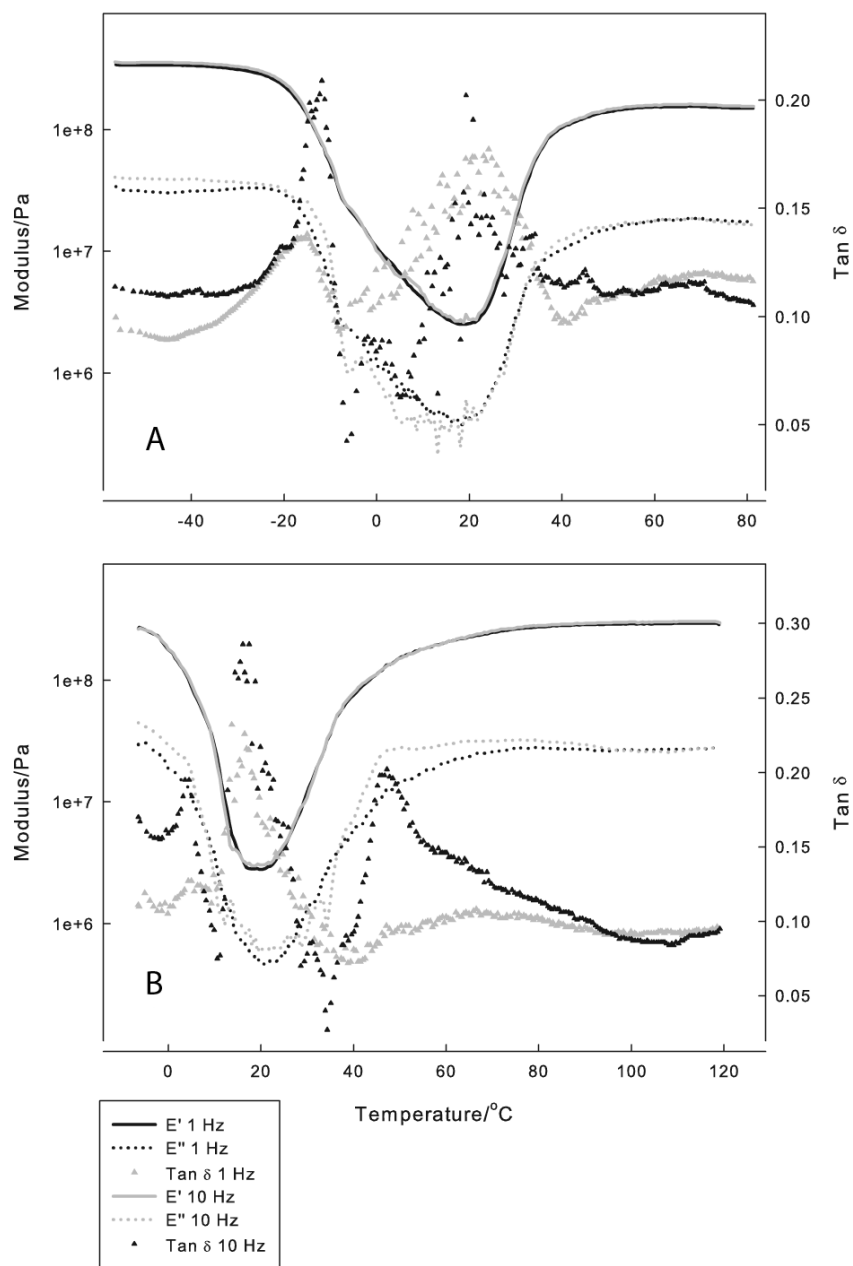


Figure 3.21: Temperature sweep DMA of 0% v-d AM (1)

Two temperature-sweep DMA traces of three-ply strips of 0% v-d AM are shown. In **A**, the temperature is reduced to -50°C and then raised to 80°C while DMA is performed with two oscillatory frequencies (1 and 10 Hz). In **B**, the temperature range is between -10°C and 120°C . Both traces indicate a transition from a glassy to a rubbery state, with a reversal beginning at $\sim 20^{\circ}\text{C}$.

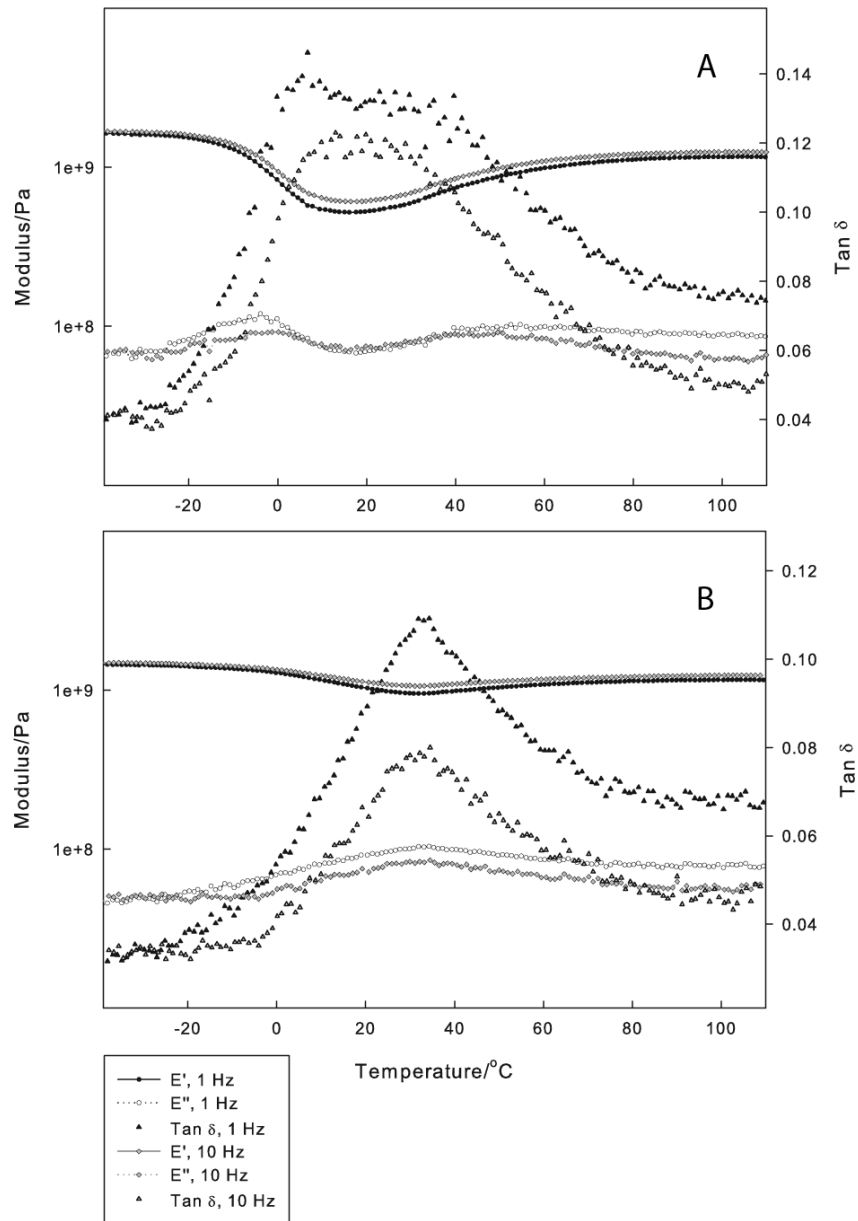


Figure 3.22: Temperature sweep DMA (2)

Two temperature sweep DMA traces were obtained from single-ply 5 mm × 5 mm 0% v-d AM strips (A and B). These were both tested between -40 and 110°C. In both traces, the samples undergo changes in modulus of less than one decade.

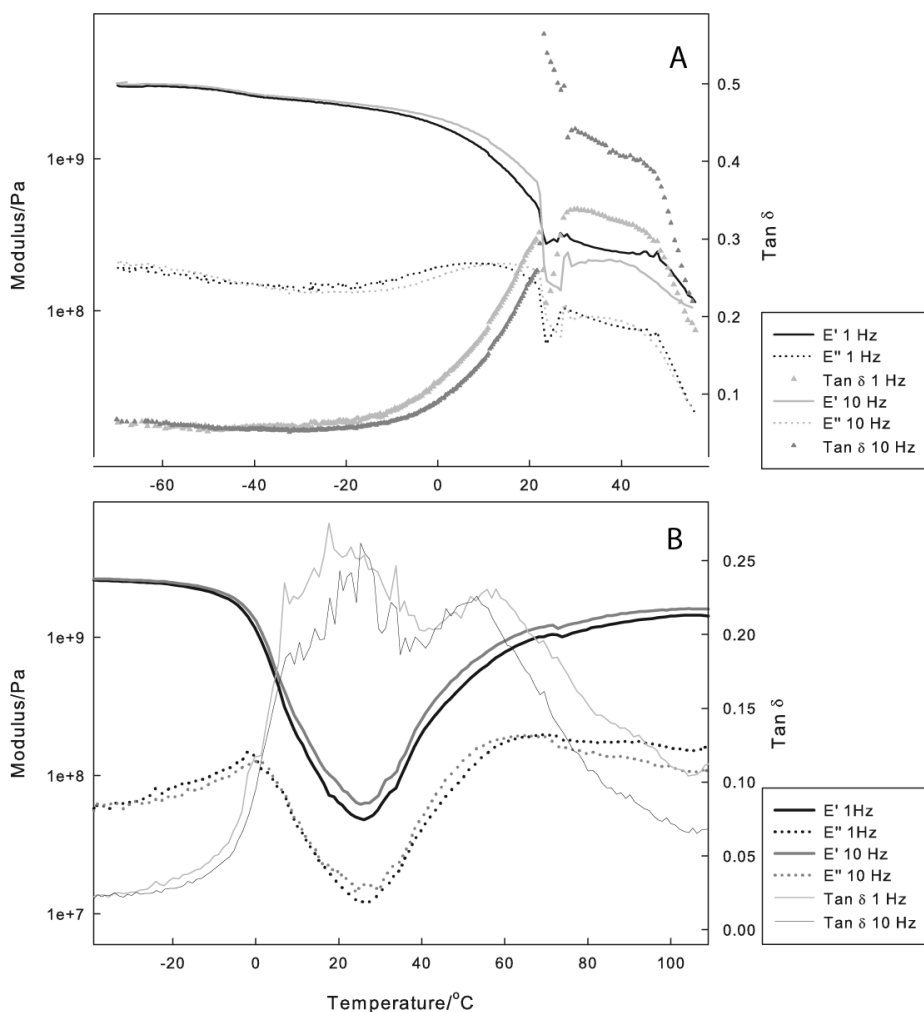


Figure 3.23: Temperature-sweep DMA of 5% v-d AM

Temperature sweep DMA traces of 5% v-d AM strips are shown. Trace **A** was obtained from an 8-ply strip and **B** was obtained from a single-ply strip. The samples were subjected to DMA at two oscillatory frequencies (1 and 10 Hz) between -70°C and 50°C (**A**) and -30°C and 110°C (**B**). Non-recoverable slippage occurred in sample **A**.

to the 10 mm-long samples, these show falls in E' and E'' of less than one decade. In both cases, the $\tan \delta$ peaks appear to be merged together, and the $\tan \delta$ peak in sample **B** occurs at a higher temperature than previously seen. These traces indicate that the samples remain glassy, undergoing attenuated falls in E' without a complete T_g .

Trehalose-treated v-d AM A successful DMA trace was obtained from an 8-ply strip of 5% v-d AM ($10.0\text{ mm} \times 10.0\text{ mm} \times 123\text{ }\mu\text{m}$) (figure 3.23 **A**). The temperature range was between -70°C and 50°C . The initial value of

Table 3.9: T_g events of 0%, 5% 10% v-d AM

Sample	Maximum E'	E' onset	E' inflection	E'' peak	Tan δ peak
0% v-d AM	8.4×10^8 Pa	-8.0°C	-2.8°C	-5.5°C	-1.2°C
5% v-d AM	3.1×10^9 Pa	-3.9°C	5.0°C	-1.7°C	6.7°C
10% v-d AM	4.7×10^9 Pa	7.4°C	17.8°C	10.9°C	14.7°C

E' was 3.1×10^9 Pa. Above temperatures of -25°C, the E'' and tan δ values separate by frequency of oscillation, demonstrating strain-rate dependence. There is likely sample slippage at 21.9°C. A T_g is indicated by an E' onset at 1 Hz of 0.6°C and a tan δ peak at 23.5°C. A further DMA run was carried out on a different 5% v-d AM sample (5.0 mm \times 5.2 mm \times 16 μ m) (figure 3.23 B). The initial value of E' was 2.6×10^9 Pa, and a T_g occurs at a temperature between \sim -5°C and 15°C. A further 5% v-d AM trace (5.0 mm \times 5.2 mm \times 12 μ m) returned an initial E' of 5.3×10^9 Pa. The temperature range was between -40°C and 150°C. There was no evidence of a T_g occurring at room temperature (figure 3.24 A). A successful trace was obtained for a 10% v-d AM strip (5.0 mm \times 5.0 mm \times 19 μ m) (figure 3.24 B). The initial value of E' of 10% v-d AM was 4.7×10^9 Pa, and the T_g temperature occurs between 7.4°C and 14.7°C. Zoomed-in details of representative DMA traces of 0%, 5% and 10% v-d AM undergoing T_g at room temperature illustrate the effects of trehalose (figures 3.25 A, B and C). The E' , E'' and tan δ measurements of the three samples are compared in table 3.9 showing increased stiffness and an upward shift in T_g temperature in the three traces.

3.4.4 Surface analysis

3.4.4.1 X-ray diffraction

XRD traces were obtained for duplicate samples of 0% and 10% v-d AM. A normalised trace of 0% v-d AM is shown in figure 3.26 A, with an empty holder provided as a background comparison. In figure 3.26 B, representa-

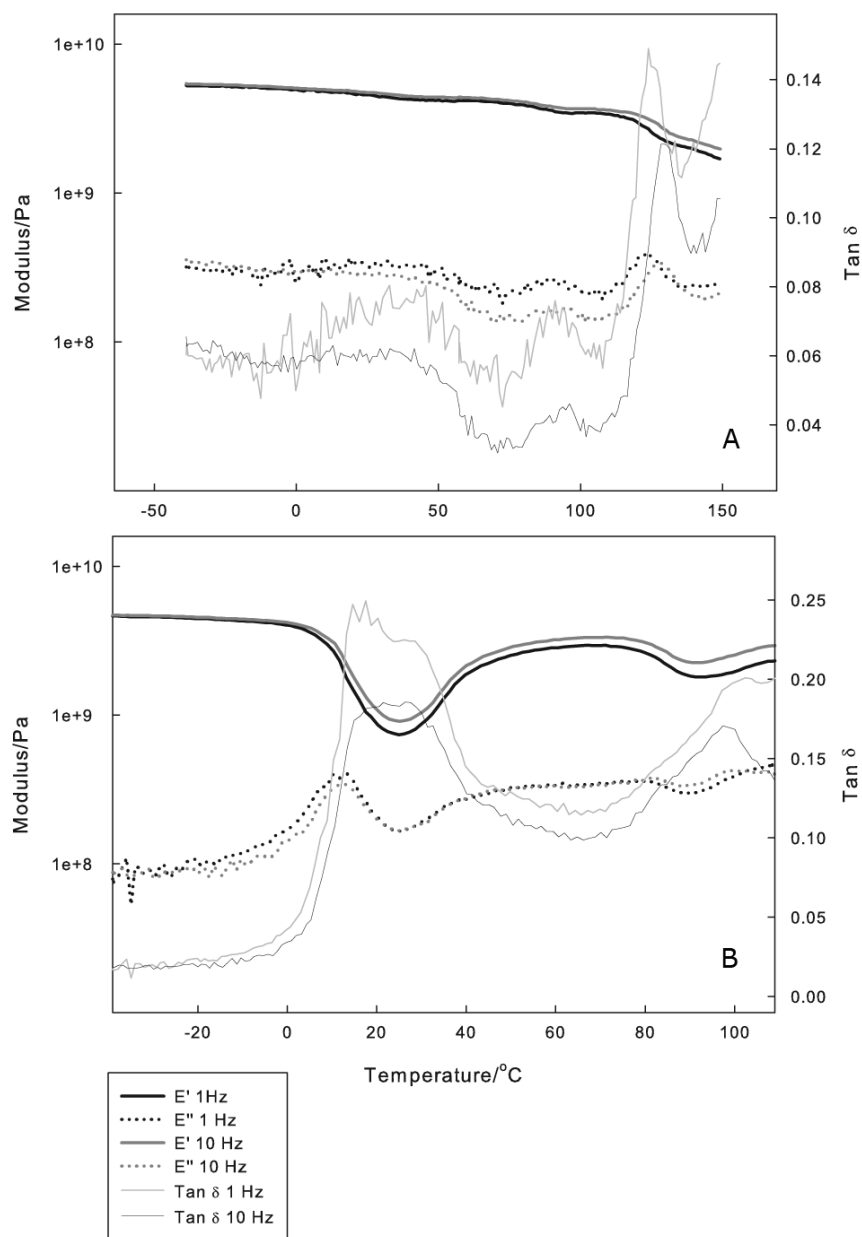


Figure 3.24: Temperature sweep DMA of 5% and 10% v-d AM

A A temperature sweep test was performed in a 5mm strip of 5% v-d AM at two oscillatory frequencies (1 and 10 Hz) between -40°C and 150°C . The trace shows no evidence of a T_g occurring at room temperature. **B** This DMA trace was obtained for a single-ply strip of 10% v-d AM at two oscillatory frequencies (1 and 10 Hz) between -30°C and 110°C . It demonstrates a transition of less than one decade occurring between 7.4°C and 14.7°C .

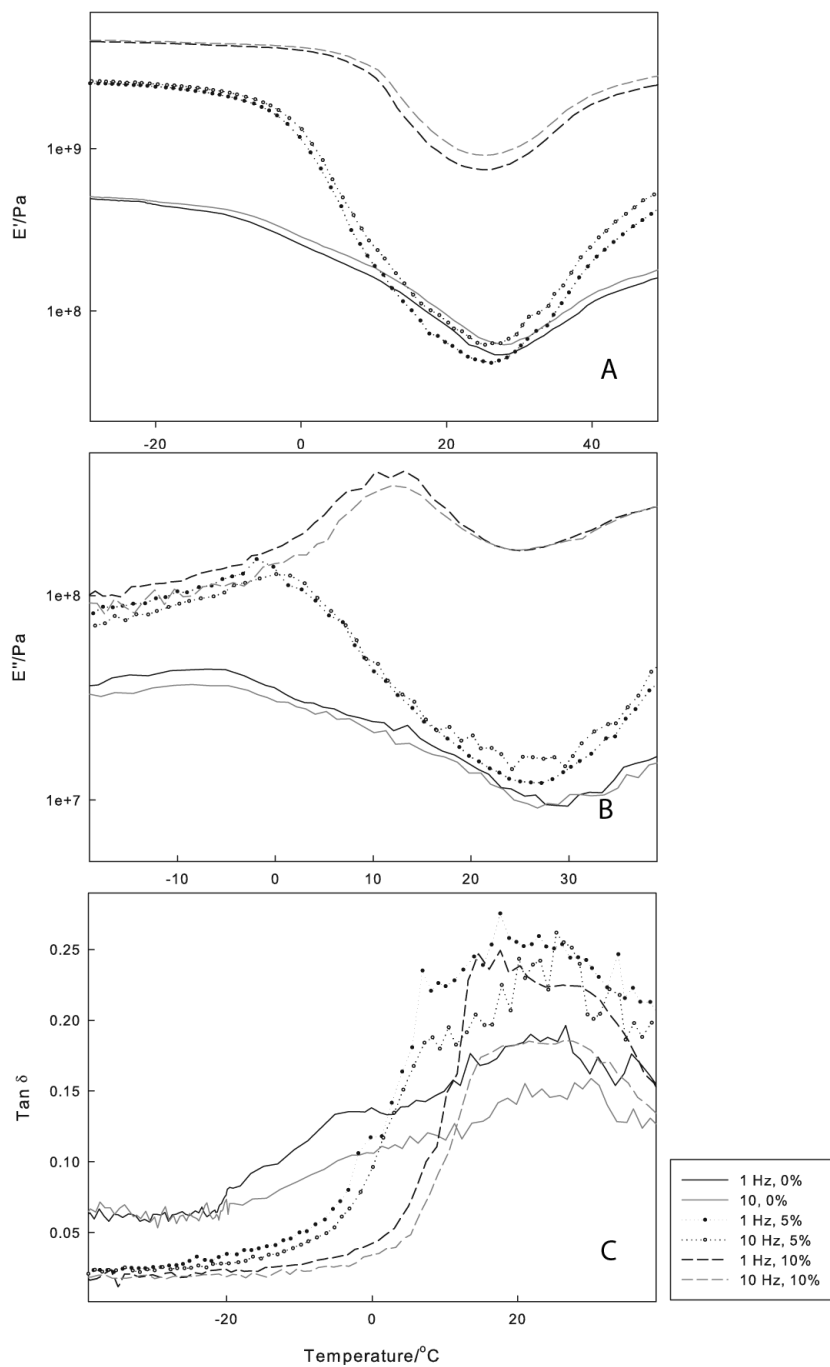


Figure 3.25: Moduli and $\tan \delta$ of 0%, 5% and 10% v-d AM

Details of representative DMA traces of E' (A) and E'' (B) and $\tan \delta$ (C) of 0%, 5% and 10% v-d AM samples show an upwards temperature shift in T_g temperature with increased trehalose loading.

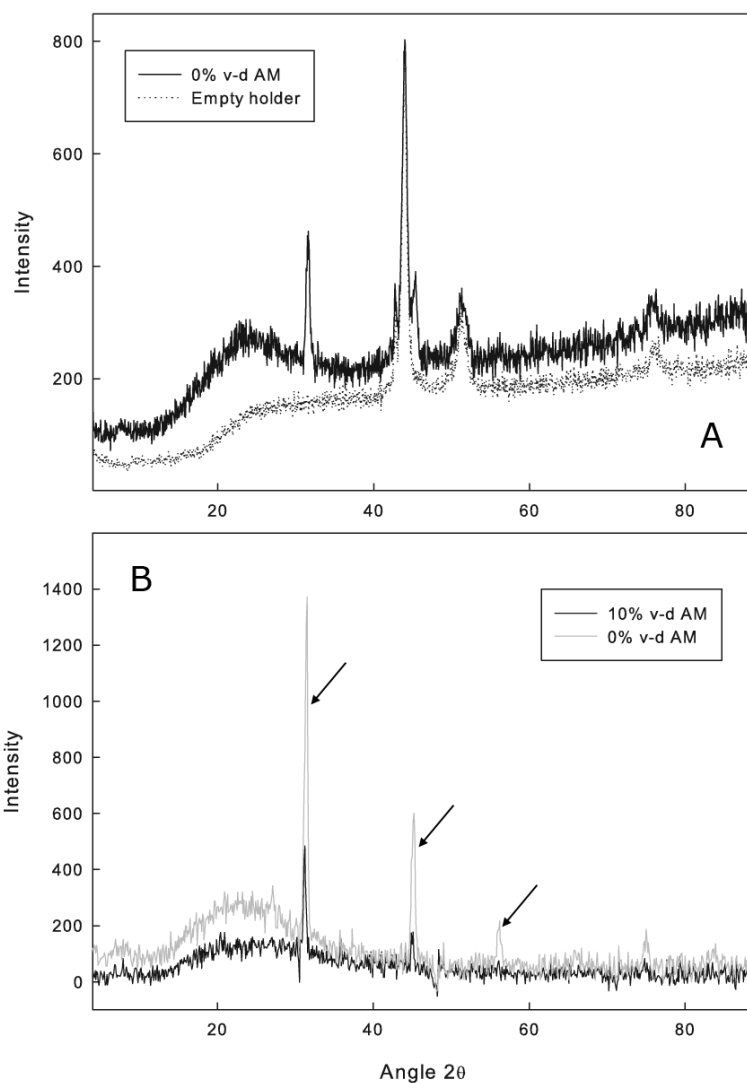


Figure 3.26: XRD of v-d AM

A normalised XRD trace of 0% v-d AM is shown with a background trace of the empty stainless steel holder (A) The background diffraction from two representative traces of 0% and 10% v-d AM has been subtracted in B. Three prominent peaks present in v-d AM represent NaCl (arrows).

tive XRD traces of 0% and 10% v-d AM are shown with background diffraction from the sample holder removed and a sampling proportion of 0.5. The plot represents the sum of amorphous and crystalline elements within the sample, and demonstrates three prominent peaks, at diffraction angles 31-32, 45-46 and 56 representing NaCl (black arrows). The proportion of crystallinity in the v-d AM samples is estimated to be <10%. This suggests that the AM is principally amorphous, with the crystalline peaks being related to salt. No additional peaks were detected in the 10% v-d AM samples.

3.4.4.2 Infrared spectroscopy

Normalised IR absorbance spectra are shown for 0%, 5% and 10% v-d AM (figure 3.27, above). They were obtained using a Bio-Rad spectrometer equipped with a thallium bromo-iodide crystal. The spectrum for trehalose dihydrate powder is shown for reference. Characteristic peaks for AM and for trehalose dihydrate are labelled for reference (arrows). The trehalose-treated samples show a broad and intense band between 3000 and 3600 cm^{-1} , labelled O-H stretching. A detail of the spectra of 10% v-d AM and trehalose dihydrate powder is shown in figure 3.27 (below). The trehalose dihydrate spectrum contains peaks at 994 and 954 cm^{-1} . These are shifted downwards to 986 and 943 cm^{-1} in the 10% v-d AM sample. ATR-FTIR was performed on six 10% v-d AM samples and untreated controls using a Bruker spectrometer with a diamond crystal probe. A representative sample is shown in figure 3.28 A. Four of the samples had trehalose fingerprint peaks at 994 and 956 cm^{-1} , whereas two had peaks at 991 and 941 cm^{-1} (figure 3.28 B).

3.4.4.3 Mass spectrometry

Tof-SIMS was performed with PCA to identify major chemical differences between duplicate samples of 0%, 5% and 10% v-d AM (both sides). Ex-

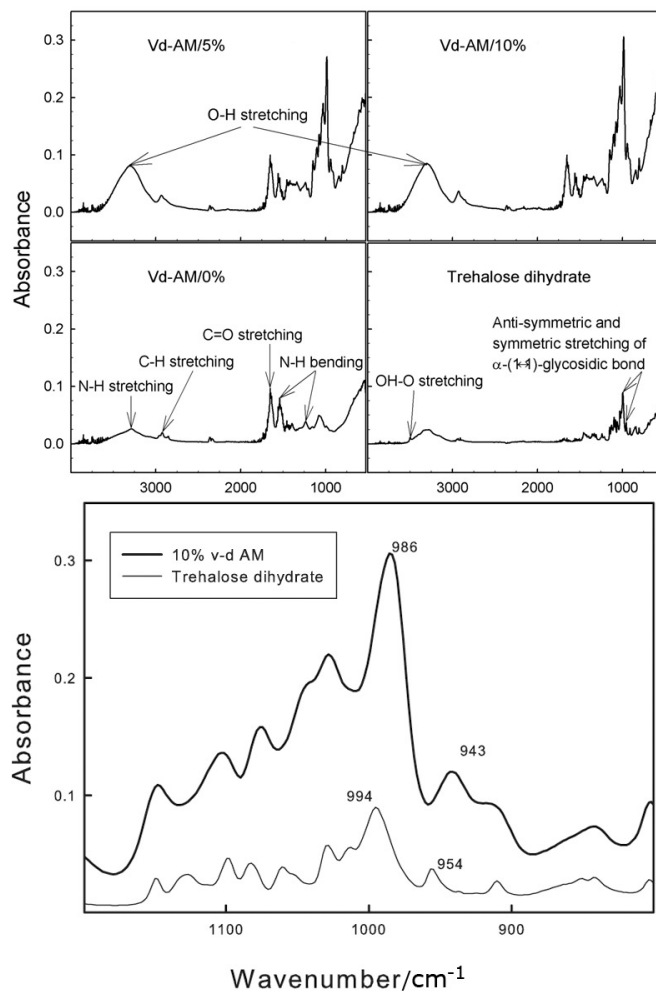


Figure 3.27: FTIR absorbance spectra

Normalised ATR-FTIR spectra are obtained for trehalose dihydrate and 0%, 5% and 10% v-d AM samples. There is a broad band of O–H stretching between 3000 and 3600 cm^{-1} in the 5% and 10% traces. In the fingerprint region of trehalose (detail below), a wavenumber shift is shown, from 994 and 954 cm^{-1} in trehalose dihydrate powder to 986 and 943 cm^{-1} in 10% v-d AM.

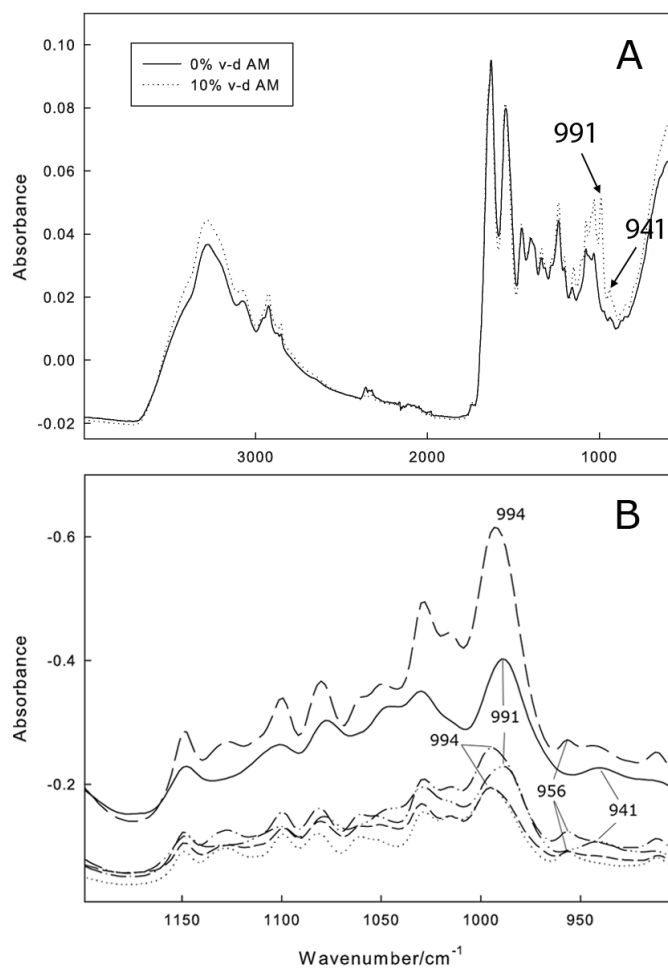


Figure 3.28: FTIR of v-d AM

*ATR-FTIR was conducted on six paired samples of 0% and 10% v-d AM using the Bruker spectrometer. The traces were normalised by an automated non-quantitative vector method. Representative traces of the spectra for one pair are shown in **A**. Traces representing the six 10% v-d AM samples are shown in **B**. Peaks appear at 991 and 941 cm⁻¹ in two samples and at 994 and 956 cm⁻¹ in four samples.*

Table 3.10: Chemical species identified by PCA

Loading (+ve)	m/z	Species	Loading (-ve)	m/z	Species
6.35E-01	80.9519	Na ₂ Cl ⁺	-2.79E-01	34.9702	Cl ⁻
3.49E-01	22.9913	Na ⁺	-2.08E-01	92.9286	NaCl ₂ ⁻
2.45E-01	82.949	Na ₂ ³⁷ Cl ⁺	-1.54E-01	86.109	C ₆ H ₁₄ ⁺
2.37E-01	138.9115	Na ₃ Cl ₂ ⁺	-1.36E-01	94.9256	NaCl ³⁷ Cl ⁻
2.16E-01	62.9855	PNOH ₂ ⁺	-1.33E-01	36.9669	³⁷ Cl ⁻
1.48E-01	140.9097	KNaPO ₃ ⁺	-1.01E-01	58.0696	C ₃ H ₈ N ⁺
1.15E-01	38.9675	K ⁺	-8.27E-02	150.8841	Na ₂ Cl ₃ ⁻
8.58E-02	96.9271	Ca ₂ OH ⁺	-7.89E-02	152.8813	Ca ₃ O ₂ H
7.85E-02	96.97	PH ₂ O ₄ ⁻	-5.45E-02	184.1101	C ₁₄ H ₁₆ ⁺
5.23E-02	62.964	PO ₂ ⁻	-5.25E-02	43.0574	C ₃ H ₇ ⁺

cluding positive and negative hydrogen species, there were in total 2938 peaks detected by ToF-SIMS. The eigenvalues for PC1 to PC4 accounted for 98.17% of total variance captured. These four PCS were used for further analysis. The Hotelling T^2 statistic for the scores was 10.08 for each AM preparation, suggesting equal variance. Scores on PC1 are plotted against scores on PC2 (figure 3.29 A), highlighting two samples showing maximal variation in comparison to the remaining samples. These are the b side of 0% v-d AM and the a side of 10% v-d AM. A plot comparing PC3 to PC4 showed less marked variation between the samples, and is not shown. A loadings plot is shown for PC1 (figure 3.29 B), which accounts for 62.82% of the variance. The individual species farthest away from the means cluster were identified by their m/z ratio. The 10 most variable positive and 10 most negative loadings are listed in table 3.10. The main differences include combinations of ionic salt species, such as Na⁺ and Cl⁻, but also aliphatic ammonium ions (e.g. C₃H₈N⁺, m/z 58), carbenium ions (e.g. C₃H₇⁺, m/z 43) and saturated hydrocarbon chains (e.g. C₆H₁₂⁺). Many of these species are also identified as variable by PC2, PC3 and PC4 (not shown). Species not identified by PC1, but identified by PC2, PC3 or PC4 include CN⁻ and CNO⁻, which are present in all amino acids. There were no identifiable amino acid

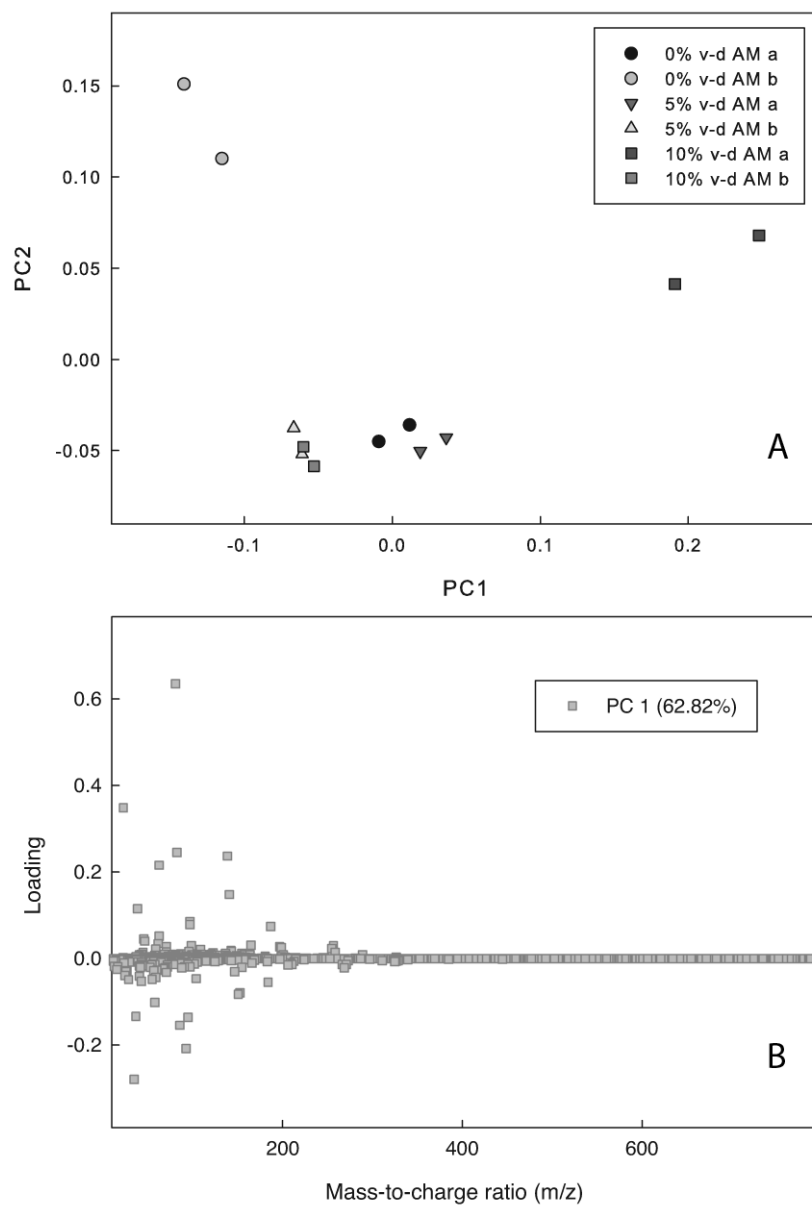


Figure 3.29: Scores and loadings plots

ToF-SIMS/PCA was performed in duplicate on both sides of 0%, 5% and 10% v-d AM. The PC1 and PC2 scores are plotted for the 12 v-d AM samples (A). This indicates that the b side of 0% v-d AM and the a side of 10% v-d AM can be discriminated from the remaining samples by both PC1 and PC2. A loadings plot is shown highlighting the fragment ions with the largest variation across AM samples (B). A small number of ions were identified by the m/z ratio as positive or negative loadings.

fragments ions in any of the PCs. A plot showing the spectral peak densities by AM preparation is shown in figure 3.30. Most of the variation is found in a small number of positive species on one side of 10% v-d AM, and in a small number of negative species on one side of 0% v-d AM. This indicates that the variation found is not a consequence of the trehalose treatment, but is more likely to reflect the normal range of minor variation between samples.

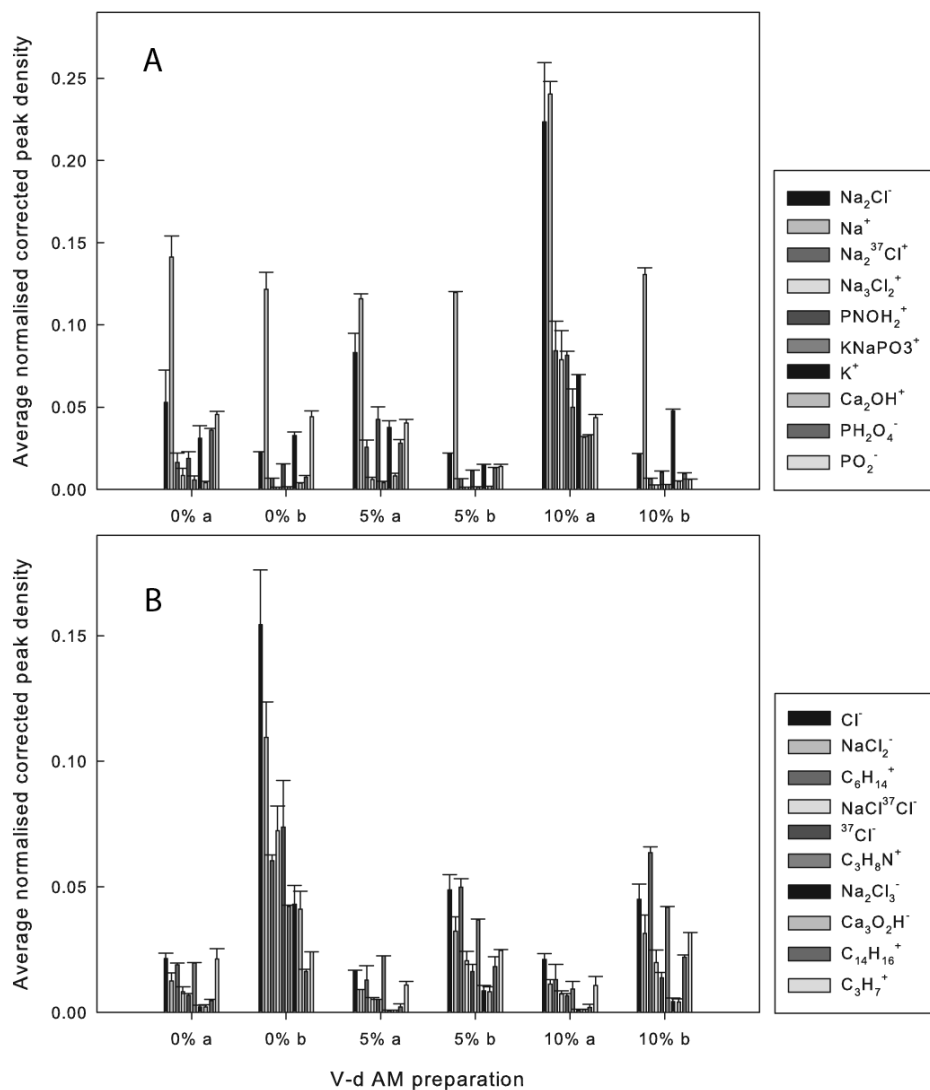


Figure 3.30: Chemical species

Chemical species were identified from the positive loadings (A) and negative loadings (B). The peak densities of the main chemical species identified were elevated on one side of 10% v-d AM. The main chemical species identified as variable negative loadings register high peak densities on one side of 0% v-d AM. No amino acids are identifiable.

Table 3.11: Summary of findings

Investigation	Main finding
DVS	Provides correlation between A_w and moisture content
TGA	End moisture of v-d AM between 10 and 18% (closed pan)
DSC	Enthalpy of sorption/desorption increased by trehalose
DMA	V-d AM in glassy phase at room temperature at RH < 60%
XRD	Amorphous traces shown of 0% and 10% v-d AM samples
FTIR	Three trehalose polymorphs identified
Tof-SIMS	No amino acids identified

3.5 Discussion

The relationships between AM, trehalose, temperature and moisture were investigated by moisture sorption, thermal, dynamic mechanical and surface analytical techniques. This work constitutes a framework for optimising v-d AM and for quality assurance by linking end moisture content (obtained by TGA) to A_w (DVS) and to T_g (DMA, DSC) of the product. In addition, it provides a platform for investigating the excipient phase (XRD, ATR-FTIR). While Tof-SIMS/PCA failed to yield meaningful data, the technique may be optimised for future work. These are essential lines of investigation in optimising the production, storage and clinical use of v-d AM, since if the material is stored above the T_g temperature, or its A_w is too high, its shelf life will be shortened and its quality compromised, whereas if the material is too rigid, it may crumble. A summary of findings table is provided (table 3.11).

3.5.1 Moisture sorption analysis

Moisture content is of critical importance because of its correlation with A_w . The DVS drying curves (figure 3.7) indicated that vacuum-drying the samples for a total of 3 hrs (A and B) produced lower equilibrium moisture contents than drying the samples for half that time (C). Samples A and B were analysed together. The A and B curves demonstrate that the moisture sorption characteristics of v-d AM are altered by the addition of trehalose.

At the end of drying, the percentage loss in mass in the 0% v-d AM samples (9.95%) was higher than that of 10% v-d AM samples (6.84%). However, the 10% v-d AM final drying slopes were significantly steeper, indicating that the 10% v-d AM samples was not fully equilibrated by the end of 500 mins. This suggests that moisture is retained by the trehalose-treated samples.

Samples C were less dry, suggesting either insufficient drying times or excessive exposure to ambient air. As seen in the water vapour sorption kinetic plots, AM is highly hygroscopic (figure 3.8). Therefore, once dried, it may rapidly equilibrate with the atmosphere, either gaining or losing moisture. In addition, the effects of trehalose in the 10% v-d AM C sample, which had a final wash before vacuum-drying, were partially lost, as evidenced by the flatter drying curve.

The remaining discussion concerns samples A and B. The water vapour sorption kinetic plots (figure 3.8), demonstrated a significantly lower change in per cent dry mass in the trehalose-treated samples, suggesting that more energy is needed to sorb and to desorb moisture. In the untreated v-d AM, there was a steep rise in the change in mass at ~70% RH. This change occurred at around 80% RH in the trehalose-treated samples, and was less marked. Thus, treatment of v-d AM with trehalose appears to make it less hygroscopic than its untreated counterpart. One explanation for this could be that the trehalose is in a non-protective crystalline phase, since this does not retain sorbed water (Surana et al., 2004b). An alternative explanation is that the trehalose is in the dihydrate crystal form and is saturated with water. At temperatures below 70°C, water is bound to trehalose dihydrate in an ice-like crystalline state (Akao et al., 1998). Above this temperature, the bound water undergoes a thermal transition to a liquid-like state and can evaporate. In contrast, water is not as strongly bound to anhydrous, amorphous and glassy trehalose, which can easily sorb and desorb water (Surana et al., 2004a; Hunter et al., 2010).

The question of A_w , and therefore end moisture content, of v-d AM has not been addressed in the literature. Although fungal growth is possible at and below a A_w of 0.65, depending on environmental factors, this level of A_w is safe for many foodstuffs (Abdullah et al., 2000), and may be a suitable upper limit for the A_w of v-d AM. The sorption-desorption plots (figure 3.9) can be used to determine the upper safety limit of equilibrium moisture content, depending on the desired stringency level. With an equilibrium moisture content of 20%, the A_w of the 10% v-d samples was 0.70, whereas that of the 0% samples was 0.61. Applying a safety limit of A_w of 0.65 would therefore eliminate the treated samples. The drying curves returned end moisture contents of 9.95% for 0% v-d AM and 6.84 for 10% v-d AM, equivalent to A_w values of ~ 0.35 . However, the slopes of the drying curves were significantly steeper in the trehalose-treated samples. This indicates that they were not at equilibrium as a result of bound water. Therefore, the true A_w value of 10% v-d AM may be even higher than 0.35.

According to Sitaula and Bhowmick (2006), the A_w of a trehalose:PBS mixture should be less than 0.23 to remain in the glassy phase. From the sorption-desorption plots, for 10% v-d AM, this would require a moisture content of below 5%. This may be difficult to achieve, and may even cause brittleness, which is a feature of amorphous glasses that may become more evident with ageing of the product (Surana et al., 2004a). A level of A_w of 0.5, as proposed by Costantino et al. (1998b), can be achieved in 10% v-d AM with a moisture content of $\sim 10\%$, and may therefore be a more realistic compromise. The sorption-desorption isotherms demonstrate that the 0% v-d AM samples have significantly more hysteresis than the 10% samples, indicating that the 10% v-d AM samples are more stable with respect to changes in humidity. The effects of this in terms of the quality of the samples are unclear.

Data from the desorption isotherm can be fit to a two-parameter mathe-

mathematical model known as the Brunauer-Emmett-Teller (BET) equation (Zhang and Zografi, 2000). Sitaula and Bhowmick (2006) quantified the desorption data of trehalose-PBS mixtures using the BET equation. The model indicated that increasing the concentration of PBS shifted the modelled desorption curve from sigmoidal to hyperbolic. A sigmoidal isotherm is protective at low A_w values since, for a given moisture content, A_w is lower than in a hyperbolic isotherm. The researchers were able to optimise the concentration of PBS according to the curve shape. While the current study data was not fit to model curves, the actual desorption isotherms of 0% and 10% v-d AM did not differ substantially in shape, suggesting a modest, if any, protective influence from the added trehalose. The Young and Nelson parameters indicated increased multilayer adsorption (caused by water-water hydrogen bonds) and absorption in the 0% v-d AM compared to 10% v-d AM (figure 3.10). Trehalose-water hydrogen bonding at the surface monolayer of treated v-d AM samples may occur in preference to multilayer adsorption and absorption. This may be analogous to other systems, such as acrylic-carbohydrate copolymers (Bravo-Osuna et al., 2005), in which the addition of acrylics to starch derivatives modifies their hygroscopicity and their water distribution, protecting them against the effects of plasticisation at high RH.

3.5.2 Thermal analysis

End moisture content measurements were carried out by TGA. In open pan TGA, a linear slope at the beginning of heating indicated that the samples were highly sensitive to temperature variation (figure 3.11). Using the open method with a cut-off of 19.5°C and a heating rate of 5°C min⁻¹, the moisture content varied between 8.7 and 11.9%, whereas at a heating rate of 10°C min⁻¹ and a cut-off of 25.2°C, the moisture content varied between 6.9 and 10.4%. This suggested that end moisture content was influenced by

the cut-off temperature. The closed pan method produced sigmoidal slopes (figure 3.14), making it more robust to minor variations in temperature. As measured by the closed pan method, the tissue moisture content ranged from 10.0% to 17.7% of total mass. Faster heating rates can improve the sensitivity of DSC by making the transition steps larger, which may partly explain why the results vary across methods. Since room temperature is not standardised, a representative temperature, e.g., 21°C, would be useful for moisture content analysis of AM. Other reasons for the variability could include variations in the preparation protocol, retention of moisture in the AM folds and water absorption from the atmosphere before packaging or after opening. The values of end moisture content obtained by TGA are substantially higher than those obtained from the DVS, which does not apply heat. From the sorption-desorption isotherms it can be seen that even moisture contents at the high end of this range are associated with an acceptable A_w . Nonetheless, the protocol for drying AM may need further optimisation to lower the A_w . Options include modifying the parameters of vacuum-drying by using higher vacuum and longer drying times. A more costly alternative may include using temperature-control shelves to lyophilise the samples. Heating the samples is not considered an option, as it is judged to be harmful to the material. In addition, a comparison of drying methods showed that vacuum-drying was more effective at removing moisture than heat-drying for 24 and 48 hrs, and only slightly less effective than drying in a vacuotherm oven for 48 hrs (figure 3.13).

The increase in energy required for moisture desorption in trehalose-treated samples, indicated by the DVS, is confirmed by TGA. First derivatives of the closed pan TGA curves allowed identification of the maximal rate of moisture loss as 80.5°C (0% v-d AM), 95.5°C (5% v-d AM) and 100.4°C (10% v-d AM). The addition of trehalose increases the enthalpy of moisture loss from AM. The TGA experiments suggested that moisture content

increases with increasing concentration of trehalose. This again suggests that the trehalose is in the dihydrate crystal form, bound to water (Akao et al., 2001). The DVS drying curves are consistent with this, as the trehalose-treated AM was not in equilibrium by the end of 500 mins, indicating bound water.

The TGA curves obtained were similar to the those of artificially cross-linked AM-derived collagen reported by Kumar et al. (2003), who described water loss as occurring between 60°C and 90°C and decomposition between 270°C and 330°C. AM undergoes changes similar to pure extracted collagen, suggesting that the collagen profile predominates in thermo-analytical testing. TGA and DSC can be performed simultaneously, enabling endotherms to be matched to thermogravimetric events conducted under the same conditions. This can give a clearer understanding of the thermal analysis, and is recommended for further AM work.

In ramp mode DSC (figure 3.15), the temperature of first principal endotherm occurred at ~75°C in 0% v-d AM. There was a second endotherm at 219°C, representing the melting of collagen (Kumar et al., 2003). In 10% v-d AM, the moisture loss endotherm occurred at 86°C, whereas a second endotherm occurred at 171°C. The significance of the variance in the second endotherm is unknown, but it could represent an earlier decomposition event. As the melting temperature of the anhydrate trehalose crystal is 215°C (Akao et al., 2001), this is unlikely to be the cause. Peak decomposition of treated samples was shown by closed pan TGA to occur at ~30°C lower than untreated samples (from ~279.0°C to 309.4°C). These findings suggest that the decomposition of AM is accelerated by the addition of trehalose.

The cyclic DSC runs showed distinct endotherms for 0% v-d AM peaking at 51.6°C and 102.3°C (figure 3.17). The first peak occurred at higher temperatures in the 5% v-d AM samples (65.3°C) and the 10% v-d AM samples

(75.7°C), again reflecting the water binding effect of trehalose. The mean enthalpy value of the first endotherm was increased by the addition of trehalose from 1.9 Jg⁻¹ in 0%, to 11.3 Jg⁻¹ in 5% and 40.0 Jg⁻¹ in 10% v-d AM, which confirms the water binding effect of trehalose. The second endotherm at ~100°C identified in the current study may represent protein denaturation. The cyclic DSC plot of the vacuum-dried trehalose:PBS mixture (3.16) indicated that the trehalose was not in a glassy state at room temperature, with an inflection point occurring at 14.9°C. Sitaula and Bhowmick (2006) found that an increase in the A_w of a trehalose/PBS mixture from 0.02 to 0.11 shifted the T_g downwards by around 50°C to ~40°C, which suggests that the A_w of trehalose/PBS in the current study is considerably higher. The isotherms of the 10% v-d AM samples indicate A_w values of ~0.35, which would not produce a glass at room temperature.

3.5.3 Dynamic mechanical analysis

One of the main achievements of using DMA testing was to demonstrate the transition of v-d AM from a glassy to a rubbery state. The starting modulus values, of the order of 10⁹ Pa, are typical of glassy materials (Patist and Zoerb, 2005). This has not been shown before in dried AM, and is useful in interpreting the mechanical behaviour of the material. The frequency sweep tests did not return modulus values that were suggestive of a glassy material (~10⁷ Pa), which probably reflects suboptimal test conditions as a result of failure to apply automatic tension mode. This was applied in the subsequent tests. The humidity sweep DMA tests demonstrated that v-d AM could be glassy at room temperature, and that rising levels of RH could precipitate a T_g (figure 3.20). This is a demonstration of the plasticising effect of moisture on v-d AM: as the T_g temperature is brought to ambient temperature by the rising RH, a transition occurs. In this regard, v-d AM is similar to synthetic hydrophilic polymers that sorb water, such

as polypropylene/ethylene alcohol vinyl (PP/EVOH) (Lasagabaster et al., 2006), and hydrogels used in the pharmaceutical industry, such as polyhydroxy ethyl methacrylate (pHEMA) (Roorda et al., 1988).

Temperature sweep tests demonstrated a variety of outcomes. For some samples, there was a glassy state at low temperatures and a transition occurring over two decades, starting at temperatures as low as $\sim -20^{\circ}\text{C}$ (table 3.21), whereas others showed minimal, or even no relaxation (table 3.22 and table 3.24 A respectively). The explanation for this discrepancy is likely to reflect differences in RH. The transition to a rubbery state starting at $\sim -20^{\circ}\text{C}$ in some samples of 0% v-d AM could be a consequence of water absorption from the thawing of ice on the sample surface. Since RH was uncontrolled, moisture may have condensed on the sample, becoming frozen during the cooling phase of the experiment. The presence of salts on the sample surface may have contributed to the ice thawing at temperatures approaching -21.2°C , the eutectic point of saline water. The fact that this was not observed consistently may be an indication of different ambient RH.

The reversibility in the transition is further evidence of the plasticising effect of water. The reversal from a rubbery to a more rigid state was seen in conditions of decreasing RH (table 3.19) and increasing temperature, both cases suggesting an effect of drying. This is consistent with the observation from open pan TGA traces that v-d AM loses moisture rapidly over small rises in temperature. Another possibility is that the AM undergoes shrinkage, although this typically occurs at temperatures of above $\sim 50^{\circ}\text{C}$ (Ma et al., 2010).

In addition, the DVS, DSC and TGA findings all point to increased enthalpy of water sorption in trehalose-treated v-d AM. Therefore, trehalose would be expected to mitigate the effects of RH, increasing the T_g temperature by preventing plasticisation. This effect is indeed observed in a com-

parison of three representative DMA runs of 0%, 5% and 10% v-d AM (table 3.25). In this comparison, the temperature of three thermodynamic events associated with T_g is raised by $\sim 30^\circ\text{C}$ with increasing concentrations of trehalose.

Since the RH in the temperature sweep tests was unknown, further temperature sweep tests at constant RH are required to characterise the properties of v-d AM in greater detail. In DMA, the v-d AM behaved in a manner highly reminiscent of an amorphous or semi-crystalline polymer (Duncan, 2008). However, in these, the effects of plasticisation are not usually so evident. Hence, it is possible to perform DMA on a polymer in ambient humidity and achieve highly consistent results. That this proved difficult in v-d AM is an index of its exceptional sensitivity to the effects of moisture. Thus, it was not possible to isolate the relaxation, or T_g , of collagen, expected at 40°C according to Li (2000), because of the plasticising effects of water molecules (Ntim et al., 2006). In reality, there is no single T_g temperature for any material. In practice, the viscoelastic behaviour of v-d AM could be defined over a range of RH values.

DMA proved to be a difficult technique, with a high rate of tissue breakage. This could be due to many factors, including sample size and trehalose treatment. The best results were obtained on $5\text{ mm} \times 5\text{ mm}$ samples with an additional static force of 0.2 N or higher. The trehalose was felt to cause more brittleness, leading to increased sample loss from crumbling. This is evidenced by a failure to obtain humidity DMA traces on treated samples, and has implications for the quality of the membrane. Despite this, evidence for a glassy state of trehalose on v-d AM was unclear, with the possibility remaining that it was amorphous or crystalline.

3.5.4 Surface analysis

Questions regarding the conformational state of trehalose were addressed by surface analytical techniques. XRD traces obtained for 0% v-d AM and one for 10% v-d AM suggested a predominantly amorphous content, while crystalline peaks matching the profile for NaCl stood out. The lack of any crystalline component in the XRD trace other than the NaCl crystal peaks suggests a masking effect of the abundant amorphous constituents of AM. Even peaks for KCl, another major component of PBS, were not found. In the 10% v-d AM sample, the trehalose dihydrate XRD profile, present in freeze-dried solutions (Santagapita and Buera, 2008), could not be detected. The XRD profiles of anhydrous and other crystalline forms of trehalose, as reported by Nagase et al. (2002), were searched for unsuccessfully. XRD traces of type I and type III collagen, which can be obtained from purified protein (Cameron et al., 2002), were also absent.

Three different forms of trehalose were identified in this study by ATR-FTIR (Figures 3.27 and 3.28). These had characteristic spectral peaks at 986 and 943 cm^{-1} , 991 and 941 cm^{-1} and 994 and 956 cm^{-1} , representing symmetric-asymmetric stretching of the glycosidic bond in different trehalose polymorphs (Akao et al., 2001). Respectively, the first two of these are the anhydrate crystal and a form obtained by freeze-drying aqueous solutions of trehalose. In the anhydrate crystal form, trehalose molecules are densely packed and water cannot penetrate easily, whereas the freeze-dried form may be similar to the protective anhydrous form that preferentially bind water to produce the dihydrate molecule. A third polymorph, with peaks at 994 and 956 cm^{-1} , has not been identified. It may be similar to the trehalose dihydrate crystal which can have peaks both at 994 and 954 cm^{-1} and 998 and 956 cm^{-1} . The amorphous form (983 and 931 cm^{-1}), without which a glass cannot be formed, was not detected. However, the trehalose in the 10% v-d samples does not appear to be in a crystalline form. This gives

characteristic sharp peaks at 3500 cm^{-1} and in the C–H stretching region between 3000 and 2800 cm^{-1} (Wolkers et al., 2004), which are missing in the treated samples. It suggests that the trehalose is simultaneously present as a mixture of amorphous and crystalline forms. Further drying may produce detectable levels of the amorphous form. Since the physical properties of amorphous trehalose change as a result of sample preparation (Surana et al., 2004b), exposure to moisture Akao et al. (2001) and aging (Surana et al., 2004a), ATR-FTIR will be a useful guide in characterising the different states of treated v-d AM produced under different conditions in future work. In the absence of evidence of glassy trehalose, it is not clear from these findings whether the trehalose has any protective function. In pharmaceutical systems, crystalline excipients cause instability of the amorphous ingredients (Costantino et al., 1998a). This suggests that v-d AM may be more stable by having no stabilising excipient than by having a crystalline sugar.

This O–H stretching band located between 3000 and 3600 cm^{-1} in the trehalose spectrum, as seen in the treated v-d AM samples, indicates a wide range and orientation of hydrogen bonds (Wolkers et al., 2004). Sitaula and Bhowmick (2006) reported that excessively high levels of PBS diminished the hydrogen bonding capacity of trehalose, producing an upward shift in the trehalose C–H stretching band and a decrease in the absorbance and width of the O–H stretching band. The peak intensities of the O–H bands of the trehalose-treated samples are increased with respect to the untreated samples, indicating abundant hydrogen bonding and appropriate levels of PBS.

The ToF-SIMS analysis revealed no significant differences between samples. The sodium ions are known to exert a matrix effect on the SIMS fragmentation process, which could have affected the ionisation of the analytes, resulting in their suppression (Wagner and Castner, 2001). Trehalose is also known to suppress ionisation. Indeed, Xia et al. (2002) stipulated that

a w/v concentration of higher than 0.5% trehalose should not be used for protein detection. However, since the untreated AM was similarly characterised, it seems most likely that the high concentration of sodium may have prevented the ToF-SIMS from identifying amino acid fragments. The differences found between the samples are likely to reflect sample heterogeneity rather than a protective effect of the trehalose treatment.

3.6 Conclusion

This work is a sentinel study of the moisture, thermal, dynamic mechanical and surface analysis of v-d AM, comprising a new approach to the understanding of this biomaterial. These analyses provided an interconnected framework for optimising the dry preservation of v-d AM. A thorough understanding of the effects of moisture and excipients on the material properties of AM was achieved once an overview of the different investigations became available. The concepts of A_w and T_g , rarely discussed in clinical *milieux*, were particularly significant in this regard. In the next chapter, I investigate the material properties of rehydrated v-d AM as an alternative to f-t AM.

Chapter 4

PHYSICAL CHARACTERISATION OF AM

4.1 Introduction

As demonstrated in the last chapter, the physical properties of v-d AM depend on moisture content and temperature. For surgical application, v-d AM can be reconstituted with water or kept dry, depending on the precise clinical indication. A dried AM patch can be glued inside an area of denuded cornea, while, as a hydrated patch, AM can drape over the corneal surface without impeding blinking. From a surgical perspective, AM needs to be handled easily without tearing, and to last long enough on the ocular surface to have a clinical effect before undergoing enzymatic degradation. Thus, the quality attributes that make AM a useful and versatile material in ophthalmic surgery include its biocompatibility, pliability, strength and resistance to degradation. It should also be transparent and permeable. Fully rehydrated v-d AM should be comparable in these qualities to the current standard, frozen AM, if it is to gain popularity among surgeons. The characterisation of the material properties of v-d AM is therefore an important aspect of this research. I conducted imaging studies and mechanical property tests to characterise differences between the preparations. Tools for imaging AM included optical, electron and atomic force microscopy (AFM).

The mechanical properties of the preparations were explored with uniaxial tensile tests and non-destructive tests such as nanoindentation and acoustic wave impedance. I used a mathematical model to define and predict the mechanical properties of the tissue, which I then attempted to modify by cross-linking the collagenous matrix.

4.2 Literature review

4.2.1 Physical properties of natural AM

The measurable properties of the foetal membranes near full term, including mechanical properties, have been extensively studied in connection with their premature rupture (Parry and Strauss, 1998). AM provides the majority of the tensile strength of the intact chorioamniotic membrane, and is therefore of particular interest (Oyen et al., 2006). As a viscoelastic material, AM exhibits characteristic properties, including a strain rate-dependent stress response, relaxation at a fixed displacement and creep at a fixed load (Lavery and Miller, 1977). These responses exhibit regional variability, reflecting structural heterogeneity within the membrane and a broad property range (Joyce et al., 2009). There is regional variation in the structural composition of AM, which is thickest near the placenta and thinnest near the rupture site (Artal et al., 1976). A zone of ‘altered morphology’ can be found overlying the cervix, both in spontaneous vaginal deliveries (Malak and Bell, 1994) and in elective caesarean sections in the absence of labour (McLaren et al., 1999). At this zone, biochemical changes give rise to localised thinning and mechanical weakening of AM in anticipation of rupture (El Khwad et al., 2005, 2006). This has been correlated with MMP activation, collagen remodelling and cell apoptosis, supporting the concept of a programmed natural dissolution of the membrane around the time of birth (Moore et al., 2006). The maintenance of mechanical strength

in AM involves a balance between collagen production on one hand and enzymatic degradation, mediated primarily by the MMPs, on the other (Parry and Strauss, 1998). At around the time of rupture the balance shifts decisively in favour of collagenolysis. It is thought that MMPs play a central role in the premature rupture of the membranes (PROM), a significant cause of perinatal mortality that is associated with infection (Parry and Strauss, 1998).

4.2.1.1 Structural components

Collagens and non-collagenous proteins make up the structural components of the BM, the compact layer and the fibroblast layer. Besides numerous collagens and elastin, AM contains numerous proteoglycans, glycoproteins and proteins as part of the structural network (see table 4.1). Large proteoglycans, such as osteoglycin, are amongst the most abundant stromal proteins (Baharvand et al., 2007). Glycoproteins such as fibronectin, present throughout the AM stroma, are thought to have a significant strengthening function (Bryant-Greenwood, 1998). Small leucine rich proteoglycans such as decorin, mimecan and biglycan interact with collagen networks, increasing the overall mechanical strength (Meinert et al., 2001).

The BM consists largely of collagens III and IV (Malak et al., 1993), with smaller quantities of type V (Modesti et al., 1989), secreted by the AEC. Type V and VI collagens form filamentous connections between the BM and the ECM (Malak et al., 1993). The BM supports the assembly of a network containing laminin, entactin and heparan sulphate (Endo et al., 2004). The compact layer and the fibroblast layer consist of stromal interstitial type I and type III collagens (Aplin et al., 1985). The stroma consists of approximately 10% randomly-arranged types I and III collagen and 2% elastin (wet weight) (Jabareen et al., 2009). Type I collagen forms parallel bundles that provide mechanical integrity (Malak et al., 1993). Together with

Table 4.1: Non-collagenous AM matrix proteins

Constituent	Role	Localisation	Reference
Laminin-5	Embryonic cell organisation	BM	Koizumi et al. (2007)
Laminin-1	Embryonic cell organisation	BM	Dietrich et al. (2005)
Entactin	Cell adhesion, collagen interaction	BM	Dietrich et al. (2005)
Nidogen-2	ECM interactions	BM	Dietrich et al. (2005)
Fibronectin	Cell adhesion, migration	BM, stroma	Linnala et al. (1993)
Heparan sulphate proteoglycan	Angiogenesis	BM	Dietrich et al. (2005)
Lumican	Cell migration	Stroma	Baharvand et al. (2007)
Integrin $\alpha 6$	Embryogenesis	AEC	Koizumi et al. (2007)
Transglutaminase 2	Protein cross-linking	Cytoplasm	Baharvand et al. (2007)
Mimecan	Collagen interactions	Stroma	Hopkinson et al. (2006a)
Decorin	Collagen interactions	Stroma	Baharvand et al. (2007)
Integrin $\beta 4$	Laminin receptor	BM	Koizumi et al. (2007)
Tenascin-C	Epithelial-mesenchymal interactions	Stroma	Dietrich et al. (2005)
Biglycan	Collagen interactions	Stroma	Meinert et al. (2001)
Matrilin-4	Filamentous network formation	Stroma	Dietrich et al. (2005)

BM, basement membrane; ECM, extracellular matrix.

smaller amounts of types V, VI and VII collagen, they are synthesized predominantly by mesenchymal cells (Casey and MacDonald, 1996). In a small angle light scattering study of the collagen bundles, no preferred fibre orientation was detected in the horizontal plane, although there were small regions of homogeneous alignment (Joyce et al., 2009). X-ray diffraction and electron microscopy studies have shown that collagen fibrils are more loosely spaced and less compact close to the rupture site (Connon et al., 2007).

Besides their possible roles in strengthening the AM, many of the proteins have functions in promoting healing. For example, the laminins, all of which are secreted by AEC with the exception of $\alpha 1$ and $\alpha 4$ (Takashima et al., 2008) are implicated in cell differentiation (Cheng et al., 2009). Human lumican, a glycoprotein, was found to promote epithelial healing in experiments on lumican-knockout mice (Yeh et al., 2005). Proteoglycans and glycoproteins found in the AM stroma, including perlecan, agrin, tenascin C and nidogen-2 are also found in the human limbal epithelium, which may favour the role of AM as a substrate for epithelial expansion (Dietrich-Ntoukas et al., 2012). Laminins and tenascin C act in cooperation to promote adhesion and spreading of corneal epithelial cells (Katz et al., 2006).

4.2.1.2 Therapeutic preparations

The structural components of therapeutic preparations of AM are similar to those of the natural tissue. Frozen and lyophilised AM both contain intracytoplasmic vacuoles, a sign of devitalisation (Rodríguez-Ares et al., 2009). Ultrastructural EM studies have demonstrated few differences between the two preparations (Libera et al., 2008). Collagen types I, III, IV and V and fibronectin are all found throughout lyophilised AM, and collagen Type VII and laminin 5 are retained in the BM (Nakamura et al., 2004, 2008). These features are morphologically similar to those of f-t AM, although lyophilised

AM is more compact. While its overall structure may be retained, v-d AM is significantly thinner than f-t AM (von Versen-Höyneck et al., 2004).

4.2.2 Mechanical characterisation

4.2.2.1 Uniaxial testing

Mechanical testing of AM has included three different approaches: uniaxial testing, biaxial burst and biaxial puncture (Calvin and Oyen, 2007). Uniaxial tests of AM can be used for force-distance and stress-strain analyses. Force-distance analyses generate information on the force needed to produce rupture (ultimate tensile strength, UTS, measured in Newtons), elongation (ΔL), a measure of reversible (elastic) and irreversible (plastic) deformation of AM, and the work required to cause rupture (Artal et al., 1976). Failure strain (ε_f) can be calculated from ΔL . Stress-strain calculations can be produced once geometrical information on the tissue being tested is known (initial length and cross-sectional area). These include nominal failure stress at failure (σ_f^N), Young's modulus of elasticity (E) and toughness (T), measured as the area under the stress-strain curve. Force-distance and stress-strain measurements can be applied to uniaxial deformation more easily than to the more complex tests of burst and puncture strength (Joyce et al., 2009). Unlike burst and puncture tests, they do not mimic physiological conditions, but give useful information about membrane strength (Moore et al., 2006; Joyce et al., 2009). Thus, uniaxial tests constitute a practical approach of assessing the 'robustness' of AM as a biomaterial and provide an index of its surgical worth. Nakamura et al. (2004) reported no difference between lyophilised AM samples and wet-preserved controls, although the sample size was very small ($n = 6$).

4.2.2.2 Stress-strain analysis

Stress-strain analyses of AM are constrained by the requirement to obtain the geometric dimensions, as the thickness of AM samples is difficult to measure accurately and is non-uniform. The main methods of measurement can deform the tissue. These include micrometry (von Versen-Höynck et al., 2004) and optical microscopy (Connon et al., 2010; Jabareen et al., 2009). Micrometry can be performed directly with a screw-gauge micrometer (von Versen-Höynck et al., 2004), or by sandwiching the tissue between two Plexiglass plates, a method described by Lavery and Miller (1979). Optical microscopy is suggested by Jabareen et al. (2009) to be the most accurate method of AM measurement. They recorded a mean thickness of AM of $111 \pm 78 \mu\text{m}$, which is approximately twice that recorded by previous studies (Oxlund et al., 1990; Prévost, 2006). Alternative methods have included the use of confocal laser (Nakamura et al., 2008). AM thickness is variable, decreasing from approximately $100 \mu\text{m}$ in areas proximal to the placenta to approximately $65 \mu\text{m}$ in areas distal to it (Connon et al., 2010). In addition, it is highly dependent on hydration. Measuring approximately $20 - 30 \mu\text{m}$ in thickness, dried AM is significantly thinner than both fresh AM (Nakamura et al., 2008) and f-t AM (Chuck et al., 2004; von Versen-Höynck et al., 2004). In the absence of thickness measurements, some authors have restricted the analysis to force-distance, avoiding stress-strain calculations altogether (Fujisato et al., 1999; Nakamura et al., 2004). Joyce et al. (2009) used membrane tension as an alternative stress measure, expressed as force/unit length, to avoid difficult and inaccurate thickness measurements. Oyen et al. (2004) conducted a stress-strain analysis by assuming the thickness of AM to be uniform, whereas Chuck et al. (2004) and von Versen-Höynck et al. (2008) reported stress-strain data for therapeutic preparations of both dried and f-t AM with measured thickness.

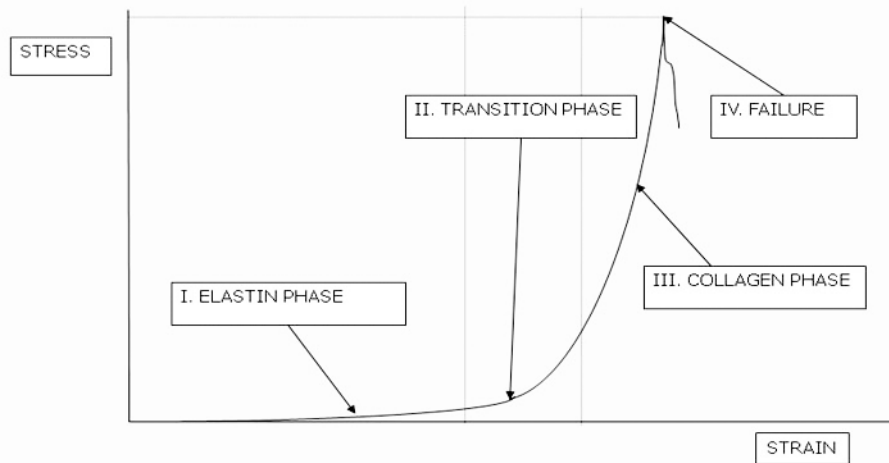


Figure 4.1: Phases of stress-strain behaviour in soft tissue

The stress-strain behaviour of soft tissues is represented diagrammatically. Following the initial stretching of elastin fibres, collagen fibres become sequentially straightened, causing the gradient (modulus) to increase at higher strain.

4.2.2.3 Stress-strain characteristics

Biological soft tissues have similar characteristics that include viscoelasticity and non-linear stress-strain behaviour (Fung, 1984). In many soft tissues, this is characterised by a slow initial rise as elastin fibres are recruited (elastin phase) (Korossis et al., 2002). In AM, the initial ~10% strain is accompanied by very little stress (Oyen et al., 2004). The initial phase is followed by an upwardly concave transitional phase in which crimped type I collagen fibres begin to straighten sequentially (Joyce et al., 2009). There is then a steep rise in which limited collagen elongation occurs (collagen phase). The phases are represented by a diagram (figure 4.1). The gradient of the the elastin phase is known as the low-strain modulus E_1 , while in the collagen phase it is called the high-strain modulus, E_2 (Fung, 1993). Stress-strain curves with two different moduli have been described as having bi-linear behaviour (Fung, 1993). In AM, there are direct correlations between the elastin content and E_1 , and between the soluble collagen content and E_2 (Jabareen et al., 2009). The collagen phase is concave, rather than linear, as the modulus increases with strain (Oyen et al., 2004). The modulus of AM has been termed pseudolinear, and can be measured as the gradient

of a tangent of the stress-strain curve. In contrast, Young's modulus (E) is usually reserved for linear (i.e., Hookean) behaviour. The pseudolinear high strain modulus increases with with greater peak force, and therefore does not adequately describe the stress-strain response (Oyen et al., 2004). Researchers have reported a range of pseudolinear modulus values for natural AM, from 1.62 MPa (Benson-Martin et al., 2006), 19.0 MPa (Oxlund et al., 1990) and up to 29.5 MPa (Oyen et al., 2004), although the test conditions and sample sizes varied.

4.2.2.4 Mathematical modelling of AM behaviour

Since a single pseudolinear modulus does not adequately describe the elastic response of AM, researchers have described its non-linear behaviour in mathematical terms (Oyen et al., 2004; Jabareen et al., 2009). Whereas Oyen et al. (2004) proposed a quadratic constitutive equation to explain the non-linear stress-strain behaviour of AM, Jabareen et al. (2009) went further, describing the behaviour of AM with a two-parameter constitutive model. Constitutive models are highly useful methods of describing the complex behaviour of soft tissues in response to external loading (Fung, 1993). They can be used to predict behaviour and to compare tissue characteristics, and can lead to an improved understanding of biological systems. Rubin and Bodner (2002) proposed constitutive mathematical equations to describe the viscoelastic behaviour of facial skin. The Rubin-Bodner equations were based on an assumption of the composite nature of skin, consisting of an elastic component and a viscous (dissipative) component. They designated two parameters: q , a material constant having the units of stress, and μ_0 , a dimensionless constant accounting for non-linearity of the moduli (Rubin and Bodner, 2002). Using these parameters, Jabareen et al. (2009) proposed a model to describe the mechanical behaviour of AM, assuming it

to be an incompressible material:

$$\sigma^N = \frac{E_1}{3} \exp^{((qE_1/3\mu_0)(\alpha_1-3))} \left((\varepsilon^N + 1) - \frac{1}{(\varepsilon^N + 1)^2} \right) \quad (4.1)$$

$$\alpha_1 = (\varepsilon^N + 1)^2 + \frac{2}{(\varepsilon^N + 1)} \quad (4.2)$$

The values of the low-strain modulus, E_1 , and the nominal strain, ε^N , were derived from the data. The values of q and μ_0 were determined simultaneously by searching for the best possible fit of the experimental stress–strain curve data to the model. This enabled differences between membranes to be quantified. For example, a high correlation was found between elastin content (determined biochemically), E_1 and the ratio $\frac{q}{\mu_0}$.

4.2.3 Accelerated degradation

In cases of acute inflammation, as after acute burns, AM undergoes necrosis on the ocular surface, leading to treatment failure (Ma et al., 2002). Even in the absence of inflammation, the tissue is degraded by endogenous enzymes after a few days (Spoerl et al., 2004). The effects of enzymatic degradation on tissue can be assessed by accelerated degradation assays, a useful tool in the characterisation of biological products (Matejtschuk and Phillips, 2007). *In vitro* degradation assays on therapeutic AM have included qualitative imaging studies (Chau et al., 2012) and quantitative assays (Fujisato et al., 1999; Ma et al., 2010). In these studies, degradation assays were used to analyse the effects of chemical cross-linking on AM. It is not known whether dried AM preparations undergo faster degradation than fresh or f-t counterparts. The clinical application of cross-linked dried AM illustrates this concern (Kitagawa et al., 2011).

4.2.4 Non-destructive tests

While the uniaxial test can provide a useful measure of the gross material properties of AM, it destroys the samples being tested. Non-destructive tests are available that can provide subtle characterisation of the different preparations of AM. These include high frequency rheology, AFM and DMA (discussed in a Chapter 3).

4.2.4.1 High frequency rheology

High frequency rheology measurements give information on the high frequency shear modulus (G^*) of complex fluids and polymers (Raimbault et al., 2010). The shear storage modulus (G') and the loss modulus (G'') respectively measure the elastic and viscous components. These can be measured by acoustic wave biosensors, instruments that are sensitive enough to detect proteins, DNA, bacteria and lipid bilayers (see review by Länge et al., 2008). Different instruments are available, some of which are able to sense shear horizontally polarised surface acoustic waves (SH-SAW) propagated between two interdigital transducers on a piezoelectric substrate. One of these is known as the Love wave device, which has transducers coated with a guiding layer of silicon dioxide on an ST-cut quartz substrate (Kovacs et al., 1994). ST-cut quartz is a particular cut that enables interdigital transducers to generate a wave in the silicon guiding layer. Loading a sample onto the guiding layer between the transducers changes the surface impedance and shifts the propagation constant of the acoustic wave, result in its attenuation and a downshift in its centre frequency. From measurement of the received signal amplitude and centre frequency, and through comparison with the reference signal, the wave attenuation, centre frequency shift and hence propagation constant can be determined. Small changes in viscosity can be detected this way (Jakoby and Vellekoop, 1998). In a study comparing chemically cross-linked AM to controls, a significantly

higher G' in AM treated with transglutaminase (TG) was interpreted as an indication of increased mechanical strength (Chau et al., 2012).

4.2.4.2 Atomic force microscopy

AFM is an ultra-high resolution technique widely used in the life sciences for imaging and surface analysis (see review by Parot et al., 2007). It can provide a wealth of information about the mechanical properties of a material, providing the correct techniques and interpretation are applied (Oyen and Cook, 2009). The instrumentation requires less sample preparation than other materials testing methods, such as uniaxial tests or dynamic mechanical analysis, but interpreting the results requires care.

The technique relies on a nanostylus (tip) attached to a microcantilever that is used to scan an immobilised sample, such as a film of tissue. The cantilever is connected to a piezoelectric transducer ('piezo'), in which voltage induces movement. A laser beam connected to a photo sensor registers the cantilever movements, which are fed back to the piezo, enabling the tip pressure to be applied at constant force. For soft biological samples, the preferred method of surface imaging is by oscillating a crystal silicon cone tip over the surface (Parot et al., 2007). This does not result in actual contact between the tip and the surface (non-contact mode). Van der Waals forces at the surface decrease the resonance frequency of the cantilever. The vertical (z) position of the piezo changes in response to the oscillation amplitude of the cantilever as it approaches the tissue, maintaining a constant average distance between the tip and the sample. The movement of the tip over the surface can be recorded as a topographical image resolved from the nanometric scale to a few microns. An alternative to the non-contact mode has been developed in which the tip comes into intermittent contact with the sample without damaging it ('tapping') (Zhong et al., 1993).

Nanoindentation is a related technique used to investigate the differ-

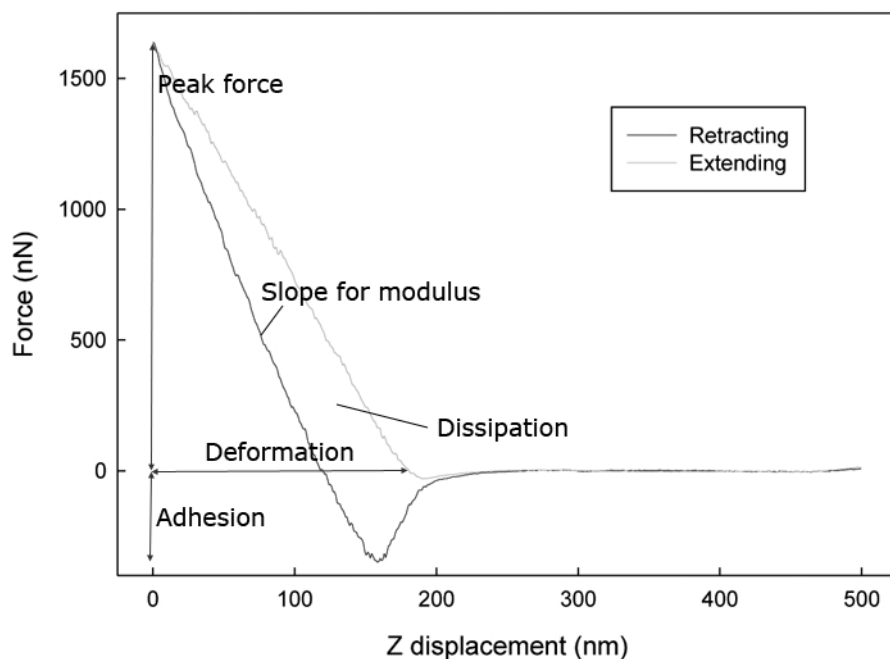


Figure 4.2: Force-displacement nanoindentation plot

An example of a force-distance curve obtained from nanoindentation of v-d AM is shown. From right to left, the cantilever is approaching the sample. Attractive forces overcome the cantilever stiffness to pull the tip towards the sample surface. The force increases until a peak force is reached. The probe then starts to withdraw. Adhesive forces cause a downward dip, until the cantilever is freed.

ent modes of mechanical deformation in biomaterials: elastic, plastic, viscous and fracture (Oyen and Cook, 2009). In static force spectroscopy mode, AFM permits direct force measurements of tip-sample interactions. The tip is extended towards the sample and retracted, while the cantilever deflection signal is measured in volts. The signal can be calibrated to give force measurements. Each force measurement results in a force curve showing the cantilever deflection recorded as the tip vertically approaches and then retracts from the sample surface. The hardness of the sample, as well as adhesive forces between the tip and the sample and energy dissipation, can be estimated from a force plot generated for every extension-retraction cycle. A spherical tip can be used in place of a conical tip for this purpose.

An example of a force curve on an AM sample is shown below (figure 4.2). The trace should be followed from right to left, as the cantilever approaches the sample. There is an upward slope at the point of deflection as the ex-

tending cantilever comes into contact with the surface. As the sample is viscoelastic, the slope of the retracting curve indicates hysteresis, i.e., there is dissipation of the energy delivered during indentation. The downward dip during retraction is caused by adhesion forces between the tissue and the sample.

A variety of mathematical models exist for the different material response types of the samples being tested (Oyen and Cook, 2009). The responses include combinations of elastic, brittle, plastic and viscous. For non-linear data, the data are commonly analysed with automated software and solved by a mathematical algorithm known as the Oliver-Pharr analysis, which differentiates the retractile slope at maximum displacement (Oliver and Pharr, 1992). The sample surface hardness and Young's modulus (in Pa) are calculated from the slope data. The Derjaguin-Müller-Toporov (DMT) model (Derjaguin et al., 1975) is fitted using data from the contact part of the force curves. It can be used to generate data on adhesion, energy dissipation and plasticity. Tip-sample adhesion can be measured from the maximum negative deflection force of the cantilever while retracting from the surface. The energy dissipation (in J) is the force integration during a full extending-retracting cycle. This can be measured as the area between the extending and retracting curves. Plasticity is calculated as a ratio, and therefore takes no unit.

AFM has been used to study the surface of air-dried denuded and intact AM (Cooper et al., 2005). The presence of an intact layer of glycocalyx prevented the topographical mapping of the microvillous surface of the epithelium. In denuded tissue, the uppermost layer of the basal lamina was determined to be smooth, suggesting its integrity following removal of epithelium. In a study of therapeutic freeze-dried AM, AFM was used to document damage to collagen fibres by γ -irradiation (Deocarís and Abad, 2005). Lim et al. (2010) used AFM to depict variations in the height and hardness

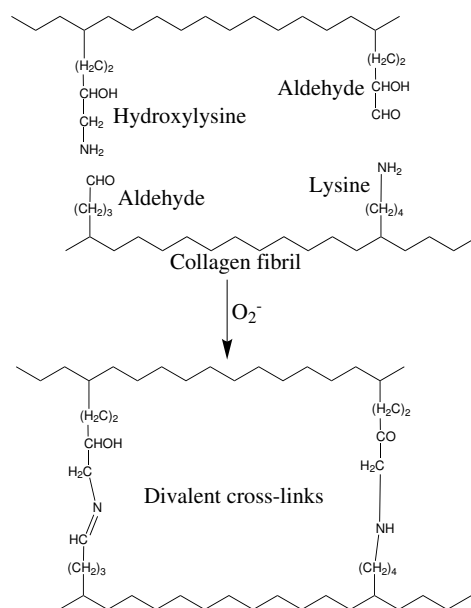


Figure 4.3: Cross-linking mechanism

In fibrillar collagens, divalent covalent cross-links can occur between telopeptide aldehydes, formed by the actions of lysyl oxidase, and helical lysine and hydroxylysine residues. Trivalent cross-links can also occur (adapted from Eyre et al., 2008). Free radicals, generated by ultraviolet irradiation of riboflavin, can generate cross-linking reactions.

of the basal lamina of decellularised AM.

4.2.5 Cross-linking of AM

Collagen molecules consist of three helical peptides containing polar amino acid side chains that can form intermolecular cross-links (Bailey et al., 1964). In fibrillar collagens, covalent cross-linking occurs between amine groups ($-\text{NH}_2$) of helical lysine and hydroxylysine residues and carboxyl groups ($-\text{CHO}$) of telopeptide aldehydes, produced enzymatically by lysyl oxidase (Eyre et al., 2008) (figure 4.3). Both divalent and trivalent cross-links can occur between collagen fibrils, which are typically found in load-bearing tissues. Artificial cross-linking may be induced by different methods including using ultraviolet light with and without sensitisers and aldehyde reactions (Spoerl et al., 1998). Photo-sensitisation produces free radicals, which break the hydrocarbon chains in aldehydes (Goodeve and Kitchener, 1938), allowing them to covalently bind amine groups. Cross-linking in collagen may

also be induced by nonenzymatic glycation, which occurs as a result of ageing and diabetes. Natural and artificial cross-linking of tissues is thought to have many benefits, including increased resistance to proteolytic breakdown and absorption as well as improved mechanical strength, thermal stability and biocompatibility (Spoerl et al., 1998; Lee et al., 2001).

Photo-cross-linking of collagen gels by visible light irradiation in the presence of a photoinitiator was found to improve the mechanical properties of collagen, while maintaining the triple helical structure (Brinkman et al., 2003). In recent years, much attention has been given to artificial induction of cross-linking of human corneal collagens as a means of increasing its mechanical strength and resistance to enzymatic digestion in the treatment of keratoconus and bacterial keratitis (Spoerl et al., 2004; Wollensak et al., 2003). Currently, UVA/riboflavin is widely used in ophthalmology to treat pathological thinning of the cornea by cross-linking (Wollensak et al., 2003)

Comprising large amounts of type I collagen, AM can also undergo artificial cross-linking, the putative benefits of which could include increased toughness and resistance to degradation. Fujisato et al. (1999) first attempted to cross-link AM, both by irradiation (γ -irradiation or electron beam) and chemically (with glutaraldehyde). They conducted stress-strain measurements on the cross-linked AM. Irradiation weakened the AM, consistent with the observation that it causes scission of the covalent bonds in collagen, leading to disorganisation (Grant et al., 1973) and increased susceptibility to trypsin digestion Liu et al. (1989). Subsequently, Spoerl et al. (2004) developed the technique of cross-linking AM with 0.1% glutaraldehyde further. In force-elongation experiments on AM strips, the force of the cross-linked AM was significantly increased. Furthermore, the cross-linked AM was significantly more resistant to digestion in a solution of 0.1% collagenase. Hyperdry AM cross-linked with 0.1% glutaraldehyde is currently

used clinically in some centres, for example in the treatment of corneal perforations (Kitagawa et al., 2011). However, glutaraldehyde may cause calcification on the ocular surface (Wilshaw et al., 2008), prompting a search for alternative methods. Kumar et al. (2003) used chitosan to cross-link AM-derived collagen scaffolds, finding increased thermodynamic stability in the cross-linked tissue. Recent developments include the treatment of whole AM with EDC, which is non-toxic (Ma et al., 2010), and with microbial TG (Chau et al., 2012). Collagen hydrogels have been successfully cross-linked with 0.1% riboflavin and UVA irradiation (frequency 370 nm) (Ahearne et al., 2008), suggesting that it might also be a useful technique for cross-linking AM.

4.2.5.1 Assessment of cross-linking

A number of methods are available to determine the effects and extent of cross-linking of AM. Measurements of the effects of cross-linking include stress-strain measurements and assays of enzymatic digestion Spoerl et al. (2004). In polymers, stiffness increases in direct proportion with the number of cross-links. In the rabbit cornea, cross-linking changes the diameter and interfibrillar distance (IFD) of the collagen fibres (Wollensak et al., 2004). One elaborate method of analysing cross-links in tissue combines ion-trap mass spectrometry (MS) with peptide-specific antibodies against specific collagen cross-linking domains (Eyre et al., 2008). Most techniques are more accessible, but less specific. In a study of corneal collagen cross-linking, Wollensak and Redl (2008) used gel electrophoretic methods to confirm the presence of a very high molecular weight protein, which they assumed to be a cross-linked polymer of Type I collagen. Mature human AM collagen molecules are trimeric, containing two α_1 chains of 139 kDa and an α_2 chain of 129 kDa. Monomeric (α), dimeric (β) and trimeric (γ) bands can be resolved by gel electrophoresis of AM-derived collagen (Spira et al., 1994).

While it is unclear whether cross-linking of AM collagen can modify the gel electrophoretic pattern, it is known to result in the uptake of amino side-chains (Ma et al., 2010). Colorimetric assays, such as the ninhydrin assay, can determine the proportion of free amino groups as an inverse marker of cross-linking.

4.3 Materials and methods

4.3.1 Imaging studies

4.3.1.1 Transparency assay

A transparency assay was modified from the methods used by Ma et al. (2010) and Chau et al. (2012). Samples of 0%, 5% and 10% v-d AM were photographed with a compact digital camera (Praktika DCZ, Pentacon, Dresden, Germany) against printed material and against a dark, granulated background.

4.3.1.2 Electron microscopy

AM samples were cut to the required size after discussion with the microscopy staff at the Department of Histopathology, who supplied the fixatives. Samples of fresh, f-t and v-d AM were submitted for further processing as described below. For imaging studies of the intact AM, SEM and TEM photographs were taken of fresh, f-t and v-d AM. For imaging of the BM, the epithelium was first removed by the thermolysin method as described previously.

The AM was fixed and processed before proceeding to SEM or TEM. First, 0.5 mL of stock 25% glutaraldehyde solution, stored at 4°C, was mixed with 4.5 mL of sodium cacodylate buffer. Tissue samples, 1 cm × 1 cm, were dropped into the 2.5% glutaraldehyde:cacodylate solution and stored at 4°C

for 24 hr prior to further processing.

4.3.1.3 Sample processing¹

The samples were washed in 0.1M sodium cacodylate buffer and then post-fixed in 1% osmium tetroxide for 2 hr. They were then washed in distilled water and dehydrated in a series of ascending grades of alcohol to three changes of absolute alcohol. For SEM, the samples were dried to a critical point drying with a Tousimis® (Virginia, USA) Samdri®-PVT-3 dryer. The samples were mounted onto aluminium stubs and sputter-coated with gold (Balzer Union SCD030 sputter coater, Leica, Wetzlar, Germany). For TEM, fixed samples were washed $\times 2$ in 100% acetone before being embedded in an epoxy resin (TAAB Laboratories Equipment Limited, Berkshire, UK). Polymerisation was achieved by heating to 65°C for 16 hr. The polymerised blocks were cut into 0.5 μm sections on a Reichert Ultracut E microtome. Following staining with 1% toluidine blue in 1% borax, they were examined by light microscopy. Areas selected for ultramicrotomy were sectioned to 80 nm. The ultramicrotome sections were mounted on copper grids and stained with saturated uranyl acetate in 50% ethanol. This was followed by Reynolds lead citrate staining.

4.3.1.4 Scanning electron microscopy

A JEOL JSM840A scanning electron microscope (JEOL UK Ltd., Welwyn Garden City) and iScan™ software were used to produce digital images of the samples. The JEOL 840 Instructions booklet were referred to for detailed instructions on photography. The specimen was obtained fixed to a brass carrier (stub). Sample stubs were fastened in the brass insert holder with small set screws, so that the specimen was in the same plane as the rims of the holder. The holder was mounted in a brass carrier and fixed

¹Sample processing for SEM and TEM was carried out by Mr Trevor Gray of the Department of Histopathology.

with the set screw. The specimen carrier was screwed onto an exchange rod with a plexiglass block. The carrier and rod assembly were placed in position in the exchange chamber. The plexiglass block was held flat against the chamber seal and a red vacuum operation button was pressed once. When vacuum was achieved, the red light went out (~55 secs). At this point, the specimen exchange chamber isolating valve was opened. The specimen was inserted onto a dovetailed stage. The exchange rod was unscrewed and carefully withdrawn. The specimen chamber isolating valve was closed. The red vacuum operation button was pressed to release the vacuum and dislodge the exchange rod. The current meter was lit with contrast and brightness turned fully counterclockwise. The specimen working distance was adjusted to 10-12 mm. The detector (Secondary Electron Imaging) and accelerating voltage switches were turned on. Coarse focus was adjusted to bring the specimen into view. The current meter was lit, and the probe current was set at 10^{-10} Amps. Brightness was gradually increased until a line was visible on the cathode ray tube. The filament knob was slowly turned clockwise and the line scan profile was sharpened with fine focus, keeping the beam current was kept at $< 100 \mu\text{A}$. A small round feature was selected for viewing. The X and Y stigmators were rotated to achieve maximum clarity. This was repeated several times until there was no blurring. The Digital Scan Generator was turned on and the iScanTM software was launched. Image brightness and contrast were adjusted to obtain an adequate dynamic range, which varied with scan time. Micrographs were taken of the epithelial surface and the loose collagenous layer on the underside at various magnifications (from $\times 1000$ to $\times 20\,000$). Defects in the AM samples were examined for imaging of the compact collagenous and BM layers. *En face*, oblique and cross-sectional images of the AM specimens were sought. The image was captured after the scan, and photographs were saved as .tif files.

4.3.1.5 Degradation assay

An accelerated degradation assay was performed to compare fresh, f-t and v-d AM. This was carried out in duplicate. Samples of the different preparations were punched out of the tissue with a 6 mm skin biopsy punch (GlaxoSmithKline GmbH & Co., Bad Oldesloe, Germany) and placed into 8 mm wells in multiwell culture plates (Sigma-Aldrich, UK) in 100 μ L of medium. The test medium consisted of DMEM and keratocyte supernatant culture medium² in a 2:1 ratio with 0.01 mg/mL of lyophilised collagenase extracted from *Clostridium Histolyticum* (Cat. No. 17018-029, Gibco®, UK). This collagenase is specific for the neutral amino acid-glycine bonds in collagen and can degrade triple helical collagen. 0.1 mg of collagenase (25 U) were added to 10 mL of medium. The control medium consisted of DMEM. The AM samples were incubated in 5% CO₂ at 37°C for 72 hrs and then frozen at -80°C. Next, they were freeze-dried overnight. The lyophilised tissues were processed for SEM without fixative, and photographed for comparison. The degradation assay was a basic qualitative test of the different preparations, and no outcome measure was decided beforehand.

4.3.1.6 Transmission electron microscopy

A JEOL JEM1010 transmission electron microscope (JEOL UK Ltd.) was used to view the sections. Digital images were captured with a SIS MegaView III charge-coupled device camera (Olympus Soft Imaging Solutions, Lakewood, CO, USA) system. The specimen holder was by pulled out and turned counterclockwise. It was pulled slowly against the vacuum. The specimen clamps on the specimen holder were opened with forceps. The copper grids containing the specimens were placed between the clamps. The specimen holder was then pushed in for the green vacuum light to go on. After the light went off (~40 secs), the holder was turned clockwise and gently eased

²Courtesy of Dr Khurram Hashmani.

with the vacuum into position. The beam current was switched on with the high tension button (to about 80 kV), and brightness and contrast were adjusted. The image was focused by bringing a small focus screen into view and using a wobbler image shift system for coarse and fine focus. The illumination was centred by bringing the illumination to a small spot and using X and Y shift. The microscope and camera were linked, and the software was launched. Magnification was set to $\times 10\,000$ and a continuous image of a selected sample area was obtained. Focus was adjusted with the microscope focus knobs. The 'Start Acquire' button was pressed to record images, which were saved as .tif files.

4.3.1.7 Atomic force microscopy³

A Digital Instruments Nanoscope IIIa D3000™ scanning probe microscope (Bruker AXS Corporation, Santa Barbara, CA) was used to compare the topography of stromal and epithelial surfaces of AM samples, with and without trehalose pre-treatment. A piece of double-sided adhesive tape was placed onto a 1.5 cm diameter steel disk. A square of v-d AM of approximately 1.0 cm \times 1.0 cm was placed gently on top of the double-sided adhesive tape, taking care to lay the sample flat with a minimum of folds or creases. Another square from the same sample of amnion was inverted and similarly laid onto another steel disc with double-sided tape to present the opposite face of the same membrane. The disc was then attached magnetically to a sample stage of the microscope. The samples were imaged in air using the Tapping Mode™. Images were acquired with a silicone probe (RTESP; Veeco Digital Instruments, Santa Barbara, CA) of inverse pyramidal shape (effective sphere radius 2 nm and effective half-cone angle 19°) at the resonant frequency of the AFM cantilever of approximately 300 kHz. The cantilever spring constant had a nominal value of 30 Nm⁻¹, provided by

³This work was carried out in collaboration with Dr Chen Xinyong of the School of Pharmacy at the University of Nottingham.

the manufacturer. Flat areas of tissue, 10 μm by 10 μm , were selected for scanning. Each sample was scanned in triplicate. The scan rate was 1 Hz, and images were acquired across 512×512 points.

4.3.2 Optical microscopy

Optical microscopy was performed on four samples each of f-t AM and v-d AM for thickness measurements. In addition, samples were stained with haematoxylin and eosin for visual comparison.

4.3.2.1 Embedding of AM samples

Aluminium foil cups, 1 cm in diameter and 3 cm deep, were fashioned and filled with optimal cutting temperature (OCT) embedding medium (Jung Tissue Freezing Medium, Sigma-Aldrich, Missouri, USA). The cups were lowered into 100 mL beakers containing 5 mL of isopentane, overlying a liquid N_2 bath, for a few seconds until the OCT began to harden. Strips of AM of approximately 10×30 mm were laid flat onto a sticky plastic backing, or wrapped around a frozen OCT core, to ensure correct orientation of the tissue, and placed into the cups. These were vapour-frozen in a beaker that until the strips solidified completely. They were stored at -80°C .

4.3.2.2 Slide preparation

SuperFrost slides (LSL, Rochdale, UK) were placed in racks and washed in 100% acetone for 1 min. They were then placed in 300 mL acetone containing 2% 3-aminopropyltriethoxysilane (APES, Sigma-Aldrich), washed in distilled water and left to dry in a fume-hood overnight, before being stored in their original packaging in a dark environment.

4.3.2.3 Cryostat sectioning

The Leica CM1900 Rapid Sectioning Cryostat was switched on with a temperature setting of -25°C and cleaned with 100% ethanol. The cryostat heads were cleaned with acetone. The solid media pellets were mounted onto the cryostat sectioning chuck using OCT as glue. The cryostat section thickness was set at 6 µm. Samples were advanced and sectioned onto APES-coated slides for staining or thickness measurements.

4.3.2.4 Thickness measurement

Mounted AM strips were viewed under a Leica DB4000B light microscope equipped with digital capture. Samples were photographed, and areas of AM that were free of folds were selected for measurement. Analysis was performed with Openlab software (PerkinElmer, USA). Measurements were made by placing the cursor on BM and dragging it to the stromal edge. The computer software returned distance values for the linear measurements. Three to nine measurements were made for each strip, and the mean thicknesses of f-t and v-d AM were compared.

4.3.2.5 Haematoxylin and Eosin staining

Slides with tissue sections were placed in trays and immersed in 3% v/v acetic alcohol before being washed in Tris-buffered saline (TBS), pH 7.6, for 1 min. They were then stained in haematoxylin for 1 - 2 mins in the fume hood and washed in gently running tap water until they lost their purple colour. They were then immersed in Scott's Tap water for 1 min, washed in distilled water and placed in eosin Y for 1 min for the sections to retain pink colour. The slides were washed under tap water. A drop of warmed Glycergel® mounting medium (Dako Ltd., Ely, UK) was gently placed on the tissue section, and a coverslip placed over the slides, which were allowed to dry.

4.3.3 Uniaxial testing

Fresh, f-t and 0% v-d AM samples from a total of 19 donors were subjected to uniaxial testing. Samples were obtained from one, two or all three preparation methods for each donor. Between one and ten samples were tested for each preparation method. Samples of AM were tested using the Heavy Duty Texture Analyser (TA.HD*plus*) from Stable Micro Systems Ltd. (Surrey, UK). The samples were tested after obtaining fresh AM, after 30 mins thawing of frozen AM or after reconstitution of dried AM in water. All v-d samples were rehydrated for 5 mins in DI H₂O just before the uniaxial tests.

A 10 mm by 30 mm template was drawn onto the surface of a 9 cm diameter PTFE disc with indelible ink (figure 4.4 A). A 90 mm Petri dish lid (Sterilin, UK) was placed on the PTFE base to provide a hard, disposable surface for cutting AM samples. A layer of Parafilm® was stretched over the Petri dish as a scaffold for the AM. Each AM sample was laid out directly onto the Parafilm®. Next, the AM could be cut directly over the visible template drawing to the specified dimensions. A No. 22 Carbon Steel Swann-Morton scalpel blade was used to cut 10 mm by 30 mm AM strips by rolling (not dragging) the curved edge of the blade to avoid feathering of the edges (figure 4.4 B). Digital micrometry was performed with a low-force digital micrometer with resolution of 1 µm (Mitutoyo UK Ltd., Coventry, UK). Next, the AM strips were placed onto slightly larger split cards of similar dimensions (cut from microplate sealer tape), and the Parafilm® was peeled off. The horizontal split, two thirds the way down the card, served to allow mounting of the sample (figure 4.4 C). The AM was gently unfolded with forceps on the card for correct alignment and to eliminate any folds, taking care not to introduce holes. The AM-split card bilayer strips were then mounted at 90° between the gnarled mini-tensile grips (Stable Micro Systems). The top grip was finger-tightened first, clamping 5 mm of AM-card with the split downwards (figure 4.4 D). Next, the bottom grip was tightened

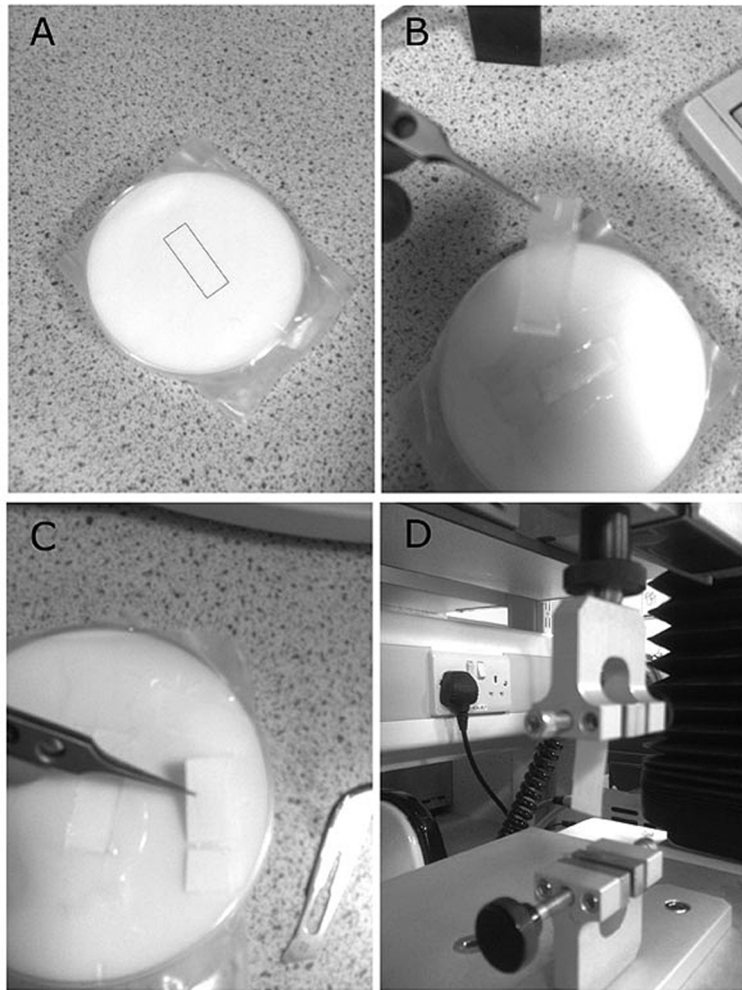


Figure 4.4: Uniaxial testing of AM strips

AM strips were cut to a 10 mm × 30 mm template (A) with Parafilm® backing (B). This enabled the AM strip to be mounted onto split card (C), which was then clamped between mini-grips (D) for uniaxial testing.

with the bottom 5 mm of AM-card in place.

The TA.HD*plus* was calibrated before every batch of tests. A load cell of 5 kg was used. The vertical height difference between the grips was standardised in order to achieve an exposed product height of 20 mm. The tests were run at 100 mm min⁻¹, which gives a strain rate, defined as the rate of change of length divided by the original length, of 0.083 s⁻¹. The test was run for a set distance of 20 mm. Force-distance curves were generated with these parameters. The inclusion of a cross-sectional area permitted stress-strain curves to be generated. The traces were processed using an integrated 32-bit Exponent software package, which permitted the data to be exported in Microsoft Excel files. A total of 208 traces were obtained for 95 fresh AM, 55 f-t and 58 v-d AM samples.

4.3.3.1 Data synthesis

Uniaxial tests were performed on 208 samples of fresh (n = 95), f-t (n = 55) and v-d (n = 58) AM from a total of 19 donors. The range of traces obtained per donor ranged from 1 to 28. Data from four donors was obtained across all three preparation methods, data from three donors was obtained across three methods and data from 12 donors was obtained for just one method. The uniaxial tests gave data on UTS (in N) and the change in length, ΔL (mm), for force-distance analysis. The values of nominal stress at failure (σ_f^N) and true stress at failure (σ_f^T) (in MPa) were obtained once the cross-sectional area (mm²) was known. The strain at failure, ε_f , was calculated from ΔL and expressed as a percentage. These data permitted conversion of the force-distance curves into stress-strain curves. A pseudolinear modulus, E_1 , was calculated as the tangent of the stress-strain curves between 0.495 and 5 % strain (in MPa). A second pseudolinear modulus, E_2 , was calculated as the tangent of the stress-strain curves between 90 and 100% strain. Toughness (T), measured in Joules (J) per mm³, was obtained by

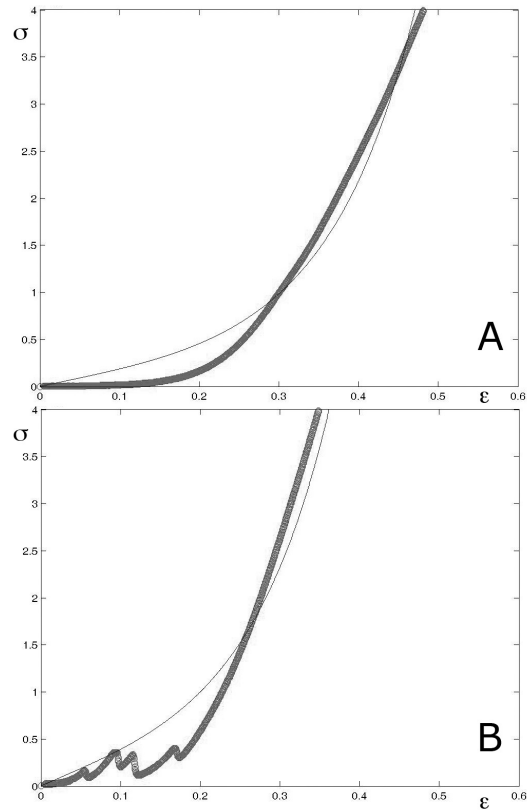


Figure 4.5: Uniaxial test data filtration

*Stress-strain curves obtained from uniaxial tests were filtered by visual inspection (two examples of 208 shown). Stress measurements were plotted on the X axis in MPa. Strain is plotted as a decimal fraction on the Y axis. The thick line represents experimental data. The thin line represents a modelled curve. The experimental curve in **A** is smooth and was retained for further analysis. The curve in **B** was classified as non-smooth and was eliminated from the analysis.*

integrating the area under the stress-strain curves.

4.3.3.2 Data filtering

For all stress-strain curves, the data points between 0% and 0.495% strain were deleted to eliminate noise caused at the start of the test. Data filtering was conducted by screening each stress-strain curve by visual inspection and by eliminating all non-smooth curves from the analysis. Examples of smooth and non-smooth curves obtained from experimental data are shown below (figure 4.5, thick lines). The experimental curves are shown alongside mathematically modelled curves of the data (thin lines; see below). Solitary and minor inflections in curve smoothness were tolerated. The curves

were filtered with no reference to the preparation method. The proportion of traces that were eliminated and the RR of a trace being non-smooth were calculated for each preparation category as an index of the quality of the samples.

4.3.3.3 Mathematical modelling

A mathematical model (Equation 4.4) was used to describe the mechanical behaviour of the AM samples. The parameters G' and d were derived from the experimental data by specialist mathematical computer software (MATLAB, MathWorks, Ma, USA).

Equation 4.1 was adapted by introducing a new parameter d :

$$d = \frac{qE_1}{3\mu_0} \quad (4.3)$$

Since $\varepsilon = \lambda_1 - 1$ and $E = 3G$,

$$\sigma^N = G' \exp^{d(\lambda_1^2 + \frac{2}{\lambda_1} - 3)} \left(\lambda_1 - \frac{1}{\lambda_1^2} \right) \quad (4.4)$$

As it is applied to the exponential, d is dimensionless. Since $\sigma^T = \lambda_1 \sigma^N$, experimental data for σ_f^T and λ_1 at failure were used to generate the values of G' and d by equation 4.4 for each set of stress-strain data of AM undergoing uniaxial deformation. The filtered stress-strain data from the uniaxial tests were obtained in Microsoft Excel spreadsheets and processed using MATLAB⁴. This was programmed to optimise the closest possible fit to the experimental curves by using Equation 4.4, simultaneously generating values of G' and d . To illustrate the effects of change in the values of d and G' , simulated curves have been plotted of σ^N against λ_1 (figure 4.6). Increasing the value of d while G' is kept constant does not affect the gra-

⁴This work was carried out in collaboration with Dr Davide De Focatiis, of the School of Chemistry in the University of Nottingham.

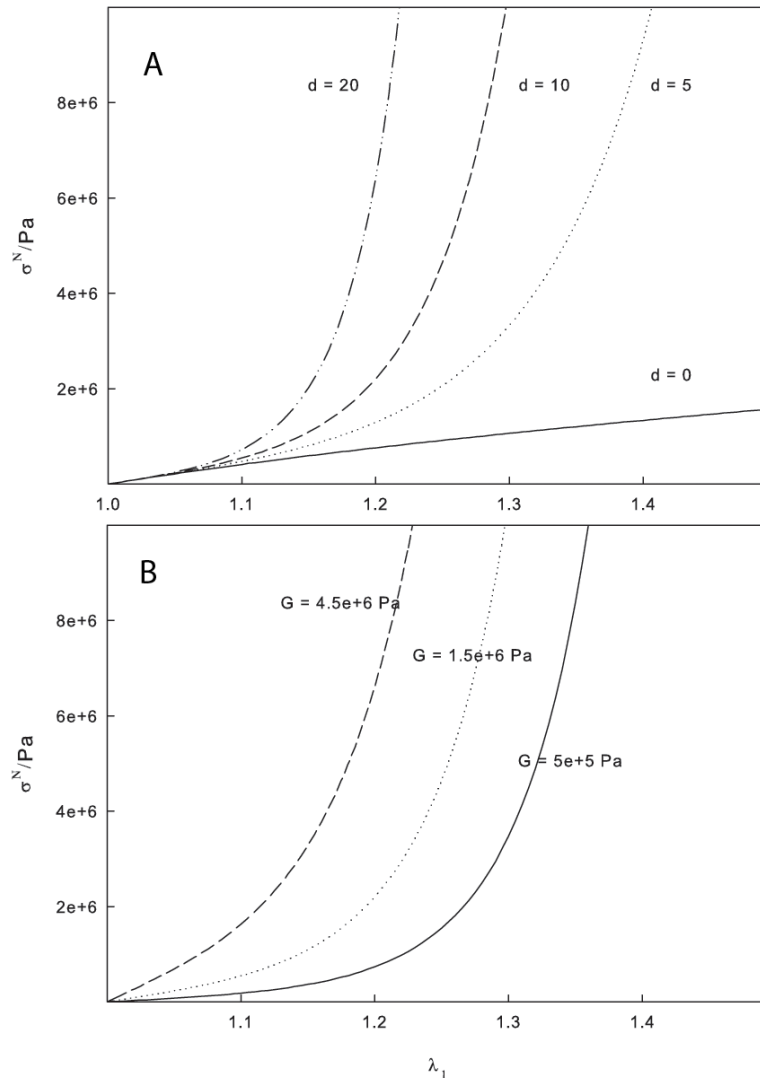


Figure 4.6: Nominal stress versus stretch ratio

A mathematical model was proposed to describe the stress-strain characteristics of AM (Equation 4.4). The value of the storage modulus G' was calculated by using data between 0.495 and 100% strain. Together with a dimensionless parameter d , this was used to model the tissue behaviour. **A** Curves illustrating the effects of changing the value of d are shown. G' is constant (1.5×10^6 Pa). As d increases, the initial gradient is unchanged. At higher strains, the gradient increases, except in the special case of $d = 0$. **B** The effects of changing the value of G' at constant d are shown ($d = 10$). As G' increases, the initial gradient increases. At higher strains, the gradient approaches constancy. σ^N , nominal stress (MPa); λ_1 , ratio of final length to original length.

dient at low strain, yet it causes the pre-terminal gradient (equivalent to a high strain modulus) to increase. At a value of $d = 0$, the curve represents the case of Gaussian elasticity. Conversely, increasing G' with a constant d increases the initial gradient (equivalent to a low strain modulus), while the pre-terminal gradient remains constant.

Three separate fittings were made using the mathematical model and the experimental data. For the first fitting, a value of G' were obtained by using the experimental data from the whole curve between 0.495 and 100% strain. G' and d were obtained simultaneously by searching for the pair of values that minimise the error over the whole curve. The error is defined as the square root of the sum of the difference between the measured stresses and the stresses computed from the model. This was calculated using the equation

$$RMS = \sqrt{\frac{1}{n} \sum_{i=1}^n (\sigma_{i,model}^N - \sigma_{i,experimental}^N)^2} \quad (4.5)$$

where n is the number of data points and i represents each data point. The errors were normalised to the number of data points, n . Two examples of model curves of σ^N versus λ_1 plotted alongside experimental data from two uniaxial tensile tests are shown in figures 4.7 A and B. The model and experimental curves in figure 4.7 A demonstrate a close fit, with a RMS of 7.49 kPa, while figure 4.7 B demonstrates a poor fit, with a corresponding RMS of 11.90 kPa.

For the second fitting, the value of G' (designated G'_2) was determined from the initial gradient between strain levels of 0.495% and 5%. A new value of d (designated d_2) was then obtained by searching for the value which minimises the error, based on the initial modulus. All the modelled curves were plotted alongside the experimental curves. The closeness of the optimised fit was indicated by the RMS error (RMS₂).

For the third fitting, a third parameter was introduced. To compensate

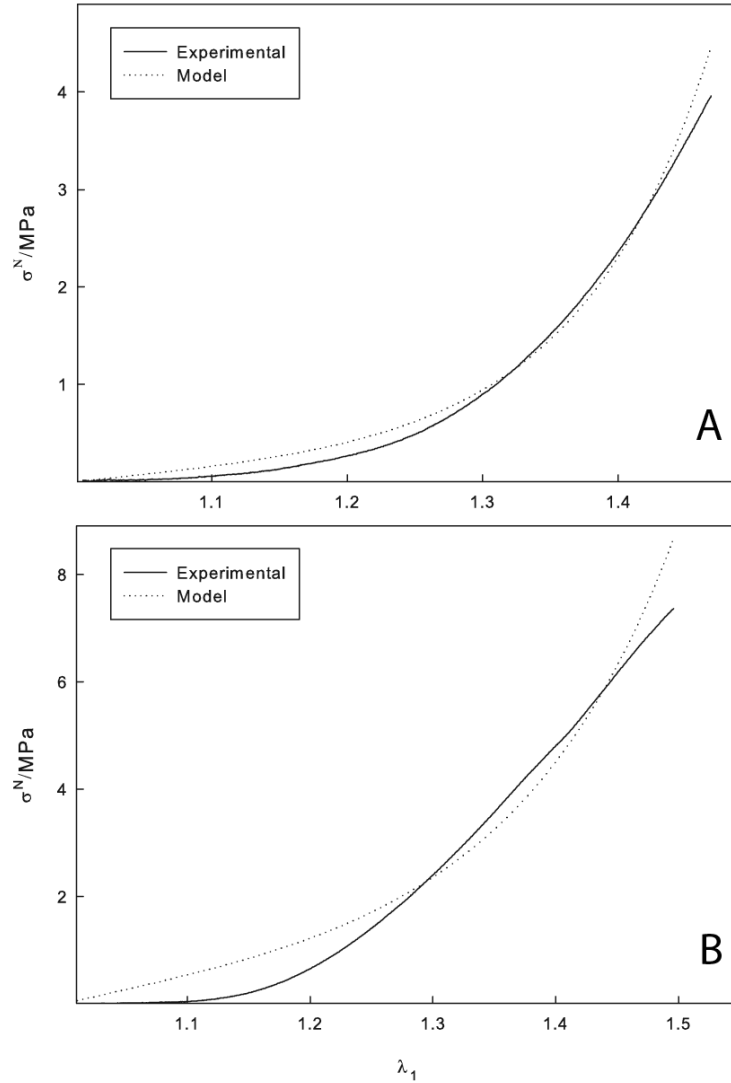


Figure 4.7: Experimental and model curves

A mathematical model was used to describe the stress-strain characteristics of AM (Equation 4.4). In the fitting shown, the storage modulus G' was obtained between 0.495 and 100% strain. The closeness of fit of the model is described by the root mean squared of the error (RMS). A close fit of model and experimental curves is shown (**A**, RMS = 7.49 kPa). The model and experimental curves in **B** demonstrate a less close fit (RMS = 11.90 kPa). σ^N , nominal stress (MPa); λ_1 , ratio of final length to original length.

for the amount of slack or tension in each sample at the start of testing, λ_1 was adjusted by varying the starting point. Thus, the model simultaneously searched for a triplet of values that minimise the error (RMS_3) over the whole curve: G'_3 , d_3 and λ_1 .

4.3.3.4 Statistical analysis

The effects of method of AM preparation and AM donor on the dependent variables were assessed. All statistical analysis was carried out using statistical software (SPSS®, version 20, IBM Corporation, New York, USA). Detailed instructions for using SPSS® (Pallant, 2007) were followed. Where possible, normally distributed data were analysed by parametric tests, including general linear models such as univariate and multivariate analyses of variance (ANOVA). Univariate tests of normality were used to explore the distribution of the data for each dependent variable. Normality was assessed by comparing the 5% trimmed mean to the actual mean, by checking the kurtosis and skewness values (< 1) and the Kolmogorov-Smirnov statistic ($> .05$) and by assessing normal Q-Q and detrended normal Q-Q plots and histograms. Outliers were identified by boxplot analyses. Data values of more than three times the *SD* were considered to be extreme outliers. Main effects of independent variables were only interpreted if no significant interaction effects were identified.

Multivariate analysis of normality of distribution were conducted by linear regression. Scatter plot matrices were generated to check for linearity. Further tests were carried out to assess the assumption of homogeneity of variance-covariance matrices (Box's Test) and the assumption of equality of variance (Levene's Test). The presence of outliers was assessed by generating Mahalanobis distances and checking them against critical values. Tests of correlation between dependent variables (Pearson correlation coefficient, r) were performed, using Cohen's guidelines to classify the strength of

the correlation (Pallant, 2007). Post-hoc comparisons were made using the Tukey Honestly Significant Difference (HSD) test. Non-Gaussian data were transformed either by removing a small number of outliers or by logarithmic conversion of the data. If the data could not be transformed, non-parametric tests were carried out. For non-parametric testing of independent samples, the Kruskal-Wallis test was used. Post-hoc tests (Mann Whitney U test) were conducted to confirm or reject statistically significant findings. To interpret the strength of the different effect sizes, Cohen's guidelines were used: .01 was considered small, .06, medium and .138, large (Cohen, 1988).

4.3.4 Non-destructive tests

4.3.4.1 Acoustic impedance⁵

A Love wave surface acoustic device was used to probe the mechanical properties of AM through determination of the sample shear storage modulus (G') and the loss modulus (G''). Four different membrane compositions were studied: fresh AM, f-t AM, rehydrated v-d and thermolysin-denuded, with three separate sections of the membrane being studied in each case and the measurements. Samples of the AM preparations, about 2-3 mm in length, were placed across a sensor with two delay lines, one of which acted as a reference signal. Waves were transmitted across transducers separated by a path 6 mm in length at an operating frequency of 118 MHz. A control unit provided power to the device and an oscilloscope was used to detect the received signals. First, a measurement of the received signal with the device unloaded was made as a reference. Next a small square of the membrane was placed on the device covering the path between the two transducers. The received signal was then measured. The received signals were digitised and analysed using MATLAB software (The MathWorks Ltd., Cambridge,

⁵This work was carried out in co-operation with Dr Melissa Mathers of the Centre for Biomolecular Sciences in the University of Nottingham.

UK). From a determination of the change in the propagation constant (γ), material properties were calculated from the following equation for G' and G'' :

$$\frac{\Delta\gamma}{\beta} = \frac{\Delta\alpha}{\beta} + i\frac{\Delta\beta}{\beta} = \sqrt[s]{(G' + iG'')\rho\left(1 - \frac{G' + iG''}{\rho v^2}\right)} \quad (4.6)$$

where α is attenuation, β is the unperturbed wavenumber, s is the device sensitivity, ρ is the sample density and v is the Love wave phase velocity. The measurements were carried out in quadruplicate, although not all measurements were successful. The means and SD were obtained and plotted for each AM category.

4.3.4.2 Nanoindentation

Nanoindentation was performed to compare the surface properties of 0% and 10% v-d AM. Samples were mounted on steel discs in the Digital Instruments Nanoscope IIIa D3000™ as described previously for AFM scanning. Force measurements were conducted in static force spectroscopy mode. Measurements on one AM were conducted using bare tips with an effective spherical radius of 2 and 15 nm. A second AM was tested using tips attached with glass spheres of radius of 5 and 15 μm . The surface of both aspects of the membrane were examined. Between 24 and 127 force measurements were performed on each area. Data was obtained on force and relative displacement. An Oliver-Pharr analysis was also conducted to assess the modulus of the retraction curve and contact hardness.⁶ Information on plasticity, adhesion and dissipation was acquired from the DMT model.

4.3.5 Cross-linking study

Fresh AM samples were treated with ultraviolet A (UVA)/riboflavin to cross-link the collagen matrix. The extent of cross-linking was analysed by gel electrophoresis, MS and western blotting of the purified collagen, tensile

⁶Conducted with the help of Professor Chen Xinyong.

testing and mathematical modelling, IFD measurement in TEM images and the ninhydrin assay.

4.3.5.1 Ultraviolet irradiation

AM was harvested and prepared in the usual way and treated with thermolysin (12.5 mg in 100 mL PBS) in the usual way. 0.1% riboflavin-5-phosphate solution (Sigma-Aldrich, St. Louis, MO, USA) was prepared using deionised (DI) H₂O (100 mg in 100 mL). AM was soaked for 30 mins in 25 mL of riboflavin solution in Petri dish lids. Next, six long UVA fluorescent tubes with a peak wavelength of 365 nm were used as a source of unfocused UVA irradiation (Fluo-Link TFL-312, Vilber Lourmat, Marne la Vallée, France) placed 4 cm above the AM in Petri dishes for 30 mins. Irradiance was approximately 16 mW/cm².

4.3.6 Analysis of cross-linking

4.3.6.1 Extraction of type I collagen

The method used is a modification of the one described by Spoerl et al. (2004). Irradiated and non-irradiated AM samples were ground in liquid N₂ and the extracts were placed in 50 mL 0.1 M Na acetate on a rocker overnight at 4°C to dissolve proteoglycans. The suspension was centrifuged at 4°C for 30 mins at 4000 × *g*, and the pellet re-suspended in 35 mL of 0.5 M acetic acid containing 2 mg pepsin per mL. This was left overnight at 4°C to digest the N- and C- telopeptides containing natural cross-links. After centrifugation at 4°C at 4000 × *g*, the supernatant was neutralised to pH 7.0 – 8.0 with NaOH at room temperature. The new pellet, containing insoluble collagen, was discarded. The supernatant was dialysed overnight (Spectra/Por® 6 Dialysis Membrane, Spectrum Laboratories Inc., CA, USA) against 15 L of 2.5 M NaCl in 0.5 M acetic acid to precipitate the solu-

bilised type I collagen. This was then centrifuged for 30 mins at 4°C and re-suspended in 0.5 mL 0.1 M acetic acid. The new suspension was dialysed overnight against 15 L 0.1 M acetic acid to remove residual salt.

4.3.6.2 Protein purification

The 2-D Clean-Up kit (Amersham Biosciences) was used to purify proteins for electrophoresis. A volume of 100 µL of sample was placed in a 1.5 mL Eppendorf tube. 300 µL of precipitant was added, and the mixture vortexed briefly and incubated on ice for 15 mins. Next, a co-precipitant was added, the mixture vortexed and centrifuged for 5 mins at 4°C at $15\,000 \times g$. The supernatant was discarded and 40 µL of co-precipitant placed on the pellet, on ice for 5 mins. After centrifugation, the pellet was re-suspended in 25 µL DI H₂O. One mL of wash buffer pre-chilled at -20°C for 1 hr, and 5 µL wash additive, were added. The mixture was vortexed extensively between incubation periods at -20°C. After 5 mins centrifugation, the supernatant was discarded.

4.3.6.3 Protein quantification

The 2D Quant kit (GE Healthcare Life Sciences, Amersham, UK) was the preferred means of measuring the quantity of protein in solution. The manufacturer's instructions were followed. Briefly, a standard curve was prepared using incremental quantities of 2 mg/mL bovine serum albumin (BSA) in 1.5 mL Eppendorf tubes. A volume of 1 - 50 µL of each sample to be assayed was pipetted into separate Eppendorfs (depending on the expected protein concentration). A volume of 500 µL of precipitant was added to the tubes, which were vortexed briefly. A volume of 500 µL of co-precipitant was added, and the tubes inverted before centrifugation at $10\,000 \times g$ for 5 mins. The supernatants were removed completely using a micropipette. A volume of 500 µl of 20% copper solution in DI H₂O was added to the pellets, followed

by 1 mL of working colour reagent. The samples were incubated for 15 - 20 mins. Absorbance was read at 490 nm, and compared to the BSA standard curve using Softmax® software (MDS Analytical technologies, Toronto, Canada). Protein quantification was carried out as described, and samples were concentrated if necessary using spin columns with a 3 kDa molecular weight cut-off (MWCO) to achieve protein concentrations of 1 - 2 µg/µL.

4.3.6.4 Gel electrophoresis

The pellet was re-suspended in 15 µL of sample buffer made up of 20 parts 1 × lithium dodecyl sulfate (LDS) to 1 part dithiothreitol (DTT). Samples were heated to 70°C for 10 mins before being loaded onto a 3-8% Tris-Acetate gel (NuPAGE® Novex®, Invitrogen). Buffer chambers were loaded with Tris-Acetate SDS Running Buffer (NuPAGE®) and 500 µL antioxidant loaded in the upper chamber. The HiMark™ Unstained Standard (Novex®, Invitrogen), consisting of nine proteins, was used as a high molecular weight marker. Samples were run for 60 mins at 150V. Gels were then washed three times in DI H₂O and stained for 3 hrs in SimplyBlue™ SafeStain Coomassie® G-250 stain. De-staining was carried out in DI H₂O overnight, prior to scanning.

4.3.7 Mass spectrometry

The bands were removed from the gels with a Swann-Norton No. 22 blade and placed in 1.5 mL Eppendorf tubes in DI H₂O. A strict no-touch technique was used to avoid contaminating the bands with keratin. The tubes were sent to the School of Biosciences at the University of Nottingham for mass spectrometry.⁷

The gel bands were cut into smaller pieces and placed into a 96-well microtitre plate for destaining, reduction and alkylation on a MassPREP

⁷Courtesy of Dr Susan Liddell.

robotic liquid handling station (Waters Corporation, Milford, MA, USA). The bands were incubated in 100 μL of de-stain solution (50 mM ammonium bicarbonate, 50% acetonitrile) for 10 mins \times 3 at 40°C. Following removal of the final aliquot, the samples were dehydrated by incubation at 40°C in 50 μL of acetonitrile for 5 mins. The acetonitrile was removed and evaporation allowed to proceed for 10 mins. The samples were reduced by incubation in 50 μL of reducing solution containing 10 mM DTT and 100 mM ammonium bicarbonate for 30 mins at 40°C. Following removal of the reducing solution, the samples were incubated in 50 μL of alkylation solution (55 mM iodoacetamide, 100 mM ammonium bicarbonate) for 20 mins at 40°C. The gel pieces were then washed at 40°C in 50 μL of 100 mM ammonium bicarbonate for 10 mins and 50 μL of acetonitrile for 5 mins. They were then dehydrated by double 40°C washes in 50 μL of acetonitrile for 5 mins and allowed to evaporate for 5 mins. The microtitre plate containing the gel slices was cooled to 6°C for 10 mins before addition of 30 μL per well of trypsin gold (Promega), diluted to 10 ng μL^{-1} in 50 mM ammonium bicarbonate. The plate was incubated at 6°C for a further 20 mins to permit trypsin to infiltrate the gel plugs with minimal protein autocatalysis. A further incubation proceeded for 4 hrs at 37°C. The samples were stored at 4°C until MS analysis.

The extracted peptides were delivered via a nanoscale LC system to a Q-ToF™ 2 mass spectrometer (Waters®). The peptides were separated using a 15 cm PepMap C18 reversed phase column with an inner diameter of 75 μm (LC Packings, Sunnyvale, CA) on a CapLC system (Waters®). This was attached to a Q-ToF™ 2 mass spectrometer equipped with a nanolock-spray source and operated with MassLynx Version 4.0 acquisition software. Selected peptides were automatically analysed by electrospray ionisation MS/MS. Tandem MS data were acquired using a data-dependent switching between MS and MS/MS scanning, based upon ion intensity, mass and

Table 4.2: Mascot Peptide Summary Report data

Mascot variable	Explanation
Protein Score	Combined scores of observed mass spectra matched to amino acid sequences
Protein sequence coverage	Percentage of database protein sequence covered by matching peptides
Matches	Number of MS/MS spectra matched to the protein

charge state. Charge state recognition was used to select doubly, triply and quadruply charged precursor peptide ions for fragmentation. Up to four precursor masses at a time were chosen for tandem MS acquisition. Collision energy was automatically adjusted between 15 and 55 eV, based on charge and mass of each precursor. ProteinLynx Global SERVER version 2.0 was used to process the uninterpreted MS data into peak list (.pkl) files.

Each MS/MS spectrum was searched ('queried') against known human sequences in the SwissProt and/or National Center for Biotechnology Information (NCBI) non-redundant databases in Mascot MS/MS Ion Search mode (www.matrixscience.com) (Perkins et al., 1999). Carbamidomethylation of cysteine and oxidation of methionine and proline were set as variable modifications. Two missed trypsin cleavages were allowed. Default search values were entered, with the exceptions of file type (Micromass pkl) and instrument type (ESI-Q-ToF™ 2). The nomenclature used was assigned by the Human Genome Organisation (HUGO) Gene Nomenclature Committee. Protein identifications were accepted only if the probability-based Molecular Weight Search (MOWSE) scores were above a threshold of $p < .05$. The percent coverage, or approximate relative abundance level of each peptide was recorded in a Peptide Summary Report. An explanation of the data from the report is summarised below (table 4.2).

4.3.8 Western blotting

4.3.8.1 Preparation of samples

The purified collagen extracts from cross-linked AM and control samples were subjected to western blotting under reducing conditions. This was performed on three AM samples. A loading buffer was prepared by mixing 4 × NuPage® LDS sample buffer (5 parts), 1.0 M DTT (1 part, made up by adding 0.154 g stock powder to 1 mL DI H₂O) and 14 parts DI H₂O. The loading buffer was added to the protein extract to obtain a protein concentration of approximately 1.0 µg/µL. The samples were denatured by heating to 95°C for 4 mins in a thermal cycler (Thermo Hybaid PCR Express Thermal Cycler, Hybaid, Hampshire, UK), and vortexed prior to loading.

4.3.8.2 Protein electrophoresis

A running buffer was prepared by diluting 20 × concentrated 2-(N-morpholino) ethanesulfonic acid (MES)/sodium dodecyl sulfate (SDS) buffer with DI H₂O. The gels used were NuPAGE® 3-8% Tris-Acetate 1.0 mm 10-well Novex gels (Cat. No. WG1601A, Invitrogen, Paisley, UK), recommended for high molecular weight proteins. The white strip and the plastic comb were removed from the gel packaging, and the gels washed in DI H₂O. One gel was loaded into the Novex II module tank, which was filled with running buffer to completely cover the wells. Next, 500 µL of NuPage® antioxidant was added to the central tank. The tank was then inserted onto the Novex PowerEase® 500 Power Supply for electrophoresis. Long tip dispensers were used to load 10 µg of protein to each well. A stained HiMark™ molecular weight marker (Invitrogen) was loaded into the first well. Electrophoresis was carried out for 35 mins at 200 mV.

4.3.8.3 Protein transfer

A transfer buffer was made up by adding 200 mL methanol to 750 mL DI H₂O and 50 mL of NuPage® Transfer Buffer (20 ×). Immobilon polyvinylidene fluoride (PVDF) membranes (Millipore, Massachusetts, USA) were soaked in methanol and then transferred to a tray containing sponges and blotting papers soaked in transfer buffer. The gel was retrieved from the casing. The blotting apparatus was assembled by sandwiching the membrane and the gel between sheets of blotting paper and sponges, keeping the combination as wet as possible with transfer buffer. The blotting apparatus was loaded into the tank and topped up. The running time was 1 hr at 30 V. The membrane was washed and transferred to a tray containing TBS-TM blocking buffer (5% non-fat dry milk in TBS containing 0.1% Tween 20) for 1 hr on a rocker.

4.3.8.4 Incubation with primary antibody

A rabbit anti-human antibody (Ab34710, Abcam®, Cambridge, UK) was used as a primary antibody against the type I collagen at a concentration of 1:5000. The membranes were then transferred into trays containing 10 mL of primary antibody in TBS-TM. The trays were left on a rocker at room temperature for 4 hrs.

4.3.8.5 Detection of protein bands

The membranes were washed in TBS containing 0.1% Tween 20 (TBST) for 15 mins, followed by three quick washes. An alkaline phosphatase (AP)-conjugated donkey anti-rabbit secondary antibody (Cat. No. 31345, Pierce, Rockford, IL, USA) was added for 1 hr (1:20 000 dilution in antibody buffer), followed by a 15 min wash and three washes for 5 mins each in TBST. A substrate solution of 5-Bromo-4-chloro-3-indolyl phosphate/Nitro blue tetrazolium chloride (BCIP/NBT purple liquid substrate, Sigma) was added for 5

- 10 mins until the protein bands began to appear. The reaction was stopped by washing the blots in DI H₂O before air-drying.

4.3.9 Analysis of cross-linking by other methods

4.3.9.1 Interfibrillar measurement

A software macro was developed to measure the spaces between the collagen fibres visible on TEM sections at a magnification of 50 000. The macro automatically optimised brightness and contrast and placed markings separating the dark fibres from the light spaces, providing over 1000 measurements per sample. Six AMs were divided into two sections. One section was treated with 0.1% riboflavin-5-phosphate and 30 mins exposure to UVA (at 16 mW/cm²). The other section was kept in PBS solution. Sections were prepared for TEM. Three specimens were selected from each section to give a range of collagen densities. Each specimen was visualised with a magnification of $\times 50\ 000$. The compact layer was identified as the area beneath the BM. The image was rotated for the BM margin to be aligned with the vertical axis. The BM was positioned immediately to the left or right of the frame in order to capture the sub-BM compact layer. An area of 100 μm^2 was photographed. The software macro was launched to measure the IFD across approximately 30 intercepts, returning a mean and standard deviation for each image. Three different areas of each AM specimen were photographed. In total, this produced nine results from several thousand measurements for each AM section, giving an estimate of the collagen density. A two-way ANOVA was performed to compare the treated and untreated AM sections across the six different donors.

4.3.9.2 Uniaxial tensile tests

Uniaxial tensile tests were performed on strips of riboflavin/UVA-treated AM and untreated controls from five AMs ($n = 80$) as described above (Subsection 4.3.3). The data was filtered and fit to the mathematical model described previously. Statistical analysis was performed on force-distance, stress-strain and model data to compare the effects of treatment on AM samples.

4.3.9.3 Ninhydrin assay

Five samples of v-d AM were soaked in 0.01% riboflavin for 30 mins, and exposed to UVA for 5, 7.5, 10, 12.5 and 30 mins. Two further samples were immersed in 0.1% and 1% glutaraldehyde as positive controls. Each test sample was heated in 2% ninhydrin solution for 20 mins at 95°C. The solution was allowed to cool, and the optical absorbance was measured with a UV-visible spectrophotometer at 570 nm. The amount of free amino groups in AM before (C_b) and after (C_a) cross-linking is proportional to the optical absorbance. The extent of cross-linking was measured as a cross-linking index as follows:

$$((C_b - C_a) / C_b) \times 100 \quad (4.7)$$

4.4 Results

4.4.1 Transparency assay

Representative samples of 0% and 10% v-d AM, 5 cm in diameter, are shown in figure 4.8 A and B. Against print, 0% v-d AM appears more opaque than 10% v-d AM. Against a dark background, a white residue is visible on the 0% v-d AM sample. This fades as the concentration of trehalose increases. There are several folds visible in the dried tissue; these impede the clarity

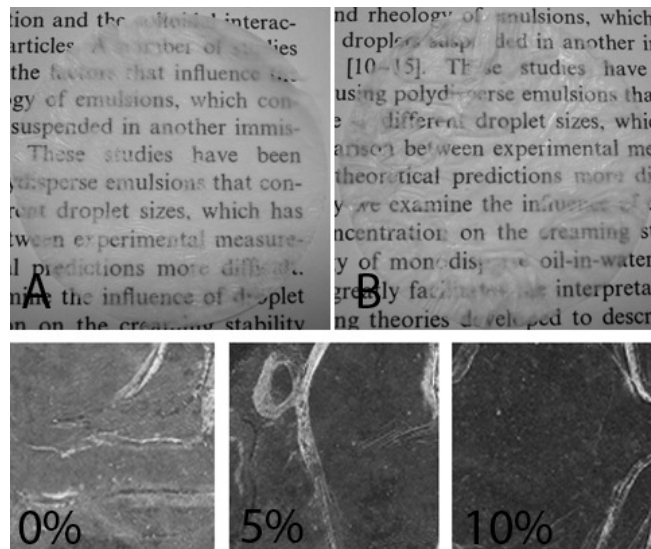


Figure 4.8: Transparency assay

A transparency assay was performed on 0% (A) and 10% v-d AM (B) by digitally photographing samples overlying print (above). Further samples (0%, 5% and 10% v-d AM) were photographed against a dark, granulated background (bottom strip) (representative samples shown).

and the uniformity of the product.

4.4.2 Scanning electron microscopy

Multiple SEM images were taken of intact and denuded fresh AM and 0% and 10% v-d AM from three donors, and images selected for their quality. Representative images are shown of epithelial, BM and collagenous layers. Selected SEM images of denuded v-d AM from are also shown to illustrate important features. *En face* images of intact fresh AM and 0% v-d AM are shown in figure 4.9 (A-F, $\times 1000$). Microvilli form a carpet on the AEC in fresh tissue (A). The polygonal shapes represent the cell borders. There are furrows between the devitalised cells, indicating depth. In the v-d AM sample (B), the microvillous layer is sparse. The polygonal shapes are still discernible, but there is no depth between the cells, suggesting tissue collapse. At higher magnification ($\times 4000$), it can be seen that the microvilli in fresh AM (C) retain their shape and density. A few individual microvilli are still discernible on v-d AM (D). However, the majority of microvilli have

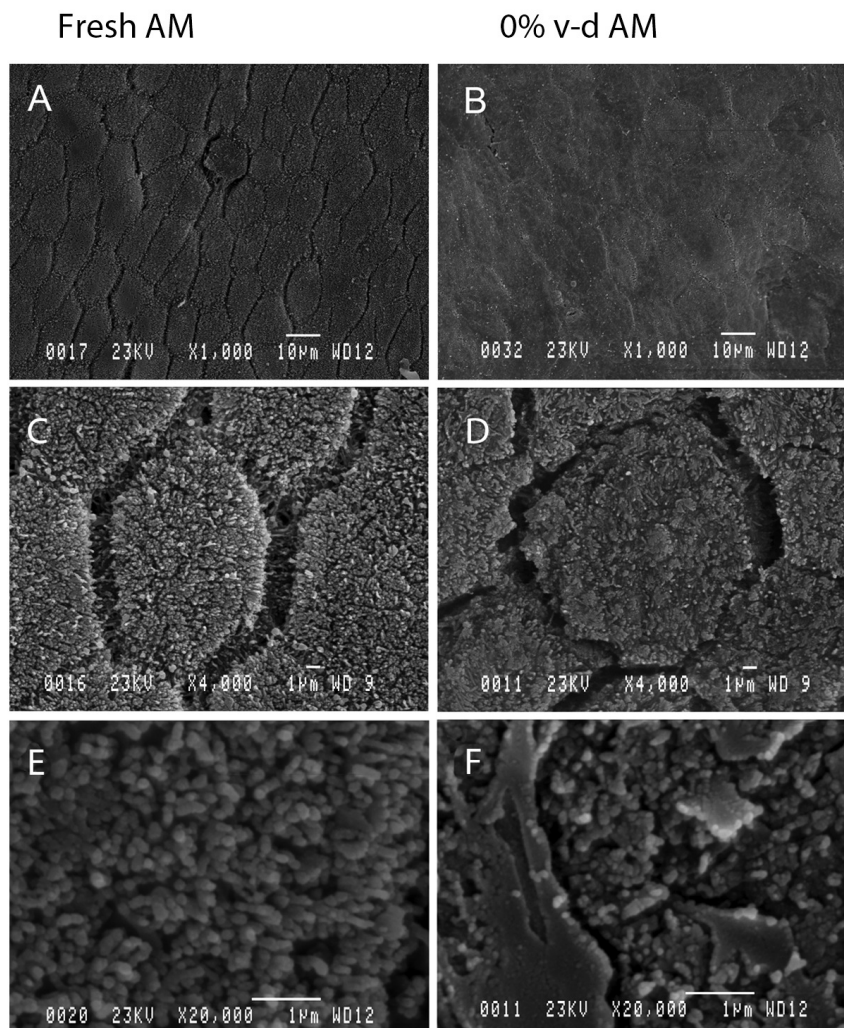


Figure 4.9: SEM of fresh and v-d AM epithelium

In fresh AM (A), AEC appear full in contrast to the compacted cells in v-d AM (B) ($\times 1000$); The polygonal shape of fresh AEC (C) is maintained, whereas it is distorted in v-d AM (D), ($\times 4000$); Microvilli appear integral in fresh AM (E) and sparse in v-d AM (F), ($\times 20\ 000$).

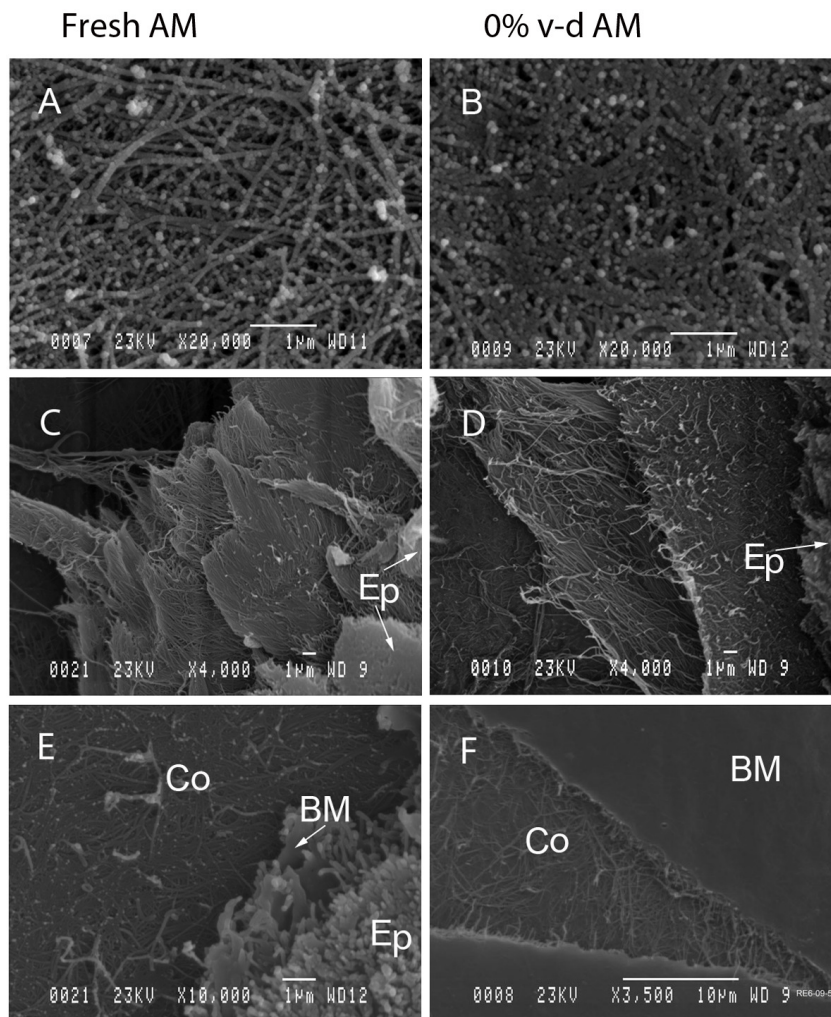


Figure 4.10: SEM of collagenous layers

SEM of reticular layer in fresh AM (A) and v-d AM (B) ($\times 20\,000$); The compact collagenous layers in fresh AM (C) and v-d AM (B). The epithelium is visible at the right of the images (E) ($\times 4000$); Epithelial (Ep), basement membrane (BM) and compact collagenous (Co) layers in fresh AM (E, $\times 10\,000$); BM of denuded v-d AM (F, $\times 3500$). The compact layer is exposed by localised damage.

become effaced, and the resultant density is much lower. This is confirmed at higher magnification ($\times 20\,000$). The microvilli in v-d AM appear attenuated (F), and in some areas are no longer recognisable as microvilli, indicating damage to the cell membrane. The microvillous layer in fresh membrane (E) is intact. Images of the compact and loose collagen layers were obtained by focusing onto defects in the v-d AM and onto the underside respectively (Figures 4.10 A-F). The compaction seen on the epithelial side of v-d AM is also seen in the loose collagen layers (B), compared to fresh AM (A) ($\times 20\,000$). However, it is less evident in the compact collagenous

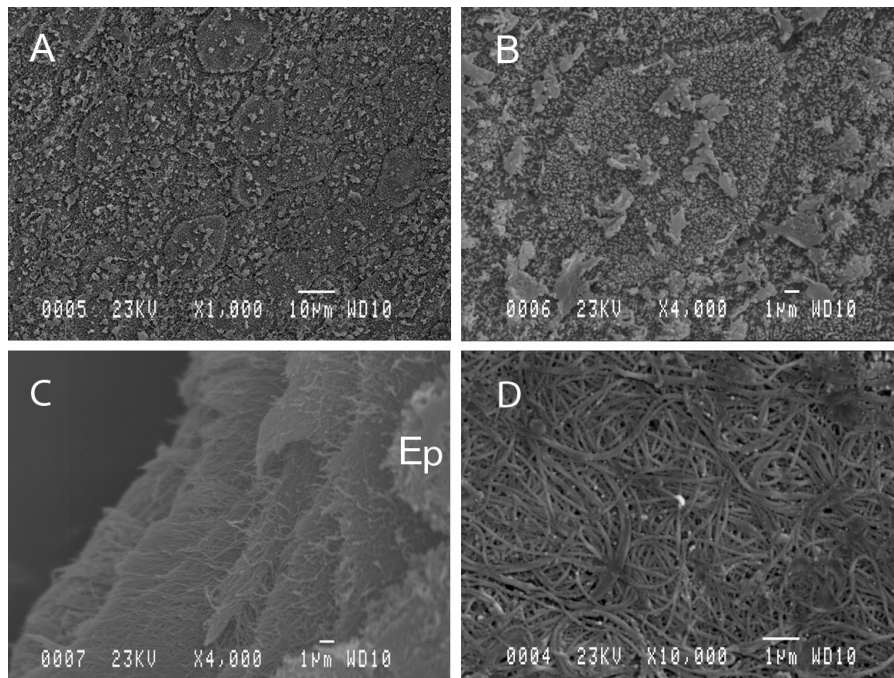


Figure 4.11: SEM images of 10% v-d AM

Epithelial surface, 10% v-d AM, showing preserved microvilli and polygonal shapes (A, $\times 1000$; B, $\times 4000$); Collagenous layers, 10% v-d AM, showing lamellae and compaction (C, $\times 4000$; D, $\times 10\,000$). Ep, epithelium.

layer, in which the collagen fibres are already densely interpositioned (C, D) ($\times 4000$). The collagen fibres appear to be distributed in lamellae. The BM is seldom seen in intact AM. In figure 4.10 E, a the BM is shown separating the epithelium from the compact collagenous layer. figure 4.10 F the BM appears smooth. The compact collagenous layer is seen immediately underlying the BM. On the epithelial surface of 10% v-d AM, the deep furrows between the cells seen in fresh AM are absent, yet the polygonal shapes appear well-maintained (figure 4.11 A). There is scattered cellular debris on the surface. The microvillous layer (B) is well-preserved in comparison to the untreated samples (4.11 B). The collagen layers demonstrate the compaction and lamellar distribution seen previously (figure 4.11 C and D).

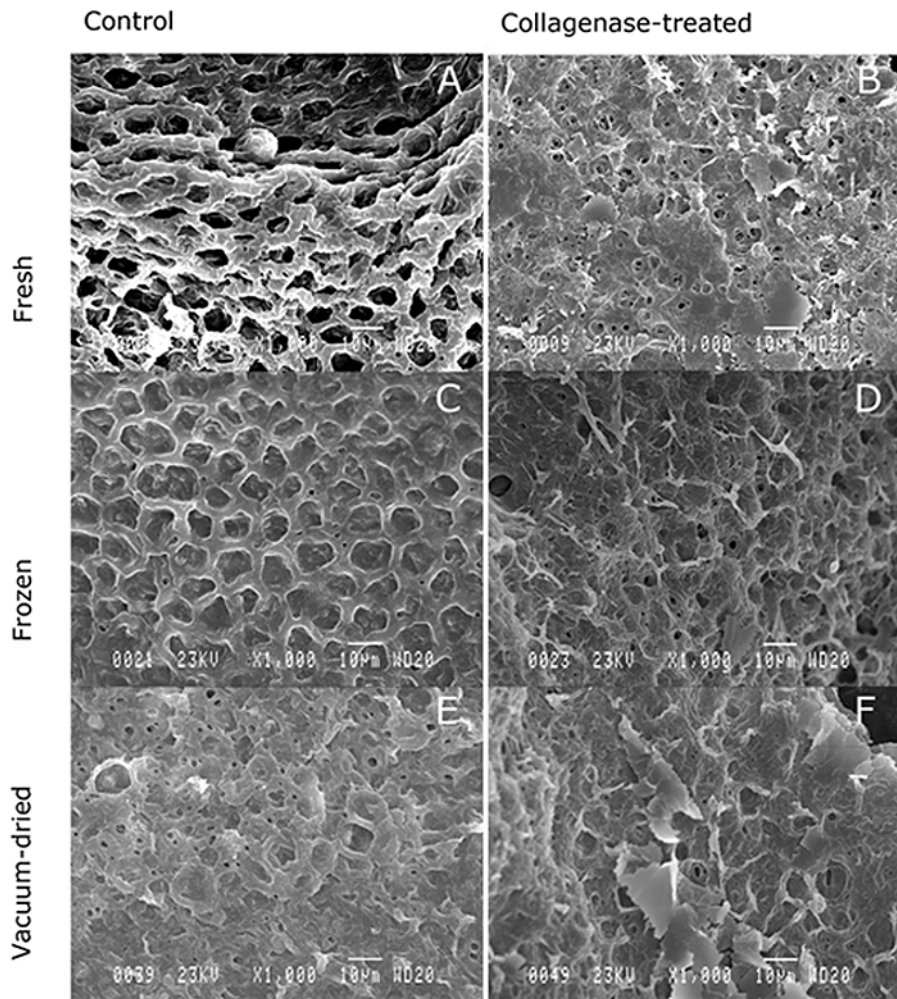


Figure 4.12: Accelerated degradation assay

Accelerated degradation assays were performed to compare fresh, f-t and v-d AM. Samples were incubated in 1% collagenase solution for 72 hrs and lyophilised for SEM. SEM images of fresh (B), f-t (D) and v-d AM (F) ($\times 1000$) treated with collagenase are shown with untreated controls (A, C and E). One of two representative samples are shown.

4.4.2.1 Degradation assay

Accelerated degradation assays were conducted in duplicate on fresh, f-t and v-d AM. These were lyophilised in their respective media as a method of fixation. Representative SEM images from one sample (of two) are shown in figure 4.12. There is a meshwork of whorls forming a pattern on the stromal side of the tissue (A, C and E) which could be due to the deposition of DMEM solutes during freeze-drying. The untreated v-d AM sample (E) differs from the fresh and f-t controls (A and C) in having a compacted appearance, although whorls are still visible. As the meshwork was consis-

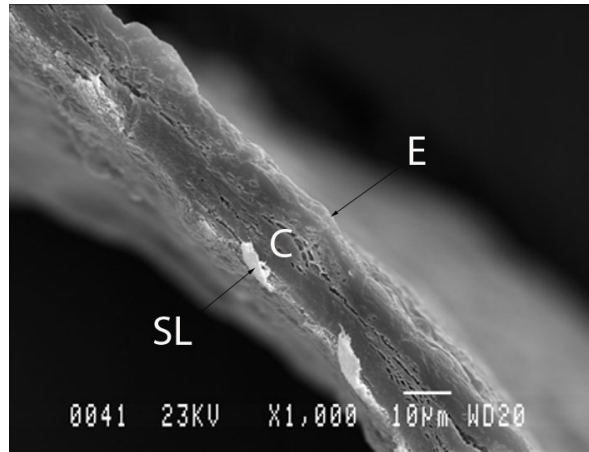


Figure 4.13: Cross-section of v-d AM

One SEM image of v-d AM in cross-section is shown ($\times 1000$). This sample is approximately $20\ \mu\text{m}$ in thickness. SL, spongy layer; C, collagenous stroma, E, epithelium.

tent and pronounced, covering virtually the entire stromal surface, this was used as a reference to compare to the treated samples (B, D and F). It can be seen that the collagenase-treated tissue is in an advanced state of decay compared to the controls, with the formation of large lacunae through the entire thickness of the membrane and the loss of recognisable features. The three preparations are in broadly similar states of decay. A further image from the degradation assay corresponds to a control sample and is included as an illustration of compaction of v-d AM (figure 4.13).

4.4.3 Transmission electron microscopy

Multiple TEM images were taken of intact fresh AM and 0% v-d AM from three donors, of which representative images were selected and are shown. Images of fresh AEC (A and C, $\times 50\ 000$) and v-d AEC (B, $\times 80\ 000$; D, $\times 25\ 000$) are shown in figure 4.14. In fresh AM, villous folds were seen to form distinct fingerlike projections in the channels between the AEC (A). Hemidesmosomes are visible in v-d AM (B), while desmosomes or villous folds were less distinct. The cell nucleoplasm in fresh AM is dense and variegated, suggesting that the nucleus membrane is intact (C). The microvilli are erect and numerous, and the cytoplasm is organised and contains dis-

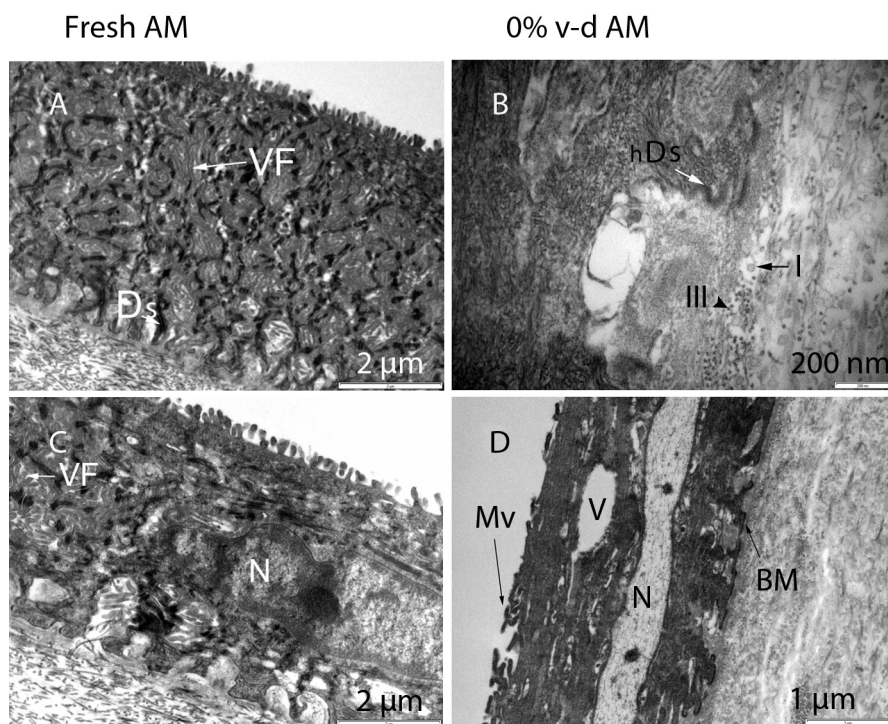


Figure 4.14: TEM images of fresh and v-d AEC

AEC of fresh (A and C, $\times 50\,000$) and v-d AM are shown (B, $\times 80\,000$; D, $\times 25\,000$). V-d AEC appear devitalised and flattened, with a loss of distinct features in the cell cytoplasm, membrane and nucleus. Mv, microvilli; BM, basement membrane; VF, villous folds; Ds, desmosome; hDs, hemidesmosome; I, type I collagen transverse fibre; III, Type III collagen transverse fibre; N, nucleoplasm; V, vacuole.

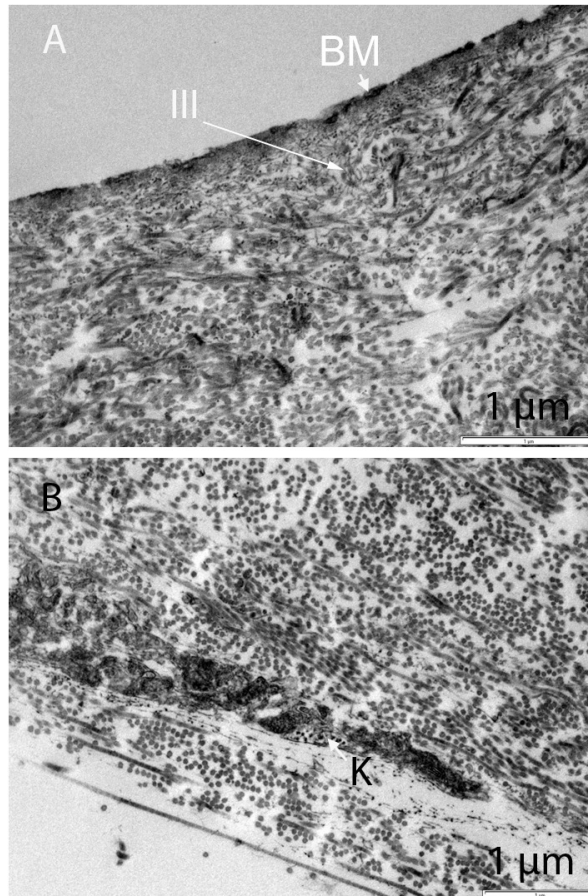


Figure 4.15: TEM of denuded v-d AM

This TEM image shows the BM and stromal aspects of denuded v-d AM ($\times 25\ 000$). A fine meshwork visible close to the BM is suggestive of type III collagen. Transverse and longitudinal type I collagen is visible throughout, with occasional keratocytes seen in the loose layer. BM, basement membrane; III, Type III collagen fibres; K, keratocyte.

cernible features. The AEC of v-d AM are devitalised, evidenced by the flattened appearance of the cells and microvilli (D). The signs of devitalisation include condensed nucleoli, an optically clear and uniform nucleoplasm and large intracellular vacuoles. There is an absence of detail in the intracellular environment, which appears dense and disorganised. A fine network of collagens, most likely type III, is visible close to the BM in figure 4.14 B, where it is interspersed among type I fibres. Figures 4.15 A and B shows the bulk of the stroma to be made up of small amounts of type III and abundant thick fibres of type I collagens, visible as longitudinal and transverse structures (round in cross-section) ($\times 25\ 000$). On the loose collagenous side of v-d AM, occasional keratocytes may be seen. At a magnification of $\times 50$

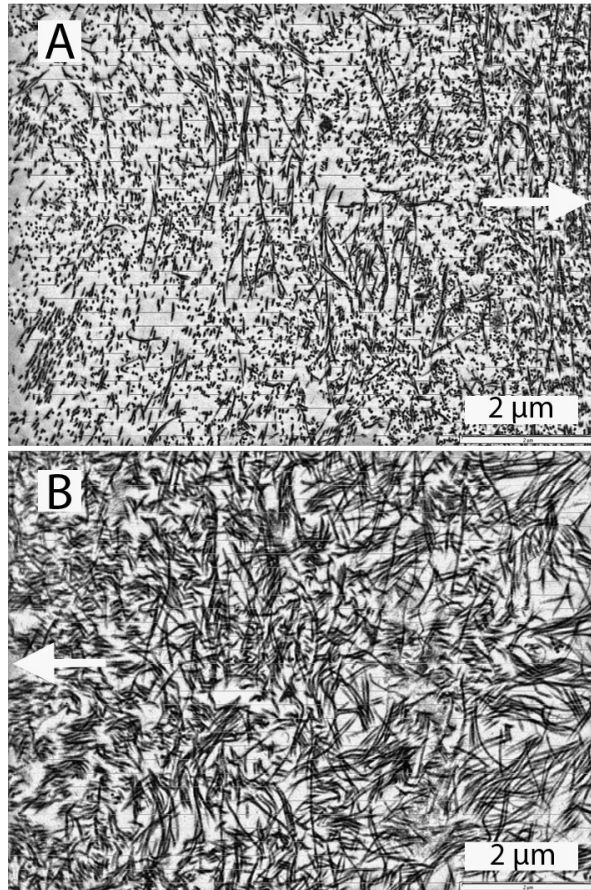


Figure 4.16: IFD measurements

Compact zone collagen fibres with markings for IFD measurements are shown. The images are representative of fresh AM (A) and v-d AM (B) ($\times 50\ 000$). The zones selected are adjacent to BM, the direction of which is indicated by the white arrows.

000, a TEM image of fresh and v-d AM stroma adjacent to the BM (indicated by white arrows) shows an abundance of collagen fibres appearing as pairs or clusters of lines (figure 4.16). Scale markings have been placed by the camera software, and enlarged figures have been added for clarity. Measurement of the IFD was obtained from such images.

4.4.4 Atomic force microscopy

Triplicate AFM images were taken of three samples of 0% and 10%. Representative images are shown. Crystalline structures are visible on the epithelial and stromal aspects of 0% v-d AM (white arrows, A, C) (figure 4.17). These are not visible in 10% v-d AM (B, D). Microvilli are visible on the ep-

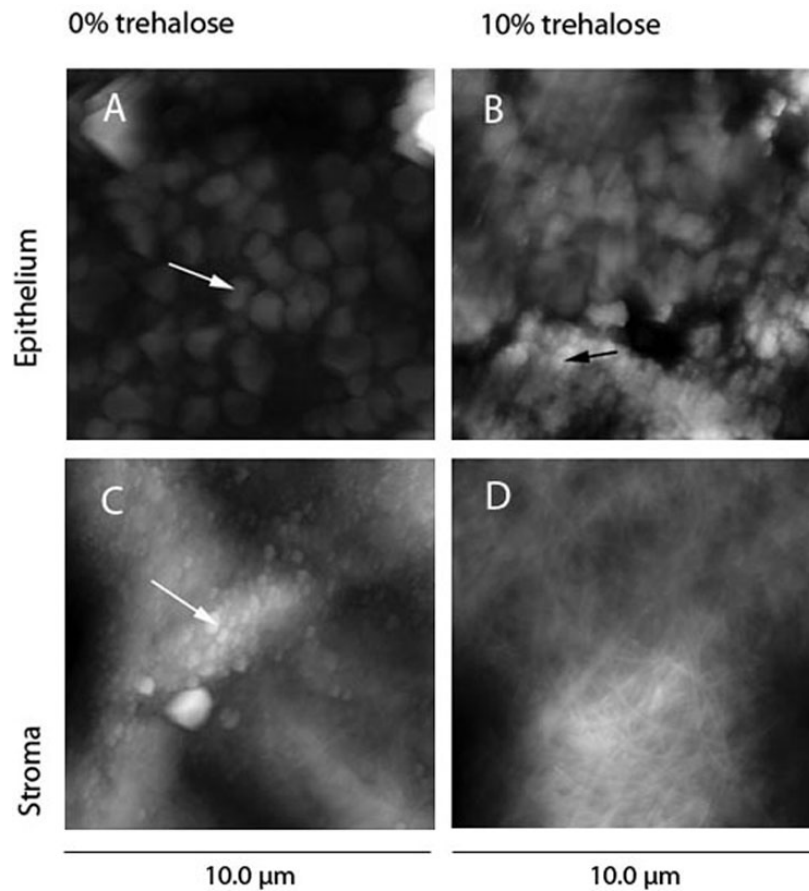


Figure 4.17: AFM images of v-d AM

Atomic force microscopy images of stromal and epithelial aspects of 0% and 10% v-d AM are shown. The untreated AM (A, C) is characterised by abundant crystalline structures, possibly salts, obscuring the tissue details (white arrows). AFM images of the treated AM may indicate microvilli (black arrow, B) and stromal collagens (D) (z scale not shown).

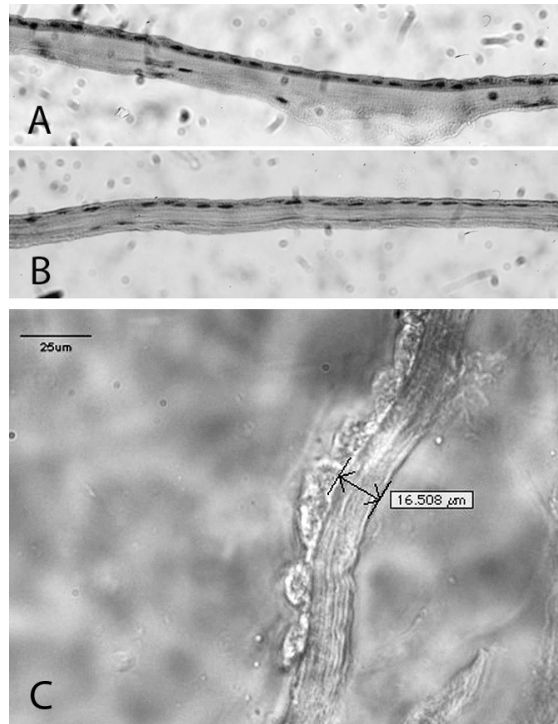


Figure 4.18: Optical microscopy ($\times 40$)

Optical microscopy images of representative samples of v-d AM (B) and f-t AM (A) suggest compaction of the dried sample (1 pair of three shown). Thickness measurements of AM sections showed no significant difference between v-d AM and f-t AM samples.

ithelial aspect of the 10% v-d AM (black arrow). The stromal collagen fibres are clearly discernible in D, but they are partially obscured by salt crystals on the membrane in C.

4.4.5 Optical microscopy

4.4.5.1 Optical microscopy

A comparison of f-t and v-d AM samples was made by optical microscopy (representative samples shown in figure 4.18 A and B). The epithelial and collagenous layers in the v-d tissue (B) appear flattened in comparison with f-t AM (A). Random thickness measurements were obtained from samples of unstained and unfixed AM preparations (figure 4.18 C). F-t and v-d samples were obtained from a total of four AMs. Three sections were processed for each sample, and a minimum of three measurements were obtained from each section ($n = 134$). The mean thickness of f-t AM was $23.9 \mu\text{m}$ ($SD 9.0$;

n = 38), and for reconstituted v-d AM it was 25.9 μm (SD 6.8, n = 96), indicating high variability and no significant difference in thickness between the two preparations (t test; $p = .22$).

4.4.6 Uniaxial testing

4.4.6.1 AM micrometry

Thickness measurements were conducted on 185 samples (80 fresh, 47 f-t and 58 v-d) from 14 donors. Univariate tests of normality showed that thickness measurements were not distributed normally, indicated by positive skewness and kurtosis, a Kolmogorov-Smirnov statistic of .002 and three outliers. Therefore, a Kruskal-Wallis test was used to compare the effect of preparation method on thickness. It revealed a statistically significant difference in thickness across the three preparation methods, $\chi^2(2, n = 208) = 57.43, p < .001$. The median values were: fresh AM, 49 μm (range 31 to 86, n = 80), f-t AM 41 μm (range 31 to 58, n = 47) and v-d AM 28 μm (range 17 to 55, n = 58). Post-hoc Mann Whitney U tests revealed a significant difference between fresh and v-d AM, $U = 688.5, z = -7.04, p < .001$ with a large effect size ($r = .60$), between fresh and f-t AM, $U = 1190, z = -3.45, p = .001$ with a medium effect size ($r = .31$) and between f-t and v-d AM, $U = 622.5, z = -4.78, p < .001$ with a large effect size ($r = .47$).

4.4.6.2 Data filtration

Seventy traces that were categorised as non-smooth by masked visual inspection (22 fresh, 17 f-t and 31 v-d) were removed from the analysis. Five traces with an initial E that had a negative value (4 fresh, 1 v-d) were also removed. From the original data set of 208 traces, 75 in total were eliminated. The proportions of traces eliminated represent 27.4% of fresh AM, 30.1% of f-t AM and 55.2% of v-d AM samples. The RR of a trace of a v-d

sample being eliminated was 2.02 (95% CI 1.35 to 3.01, $p < .001$) in comparison to a fresh sample, and 1.75 (95% CI 1.11 to 2.79, $p = .016$) in comparison to a f-t sample. In contrast, the RR of a f-t sample was not statistically significant in comparison to a fresh sample. Following the elimination of these traces, 133 traces from 17 donors remained for analysis (69 fresh, 38 f-t and 26 v-d AM). Force-distance and stress-strain analyses and mathematical modelling were performed on these data.

4.4.6.3 Force-distance analysis

Univariate tests of normality were conducted on 133 traces from 17 donors, using UTS and ΔL as dependent variables ('pooled data'). These tests detected positive skewness and kurtosis, clustering of the detrended normal Q-Q plots and multiple outliers, all suggestive of non-Gaussian distribution. Kruskal-Wallis tests were used to compare UTS and ΔL across three preparation methods. There were no statistically significant differences in UTS, $\chi^2(2, n = 133) = 3.48, p = .176$, and ΔL , $\chi^2(2, n = 133) = 5.11, p = .078$. The median and mean scores in UTS and ΔL are shown in table 4.3. An inspection of the UTS scores shows that fresh AM samples had the highest score ($Md = 2.09$ N), f-t AM had an intermediate score ($Md = 1.95$ N) and v-d AM had the lowest score ($Md = 1.58$ N). The median scores in ΔL shows that fresh AM samples had the lowest score ($Md = 7.30$ mm), f-t AM had an intermediate score ($Md = 7.53$ mm) and v-d AM had the highest score ($Md = 7.96$ mm). A further Kruskal-Wallis test was performed to compare UTS and ΔL across 17 donors. There were statistically significant differences across the donor groups in UTS, $\chi^2(16, n = 133) = 54.34, p < .001$, and ΔL , $\chi^2(16, n = 133) = 38.18, p = .001$, indicating inter-donor variability.

In order to minimise the statistical effects of variability between donors, UTS and ΔL were compared between groups of AM samples matched by donor for at least two preparation methods ('matched data'). This resulted

Table 4.3: UTS and ΔL of AM

AM	Fresh (69)	F-t (38)	V-d (26)
Total (133)	<i>Md</i> UTS/ΔL (n)		
1 (2)	-	1.71/10.26 (2)	-
2 (2)	-	-	1.40/7.76 (2)
3 (5)	-	-	1.70/9.68 (5)
4 (15)	1.70/8.43 (2)	2.56/6.61 (8)	1.28/7.48 (5)
5 (10)	2.59/9.48 (3)	1.87/7.88 (7)	-
6 (4)	2.09/8.86 (2)	-	-
7 (1)	-	1.94/5.80 (1)	-
8 (18)	2.63/8.40 (8)	3.04/9.66 (4)	3.09/7.40 (6)
9 (1)	-	-	1.50/9.03 (1)
10 (14)	1.69/6.19 (6)	1.39/5.85 (7)	1.20/9.98 (1)
11 (10)	2.05/8.24 (7)	-	1.59/9.60 (3)
12 (21)	2.20/8.08 (9)	1.50/8.61 (9)	1.32/7.51 (3)
13 (6)	2.40/7.14 (6)	-	-
14 (6)	2.22/6.85 (6)	-	-
15 (6)	2.33/6.82 (6)	-	-
16 (5)	1.81/6.32 (5)	-	-
17 (7)	1.69/6.95 (7)	-	-
<i>Md</i> UTS/N (range)	2.09 (0.82 - 4.29)	1.95 (1.00 - 4.32)	1.58 (0.93 - 3.91)
<i>M</i> UTS/N (<i>SD</i>)	2.10 (0.67)	2.11 (0.82)	1.87 (0.82)
<i>Md</i> $\Delta L/mm$ (range)	7.30 (3.77 - 10.48)	7.53 (4.96 - 12.61)	7.96 (5.75 - 12.24)
<i>M</i> $\Delta L/mm$ (<i>SD</i>)	7.42 (1.40)	7.83 (2.00)	8.31 (1.61)

UTS, ultimate tensile strength (N); ΔL , change in length (mm); *n*, number of samples

in a total of 88 traces (35 fresh, 35 f-t and 18 v-d) from six donors (6 fresh, 5 f-t and 5 v-d). Univariate and multivariate tests of normality were conducted. Despite a degree of positive skewness (.639) in UTS and a Kolmogorov-Smirnov statistic of .039, the univariate analysis indicated that the matched data were distributed normally. There was one outlier in the ΔL data which could safely be retained in the analysis. In the multivariate analysis, the maximum Mahalanobis distance was below the critical value, indicating an absence of multivariate outliers. The assumption of linearity was satisfied, and there was a small correlation between UTS and ΔL ($r = .07$). A two-way MANOVA was conducted using donor and preparation method as categorical variables. The data did not violate the assumption of homogeneity of variance-covariance matrices (Box's test .525) or equality of variance (Levene's test: UTS, .534, ΔL , .606). A Bonferroni adjustment was applied to account for two variables, giving a new alpha level of .025. There was a statistically significant difference in the combined dependent variables across donors, $F(10, 144) = 3.79$, $p < .001$, Pillai's trace .42, partial eta squared = .21 (large effect size), but not across preparation categories $F(4, 144) = .95$, $p = .436$, Pillai's trace .05, partial eta squared = .03. The estimated marginal means indicated a mean UTS score of v-d AM of 1.79 N, $SE = .19$, which was lower than the scores of both fresh AM ($M = 2.14$ N, $SE = .12$) and f-t AM ($M = 2.19$ N, $SE = .15$). The estimated marginal mean ΔL score of v-d AM ($M = 8.45$ mm, $SE = .46$) was higher than the scores of both fresh AM ($M = 7.86$ mm, $SE = .31$) and f-t AM ($M = 7.86$ mm, $SE = .28$). The matched data demonstrated the same effects of preparation method and donor on UTS and ΔL as the pooled data.

4.4.6.4 Stress-strain analysis

The pooled data set ($n = 133$) was used for stress-strain analysis. Five fresh and two f-t AM samples did not have thickness measurements. These were

Table 4.4: Stress-strain measurements by AM category

AM	E_1 (MPa)	σ_f^N (MPa)	σ_f^T (MPa)	ε_f (%)	Area (mm ²)	E_2 (MPa)	T (J/mm ³)
Fresh (69)	0.45	4.09	5.64	36.5	0.50	24.05	0.45
F-t (38)	0.62	4.97	6.45	37.6	0.43	27.71	0.49
V-d (26)	1.01	5.28	7.52	39.8	0.34	29.90	0.61
χ^2	.87	9.23	10.52	5.11	31.74	7.52	10.37
p	.65	.010	.005	.078	< .001	.023	.006

Median values of dependent variables shown. σ_f^N , nominal failure stress; σ_f^T , true failure stress; ε_f , failure strain; T, toughness; MPa, megaPascals; J, joules; E_1 , initial modulus; E_2 , final modulus.

given nominal thickness values of 40 μm . Univariate tests of normality were performed for seven dependent variables: cross-sectional area, E_1 , σ_f^N , σ_f^T , ε_f , E_2 and toughness. Of these, only ε_f was distributed normally. Therefore, non-parametric testing was performed throughout. Kruskal Wallis tests were used to compare each of these dependent variables across preparation categories (table 4.4). These revealed statistically significant differences in area, σ_f^N , σ_f^T , toughness and E_2 , but not in ε_f or E_1 . An examination of the median scores reveals values of σ_f^N , σ_f^T , E_1 , E_2 and toughness that are lowest for fresh AM, intermediate for f-t AM and highest for v-d AM. The trend for cross-sectional area is in the opposite direction. A post-hoc Mann Whitney U test was performed to compare the toughness of v-d AM with fresh AM. It revealed a significant difference, $U = 520$, $z = -3.15$, $p = .002$, $r = .3$ (medium effect size). The relationship between area and toughness was investigated using Pearson product-moment coefficient. A medium negative correlation was found, $r = -.30$, $n = 88$, $p = .004$. Similar correlations were observed between area and σ_f^N ($r = -.33$, $p = .002$) and between area and σ_f^T ($r = -.32$, $p = .002$).

To illustrate the effects of thickness measurement on the dependent variables, a new measurement of σ_f^N was calculated based on a uniform thickness of 50 μm for all three preparations. A Kruskal Wallis test demonstrated

Table 4.5: Modelling data by AM category

AM	d	G' (MPa)	RMS (kPa)	d_2	G'_2 (MPa)	RMS ₂ (kPa)	d_3	G'_3 (MPa)	RMS ₃ (kPa)
Fresh (69)	4.16	1.24	6.18	10.91	0.15	21.87	4.36	1.31	6.45
F-t (38)	4.45	1.50	6.95	10.49	0.21	23.44	4.77	1.45	6.64
V-d (26)	3.86	1.18	6.46	8.48	0.34	21.56	3.86	1.18	6.46
χ^2	2.41	.66	3.19	8.33	.88	1.98	4.18	.23	.30
p	.30	.30	.20	.016	.65	.37	.12	.89	.86

Median values of dependent variables shown. Comparisons made by Kruskal Wallis testing. RMS, root mean square of the error; d , G' , model parameters.

a statistically significant difference between the values, $\chi^2(2, n = 133) = 7.88, p = .019$. An inspection of the median values shows σ_f^N to be highest for fresh AM (4.19 MPa), intermediate for f-t AM (3.91 MPa) and lowest for v-d AM (3.16 MPa).

4.4.6.5 Model fitting

For the first curve fitting, model parameters G' and d were derived simultaneously from the experimental data of the entire stress-strain curves, generating model curves. The difference between the experimental and model curves was expressed as a RMS error. Since the data were non-Gaussian, Kruskal Wallis tests were conducted to assess the effects of preparation method on d , G' and RMS. There was no statistically significant difference in RMS across the three preparation methods. The median values are shown in table 4.5.

A second fitting was performed using a value of G'_2 obtained from the gradient between 0.495 and 5% strain. This was used to generate model curves with new values for d (d_2), and with a new RMS error (RMS₂). Kruskal Wallis tests were performed to compare the effects of different preparation methods on G'_2 , d_2 and RMS₂ (table 4.5). A significant difference was found in d_2 of the different preparations ($\chi^2(2, 133) = 8.33, p = .016$). Post-hoc

Mann-Whitney U tests were conducted, comparing v-d AM to the other two preparations. A Bonferroni adjustment was made, reducing the alpha level to .025. The value of d_2 was significantly lower for v-d AM than fresh AM, $U = 566$, $z = -2.76$, $p = .006$, $r = .24$ (medium effect size) and f-t AM, $U = 321$, $z = -2.37$, $p = .018$, $r = .21$.

A third fitting was performed by applying an adjustment to the starting point to compensate for slackness or tension in each sample, generating new values G'_3 , d_3 and RMS_3 . An inspection of the median values show that this adjustment increases the difference in the value of d for v-d AM compared to the other preparations, although this is not statistically significant ($p = .12$).

4.4.7 Non-destructive tests

4.4.7.1 Acoustic wave impedance

The results displayed are the mean values of quadruplicate measurements taken for three different AM samples in each of four preparation groups (figure 4.19). Error bars represent standard deviations. The values of both G' and G'' vary between 0 and 20 MPa across the preparation methods.

4.4.7.2 Nanoindentation

Nanoindentation was performed on 0% and 10% v-d AM samples using bare cone tips with radii of 2 nm (cone 1) and 15 nm (cone 2) and spherical beads with radii of 5 μm (sphere 1) and 15 μm (sphere 2). Mean values and SD s of selected variables are shown in table 4.6. Using cone 1, significant differences were found in E and hardness between the stromal aspects of 10% v-d AM and 0% v-d AM ($p < .0001$). Cone 2 yielded a significant difference in hardness between stromal 10% and 0% v-d AM ($p = .0001$). However, variability was high, as evidenced by the high SD . Tests with sphere 1 and

Table 4.6: Modulus, contact hardness and plasticity

Tip	Trehalose	Aspect	n	<i>E</i>/GPa (<i>SD</i>)	Hardness/GPa (<i>SD</i>)
Cone 1	0%	Stroma	96	0.99 (0.68)	6.02 (6.35)
		Epithelium	72	7.90 (13.97)	21.41 (76.40)
	10%	Stroma	72	48.66 (34.86)	56.68 (46.87)
		Epithelium	72	28.19 (32.79)	40.18 (54.86)
Cone 2	0%	Stroma	192	0.73 (0.89)	2.33 (37.58)
		Epithelium	72	2.93 (7.42)	8.22 (87.02)
	10%	Stroma	24	4.94 (5.81)	59.03 (153.25)
		Epithelium	96	1.82 (2.05)	2.33 (7.97)
Tip	Trehalose	Aspect	n	<i>E</i>/GPa (<i>SD</i>)	Plasticity (<i>SD</i>)
Sphere 1	0%	a	28	0.27 (0.20)	0.21 (0.13)
		b	64	0.10 (0.02)	0.23 (0.24)
	10%	a	63	0.88 (0.38)	0.17 (0.07)
		b	63	0.44 (0.21)	0.23 (0.10)
Sphere 2	0%	a	127	0.03 (0.03)	0.23 (0.08)
		b	127	0.02 (0.01)	0.29 (0.07)
	10%	a	127	0.15 (0.05)	0.19 (0.07)
		b	127	0.17 (0.15)	0.18 (0.13)

Cone 1, radius 2 nm; Cone 2, radius 15 nm; Sphere 1, radius 5 μm; Sphere 2, radius 15 μm.

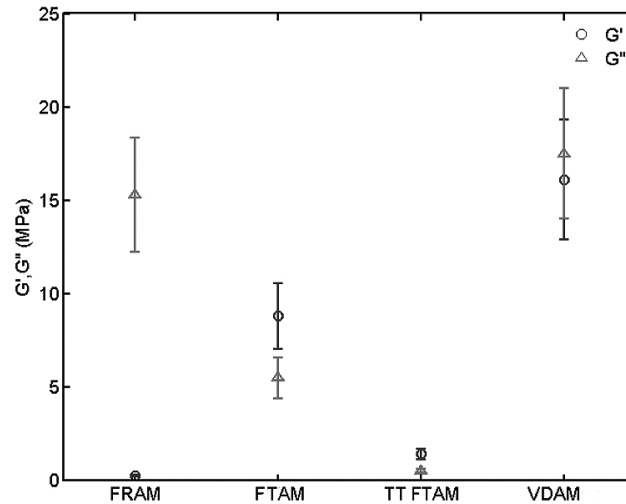


Figure 4.19: Acoustic impedance tests

The shear storage modulus (G') and loss modulus (G'') of four different AM preparations was measured by surface acoustic wave impedance. FRAM, fresh amniotic membrane; TT, thermolysin-denuded FTAM.

sphere 2 revealed no significant differences between the preparations.

4.4.8 Cross-linking

4.4.8.1 Gel electrophoresis

Collagen extract from samples treated with 0.1% riboflavin-5-phosphate and 30 mins exposure to UVA (at 16 mW/cm²) was obtained from three AMs (A, B and C) and subjected to gel electrophoresis (figure 4.20, left) after protein purification. Controls were run in the lanes to the right of the samples. An unstained HiMark™ marker was also run (shown with values). Each lane contained 10 µg of protein. The control lanes contain strong bands located at approximately 450, 240, 160 and 130 kDa. The test sample lanes (1, 2 and 3) are empty, with only a few faint bands. The strong bands in the control samples were initially presumed to represent the full type I collagen trimer, γ , the β dimer and the α monomer chains (boxed).

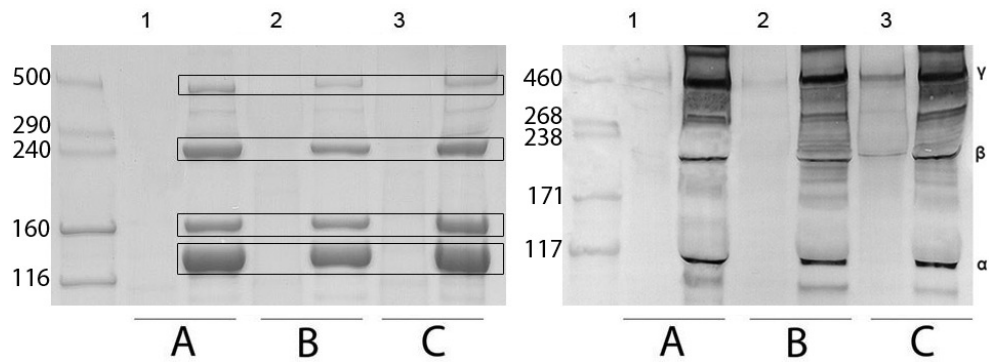


Figure 4.20: AM collagen extract

A gel (left) is shown with a western blot. AM samples treated with riboflavin-A and ultra-violet irradiation were loaded into lanes 1, 2 and 3. Untreated AM controls are shown in adjacent lanes. In the gel, strong bands highlighted by boxes were thought to represent the γ , β and α chains of type I collagen. For the blot, an anti-type I collagen antibody was used. This shows the presence of three strong bands, marked γ , β and α .

4.4.8.2 Western blotting

A western blot was carried out under denaturing and reducing conditions on the AM samples treated with riboflavin/UVA and controls to confirm the presence of type I collagen (figure 4.20, right). A stained HiMark™ marker was run alongside the samples (left). Three bands stand out at approximately 450 kDa, 200 kDa and 110 kDa, initially thought to be the γ , β and α bands. Only one of the α bands is clearly visible.

4.4.8.3 Mass spectrometry

The four principal bands identified by gel electrophoresis were sent for mass spectrometry (figure 4.21). The 450, 240, 160 and 130 kDa bands localised by gel electrophoresis were labelled a, b, c and d respectively. Two runs were performed for bands a and d, whereas bands b and c had one run each. The highest data yielded returned per run are presented in table 4.7. All four bands contain the α_1 chain of type III collagen. It has the highest Protein Score, the highest number of matches and the highest percent coverage in each band, except band c, where it has the second highest score. The scores in the bands a - d are 233, 528, 149 and 953 respectively. The α_1 chain of

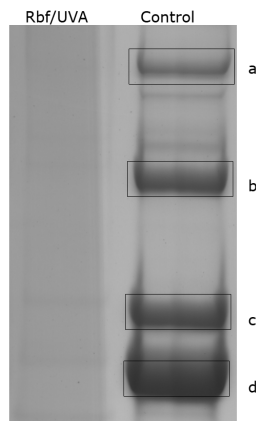


Figure 4.21: Mass spectrometry bands

Four principal bands (a-d) were identified by electrophoresis of purified collagen in fresh, untreated AM (right lane). Riboflavin/UVA-treated AM is shown in the left lane. The bands were located at 450 kDa (a), 240 kDa (b), 160 kDa (c) and 130 kDa (d). These were sent for mass spectrometry. Rbf, riboflavin.

Table 4.7: Mascot Peptide Summary Report

Band	Protein	M _r	pI	Collagen	Gene	Score	Matches	Sequences	Per cent coverage
a	CO3A1	138479	6.21	Alpha-1 (III)	COL3A1	233	25	14	16
a	CO1A1	138857	5.60	Alpha-1 (I)	COL1A1	52	3	3	3
b	CO3A1	138479	6.21	Alpha-1 (III)	COL3A1	528	29	16	19
b	CO1A1	138857	5.60	Alpha-1 (I)	COL1A1	22	3	2	3
c	CO5A1	183447	4.94	Alpha-1 (V)	COL5A1	296	20	8	7
c	CO3A1	138479	6.21	Alpha-1 (III)	COL3A1	149	3	3	3
c	COBA1	180954	5.06	Alpha-1 (XI)	COL11A1	163	6	3	2
d	CO3A1	138479	6.21	Alpha-1 (III)	COL3A1	953	54	20	22
d	CO1A1	138857	5.60	Alpha-1 (I)	COL1A1	85	4	3	3
d	CONA1	51912	6.88	Alpha-1 (XXIII)	COL23A1	144	6	1	2
d	CO5A2	144821	6.07	Alpha-2 (V)	COL5A2	57	3	3	2
d	CO2A1	141698	6.58	Alpha-1 (II)	COL2A1	41	2	2	1

type I collagen is present in bands a, b and d. The scores for type I collagen in these bands are 52, 22 and 85. Five other collagen chains are present, of which the α_1 chain of type V collagen has the highest score at 296.

4.4.8.4 Inter-fibrillar measurement

The mean IFD was calculated from three sub-BM zones of three TEM images from six cross-linked AM samples with untreated controls. The mean IFD of Riboflavin/UVA-treated AM was 230.2 nm (SD 197.2), whereas for untreated AM it was 214.3 nm (SD 180.7). A two-way ANOVA returned a Levene statistic significance level of $< .001$, indicating unequal variances in the IFD across the AM donors. There was a statistically significant interaction effect between the treatment method and the donor $F(5, 124) = 197.8, p < .001$, indicating that the main effect could not be interpreted easily. Nonetheless, there were highly significant effects for treatment and donor ($p < .001$). This suggests that the mean IFD is significantly different between treatment groups and between donors. The magnitude of the effect for preparation is small (partial Eta squared $.001$).

4.4.8.5 Uniaxial tests of irradiated AM

Eight riboflavin/UVA-treated samples and eight controls from each of five AMs underwent uniaxial testing ($n = 80$). Non-smooth curves were filtered out (three treated and 10 controls), resulting in a total of 37 traces of riboflavin/UVA-treated samples and 30 controls for analysis. The traces from the experimental and control groups were compared through an array of dependent variables including force-distance, stress-strain and modelling data by conducting Kruskal Wallis tests (table 4.8). Statistically significant differences were found in a number of dependent variables, including ΔL , E_1 , E_2 , toughness, d , G' , d_2 and G'_2 . An inspection of the median values reveals that riboflavin-UVA-treated AM had a higher ΔL and toughness and

Table 4.8: Uniaxial tests of riboflavin/UVA-treated AM

AM	Area (mm ²)	UTS (N)	ΔL (mm)	E_1 (MPa)	σ_f^N (MPa)	σ_f^T (MPa)	ε_f (%)	E_2 (MPa)	T (J/mm ³)
Experimental (37)	0.44	1.86	9.79	0.37	4.65	7.03	0.49	20.01	0.67
Control (30)	0.45	2.08	6.84	0.88	4.57	6.15	0.34	24.31	0.50
χ^2	.01	.70	39.04	17.42	.11	.87	39.04	10.75	4.54
p	.91	.40	< .001	< .001	.74	.35	< .001	.001	.03

AM	d	G' (MPa)	RMS (kPa)	d_2	G'_2 (MPa)	RMS ₂ (kPa)	d_3	G'_3 (MPa)	RMS ₃ (kPa)
Experimental (37)	2.88	0.96	5.65	7.20	0.12	20.20	2.88	0.57	3.14
Control (30)	4.16	1.75	6.75	11.20	0.29	25.27	4.52	1.78	6.00
χ^2	25.82	21.30	4.54	28.05	17.42	3.48	25.82	21.30	4.54
p	< .001	< .001	.03	< .001	< .001	.06	< .001	< .001	.03

UTS, ultimate tensile strength; E_1 , initial modulus; E_2 , terminal modulus; T, toughness; d and G , model parameters; RMS, root mean squared of error.

lower E_1 , E_2 , d , G' , d_2 and G'_2 than the control samples. The treated AM had a lower UTS, although this was not statistically significant.

4.4.8.6 Ninhydrin assay

The cross-linking indices calculated from this assay varied from 1.1% for AM exposed to UVA for 12.5 mins to -8.1% for AM exposed for 30 mins. For comparison, the AM treated in 0.1% glutaraldehyde had a cross-linking index of 28.8%, and for AM treated in 1% glutaraldehyde the index was 151.5%. This indicated that treatment of AM with riboflavin/UVA did not result in cross-linking at the solution strength and irradiation levels used.

4.5 Discussion

Extensive material testing was performed, demonstrating that v-d AM undergoes qualitative change during drying. This was shown by force-distance analysis, stress-strain analysis and mathematical modelling. Cross-linking

was unsuccessful, although a template is suggested for future analyses. Non-destructive testing was also performed. This showed high variability, suggesting a need for further refinement.

4.5.1 Physical properties of dried AM

From a clinical perspective, it is useful to know whether the process of drying the tissue causes a deterioration in its quality, and one of the ways of assessing this is through materials testing. The tests described, such as tensile tests and accelerated degradation studies, have clinical correlates like robustness and resistance to enzymatic degradation. This is illustrated by reports of successful cross-linking of AM by chemical means (Ma et al., 2010; Kitagawa et al., 2011; Chau et al., 2012). Cross-linking can change the mechanical properties of AM by modifying its structure, thereby improving its clinical effects. There is no single quality threshold for the fitness for purpose of dried AM. Therefore, tests frequently compare it to cryopreserved or fresh preparations in order to indicate its clinical usefulness.

The EM studies on v-d AM indicate that the tissue becomes compacted during the drying process (figures 4.9, 4.13 and 4.14). Both the SEM and TEM images show a flattened and featureless epithelium and a compact collagenous network. The v-d AM epithelium was found on both SEM and TEM to be devitalised, in agreement with previous studies (Rodríguez-Ares et al., 2009). The compaction of the collagenous network in comparison to the fresh tissue has also been noted previously (Nakamura et al., 2008). The collagenous layers contained multiple lamellae that were distributed in heterogeneous orientations within the planes. Since these lamellae may provide tensile strength in various directions, this leads one to question whether AM collagen is isotropic (i.e., uniform in all directions). A previous study addressed this issue, and identified regions of high collagen fibre alignment within AM (Joyce et al., 2009). The authors of this study con-

ducted biaxial tensile tests in which the response of AM was different in each axis, indicating anisotropy. Thus, mechanical testing on AM varies depending on the orientation of the samples.

SEM images were useful in demonstrating the effects of trehalose (figure 4.11). The epithelial surface appears to maintain aspects of the fresh tissue, such as the microvillous layer and polygonal shape, suggesting improved preservation. The debris seen on the surface of the cells could represent freeze-dried forms of trehalose, which are detectable by SEM (Surana et al., 2004b).

A degradation assay was performed using SEM images to judge the degree of degradation in fresh, f-t and v-d AM (figure 4.12). This was performed differently to the previous SEM by lyophilising the samples as a method of fixation. It returned broadly similar states of decay across the three preparations.

AFM imaging showed extensive crystallisation on the surface of the untreated AM (figure 4.17), probably as a result of PBS residues, of which NaCl would be the most abundant. The trehalose-treated samples were clearer, with structures such as microvilli and collagens more easily visible. This indicates that trehalose treatment improves optical clarity, as suggested by the transparency assay (figure 4.8).

Uniaxial tensile tests were performed to compare the effects of freeze-thawing and vacuum-drying on AM samples from 17 donors. The AM dimensions and strain rate (0.083 s^{-1}) used in this study were similar to other studies (Fujisato et al., 1999; Nakamura et al., 2004). The traces were filtered to include only smooth curves, and curves with a positive initial modulus. There was a significantly increased risk of non-smooth traces of v-d AM samples being eliminated, when compared to fresh and f-t samples. This suggests a change in the quality of the sample, since this testing method is highly sensitive to flaws (Oyen et al., 2004). Smooth

stress-strain curves suggest relative uniformity in the sample, whereas non-smooth curves, characterised by multiple peaks or atypical patterns, may indicate disruption of the collagen links. Since water bonds have a role in maintaining the mechanical strength of collagen (Cameron et al., 2002), this can be explained as an effect of dehydration. It may also have been caused by suboptimal alignment during mounting, although this would be expected to affect all the preparation methods equally.

The force-distance analysis demonstrated that UTS was highest in fresh samples ($Md = 2.09$ N) and lowest in v-d samples ($Md = 1.58$ N). The median value of UTS in f-t AM samples was intermediate (1.95 N), whereas the mean value was 2.11 N. Conversely, ΔL was highest for v-d AM ($Md = 7.96$ mm) and lowest for fresh AM ($Md = 7.30$ mm). This was shown in data from AM sourced from different donors and also in AM that was matched by donor. Despite the interdonor variability in UTS and ΔL , the trends across preparation methods were consistent. The distribution of data was non-Gaussian, so non-parametric tests were used in the force-distance analysis. Although the differences did not reach statistical significance, it suggests that vacuum-drying has a weakening effect on AM, and may make it more ductile. The high variability can explain why statistical significance was not reached across preparation methods. This is highlighted by a power analysis demonstrating the sample size n that would be required to detect a clinically important difference, d with a standard deviation, SD (Goodall et al., 2009). The power analysis assumes a Gaussian distribution. The mean UTS values were ~ 2.1 N for fresh and f-t AM and ~ 1.9 N for v-d AM (a difference of $\sim 10\%$), and the SD was ~ 0.7 . In a comparative study of UTS of fresh AM versus v-d AM, a t test could be used to compare means (X), where the numerator is the difference in means and the denominator is the standard error:

$$t = \frac{(X_1 - X_2)}{\frac{SD}{\sqrt{n}}} \quad (4.8)$$

t must be at least 1.96 to achieve a 5% level of significance ($p < .05$). For this, the least significant difference between the means is

$$LSD = 1.96 \times \frac{SD}{\sqrt{n}} \quad (4.9)$$

For a power analysis, to be 90% certain of detecting d , we must also satisfy the equation

$$d = LSD + 1.28 \frac{SD}{\sqrt{n}} \quad (4.10)$$

where 1.28 corresponds to the 90th percentile of a normal distribution. Solving for n , we obtain

$$n = \frac{2(1.96 + 1.28)^2 SD^2}{d^2} \quad (4.11)$$

$$\approx 21 \left(\frac{SD}{d} \right)^2$$

If we assume the UTS of a strip of fresh AM to be ~2.0 N (see table 4.3) and a 10% reduction to be clinically significant (0.2 N), then with a SD of 0.7 the number of samples required in each category would be

$$n \approx 21 \left(\frac{0.7}{0.2} \right)^2$$

$$n \approx 260$$

Thus, 520 test samples would have been required to demonstrate a statistically significant reduction of 10% in UTS between fresh and v-d AM

preparations. The null hypothesis between fresh and v-d AM could not be rejected by this force-distance analysis, yet this may be a Type II error due to an underpowered study. The large property range of AM is a major reason for the variability encountered (Oxlund et al., 1990; Oyen et al., 2004). In addition, there was a significant difference in the mechanical properties of AM across different donors, which is in agreement with other studies (Oxlund et al., 1990; Jabareen et al., 2009). The difference between fresh and f-t AM appears to be slight, suggesting that the quality of v-d AM is inferior to f-t AM. This is reinforced by the higher rate of flawed stress-strain traces in v-d AM samples.

The importance of accurate and precise dimension measurements in determining the physical properties of AM is paramount (Oyen et al., 2004; Jabareen et al., 2009). Digital micrometry is highly subjective and measures only small areas of the tissue. The tissue can easily be crushed by the instrument, potentially underestimating the histologically-derived thickness of AM by a factor of two (Jabareen et al., 2009). In this study, median thicknesses of fresh, f-t and v-d AM were 49 μm , 41 μm and 28 μm respectively, and statistically significant differences were found across all three preparation methods. The finding of different thickness of fresh and f-t AM may be a Type I error, since freeze-thawing is not known to cause tissue collapse. Conversely, v-d AM is visibly more compact than both fresh and f-t AM. Optical measurements, such as light microscopy, may be more accurate but require much more time and planning. In the study presented here, no differences were found between f-t and v-d AM in light microscopic studies of thickness, both preparations returning a value of approximately 25 μm . The method used for thickness measurements described contrasted with that of Jabareen et al. (2009), as the AM samples were neither fixed nor stained. However, it gave a quick indication of sample thickness that could be used to corroborate measurements made by digital micrometry. A direct comparison

of the two techniques was not made in this study, but could be the subject of future work, given the importance of accurate and precise measurement of geometric dimensions for stress-strain analysis.

A stress-strain analysis of the filtered data indicated that σ_f^N , σ_f^T , E_1 , E_2 and toughness were lowest for fresh AM, intermediate for f-t AM and highest for v-d AM. The differences were statistically significant with the exception of E_1 . The values reported here for fresh AM (σ_f^N , 4.09 MPa; area, 0.50 mm²; E_1 , 0.45 MPa; E_2 , 24.1 MPa; T, 0.45 Jmm⁻³) are in approximate agreement with other uniaxial studies of natural AM. Oxlund et al. (1990) measured mean AM thickness to be 47 μ m and mean σ_f^N to be 3.94 MPa, whereas Oyen et al. (2004) reported a pseudolinear modulus E_2 of 23.5 ± 6.9 MPa. Jabareen et al. (2009) reported values of E_1 of ~ 0.02 MPa in AM that was pre-conditioned by cyclic loading. The strain rate they used was 0.005 s⁻¹, in contrast to a strain rate of 0.083 s⁻¹ used in this study, which may explain some of the variance. The values for f-t AM were as follows: σ_f^N , 4.97 MPa; area, 0.43 mm²; E_1 , 0.62 MPa; E_2 , 27.7 MPa and T, 0.49 Jmm⁻³. For v-d AM, they were: σ_f^N , 5.28 MPa; area 0.34 mm²; E_1 , 1.01 MPa; E_2 , 29.79 MPa and T, 0.61 Jmm⁻³.

The apparent increase in σ_f^N and toughness in f-t and v-d AM requires further explanation, since a lower UTS and simultaneously higher σ_f^N and toughness in f-t and v-d AM may seem paradoxical. The differences are likely to reflect the sum of influences of thickness measurement and intrinsic structural changes to the processed tissues, which are considered separately.

These measurements of σ_f^N , σ_f^T , E_1 , E_2 and toughness have in common an inversely proportional relationship to cross-sectional area. In this study, an inverse correlation was noted between cross-sectional area and σ_f^N , which is representative of other thickness-dependent variables. Therefore, the differences in σ_f^N and toughness can be explained in part by the significantly dif-

ferent cross-sectional areas across the three preparation categories. Since the decrease in thickness in v-d AM is caused by compaction of the collagen fibres, rather than tissue loss, v-d AM is a thinner, denser version of the fresh tissue. The stress-strain measurements that require geometric dimensions to be known do not discriminate between a tissue that is thinned as a consequence of water loss (i.e., v-d AM) and a thinner homogeneous material that can resist more tensile force per unit area, recording values that suggest increased strength. To illustrate this, σ_f^N was re-calculated assuming a uniform AM thickness of 50 μm for all preparations, as previously reported (Oyen et al., 2004). This resulted in the new σ_f^N measurements being highest for fresh AM and lowest for v-d AM. The inverse relationship between thickness and apparent strength may explain reports of dried AM preparations (30 μm) having greater apparent strength than thawed AM (45 μm) (von Versen-Hoeynck et al., 2008). In contrast, Chuck et al. (2004) found the σ_f^N of wet AM strips to be comparable to that of rehydrated dried samples, which were significantly thinner.

While the effects of thickness on apparent strength necessitate accurate and precise measurements, the intrinsic relationship between thickness and AM strength varies between samples (Calvin and Oyen, 2007). The effects of dehydration on the collagenous matrix are likely to be deleterious (Zhang et al., 2011). Therefore, the intrinsic effects of drying on the mechanical properties of AM cannot be fully understood by stress-strain measurements. Despite having increased values of σ_f^N and toughness, it appears likely from the force-distance analysis that v-d AM is mechanically weaker than fresh and f-t AM. Due to intrinsic changes during drying, rehydration may not fully restore the tissue's former mechanical strength. Although dehydrating AM may reduce its mechanical strength, it appears to make it stiffer. Benson-Martin et al. (2006) have reported mean modulus values ranging from ~2.8 MPa for thawed AM to 17.3 MPa for partially dried AM, which

suggests an effect beyond that which can be explained by changes in thickness. In keeping with this observation, a study by Chuck et al. (2004) reported the modulus value of fully dried AM to be 86.1 MPa, whereas the lowest mean value of rehydrated dried AM was 11.8 MPa. Rehydration reversed the increased stiffness despite no increase in the thickness of dried AM preparations following rehydration. Personal experience suggests that v-d AM is more friable to handle than other preparations. While this does not preclude its use as a surgical biomaterial, it suggests a clinical disadvantage in comparison to f-t AM.

The constitutive mathematical model used in this analysis is a useful tool in describing the non-linear mechanical behaviour of AM. The differences between modelled and experimental data can lead to better constitutive models to explain tissue behaviour. The model incorporated experimental data on σ_f^N , λ_1 and G' to generate a new parameter, d . To make maximum use of the model, three fittings were tried. The first fitting calculated measurements of G' and d simultaneously over the sample's entire strain in order to construct the best possible fit by minimising the RMS. The second fitting used the value of G' derived from the initial 5% strain, generating new values of d . The third fitting was almost identical to the first, except that it incorporated an adjustment to the starting point to compensate for slackness or tension. The first and third fittings failed to expose significant differences in the mechanical properties of the different preparations, although in both cases, d was lower for v-d AM. Since d is associated with changes at higher strain, this suggests that modelled curves of v-d AM are less steep than fresh and f-t AM in the model equivalent of the collagen phase. When the value of G' was derived from the initial 5% strain, the difference in d across the preparations acquired statistical significance ($p = .016$). This indicates that with the experimental data acquired, the model exposed differences in the mechanical behaviour of the material that were

not present in f-t AM. This is advance over previous studies that recorded the pseudolinear modulus to differentiate between membranes. Using a similar constitutive model, Jabareen et al. (2009) detected a direct correlation between the soluble collagen content of AM and an increase in stiffness at higher strain. As an extension of this idea, it is possible that the decrease in d found in v-d AM may be caused by intrinsic weakness in the tissue.

The physical characteristics described by uniaxial testing are essentially surrogate quality indicators for surgical usefulness, yet these are undefined. There is no known UTS or E below which v-d AM is no longer a useful bio-material. It is assumed that the more robust the tissue, the better. Ultimately, however, the usefulness of v-d AM depends on the specific clinical indication.

Varying test conditions, such as humidity and temperature, can influence the hydration, and therefore the mechanical behaviour of collagen Pashley et al. (2003); Ntim et al. (2006). Since AM is already highly variable, this has the effect of producing data with high standard deviations. In this series of experiments, humidity and temperature were not controlled. This may have contributed to the high variability in the data produced. While fully hydrated, AM has a silky and elastic feel, but on drying it rapidly becomes sticky and friable. Thus, the experimenter has to work quickly to expertly cut and mount the sample, which rapidly loses water to the atmosphere. The elastic tissue tends to contract when laid out for cutting, so that a strip often has wider dimensions than intended. Tensile property testing can be invalidated by the AM sample drying out and by incorrect sizing of the sample.

Sample slippage and failure at the clamping points can nullify stress and strain failure calculations (Oyen et al., 2004; Jabareen et al., 2009). This can occur as a result of feathering of the edges during cutting, angulated mounting and incorrectly aligned grips. All of these factors were a potential

source of error that made it difficult to obtain consistent, repeatable results. The tests were refined over successive stages to give more control of the sample preparation and mounting steps. There was difficulty in ensuring that the samples were under the correct amount of tension at the start of the uniaxial tests. The TA.HD*plus* instrument has a force resolution of 0.1 g, which suggests that it was suitable for testing AM. However, it was not possible to adjust the static force to take up residual slack in the sample before the test run, which might have produced more consistent results.

Accelerated degradation assays of fresh, f-t and v-d AM samples were performed using microscopic imaging studies to compare the tissue appearances after incubation in 1% collagenase. The samples were fixed for SEM by lyophilisation, which gave an unusual whorl-like pattern on the stromal side of the AM. The tissues appeared to be in similar states of decay. The test is a basic assessment of the differences between preparations, and it calls for more refined qualitative assays, such as analyses of the change in weight of AM undergoing degradation (Fujisato et al., 1999; Ma et al., 2010).

Highly variable results were obtained by acoustic impedance testing, suggesting that the test was not useful in comparing AM samples. However, the results indicate that while some samples produced credible data, others failed to do so, recording values of G' that were close to zero. The reasons for this are unclear, but may reflect different levels of hydration, size and positioning or excessive noise on the instrument caused by water. The test was applied successfully to illustrate the difference between native AM and AM cross-linked by TG, although the sample size was small (Chau et al., 2012). This suggests that repeat experimentation is required to determine the specific causes of the high variability encountered.

High variability was encountered, too, using AFM. Amnion is not homogeneous, and indentation of the different components, from epithelial cells to BM and stromal collagen, produced widely differing results. The tips are

small enough to sample the different components of the tissue, and therefore the data they produce do not give an consistent impression of the material properties. Moreover, the membrane is sufficiently thin for measurement to be influenced by the surface supporting the tissue. The tendency of the tissue to form folds and tears could also contribute to the high level of variability. Although indentation with a bare tip suggested that trehalose produced increased surface stiffness and hardness, this effect was not consistent across different cone tip sizes. Conversely, indentation with a spherical bead did not return meaningful data and did not point to any differences between the AM preparations. One previous study by Lim et al. (2010) used phase images from AFM to study variations in hardness in AM; however, this did not return any objective data.

Another reason for the failure to acquire consistent data could be a failure to employ the correct analytical technique. According to Oyen and Cook (2009), the commonly used Oliver-Pharr analysis is more suited to plastic-elastic tissues such as bone. Soft tissue analyses have been characterised with models of viscous-elastic responses (Mattice et al., 2006). This is also suitable for elastomers, which have similar moduli to AM. The addition of trehalose could add glassiness to the AM surface; this would require the addition of a plastic component to the viscous-elastic model Oyen and Cook (2009).

4.5.2 Cross-linking

AM has been successfully cross-linked by chemical means (Ma et al., 2010; Kitagawa et al., 2011; Chau et al., 2012). A non-peer-reviewed study from the US Military reported successful cross-linking of AM by irradiation with blue light from a Xenon lamp, a 532 nm laser light and Ultraviolet C (Kochevar, 2010). In each case, the irradiance used was approximately 100 times lower than that used in the study presented here. In the current study, attempts

to cross-link AM by riboflavin/UVA were unsuccessful. This suggests either that the irradiance was too high or that photosensitisation was unnecessary. It seems likely that the covalent bonds in the collagen fibres were breaking down, leading to disorganisation and loss of crystallinity (Grant et al., 1973). The irradiance could not be adjusted in the instrument used in this study. Cross-linking of collagen can occur without photosensitisation, especially in thin tissues (Spoerl et al., 1998). This suggests a possible alternative approach to cross-linking AM collagens by irradiation. The use of alternative light sources should also be considered.

The methods used to detect the cross-linking are of interest. Using the method described by Wollensak and Redl (2008), soluble collagens were extracted from AM. Wollensak and Redl found evidence of cross-linked collagens by this method. The polymerised collagens formed thickened bands at the top of the gel that resisted electrophoretic movements. The absence of any bands in the UVA/riboflavin-treated AM lanes in the electrophoretic gels initially led to the supposition that the cross-linked collagens had precipitated out of solution. The four bands in the control lanes were thought to represent the trimeric, dimeric and monomeric collagen type I chains. However, the MS results indicated that most of the collagen was type III, rather than type I. The predominant peptide isolated was the α_1 chain of type III collagen. Smaller amounts of the α_1 chain of type I collagen were also present, along with smaller quantities of types V, II, XI and XXIII collagens. Types III and V collagen is present in much smaller amounts in AM than type I (Bryant-Greenwood, 1998). The type I collagen α_2 chain does not appear, suggesting its loss during solubilisation. The loss of these collagens in the riboflavin/UVA-treated AM suggests that no cross-linking has taken place.

TEM images were used to detect differences in collagen fibril packing. Since Wollensak et al. (2004) found a significant enlargement of the di-

iameter of corneal collagen fibres after cross-linking, the packing density of collagen fibrils in AM were assumed to be increased by cross-linking. The riboflavin/UVA-treated AM had a greater IFD than the non-cross-linked tissue, again suggesting that cross-linking had not taken place. XRD studies of AM by Cannon et al. (2007) showed regional variation in the packing density, suggesting that these differences could have been due to the location of AM sampling. The tensile tests further suggested that cross-linking had not occurred. The mathematical model was employed successfully, returning significant differences between the treated AM and controls in multiple variables, including ΔL , E_1 , E_2 and d_2 . These indicated that the treated AM was less stiff and more ductile than the controls, which is the opposite of what can be expected by cross-linking. The absence of cross-links which was confirmed by the ninhydrin assay, which indicated an increase in the free amine groups of the treated AM. Quick and inexpensive to perform, this was a very effective method of detecting cross-linking, as evidenced by the cross-linking index of 151% returned for the 1% glutaraldehyde-treated AM. Using this technique, Ma et al. (2010) found the maximum value of cross-linked amino groups in AM collagen molecules to be 45.6%, indicating successful cross-linking with EDC. The methodology used to determine the presence or absence of artificially induced cross-links in AM will be helpful in future studies.

4.6 Conclusion

One of the main drawbacks of vacuum-drying may be its effects on the material properties of AM. In this study, I demonstrated that v-d AM has a lower tensile strength than both fresh and f-t preparations, although the high level of variation between samples meant that statistical significance was not reached. Whereas stress-strain tests could not detect this differ-

ence because of the change in thickness across preparation categories, a novel mathematical model proved a useful discriminator. While attempts at cross-linking the membrane proved unsuccessful, the methods used to assess this can serve as a useful template. The next chapter focuses on biological aspects of the membrane, including its role in infectious and inflammatory processes.

Chapter 5

BIOLOGICAL ACTIVITY OF THERAPEUTIC AM

5.1 Introduction

The contribution of AM-derived factors to healing at the ocular surface is the subject of debate between those who favour the concept that therapeutic AM possesses biological activity, and those who take a pragmatic approach to its functionality as a physical membrane. While the physical properties of AM are essential to its therapeutic function, it has sometimes been assumed that soluble biological factors retained by therapeutic AM are beneficial to the injured eye. In this chapter, I consider the bioavailability in therapeutic AM of two classes of soluble factors, one that is potentially beneficial and the other potentially harmful. AMPs belong to a recently described class of molecules with the ability to kill pathogens. Conversely, MMPs and their inhibitors are well-known enzymes that have the potential to damage the ocular surface. I investigated the expression of AMPs in human AEC by cytometric bead analysis (CBA), western blotting and flow cytometry. Antimicrobial assays were also performed. I used zymography to demonstrate the elution of MMPs from therapeutic AM. Protein microarrays were obtained to show the relative quantities of MMPs and tissue inhibitors of MMPs (TIMPs). Questions remain as to whether AM is capable of modify-

ing the host response in a significant way. To address this, I conducted series of assays measuring the cytokine profile of stimulated human macrophages that were co-cultured with AM discs. After the assays, I performed electron microscopy on the discs to image the stromal adhesion of macrophages.

5.2 Literature review

The biological functions of AM can be viewed as those broadly concerned with homeostasis and those related to membrane rupture. Natural AM produces a wide array of cytokines, growth factors and enzymes that may be present in therapeutic AM (Dua et al., 2004). The concept of AM as a biological dressing can be traced to its use in non-ophthalmic surgical specialties (Talmi et al., 1990) and to its historical use in ophthalmology (Sorsby and Symons, 1946). Tseng et al. (2004) have made the case that IL-10, activin and protease inhibitors present in AM transplants have a role in suppressing ocular surface inflammation. Neurotrophic factors detected in AM include nerve growth factor (NGF), brain-derived neurotrophic factor (BDNF) and neurotrophin-3 (NT-3) (Uchida et al., 2000). Tseng et al. (2004) have suggested that these may contribute to scarless wound healing, as is observed in foetuses before the third trimester. Similarly, AM-derived growth factors, such as EGF, TGF- α , keratinocyte growth factor (KGF), hepatocyte growth factor (HGF), TGF- β 1 and TGF- β 2 were considered to contribute to epithelial healing (Koizumi et al., 2000). This thinking lies behind the experimental use of topical amniotic fluid (Castro-Combs et al., 2008) and amniotic membrane extract (He et al., 2008) to treat epithelial non-healing and ocular surface inflammation.

Not all the factors produced fit the narrative of a therapeutic tissue. For example, AM is well known to produce IL-6 and IL-8, which are inflammatory cytokines (Keelan et al., 1997), whereas IL-10 was not detected in AM

conditioned media (Hori et al., 2006). In addition, TGF- β is well known for its propensity to cause surgical scarring (Cordeiro et al., 2003). All TGF- β isoforms are produced by AM (Koizumi et al., 2000b). Indeed, TGF- β 1 is one of the principal isoforms expressed in corneal wound healing, delaying epithelialisation and promoting keratocyte proliferation and myofibroblast transformation (Carrington et al., 2006). Suppression of the TGF signalling pathway may therefore be a crucial aspect of the success of AMT. To explain this apparent contradiction, Tseng et al. (2004) suggested that the intracellular pathways that are switched on by AM-derived factors both induce mitogenesis and suppress TGF- β signalling. Corneal and limbal fibroblasts cultured on the stromal side of preserved human AM matrix showed reduced expression of TGF- β 1 and TGF- β 2 (Tseng et al., 1999). As well as suppressing the expression of TGF- β isoforms, AM also appears to suppress TGF receptors in fibroblasts (Lee et al., 2000). Nonetheless, while the view that therapeutic AM possesses biological function over and above its mechanical properties persists, Baum (2002) has argued that the true value of AM is its ability to provide mechanical protection against eyelid friction whilst at the same time allowing oxygen and moisture to reach the epithelium.

Prevention of intra-uterine infection is mediated in part by effector molecules of the innate immune system that have been described as natural antimicrobials, and which include AMPs (King et al., 2007a). AM has been reported to exert antimicrobial activity through direct contact with bacteria (Talmi et al., 1991), suggested to be due to soluble tissue factors, such as defensins (Kjaergaard et al., 2001). The elution of AMPs from therapeutic AM may protect the ocular surface against pathogens.

The gene regulatory networks of AM undergo a series of changes in the weeks leading up to parturition (Li et al., 2011). This is precipitated by maternal and placental hormones and pro-inflammatory cytokines, and in-

volves the activation of toll-like receptor (TLR) pathways of the innate immune system (Challis et al., 2009). A central transcription factor appears to be nuclear factor-kappa B (NF- κ B). As a result, a wide array of cytokines, chemokines and enzymes that elicit downstream biological responses are transcribed. AEC and mesenchymal cells up-regulate the production of MMP-9 (Xu et al., 2002) and release prostaglandin E₂ (PGE₂) (Kumar et al., 2004), which plays a key role in the initiation of contractions. MMPs are enzymes that are primarily concerned with breaking down the dense collagenous membrane at the time of birth (Bryant-Greenwood, 1998). While the potential for therapeutic AM to mediate collagenolysis is not clear, the elution of MMPs may contribute to disease states, evidenced by the reported case of corneal melting following AMT (Schechter et al., 2005).

5.2.1 Antimicrobial peptides

Defensins (α - and β -) and cathelicidins are two families of peptides widely found in bacteria, plants and animals (Wang, 2010). These AMPs have a wide spectrum of activity from wound-healing to immune cell activation (Frasca and Lande, 2012), and they potentiate the immune response against bacteria, yeasts and viruses (Sørensen et al., 2008) and possibly even acanthamoeba (Otri et al., 2010). They exert both indirect and direct antibacterial actions (Koczulla and Bals, 2003). α -defensins include a subfamily known as human neutrophil peptides (HNP). Together with human β -defensins (hBDs), they constitute the human defensins. Produced in epithelia, hBD3 is the most potent of the β -defensins and the one with the broadest spectrum of activity (Buhimschi et al., 2004). The only human cathelicidin, hCAP-18 is an 18 kDa protein that is cleaved following exocytosis, releasing a 4 kDa AMP called LL-37 (Sørensen et al., 2001). This peptide alters bacterial cell membranes and binds intracellular proteins and transmembrane receptors (Bucki et al., 2010). It is produced in macrophages,

neutrophils and epithelia (Sørensen, 2005). Each β -defensin and cathelicidin has a unique range of activity against an array of pathogens (Starner et al., 2005). Besides defensins and cathelicidins, there are a number of other AMPs with less prominent roles in human immunity, including liver-expressed antimicrobial peptides (LEAPs) (Henriques et al., 2010), ribonucleases (e.g., RNase-7) (Spencer et al., 2011) and psoriasin (Garreis et al., 2011). Besides augmenting the response to microbes, AMPs can directly interact with immune cells such as macrophages to modulate the response to infection (D'Este et al., 2012).

5.2.1.1 Foetal immunity

Innate immunity in the foetus is a complex system (Levy, 2007), in which AM plays an important part (Buhimschi et al., 2004). AMPs are considered to be a first line of neonatal defence against microbial invasion at birth (Yoshio et al., 2004). They are found both in AM and in the vernix caseosa, a creamy layer found on neonatal skin that is synthesised by the sebaceous glands of the foetus. hBD3 mRNA has been detected in cultured AECs by quantitative PCR by Buhimschi et al. (2004). These researchers also detected hBD3 by immunofluorescence in AEC from normal pregnancies at baseline, although it was up-regulated under stimulated conditions. AEC respond to different infectious stimuli through TLRs on their surface, either secreting inflammatory mediators or undergoing apoptosis (Gillaux et al., 2011). The production of hBD3 by the AEC is increased following TLR stimulation (Szukiewicz et al., 2008), and levels in the amniotic fluid rise following intrauterine insults like microbial infection and inflammation (Espinoza et al., 2003). hBD1 and 2 have also been detected in AEC, both by PCR (Stock et al., 2007) and by immunohistochemistry (King et al., 2007b). Psoriasin has been detected in amniotic fluid and in AEC by PCR (Porre et al., 2005).

Besides peptides, human AECs produce antimicrobial proteins, including elafin and secretory leukocyte protease inhibitor (SLPI) (Stock et al., 2007). The role of AM in the production of a number of relevant AMPs is unclear. For example, LL-37 has been detected in amniotic fluid and vernix Yoshio et al. (2003), yet its expression in AEC has not been shown. The vernix also contains HNPs 1 to 3 (Akinbi et al., 2004) and RNase-7 (Tollin et al., 2006). LEAP-1 (hepcidin), but not LEAP-2, has been detected in amniotic fluid in the first trimester (Evans et al., 2011).

5.2.1.2 Ocular surface immunity

Since the expression of AMPs on the ocular surface was first documented by Haynes et al. (1999), these molecules have come to be seen as components of major importance in the innate immune defence of the ocular surface (Garreis et al., 2010). The expression of a spectrum of corneal epithelium-derived AMPs is regulated in a co-ordinated response to different pathogens, suggesting an array of antimicrobial activities (Otri et al., 2010, 2012). AMPs that have been detected on the ocular surface include hBD1, 2 and 3, human cathelicidin (hCAP-18), LEAP-1 and LEAP-2 (McIntosh et al., 2005), HNP1, 2 and 3 (Ikeda et al., 2005), hBD9 (McDermott, 2004), psoriasin (Garreis et al., 2011) and RNase-7 (Mohammed et al., 2011).

The presence of AMPs in therapeutic AM is compelling, since it could augment the natural antimicrobial activity of the ocular surface. In a rat model of bacterial keratitis, Barequet et al. (2008) found that corneal ulcers had lower bacterial counts when AM was used as an adjuvant treatment. Direct anti-bacterial effects of AM have been demonstrated against *streptococcus* group A, *Staphylococcus aureus*, *Staphylococcus saprophyticus*, *Escherichia coli*, and *Pseudomonas aeruginosa* (Kjaergaard et al., 2001). On the other hand, the antimicrobial properties of AM have been attributed to a reservoir effect in which antibiotics are stored and released over an ex-

tended period (Gicquel et al., 2007). AM has been found to retain netilmycin, releasing it gradually over a period of 3 days (Mencucci et al., 2006). This slow release effect has also been described for ofloxacin (Resch et al., 2011).

5.2.2 Matrix metalloproteases

MMPs are multi-domain zinc-dependent endopeptidases which exist in active and inactive isoforms and are regulated at many levels (Nagase et al., 2006). There are 23 MMPs in humans, and, while their main function is to degrade the ECM, they mediate a diverse list of intra- and extracellular biological activities including neovascularisation and inflammation. They have been categorised as collagenase, gelatinase, stromelysin, matrilysin, membrane-type and other enzymes. Most MMPs are secreted as pro-enzymes in 1:1 stoichiometric complexes with TIMPs. Neutrophil-derived MMP-9 is one exception, being released in a free form in mice (Ardi et al., 2007). The production of most MMPs is tightly controlled, with the exception of MMP2, which is expressed constitutively by many tissues, secreted in a complex with TIMP-2 and activated by cell-surface membrane-tethered MMP (MT1-MMP) (Itoh and Seiki, 2006). TIMP-2 acts as a bridge between the MMP-2 proenzyme and the MT1-MMP activator. MMP-2 and MMP-9 are gelatinases that are expressed as pro-enzymes and activated by cleavage of a pro-peptide domain, which occurs in the extracellular compartment.

5.2.2.1 Collagenolysis in AM

All of the components of the MMP cascade are present in AM (Parry and Strauss, 1998). During gestation, MMPs operate in equilibrium with TIMPs to remodel the membranes and accommodate foetal growth (Bryant-Greenwood, 1998). Around the time of labour, MMP activity in the AM becomes a highly-regulated destructive process that is precipitated by inflammatory cascades (Menon and Fortunato, 2007). The balance can shift in favour of collagenoly-

sis as a result of infection and inflammation, with increasing levels of MMP-2, MMP-3, MMP-8 and MMP-9 in amniotic fluid. In rats, up-regulation of the interstitial collagenase MMP-1 pro-enzyme occurs immediately prior to labour (Lei et al., 1996). Simultaneously, type I collagen undergoes degradation, with the accumulation of characteristic three-quarter-length collagen peptides in the amniotic fluid.

MMP-2 and MMP-9 are key components of the MMP cycle in AM (Bryant-Greenwood, 1998). Both MMP-2 and MMP-9 degrade type IV collagen, found in the BM, whereas only MMP-2 degrades type I collagen, predominantly found in stroma. MMP-9 is barely detectable until term or pre-term labour (Demir-Weusten et al., 2007). A key proteolytic mediator, it can be induced by inflammatory mediators such as tumour necrosis factor (TNF) and IL-1 β in autocrine and paracrine loops (Arechavaleta-Velasco et al., 2002). In AM, MMP-9 is normally secreted in a non-angiogenic complex bound to TIMP-1 (Fortunato et al., 1997). It becomes activated in the ECM by the MT1-MMP/MMP-2 complex, a process requiring TIMP-2, as well as by other MMPs (Toth et al., 2003). MMP-2 acts in synergy with other collagenases to degrade fibrillar type I and III collagens (Parry and Strauss, 1998). MMP-1 and MMP-8 cleave the triple helix of type I collagen, which is then further degraded by MMP-2. These enzymes also cleave elastin, laminin, type IV and V collagens and other substrates, playing a central role in ECM degradation (Nagase et al., 2006). MMPs and TIMPs are compartmentalised within the AM layers. MMP-9 is associated predominantly with the epithelial layer, whereas MMP-2, produced by fibroblasts, accumulates mainly in the stroma (Xu et al., 2002).

5.2.2.2 Ocular surface metalloproteases

In the cornea, MMP-2 is present in normal and wounded epithelium and in stroma, while MMP-9 is present in the BM and superficial stroma of the

wounded cornea (Ye and Azar, 1998). Upregulation of corneal MMP-9 has been implicated in undesirable sequelae of ocular surface burns, namely failure of re-epithelialisation (Fini et al., 1998) and stromal neovascularisation (Ellenberg et al., 2010). While MMP-2 is involved in long-term remodelling of the corneal stroma after injury, MMP-9 degrades the epithelial BM, an event that precedes corneal ulceration. In animal models, proteolytic MMPs have been implicated in corneal melting (Fini et al., 1992). MMP-2 and MMP-9 are over-expressed in peripheral ulcerative keratitis, an immune-mediated corneal melting condition that principally affects sufferers of rheumatoid arthritis (Smith et al., 1999). The levels of MMP-8 and MMP-9 have been found to be significantly higher in corneal tissue with fungal growth than in non-infected corneal tissue, suggesting that they have a role in tissue destruction (Rohini et al., 2007).

Despite the widespread use of AM in ophthalmic surgery, the elution of potentially unwanted factors such as MMPs onto the ocular surface has not been greatly considered in the literature. Conversely, AM-derived TIMPs have been postulated to exert an anti-inflammatory effect on the surface of the eye (Hao et al., 2000). In mice with induced herpes simplex keratitis, AMT caused a rapid improvement in the appearance of the ulcers and a reduction in stromal inflammation, suggested to be due to suppression of corneal MMPs by AM-derived TIMPs (Heiligenhaus et al., 2005). Similarly, a study of alkaline burns in a rabbit model found that AMT suppressed corneal expression of MMP-2, MMP-9 and MT1-MMP (Takahashi et al., 2007). Koh et al. (2007) found mRNA of both TIMP-1 and TIMP-2 in the stromal and epithelial cells of both freeze-thawed and dried preparations of therapeutic AM, suggesting that MMPs are kept in their inactive forms by their inhibitors.

5.2.3 Modulation of inflammation

While therapeutically-applied AM is frequently assumed to dampen inflammation, the opposite outcome is also possible. This is suggested by clinical reports of uveitis after primary AMT (Srinivasan et al., 2007). Therapeutic preparations of AM contain non-viable allogeneic cells, which far from retaining any immunosuppressive activity are more likely to stimulate inflammation. Fresh AEC express MHC class I molecules, but not class II (Hori et al., 2006). AM can induce donor-specific delayed hypersensitivity, leading to its rejection by the sensitised recipient following serial AMTs (Gabler and Lohmann, 2000). Despite this, a number of studies have pointed to an anti-inflammatory effect, mediated either by soluble factors or by direct contact with components of AM.

5.2.3.1 Soluble factors

In a mouse mixed lymphocyte reaction, the proliferative response was found to be suppressed if fresh AM was in the medium Ueta et al. (2002). This did not occur if the AM was fixed in 100% ethanol first, suggesting that soluble AM-derived factors were responsible. The proportion of proliferating responder cells and cytokine levels in the culture supernatants were both significantly reduced. As known inhibitory cytokines, such as IL-4, IL-10 and TGF- β 1, could not be detected, the authors attributed the anti-inflammatory effects to unknown soluble factors. Li et al. (2005) isolated AECs by trypsin digestion of fresh AM and suspended them in culture medium for 48 hours. The AEC-conditioned medium inhibited neutrophil and macrophage chemotaxis towards MIP-2 and induced lymphocyte apoptosis. The AEC expressed transcripts for anti-inflammatory mediators such as TNF, TGF- β , TNF-related apoptosis-inducing ligand (TRAIL) and macrophage migration inhibitory factor (MIF). Lymphocyte apoptosis was partially inhibited by Fas ligand (FasL) antibody, suggesting that AEC-derived FasL was a key anti-inflammatory

factor. Splenocytes from Balb/c mice stimulated with anti-CD3e antibodies were cultured in the presence of small pieces of dried, intact AM and denuded AM in the medium (Park et al., 2009). Splenocyte proliferation was suppressed by both AM preparations, but more by the epithelialised AM, suggesting that epithelial-derived factors are involved. While fresh AM may contain soluble anti-inflammatory factors, these may be lost during AM processing (Hopkinson et al., 2006b).

5.2.3.2 Direct contact

Other studies have suggested that immune suppression depends on direct cellular contact with the AM stromal matrix. Marked suppression of IL-1 α and IL-1 β and up-regulation of interleukin-1 receptor antagonist (IL-1ra) was demonstrated in limbal epithelial cells cultured on the stromal matrix of AM (Solomon et al., 2001). Temporary AM patches were placed on rabbit eyes after excimer laser ablation, and viewed by TEM following retrieval (Park and Tseng, 2000). Neutrophils in direct contact with the AM stromal matrix, but not the BM, were noted to have undergone apoptosis within 24 hours. AM patching was seen to entrap polymorphonuclear leukocytes in the stromal matrix following alkaline burns in a rabbit model (Kim et al., 2000). On the human ocular surface, neutrophils, CD14⁺ monocytes/macrophages and lymphocytes underwent apoptosis following contact with the matriceal aspect of a temporary AM graft removed after a week (Shimmura et al., 2001). Macrophages are key antigen presenting cells involved in acute and chronic immune responses. Interferon (IFN) γ -activated murine macrophages seeded onto f-t AM stromal matrix underwent apoptosis between 24 and 48 hours later, the mechanism involving NF- κ B intracellular signalling pathways (Li et al., 2006b). This effect was not seen in quiescent cells, or in cells cultured on collagen, plastic or corneal stroma. The authors speculated that an unknown component of

AM could act synergistically with IFN γ to elicit apoptosis by suppressing pathways necessary for macrophage survival. The *in vitro* activity, viability and pro-inflammatory cytokine secretion of murine monocytes/macrophage RAW264.7 cells were subsequently shown to be suppressed by soluble AM extract containing spongy layer (He et al., 2008). This is supported by the observation that AM spongy layer induces a non-specific cidal effect on a variety of cell types (Lazutina et al., 2008). *In vitro* studies have demonstrated suppression of fibrotic mediators in conjunctival and lung fibroblasts seeded on the stromal aspect of AM, including IL-8 (Solomon et al., 2005).

5.2.3.3 Suppression of neovascularisation

Corneal neovascularisation is necessary to resupply ischaemic tissue, and is a highly orchestrated process that co-involves both MMP and inflammatory pathways (Ellenberg et al., 2010). AM-derived factors may also suppress neovascularisation. BALB/c mice with induced corneal neovascularisation that received topical human AEC supernatant for two weeks had fewer vessels than a control group receiving topical human IL-1RA, suggesting a synergistic anti-inflammatory effect of combined factors derived from AM (Kamiya et al., 2005). AEC-conditioned medium applied topically to the inflamed eyes of BALB/c mice appeared to suppress suture-induced neovascularisation Hori et al. (2006), whereas, in a rat model, induced corneal neovascularisation responded to different concentrations of AM extract in a dose-dependent fashion (Jiang et al., 2006). AM-derived soluble factors reported to have anti-angiogenic effects have included PEDF (Shao et al., 2004), collagen XVIII, thrombospondin-1 (TSP-1), TIMPs -1, -2, -3 and -4, IL-1ra and IL-10 (Hao et al., 2000). High levels of TIMP-2 found in AM culture medium were considered to inhibit corneal neovascularisation induced by bFGF in mice (Ma and Li, 2005). One study noted increased corneal expression of MMP-2 and MMP-9 following AMT for acute corneal

Table 5.1: AMP antibodies

Type	Target	Fluorochrome Wavelength/ channel	Manufacturer	Cat. No.	Origin	Clonality
Unconjugated	Psoriasis		Abcam plc	13680	Mouse	Mono
Unconjugated	LEAP-2		Phoenix Ltd	G-075-40	Rabbit	Poly
Unconjugated	RNAse-7		Human Protein Atlas	005690	Rabbit	Poly
Unconjugated	hBD1		Abcam plc	14425	Mouse	Mono
Unconjugated	hBD2		Abcam plc	66072	Mouse	Mono
Unconjugated	hBD3		Abcam plc	19270	Rabbit	Poly
Unconjugated	hBD3		Abcam plc	1128	Rabbit	Poly
Unconjugated	hBD3		Abcam plc	14422	Mouse	Mono
Unconjugated	hBD9		Eurogentec	Custom	Rabbit	Poly
Unconjugated	hCAP18		Abcam plc	80895	Mouse	Mono
Unconjugated	LL-37		Abcam plc	64892	Rabbit	Poly
Conjugated	LL37	PE 575/FL2	Phoenix Ltd	G-075-06	Rabbit	Poly
Conjugated	Vimentin	PE 575/FL2	Abcam plc	49918	Mouse	Mono
Secondary	Mouse IgG	APC 647/FL4	Invitrogen	A31626	Goat	
Secondary	Rabbit IgG	FITC 488/FL1	Invitrogen	A31627	Goat	

LEAP, Liver-expressed antimicrobial peptide, RNAse: ribonuclease, hBD: Human beta defensin, PE: Phycoerythrin, APC: Allophycocyanin, FITC: Fluorescein isothiocyanate

alkali burns in a rabbit model, but, paradoxically, decreased vascularisation (Rigal-Sastourné et al., 2002). Conversely, AM-derived basic fibroblast growth factor (bFGF) may promote neovascularisation (Koizumi et al., 2000b).

5.3 Materials and methods

AMP expression in fresh AEC was investigated by western blotting, CBA and flow cytometry. A reference guide for the antibodies used for these techniques is provided in table 5.1.

Table 5.2: Western blotting of AMPs

WB	AM	AMP	Optimising step
1	2 × extract	hBD3	
2	5 × extract	hBD3	Load increased to 40 µg per well
3	1 × extract	hBD3	rhBD3 control
4	1 × extract	hBD3	AM fractionated to remove proteins >30 kDa
5	3 × extract	hBD3	Overnight incubation in TBST _x ; elution by HPLC
6	2 × AEC	hBD3	Tricine gel
7	1 × extract	hBD1, LL-37	AM fractionated to remove proteins >30 kDa
8	1 × extract	hBD1, LL-37	Unfractionated

WB, western blot; AMP, antimicrobial peptide; r, recombinant; fr, fresh; HPLC, High performance liquid chromatography

5.3.1 SDS-PAGE/western blotting

A series of western blots were performed using protein extract from whole AM or from AEC to detect hBD3 (5.1 kDa), LL-37 (4.5 kDa) and hBD1 (4.5 kDa). Optimisation steps included increasing the protein load, modifying the test conditions and adding positive controls (table 5.2).¹

5.3.1.1 Sample preparation

Samples of whole fresh and v-d AM and AEC were extracted in Tris-buffered saline containing 1% Triton X-100 (TBST_x). The whole AM extracts were prepared for loading into Bis-Tris gels, whereas the AEC samples were loaded into both Bis-Tris and Tricine gels. As positive controls, proteins from mixed placental tissue and tonsil were extracted in the same way as the whole AM. The mixed placental tissue (chorion and AM) was obtained during AM processing. Tonsil samples were obtained from elective tonsillectomy surgery. Both LL-37 and hBD1 are expressed in non-inflamed tonsil epithelium (Song et al., 2006; Chae et al., 2001). Recombinant LL-37 (Hycult® Biotech, Plymouth Meeting, PA, USA) and recombinant hBD3 (ABE1621, Source Bioscience UK Ltd, Nottingham, UK) were obtained as

¹This work was done in collaboration with Miss Beth Nancolas.

specific AMP positive controls. Rabbit polyclonal anti- β actin antibody (Cell Signaling, 4967) was obtained as a loading control to ascertain even protein distribution in the lanes.

Whole AM AM samples were weighed and placed in universal containers containing TBST_x, 1 mL per 200 mg tissue. The samples were then removed and placed in a mortar pre-cleaned sequentially with TriGene disinfectant (MediChem International, Kent, UK), DI H₂O and 100% ethanol. Liquid N₂ was poured onto the samples, snap-freezing them to make them hard and brittle. Once completely frozen, they were tapped into smaller fragments, and then ground into a powder using a sterile pestle. The fine powder was then added to Falcon™ tube (BD Biosciences, Oxford, UK) containing TBST_x and mixed briefly. The protein suspension was spun in a centrifuge (Andreas Hettich GmbH and Co. KG, Tuttlingen, Germany) at RCF 1780 $\times g$ at 4 °C for 60 mins to remove insoluble material from the AM extract. The supernatant was decanted into a separate tube. To maximise protein concentration, the samples were placed in Vivaspin spin columns (GE Healthcare) with a 3 kDa MWCO and filtrated by centrifuging for several hrs at 1780 $\times g$. The samples in one blot were also fractionated in 30 kDa spin columns to remove large molecular weight proteins. One sample of AM extract was eluted by high performance liquid chromatography (HPLC) for purification.² A sample of AM extract processed by a colleague was obtained as a positive control, as positive staining for hBD3 had been obtained following overnight incubation of the AM in TBST_x.³

AEC For AEC extract, thermolysin denudation of the AM was performed. Incubation in thermolysin solution was carried out in the presence of a protease inhibitor cocktail (Cat. No. P2714, Sigma-Aldrich, UK). The AM sub-

²Courtesy of Dr Chen Peng.

³Courtesy of Dr Manu Mathew.

strate was removed from the PBS, leaving behind a suspension of whole AEC. The single cell suspensions were centrifuged briefly at 4°C at 300 ×g, washed in PBS and placed on ice to minimise protein degradation.

5.3.1.2 Protein quantification

The 2-D Quant kit (GE Healthcare Life Sciences, Amersham, UK) was used to measure protein concentrations. The manufacturer's instructions were followed. A standard curve was prepared using incremental quantities of 2 mg/mL BSA in 1.5 mL Eppendorf tubes. A volume of 1 - 50 µL of each sample to be assayed was transferred by pipette into an Eppendorf tube (exact volume depended on the expected protein concentration). A volume of 500 µL of precipitant was added to each tube, which was then vortexed briefly. A volume of 500 µL of co-precipitant was added, and the tubes were inverted before centrifuging at 10 000 ×g for 5 mins. The supernatants were removed completely using a micropipette. A volume of 500 µL of 20% copper solution in DI water was added to the pellets, followed by 1 mL of a 1:100 dilution of working colour reagent. The samples were incubated for 15 - 20 mins. Absorbance was read at 490 nm, and compared to the BSA standard curve using Softmax® software (MDS Analytical technologies, Toronto, Canada). The desired protein concentration was approximately 1.0 - 2.0 µg/µL.

5.3.1.3 Protein extraction

Bis-Tris gels Loading Buffer (2 ×) was prepared by mixing 4 × NuPage® LDS Sample Buffer (5 parts), 1.0 M DTT (1 part) and DI H₂O (4 parts). The Loading Buffer was added to the AM extracted in TBST_x in a 1:2 ratio.

Tricine gel The AEC pellet was extracted directly into 5 mL Novex® 2 × Tricine SDS Sample Buffer containing 0.1 g DTT. For non-reducing conditions, DTT was omitted.

5.3.1.4 Sample loading

The protein load was typically between 20 and 40 μg per well in a maximum volume of 28 μL . The protein sample with the lowest concentration was taken to calculate the baseline volume required. The samples were denatured by heating to 95°C for 4 mins and vortexed prior to loading.

5.3.1.5 Protein electrophoresis

Bis-Tris gels A litre of running buffer was prepared from the concentrated MES/ SDS buffer, using DI H₂O. A protease inhibitor (Complete, Mini, Roche, Mannheim, Germany) was added to the buffer (one tablet per 7 mL). The gels used were NuPage® 12% Bis-Tris 1.0 mm 12-well Novex gels (Invitrogen, Paisley, UK). The gels were prepared as described previously and loaded into the Novex II module tank filled with running buffer. NuPage® antioxidant (0.5 mL) was added to the central tank, which was inserted onto the Novex PowerEase® 500 Power Supply for electrophoresis. Long-tip dispensers were used for loading. A volume of 3 μL of Rainbow™ recombinant protein molecular weight marker (GE Healthcare, Amersham, UK) was loaded into wells adjacent to the samples of interest, which were loaded from left to right. Electrophoresis was carried out for 35 mins at 200 mV.

Tricine gels An acrylamide gel (Novex® 10-20% Tricine gel, Invitrogen) was used to resolve the low molecular weight peptides from the AEC extract. A volume of 3 μL of Rainbow™ ultra-low molecular weight markers were used (GE Healthcare, Amersham, UK). Electrophoresis was performed using the Novex® Tricine Running Buffer.

5.3.1.6 Protein transfer

Transfer buffer was made up by adding 200 mL methanol to 750 mL DI H₂O and 50 mL of NuPage® Transfer Buffer (20 ×). Immobilon PVDF membranes (Millipore, Massachusetts, USA) were soaked in methanol and then transferred to a tray containing sponges and blotting papers soaked in transfer buffer. The gels were retrieved from the casing. The blotting apparatus was assembled as described previously and loaded into the tank. The running time was 1 hr at 30 V. The Novex® Tris-Glycine transfer buffer was used for the Tricine gels. At the end of this step, the membranes were transferred to a tray containing DI water and blocked in TBS-TM blocking buffer for 1 hr on a rocker.

5.3.1.7 Incubation with primary antibody

Primary antibody was diluted to an appropriate concentration in primary antibody buffer (TBS-TM). For whole AM extract, rabbit polyclonal anti-hBD3 (ab1128 and ab19270) and mouse monoclonal anti-hBD3 (ab14422) were used at a concentration of 1 in 750. Rabbit anti-LL-37 (G-075-06, Phoenix Pharmaceuticals Ltd) and mouse anti-hBD1 (ab14425, Abcam) were used at a concentration of 1:500. For AEC extract, two rabbit anti-hBD3 antibodies (ab1128 and ab19270, Abcam) were used at a concentration of 1:500. The membranes were transferred into trays containing 10 mL of primary antibody in TBS-TM. The trays were kept on a rocker overnight at 4°C, or at room temperature for 4 hrs.

5.3.1.8 Detection of protein bands

The membranes were washed in TBST for 5 mins × 3, washed and incubated in 10 mL of AP-conjugated goat anti-rabbit secondary antibody (Cat. No. 7054, Cell Signaling Technology, Inc., Beverly, MA) at a dilution of 1:5000 for 1 hr. They were then washed × 1 for 15 mins and × 3 for 5 mins

in TBST. A volume of 8 mL of substrate solution (BCIP/NBT purple liquid substrate, Sigma) were added for 5 - 10 mins until protein bands appeared. The blots were washed and dried before being scanned and labelled using Adobe® Photoshop® CS4 software.

5.3.1.9 Minigel staining

Gels from western blots were stained in Simply blue™ SafeStain (Invitrogen) to highlight the protein bands. The gels were placed in a glass dish with DI H₂O and microwaved × 3 for 1 min. They were then placed in 20 mL Simply blue™ SafeStain for 1 hr, rinsed off in DI H₂O for 4 hrs and dried.

5.3.1.10 Gel drying

Destained gels were washed × 3 for 2 mins in DI H₂O (50 mL per mini-gel) on a rotary shaker. Gel-Dry™ drying solution (35 mL per mini-gel) was added. The gel was equilibrated in the Gel-Dry™ Drying Solution by shaking the gel for 5 mins in the StainEase® Gel staining tray. One sheet of cellophane at a time was immersed in the Gel-Dry™ drying solution, making sure to cover both sides of the sheet with solution. One side of the DryEase® Gel drying frame was placed with the corner pin facing up, on the DryEase® Gel Drying Base. Pre-soaked cellophane was placed over the base/frame combination, so the cellophane lay over the inner edge of the frame. The gel was laid on the center of the cellophane sheet making sure no bubbles were trapped between the gel and the cellophane. The second sheet of cellophane was laid over the gel so that no bubbles were trapped between the cellophane and the gel. Any wrinkles in the assembly were smoothed out with a gloved hand. The remaining frame was aligned so that its corner pins fit into the appropriate holes on the bottom frame and the plastic clamps were sealed onto the four edges of the frames. Drying took

between 12 and 36 hrs depending on humidity and gel thickness.

5.3.2 Mass spectrometry

Mass spectrometry (MS) was performed on one band identified on western blotting. The technique is described in Chapter 4 (subsection 4.3.7).

5.3.3 Cytometric Bead Analysis⁴

CBA is a technique that can be used for detecting protein and measuring protein concentrations. It uses a system of beads of different sizes coated with different fluorophores. The beads can be conjugated to the complement-binding portion of antibodies. Thus, beads can be coated with one type of antibody that is specific for an epitope of interest. The bead-antibody conjugates can be used to ‘capture’ the relevant protein. A second, fluorochrome-labelled antibody is used to detect the protein. The beads can be discriminated by flow cytometry. This operates by directing a single wavelength beam of laser light onto a stream of liquid containing the beads of interest. Each bead both scatters and emits light. The forward scatter reflects the bead size, while the wavelength of the emitted light corresponds to the bead and the detection antibody fluorophores. The resulting signals can be converted into digital data and recorded as plots. Hence, bead mixtures can be used to detect and quantify an array of analytes of interest.

A CBA assay was performed on supernatants of fresh, f-t and v-d AM extracts from two AMs (1 and 2) to detect hCAP18. The antibody chosen for capture was a mouse monoclonal antibody to the pro-region (115-NQARGSF-121) of hCAP18 (ab80895, Abcam plc, Cambridge, UK). A purified polyclonal rabbit anti-LL-37 antibody (Catalog No.: G-075-06, Phoenix Pharmaceuticals, Inc., Belmont, CA) was used as a detection antibody. The

⁴This work was carried out with the help of Dr Sue Fox, Ms. Jane Limer of BD Biosciences and Mrs Jackie Glenn.

capture beads were pre-coated with APC.

5.3.3.1 Labelling of detection antibody

The LYNX Rapid Conjugation Kit® (AbD Serotec, North Carolina, USA) was used to label the detection antibody, G-075-06, with R-phycoerythrin (RPE). A total of 60 µg of antibody in H₂O (0.5 µg/µL) was mixed with 12 µL of Modifier reagent. This mixture was added to 100 µg of the lyophilised RPE label and incubated at room temperature overnight. Next, 12 µL of Quencher reagent was added.

5.3.3.2 Bead preparation

A Functional Bead Conjugation Buffer Set (BD Biosciences) was used to covalently link the capture antibody, ab80895, to the surface of fluorescent beads. Before starting the procedure, all reagents were brought to room temperature. The beads were covered with aluminium foil to protect from light at all times. The samples were free of detergents. Aliquots of 1.0 M DTT in H₂O were prepared. The functional beads for conjugation were vortexed for 30 secs, prior to transfer to a microcentrifuge tube (75 µL of beads for a 500 test reaction). The beads were sonicated for 1 min. A volume of 1.9 µL of 1 M DTT was added to the microcentrifuge tube containing the functional beads and vortexed for 5 secs. The beads were incubated for 1 hr at room temperature and vortexed every 15 mins. A volume of 1 mL of Coupling Buffer was added and vortexed for 5 secs. The beads were pelleted by centrifugation at 900 × *g* for 3 mins, and the supernatant discarded. This was repeated × 2. The bead pellet was resuspended with 20 µL of Coupling Buffer.

5.3.3.3 Capture antibody modification

A microcentrifuge tube containing 90 μL of the capture antibody (0.5 $\mu\text{g}/\mu\text{L}$ in H_2O) was covered with aluminium foil. A stock solution of 2 mg/mL of the 3-sulfo-*N*-hydroxysuccinimide ester sodium salt of 4-(*N*-maleimidomethyl)cyclohexane-1-carboxylic acid (sulfo-SMCC) was prepared in DI H_2O immediately before use. A volume of 2 μL of sulfo-SMCC was added to the capture antibody solution in the microcentrifuge tube and vortexed for 5 secs. The protein was incubated in darkness for 1 hr at room temperature and vortexed every 15 mins.

5.3.3.4 Buffer exchange

A Bio-Rad Spin Column (Cat No. 732-6231, Bio-Rad Laboratories, Hemel Hempstead, UK) was filled with Coupling Buffer and drained $\times 3$. The spin column was placed in a 12 \times 75 mm test tube and centrifuged at 1000 $\times g$ for 2 mins, and the tube was discarded. The spin column was placed in a new 12 \times 75 mm test tube. The entire volume of antibody/sulfo-SMCC solution was added to the spin column and centrifuged at 1000 $\times g$ for 2 mins 15 secs to transfer the modified protein into the 12 \times 75 mm test tube in Coupling Buffer.

5.3.3.5 Protein Conjugation

The modified capture antibody was transferred from the 12 \times 75 mm tube to the microcentrifuge tube containing the fluorescent beads and microcentrifuged for 5 secs. The antibody and beads were incubated for 1 hr at room temperature in darkness, and vortexed every 15 mins. Aliquots of 2 mg/mL of *N*-Ethylmaleimide (NEM) in DMSO were prepared, and 2 μL added to the microcentrifuge tube containing the functional beads and capture antibody. The microcentrifuge tube was vortexed for 5 secs and incubated for 15 mins. A volume of 1 mL of Storage Buffer was added to the microcentrifuge

tube. The beads were pelleted by centrifugation at $900 \times g$ for 3 mins and the supernatant discarded $\times 3$. The bead pellet was then resuspended in 0.5 mL of Storage Buffer. The beads were now at a final concentration of approximately 6×10^6 beads/mL and ready to be validated.

5.3.3.6 Confirmation of conjugation of beads

Confirmation of conjugation was carried out on a BD LSR II™ flow cytometer. Three 12×75 mm test tubes were labelled: (1) diluted functional beads, (2) negative control, and (3) test sample. The beads were vortexed for 5 secs. 245 μ L of Wash Buffer from one Master Buffer Kit used to run the assays was added to the diluted functional beads tube (1). A 5 μ L sample of the functional beads were added to the diluted functional beads tube (1) and vortexed for 5 secs. A volume of 50 μ L of beads were transferred from the diluted functional beads tube (1) to the negative control tube (2) and to the test sample tube (3). A volume of 50 μ L of wash buffer was added to the negative control tube (2). A volume of 50 μ L of a rabbit phycoerythrin (PE) anti-Ig Detector (BD biosciences) was added to the test sample tube (3). Both the negative and test sample control tubes were vortexed for 5 secs and incubated for 30 mins in the dark, at room temperature. A volume of 1 mL of Wash Buffer was added to both tubes, which were centrifuged at $1000 \times g$ for 5 mins. Bead pellets for both tubes were re-suspended with 150 μ L of Wash Buffer. The tubes were processed on the BD LSR II™ flow cytometer.

5.3.3.7 Cytometric analysis⁵

The BD LSR II™ flow cytometer was set up by starting the instrument and the computer, following the 2007 User's Guide (BD Biosciences). BD FACS-Diva software was activated on the desktop. The required optical filters for APC (beads) and PE (antibody) fluorochrome detection were set up. The flu-

⁵Performed by of Dr Jane Limer of Becton, Dickinson and Company, UK

idics were checked and primed. The software parameters were set up to read forward scatter and the fluorochrome intensity. An unstained control tube was installed onto the sample injection port. The control was processed and data acquired. This was used to adjust the forward and side scatter voltage and forward scatter threshold to gate the population of interest. A gate was applied to the singlet population of beads. The first sample tube was then inserted onto the sample injection port. Digitised data was recorded via channels for APC and PE. The mean fluorescence intensity (MFI) of control and test populations of 1000 beads was measured to ensure correct labelling of the beads.

5.3.3.8 Protein extraction

Protein extracts from whole f-t and v-d AM samples were obtained by grinding under liquid N₂ as previously described (section 5.3.1.1). The supernatant was obtained from the ground AM. The total concentration of protein was measured. CBA was performed directly on the AM supernatants.

5.3.3.9 Detection of antigen in samples

Mixed Capture Beads were vortexed for at least 5 secs and 25 µL added to each assay tube. A volume of 25 µL of sample was added to the assay tubes, which were mixed gently and incubated for 3 hrs at room temperature away from direct exposure to light. A volume of 10 µL of the detection antibody (10% or 20%) was added to each assay tube. The tubes were mixed gently and incubated for 2 or 4 hrs at room temperature in the dark. A volume of 1 mL of Wash Buffer was added to each assay tube and these were centrifuged at 4°C for 5 mins at 200 ×g. The supernatant from each assay tube was discarded. A volume of 300 µL of Wash Buffer was added to each assay tube and mixed gently before analysis on the BD LSR II™ flow cytometer. Appropriate BD CBA Flex Setup instrument settings were used. The MFI

of the test sample was compared to a negative (blank) sample.

5.3.4 Flow cytometry

The technique of flow cytometry can be used to analyse populations of cells. The principles of this technique have been explained in relation to CBA (above). For analysing cells, another parameter, side scatter can be measured to represent the cell's inner complexity. The cells can be labelled directly with conjugated primary antibodies, which can be detected by their fluorophores. These can be directed at the cell surface or the internal cell. Flow cytometry was performed on permeabilised AEC from five AMs (including one optimisation step), by using an array of primary antibodies against a range of AMPs to document their expression in human AEC. The AMPs investigated in this way included psoriasin, LEAP-2, RNase-7, hBD2, hBD3 and LL-37.

5.3.4.1 Preparation of single cell suspension

A technique for preparing single cell suspensions of human AEC by trypsinising whole AM in culture medium was described by Casey and MacDonald (1996). Gicquel et al. (2009) obtained total detachment of individual epithelial cells by incubating whole AM pieces in thermolysin for 15 mins at room temperature, leaving a clean BM. In the current study, AECs were lifted using the thermolysin method described in subsection 3.3.1.3. The remaining AM tissue was removed to leave a cell suspension. A wash buffer was prepared by adding 1% sodium azide and 3% BSA to 1 × PBS. The detached cells were washed in PBS and centrifuged × 2 for 5 mins at 4°C at 200 × *g*. After centrifugation, the cells were fixed by resuspending the pellet in 0.5% FA in 100 µL of wash buffer. The cells were centrifuged one more time and resuspended for 15 mins at 4°C in 100 µL of permeabilising reagent consisting of 0.2% Tween 20 in wash buffer. The cells were blocked in 300 µL of

1:10 normal goat serum (NGS) for 30 mins, They were then washed in 1 mL of permeabilising reagent in preparation for flow cytometry.

5.3.4.2 Optimisation of permeabilisation and fixation

Flow cytometry was carried out on the AEC from one AM to assess the effects of permeabilisation and formaldehyde (FA) fixation of the cells. Cells were either permeabilised and fixed in 0.5% or 3% FA or non-permeabilised and fixed in 0.5% FA. The cells were incubated with rabbit polyclonal anti-hBD3 (ab19270, 1:100) overnight at 4°C and with secondary antibody conjugated to Alexa Fluor® fluorescein isothiocyanate (FITC) for 1 hr. Negative controls were incubated with secondary antibodies conjugated to FITC without primary antibody.

5.3.4.3 Antibody staining

AEC obtained from four AMs were stained with an array of antibodies in four separate flow cytometry experiments. Separate samples were prepared to test for each AMP. For negative controls, samples were incubated with secondary antibodies conjugated to Alexa Fluor® fluorophores FITC and allophycocyanin (APC) without primary antibody. Vimentin, an intermediate filament protein, was used as a positive control for PE-conjugated antibodies. The primary antibodies used in each experiment are shown in figure 5.3. The cell pellets were resuspended in 1 mL of permeabilising reagent. A volume of 30 µL of primary antibody (1:50 - 1:100 in wash buffer) was added and left to incubate at room temperature for 2 hrs. In one experiment (no. 4), the samples were incubated overnight at 4°C, and the experiment continued the next day. The cells were then washed in 1 mL of permeabilising reagent. A volume of 30 µL of secondary antibody (1:1000) was added, incubating at room temperature in the dark for 1 hr. The cells were washed in 1 mL washing buffer, pelleted and resuspended in 500 µL PBS for flow

Table 5.3: Primary antibodies, flow cytometry

EXPT 1	EXPT 2	EXPT 3	EXPT 4
Psoriasis (m), 1:50	Psoriasis (m), 1:50	Psoriasis (m), 1:50	Psoriasis (m), 1:50
LEAP-2 (r), 1:100	LEAP-2 (r), 1:100	LEAP-2 (r), 1:100	LEAP-2 (r), 1:100
hBD2 (m), 1:50	hBD2 (m), 1:50	hBD2 (m), 1:50	RNAse-7 (r), 1:100
hBD3 (m), 1:50	hBD3 (m), 1:50	hBD3 (m), 1:50	hBD3 (r), 1:100
RNAse-7 (r), 1:100	RNAse-7 (r), 1:100	hBD3 (r) 1:100	LL-37 (r, PE), 1:50
		LL-37 (r), 1:100	

Expt, experiment; m, mouse; r, rabbit; PE, phycoerythrin-conjugated

cytometry analysis. Each sample underwent flow cytometry once.

5.3.4.4 Flow cytometry

The flow cytometers used for these experiments were either the BD LSR II™ flow cytometer or the Beckman-Coulter FC 500 Analyzer (Beckman-Coulter Inc., Pasadena, CA, USA) equipped with CXP software.⁶ The FC 500 instrument was prepared using the 2004 Cytomics FC 500 Instructions for Use. Briefly, the sheath tank was filled with water and the waste tank emptied. The computer software was activated, and protocols were created with the parameters to be acquired for each experiment, such as instrument settings. These were based on pre-ordained protocols. Panels were created to enable the number of tubes required to be programmed. The fluorescence channels selected included FL1 (FITC), FL2 (PE) and FL4 (APC). Samples were loaded onto the carousel with 32 tube positions, which was placed in the multi-tube carousel loader for automated sampling. Unstained samples were run initially to check the parameters. Polygonal gates were superimposed on the two parameter dot plots to capture representative batches of cells, avoiding extremes of forward and side scatter. Thus, cells with abnormally high or values were excluded as possible cell fragments or swollen cells. Samples were analysed in sequence, and data was saved in transfer-

⁶Performed with the assistance of Mrs Nina Lane, Flow Cytometry Technician, Faculty of Medicine & Health Sciences.

able .fcs data files.

5.3.4.5 Data analysis

The data files were analysed separately using Weasel software (version 3.0.2) available from the Walter and Eliza Hall Institute of Medical Research at the University of Melbourne, Australia. The logarithm of fluorescence at the appropriate wavelength for each sample was plotted against forward scatter on a linear scale. Cut-off markers were set for the negative and positive controls, separating 99.5% of recorded events from the remaining 0.5%. The cut-off markers were then applied to the test samples for direct comparison with the controls. This returned the percentage of positive events (antibody bound to cell antigens) for each analyte above baseline in the cell population of interest (Shapiro, 2003).

5.3.5 Antimicrobial assays⁷

Antimicrobial activity was determined from the minimum inhibitory concentration (MIC). Briefly 50 μ L/well of lysogeny broth (LB) medium was added to a 96-well plate. In column 1, 50 μ L of whole AM extract (fresh AM, f-t AM, denuded AM, v-d AM, 10% v-d AM) at 100 μ g/mL was applied in triplicate. Using a multichannel pipette serial dilutions were made across the plate leaving column 12 containing medium only to act as a control. A selection of Gram positive (*Staphylococcus epidermidis*, *Staphylococcus aureus*, and *Corynebacterium diphtheria*) and Gram negative (*Moraxella*) bacterial strains were grown up in LB broth until the optical density at 600 nm reached 0.1. Bacterial cell suspensions were then added to the plate using a multichannel, at 50 μ L/well. Plates were incubated overnight at 37°C for 24 hrs. Results were assessed visually with the MIC being equivalent to the last clear well.

⁷This work was performed by Dr Claire Allen.

Circular discs of chromatography paper were saturated with concentrated AM extract and incubated with LB agar plates seeded with the bacterial strains. Antibacterial activity was assessed using the radial diffusion method. This involved measuring zones of inhibition around the discs saturated with extract. Alternatively, 1 × 1 cm sheets of AM were directly applied to Petri dishes containing lawns of bacterial strains grown on LB agar. AM extract and bacteria were incubated for 24 hrs and antimicrobial activity was assessed visually.

AM sections were saturated in a pre-prepared antibiotic solution for 10 mins. A volume of 10 mL of the following was added to 500 mL of Endosol; Gentamicin 200 mg/mL, Imipenem 10 mg/mL, Nystatin 125,000 U/mL, Polymyxin B 10 mg/mL and Vancomycin 2.5 mg/mL. Membranes were then immersed in sterile PBS for different periods of time (10 mins, 20 min, 60 mins, 2, 6, 12, 24 and 48 hrs) before extracting proteins from the tissue using a liquid N₂ bath and a pestle and mortar. Antimicrobial MIC assays were then performed using the assay described previously.

5.3.6 Protein microarray

As part of the study on the MMP/TIMP cascade in therapeutic AM, the localisation and concentration of the enzymes and their inhibitors in the different preparations were investigated by a quantitative protein microarray. The samples were sent to an external provider (Aushon BioSystems Inc., Billerica, MA) for chemiluminescent antibody-based microarrays (SearchLight), which provide quantitative data on selected biomarkers. The following MMPs and TIMPs were selected for analysis: MMP-1, MMP-2, MMP-3, MMP-7, MMP-8, MMP-9, MMP-10 and MMP-13, TIMP-1 and TIMP-2. The SearchLight results were normalised with reference to the protein concentrations of the analysed tissues, and levels of analytes expressed as picograms per milligram of tissue.

5.3.6.1 Sample preparation

Four AMs were processed for protein microarrays.⁸ The preparations included fresh, de-epithelialised (thermolysin-treated), v-d and f-t AM. The tissue was sectioned into pieces measuring approximately 10 × 10 cm and weighing approximately 1 g. The samples were extracted by grinding in liquid N₂ and adding the homogenate to 1 mL of TBST_x per 250 mg tissue. The samples were centrifuged at 20 000 × *g* for 15 mins at 4°C to remove insoluble material. Protein quantification was carried out on all supernatants in duplicate using a 2-D quantification kit (GE Healthcare, UK).

5.3.6.2 Data analysis

Missing data were ignored rather than imputed. All of the analytes had at least two data values. The median was used for analysis. For ease of analysis, when analyte levels were below the threshold for detection, they were given a value of 0 pg/mg. Matched non-parametric tests (Friedman) with post-hoc analyses (Dunn's multiple comparison test) were used to compare the analytes in the different preparations.

5.3.7 Zymography⁹

To determine whether MMP-2 and MMP-9 are eluted from therapeutic preparations of AM, zymography was performed on AM supernatants and homogenates to investigate the presence of MMP-2 and MMP-9 in fresh and preserved AM immediately after processing the tissue for clinical use (0 hrs) and following a period of incubation (24 or 48 hrs).

⁸This work was carried out in collaboration with Dr Claire Allen.

⁹This work was carried out with the help of Dr Imran Haq.

5.3.7.1 Sample preparation

AM was obtained in the usual way. Sections of fresh tissue, 5 cm × 5 cm in size, were each placed into separate polypropylene universal sample containers containing 5 mL RPMI-1640 medium (Sigma-Aldrich). The 500 mL bottle of culture medium was pre-treated with 1mL Gentamicin/Amphotericin B suspension (Cascade Biologics Inc., Eugene, Oregon, USA). Further sections were vacuum-dried or frozen for a minimum of 3 hrs in 5 mL PBS. After drying, v-d AM was reconstituted in 5 mL of DI H₂O. F-t AM was thawed for 30 mins in a 37°C water bath.

Matched pairs of each of the fresh, f-t and v-d AM sections were removed from their respective media and placed in 1 mL RPMI-1640 medium per 200 mg of wet tissue. After 5 mins, a volume of 10 µL of supernatant from one set of samples was extracted. The containers were then sealed and incubated at 37°C. The storage and wash media of the f-t AM was also sampled to assess the elution of MMPs. At this time point (baseline, 0h), the matched samples were homogenised by grinding AM in liquid N₂ and suspending the lysate in 1 mL of TBST_x per 200 mg wet weight. The suspension were centrifuged at 12 000 × *g* to remove particulate matter. At the end of the incubation time (24 or 48 hrs), the supernatants were sampled again. The samples were then homogenised as before. In this way, supernatants and homogenates were obtained at baseline and after 24 or 48 hrs.

A volume of 10 µL of supernatant/homogenate was mixed with 10 µL of Novex® Tris-Glycine SDS sample buffer (2 ×) (Invitrogen, Carlsbad, Ca, USA). Each sample was loaded into the zymogram gels in triplicate.

Zymography was carried out on supernatants and homogenates of fresh, v-d and f-t AM from three AMs at 0h and 24h. F-t storage and wash media were also sampled. Samples were loaded in triplicate. In this initial zymography experiment protein concentrations were not standardised.

Zymography was then performed on samples from six AMs (two sepa-

rate experiments) at 0h and 48h. The initial experiment was modified. To obtain sufficient quantities of protein, homogenates were used for baseline measurements. F-t AM storage medium was also analysed. After incubation, there were sufficient quantities of protein in the supernatants, so homogenates were not necessary. Protein quantification was performed to standardise the quantities of protein per well. A total of 1.5 µg of protein was dispensed into each well in the zymograms. The protein concentrations were normalised across the wells by calculating the volume required from the sample with the lowest concentration. Remaining samples were diluted in buffer to the same concentration, so that volumes were equal in every well.

5.3.7.2 MMP markers

Recombinant human MMP-2 was obtained from R&D Systems Inc. (Cat. No. 902-MP-010, Minneapolis, MN, USA). A total of 2.5 ng of recombinant human MMP-2 in 20 µL sample buffer were loaded onto each 10% Zymogram acrylamide/gelatin gel (Invitrogen™). MMP-9 was loaded into each gel for localisation of the pro-enzyme, not for comparison of concentrations. An MMP-9 marker was obtained from a full length construct (FuGene®, Roche, Indianapolis, IN, USA). The construct was transfected into an African Green Monkey simian virus-transfected kidney fibroblast cell line, known as Cos7, using a standard protocol.¹⁰ The Cos7 cells were cultured in DMEM (Gibco®) and 10% FCS. The medium was replaced with serum-free DMEM after 24 hrs. The supernatant, containing MMP-9, was extracted 24 hrs later, and stored at -80°C.

¹⁰MMP-9 markers courtesy of Dr Imran Haq.

5.3.7.3 Gel electrophoresis

The samples were loaded into wells on a pre-cast 10% Zymogram gel (Invitrogen). MMP-2 markers were loaded into each gel, whereas MMP-9 was loaded once per experiment. Each gel chamber was filled with 500 mL Tris-Glycine SDS zymogram running buffer (Invitrogen®). Gel electrophoresis was carried out for 2 hrs at 120 – 140 V. The gels were then soaked in renaturing buffer for 30 mins \times 2 on a rocker, followed by incubation at 37°C in developing buffer overnight. After 24 hrs, the gels were stained in Coomassie Brilliant Blue R 250, and then destained in a methanol and acetic acid solution (500 mL H₂O, 400 mL methanol and 100 mL acetic acid) for 30 mins. The gels were then ready for ultraviolet transillumination (300 nm) and photography, using image capture software. Each gel was scanned using a reflected ultraviolet light photographic system with a yellow filter (Gene Genius Bio Imaging System, Syngene, Cambridge, UK), and images were captured using Syngene gel documentation and analysis software.

5.3.7.4 Band intensity measurement

The zymography band intensities were normalised to the marker intensity using ImageJ software.¹¹ The individual bands were circumscribed using the cursor. The optical densities of the demarcated zymography bands were obtained numerically from the software and normalised to the MMP-2 standard to give percentage measurements of relative density. An average reading of the triplicate bands was taken for statistical analysis.

5.3.7.5 Statistical analysis

Statistical analysis was performed using GraphPad Prism software (La Jolla, CA, USA). Non-parametric tests were performed throughout. The data were

¹¹Software developed by Wayne Rasband at the Research Services Branch, National Institute of Mental Health, Bethesda, Maryland, USA.

Table 5.4: Culture medium

Reagent	Cat. No.	Volume	Final conc.
RPMI-1640	Sigma R8758	42.5 mL	85%
Human AB serum	Sigma H4522	7.5 mL	15%
L-glutamine	Sigma G7513	500 μ L	2 mM
Penicillin/streptomycin	Sigma P4333	500 μ L	100 U/mL/100 μ g/mL
HEPES	Sigma H3375	500 μ L	10 mM

pooled to give an overall picture of MMP-2 and MMP-9 expression in processed AM. Statistical significance was sought at the level of 5%.

5.3.8 Macrophage assays

Macrophages were cultured from peripheral blood mononuclear cells (PBMCs) for inflammation assays with AM.¹² PBMCs were obtained from fresh blood or from buffy coats and cultured in Teflon-coated bottles or ultra-low adherence flasks.

5.3.8.1 Macrophage culture

Before starting, reagents were placed in a water bath to bring them to 37°C. These included Hanks' Balanced salt Solution (BSS, Sigma H9394), Histopaque®-1077 (Sigma H8889) and Roswell Park Memorial Institute medium (RPMI-1640, Sigma R8758). Culture medium was prepared by mixing RPMI-1640, 15% human AB serum, L glutamine, penicillin, streptomycin, and 4-(2-hydroxyethyl)-1-piperazine ethanesulfonic acid (HEPES, 10 mM) in the proportions shown in table 5.4. Magnetic-Activated Cell Separation buffer (MACS®, Miltenyi Biotec, Gladbach, Germany) was made up in 500 mL PBS by adding 2.5 g BSA (final concentration 0.5%) and 2 mL of 0.5 M EDTA (Invitrogen, 15575-020; final concentration 2 mM) in Dulbecco's PBS. This was sterile-filtered and refrigerated throughout the isolation pro-

¹²Special thanks are due to Sonali Singh, who showed me the techniques listed below, and to Dr Luisa Martinez-Pomares, who helped to devise the assays.

cedure.

5.3.8.2 Extraction of peripheral blood mononuclear cells

Whole blood A volume of 50 mL of freshly extracted whole blood was pooled from EDTA vacutainer tubes and transferred to a T-75 flasks under sterile conditions. The blood was diluted with an equal volume of Hanks' BSS. This mixture was divided into four new 50 mL Falcon tubes each containing 10mL of Histopaque® for 25 mL. The blood and the Histopaque® formed two distinct layers, created by holding the tube containing Histopaque® at a 45 degree angle and trickling a few drops of the blood-Hanks' mixture along the wall of the tube. By keeping the tip of the pipette just below the rim of the Falcon tube and trickling in the blood-Hanks' mixture, disruption of the Histopaque® interface was minimised. The tubes were carefully transferred to the centrifuge, again trying as far as possible to prevent admixture. They were centrifuged at $800 \times g$ at 23°C , with slow acceleration and deceleration for 30 mins. The PBMC was then removed with a 5 mL pipette, trying as far as possible to avoid admixture with RBCs, as described above. The collected PBMCs were divided into two Falcon tubes. The PBMCs in both tubes were washed once with 50 mL Hanks' solution ($350 \times g$, 23°C) for 7 mins.

Buffy coats Monocytes were isolated from buffy coats obtained from human blood banks. A volume of 50 mL of blood was poured out into T-75 flasks under sterile conditions in a laminated hood, and made up to a volume of 140 mL with PBS. 35 mL of this mixture was layered over 15 mL of Histopaque®-1077 (Sigma-Aldrich) in 50 mL Falcon tubes as described above. The tubes were centrifuged at $800 \times g$ at 23°C for 30 mins. The upper plasma layer was removed with a 25 mL pipette. The PBMC rings were collected using a sterile 5 mL pipette and transferred to two fresh 50

mL Falcon tubes. The PMCs were washed $\times 2$ with PBS ($350 \times g$, 23°C , acceleration 3, deceleration 3, 5 mins). The supernatants were cloudy due to platelet contamination; these were discarded and the PBMC pellets washed twice more with PBS.

5.3.8.3 Cell counting

The supernatant was discarded, and the PBMCs were resuspended in exactly 10 mL of Hanks' (whole blood) or PBS (buffy coat), mixing pellets from both Falcon tubes. A 100 μL aliquot was removed for cell counting. For this, a volume of 100 μL of cell suspension was mixed with 900 μL PBS. Of this, 100 μL was mixed with 100 μL Trypan blue to give a dilution of 1:20. A haemocytometer and its cover slip were washed in distilled water and wiped over with alcohol. When dry, the surface of the haemocytometer was breathed on and the cover slip quickly placed at the centre of the counting chamber. A small amount of the cell suspension/solution to be counted was taken up in a pipette. The pipette was touched against the side of the cover slip where it touches the base of a depression in haemocytometer. One drop was slowly squeezed up to fill one counting chamber with nine squares, each containing a volume of 0.1 mm^3 . Cells in five squares of the counting chamber (the four corners and the centre) were counted under the $40 \times$ objective of an optical microscope. Cells falling on the bordering triple lines were counted if they were on the top or on the left lines. The average cell count per square was calculated by dividing the total by 5. This figure was multiplied by the dilution factor (20) and by 10^4 to obtain cell density as the number of cells per mL. To obtain total cell count, this value was multiplied by 10.

5.3.8.4 Labelling of monocytes

The PBMCs were centrifuged ($350 \times g$, 23°C) for 5 mins and the supernatant aspirated. The pellets were then washed in cold, sterile MACS® buffer ($350 \times g$, 23°C) for 5 mins and resuspended in $800 \mu\text{L}$ of the same buffer per 10^7 cells. A volume of $200 \mu\text{L}$ of CD14 Microbeads (Miltenyi Biotec) were added per 10^7 cells, mixed well and incubated at 4°C in the dark for 15 mins. If fewer than 10^7 PBMCs were counted, $200 \mu\text{L}$ of CD14 beads were added. It was important to work fast, keeping cells cold, and using pre-cooled solutions to prevent capping of the antibodies on the cell surface and non-specific cell labelling. Once the incubation was over, the CD14-labelled cells were washed once with 20 mL MACS® buffer ($350 \times g$, 5 mins).

5.3.8.5 Magnetic cell separation

Magnetic cell separation columns (Miltenyi Biotec) were set up. Pre-separation filters were placed in the columns and washed with 3 mL MACS® buffer to prevent any cell clumps from entering the column and blocking it. The cells were resuspended in 3 mL MACS® buffer and placed in the columns. The columns were then washed with 3 mL MACS® buffer 3 times, so that only CD14⁺ cells were retained in the columns. These were then flushed out into 15 mL tubes with 10 mL MACS® buffer, and stored at room temperature. The cells were counted, and then centrifuged ($350 \times g$, 23°C) for 5 mins. These were resuspended in culture medium to a maximum total density of 2×10^6 cells/mL in 10 mL. A volume of $10 \mu\text{L}$ of granulocyte-macrophage colony-stimulating factor (GM-CSF, $10 \mu\text{g}/\text{mL}$ stock solution) was added to the 10 mL suspensions to give a final concentration of $10 \text{ ng}/\text{mL}$.

5.3.8.6 Monocyte culture

A volume of 5 mL of cell suspension were seeded into sterile Teflon bottles or ultra-low adherence 75 cm^3 flasks (Corning®, MA). Teflon bottle caps

were left slightly unscrewed to allow air exchange, secured with labelled masking tape and left to incubate at 37°C in 5% CO₂. After three days, the cell survival was verified by Trypan blue staining. A volume of 1.5 mL of fresh medium containing 10 ng/mL GM-CSF was added to the bottles. Macrophages were ready for harvesting by day 7.

5.3.8.7 Harvesting of macrophages

After incubation for 7 days, the medium containing the suspended macrophages was recovered and pipetted into a Falcon tube on ice. Adherent macrophages left in the ultra-low adherence flasks were removed by additional steps. The inner walls were washed with 5 mL sterile PBS. A volume of 5 mL sterile non-enzymatic cell dissociation buffer was added to each flask and incubated on ice for 40 mins. At the end of 40 mins, the flasks were checked under the microscope to confirm that all cells detached from the surface. The cells appeared round and bright instead of flat and grey. A 5 mL pipette was used to flush the cells out of the flask and add this solution to the Falcon tube. This was centrifuged at $350 \times g$ for 5 mins at 4°C. The cell pellet was washed in RPMI-1640 medium for 5 mins at 4°C, and resuspended in 10 mL of medium. The cells were counted, centrifuged and resuspended to give a cell density of 5×10^5 cells/mL. A volume of 1 μ L of 10 μ g/mL GM-CSF was added to each mL of medium.

5.3.8.8 Confirmation of phenotype

Flow cytometry was performed on cells from two different buffy coat donors to confirm their phenotype as activated macrophages. Depending on requirements, a cell suspension containing between 20 000 to 100 000 cells from the previous step was centrifuged ($350 \times g$, 4°C, 5 mins). The supernatant medium was discarded. The remaining pellet was washed in PBA for 5 mins and then centrifuged ($350 \times g$, 4°C, 5 mins). The cells were

Table 5.5: Markers of activated macrophages

Isotype	Label	Control No.	Markers	Antibody No.
IgG1	PE	130-092-212	CD16	130-091-245
		130-092-213	Mannose receptor	130-095-220
	IgG2a	FITC	130-091-837	CD11b
130-091-837			CD14	130-080-701
PCy5		130-091-836	CD3	130-080-402
			HLA-DR	130-095-297

PE, phycoerythrin; FITC, fluoroisothiocyanate; PCy5, Phycoerythrin-coupled cyanin 5.

counted in the haemocytometer, and the remaining pellet was resuspended to the required cell density. 100 μ L aliquots were separated into tubes for flow cytometry. Next, they were incubated in 100 μ L 5% mouse serum for 1 hr at 4°C. This was followed by a further wash in 400 μ L PBS. Conjugated mouse monoclonal antibodies from Miltenyi Biotec were used. Specific markers included IgG2a antibodies against HLA-DR, CD14 and CD3 and IgG1 antibodies against CD11b, CD16 and mannose receptor. Isotype controls included IgG1 labelled with FITC and PE and IgG2A labelled with FITC and phycoerythrin-coupled cyanin 5 (PCy5). (table 5.5). These were diluted to 1:10 (5 μ L Ab in 45 μ L PBA). The cells were then incubated with 5 μ L of diluted primary antibodies for 30 mins, with one tube set aside as an unstained control. After incubation with primary antibody, the cells were washed and suspended in 400 μ L PBS containing 0.5% formaldehyde. Flow cytometry was carried out on an Altra Flow Cytometer (Beckman Coulter), and Weasel software was used to interpret the data.

5.3.8.9 Inflammation assays

Inflammation assays were performed by incubating AM discs with the cultured macrophages. The macrophages were stimulated with lipopolysaccharide (LPS) or antigen from *Pseudomonas aeruginosa* obtained as a French press lysate (FPL), and the profile of inflammatory cytokines was measured

Table 5.6: Macrophage assays

Assay	MΦ	Bottles	AM	Disc (mm)	FPL (μg/mL)	LPS (ng/mL)
1	FB	Teflon	-	-	-	-
2	BC × 2	Teflon	F-t, v-d	3	1, 10	25, 100
3	BC × 2	Teflon	Fresh, f-t, v-d	4	1	25
4	BC × 2	Teflon	Fresh, f-t, v-d, 10% v-d, TT	6	0.1	10
5	BC × 1	Teflon	-	-	-	-
6	BC × 1	ULA	F-t, v-d, 10% v-d	6	0.07	100
7	BC × 1	ULA	F-t, v-d × 3	8	0.1	10

MΦ, macrophage source; *FB*, fresh blood; *BC*, buffy coat; *ULA*, ultra-low adherence flask; *FPL*, French press lysate; *LPS*, lipopolysaccharide; *TT*, thermolysin-treated.

after a period of incubation. The assays are outlined as a series of six optimising steps (Assays 1 to 6) and a triplicate experiment (Assay 7) in table 5.6. For the first five assays, Teflon bottles were used, whereas for the final two, ultra-low adherence flasks were used. AM was prepared in the usual way. The f-t AM was thawed and washed in 50 mL of a 500 mL PBS solution of containing 1 mL gentamicin/amphotericin B (Gibco). Dried preparations, including 0% and 10% v-d AM, were rehydrated separately in 50 mL of the same solution. Denuded AM was prepared using the thermolysin method (section 3.3.1.3). Discs of AM (3 to 8 mm in diameter) were punched out using a skin biopsy punch and placed at the bottom of a 96-well plate working fast and covering the wells to prevent dehydration of the samples. In one optimising step (Assay 4), the discs were moistened with 10 μL H₂O to prevent drying. Assay 7 was performed using three different AMs.

5.3.8.10 Preparation of stimulants

LPS from *E. coli* was obtained from Enzo Life Sciences Ltd. (Exeter, UK).¹³ The stock concentration was 10 μg/mL. A volume of 5 μL was added to each well, using the standard formula

¹³The LPS and PA stock solutions were kindly provided by Dr Sonali Singh.

$$\text{Concentration}(A) \times \text{volume}(A) = \text{concentration}(B) \times \text{volume}(B) \quad (5.1)$$

where A stands for initial and B stands for final, to obtain the desired concentration. The concentration used was 10 - 1000 ng/mL. FPL was prepared by passing mid-log phase *P. aeruginosa* 01 (PA01) cells through a French press until all the cells had been lysed. The stock concentration of FPL was 1092.45 $\mu\text{g/mL}$. The concentration used was 0.07 - 10 $\mu\text{g/mL}$.

5.3.8.11 Stimulation of macrophages

The macrophages were seeded onto the 96-well plate containing the AM discs. A 100 μL suspension containing 50 000 donor cells was added to each well. The cells were left to incubate at 37°C for 2 hrs, after which they were stimulated with the desired concentration of LPS or FPL. The plate was placed in the incubator for 24 hrs. After incubation, the plate was centrifuged at $400 \times g$ for 5 mins. The supernatants were extracted and placed into a second 96-well plate, taking care not to disturb the amnion sample at the bottom of the wells. The plate with the supernatants was then frozen at -80°C. The next day, cytometric analysis was performed to quantify the cytokines produced by the macrophages.

5.3.8.12 Cytometric bead preparation

Human cytokine 6-plex FlowCytomix™ kits (eBiosciences Ltd., Hatfield, UK) were obtained for TNF, IL-4, IL-6, IL-8, IL-10 and IL-13. A standard mixture of cytokines was prepared by mixing 3 μL of each of the reconstituted cytokines and adding an assay buffer to a total volume of 60 μL . Six serial 1:3 dilutions were prepared to plot a standard curve. The standard curves covered a range from 0 to 20 000 pg/mL for analytes IL-4, IL-6, IL-10,

IL-13 and TNF, and from 0 to 10 000 pg/mL for IL-8.

Cytokine antibody-labelled fluorescent beads were prepared. The final volume of bead mixture required was calculated according to the number of samples to be tested. A volume of 10 μL of bead mixture was used per sample. The bead mixture was prepared by vortexing the beads for 5 secs, mixing equivalent volumes (1/20 of the final volume) of each bead and making up the difference to the final volume with reagent dilution buffer (RDB). The biotin-conjugated antibodies of each cytokine were prepared as a mixture by calculating 1/20 of the final volume of each conjugate. The required volume was made up to the final volume with RDB. A volume of 20 μL was required per test.

Flow cytometry tubes were labelled for blanks, standards and samples. A volume of 10 μL of standard mixture solutions, samples and a blank with assay buffer only was added to designated tubes. The bead mixture was vortexed and 10 μL added to all tubes. A volume of 20 μL of biotin-conjugate was added to all tubes. The tubes were vortexed and incubated at room temperature for 2 hrs in the dark. Immediately prior to the next step, the streptavidin-PE was prepared by calculating 0.7 μL per tube and adding a volume of assay buffer sufficient to dispense a volume of 20 μL streptavidin-PE/assay buffer mixture per tube. The tubes were washed $\times 2$ with 400 μL of assay buffer and centrifuged at $350 \times g$ for 5 mins. A volume of 20 μL of streptavidin-PE was added to each tube, mixed and incubated for 1 hr in the dark. Two further washes were carried out. The pellets were then resuspended in 400 μL assay buffer and stored at 4°C for flow cytometry.

5.3.8.13 Flow cytometry

The flow cytometry analysis was carried out on a Beckman Coulter FC500 instrument as described previously. Acquired data was analysed with Flow-Cytomix Pro 2.2 software. Each sample was measured in duplicate. The

forward scatter collection angle setting was changed for bead detection. The concentrations of IL-4, IL-6, IL-8, IL-10, IL-13 and TNF were obtained in pg/mL by cytometric analysis for Assays 2-4. For Assays 5-7, IL-6, IL-8 and TNF were measured. Mean values of the duplicate measurements were taken for analysis. In the case of missing data, single measurements were used. Statistical analysis of the results was performed using Graph-Pad Prism® software. Data that surpassed the standard detection limits by more for each analyte were not analysed statistically, but were described as trends if possible. For the Assay 7, the supernatants were diluted 1:10 in RPMI 1640 for cytokine analysis. The average values with standard deviations for three AMs were calculated for statistical analysis. Negative controls were performed in duplicate.

5.3.9 Scanning electron microscopy

Following the macrophage assays, samples of the AM discs used were freeze-dried and subjected to scanning electron microscopy (technique described in Chapter 4 section 4.3.1).

5.4 Results

5.4.1 Antimicrobial peptide detection

5.4.1.1 Western blotting

Human β -defensin 3 Western blots performed on whole AM extract for hBD3 are shown in figures 5.1 A-E (left). Whole AM extracts from two AMs were used in A. Fresh AM was loaded into lanes 1 and 4, v-d AM in lanes 2 and 5, and f-t AM in lanes 3 and 6. The prominent band at ~10 kDa (black arrow) was sent for identification by MS (section 5.4.1.1). A β actin loading control and a SimplyBlue™ SafeStain gel are shown in B and C. The west-

ern blot was repeated using AM extracts from five AMs (lanes 1 to 5) (D). No low molecular weight bands are visible. A western blot of recombinant hBD3 was loaded from left to right in halving doses from 250 ng to 7.8 ng (E), indicating the dose that can be detected by this method. Further western blots are shown in figure 5.1 A-E (right). Two AM samples underwent western blotting (lanes 3 and 4) next to recombinant hBD3 in lane 1 (15.6 ng) and lane 2 (7.8 ng) (A). hBD3 was not detected in the samples. The samples in B were fractionated to remove proteins above 30 kDa. Lanes 1 and 2 contained AM extract. Lanes 3 and 4 contained placental samples. All lanes were negative for hBD3. A SimplyBlue™ SafeStain containing fractionated samples in lanes 1 and 2 and unfractionated samples in lanes 3 and 4 is shown (C). Less protein is present in the fractionated sample, suggesting that protein loss has occurred. In D, AM extract was loaded in lane 1, AEC extract in lane 2, AM extract obtained after overnight incubation in TBST_x in lane 3 and a HPLC-purified sample in lane 4. Bands of 5 kDa proteins are seen in lane 3 and 4. A western blot of a Tricine gel of samples of AEC extract is shown in E. Lanes 1 and 3 contain reduced samples, and lanes 2 and 4 were non-reduced. Low molecular weight bands are visible in lanes 1 and 3.

Human β -defensin 1/LL-37 Two western blots to detect hBD1 and LL-37 are shown in figure 5.2 A-F. In A-C, fractionated placental tissue (lane 1) and tonsil (lane 2) were run alongside AM extract (lane 3). hBD1 (A) and LL-37 (B) are negative. In B, 1 ng of recombinant LL-37 was run in lane 4. The SimplyBlue™ SafeStain image (C) shows minimal protein. Unfractionated samples were run in figure 5.2 D-E. The samples are in lane 1, with tonsillar controls in lane 2. These were negative for hBD1 (D) and LL-37 (E).

Mass spectrometry A ~10 kDa protein band from the gel obtained by western blot (shown above in figure 5.1 A) was sent for MS. The proteins

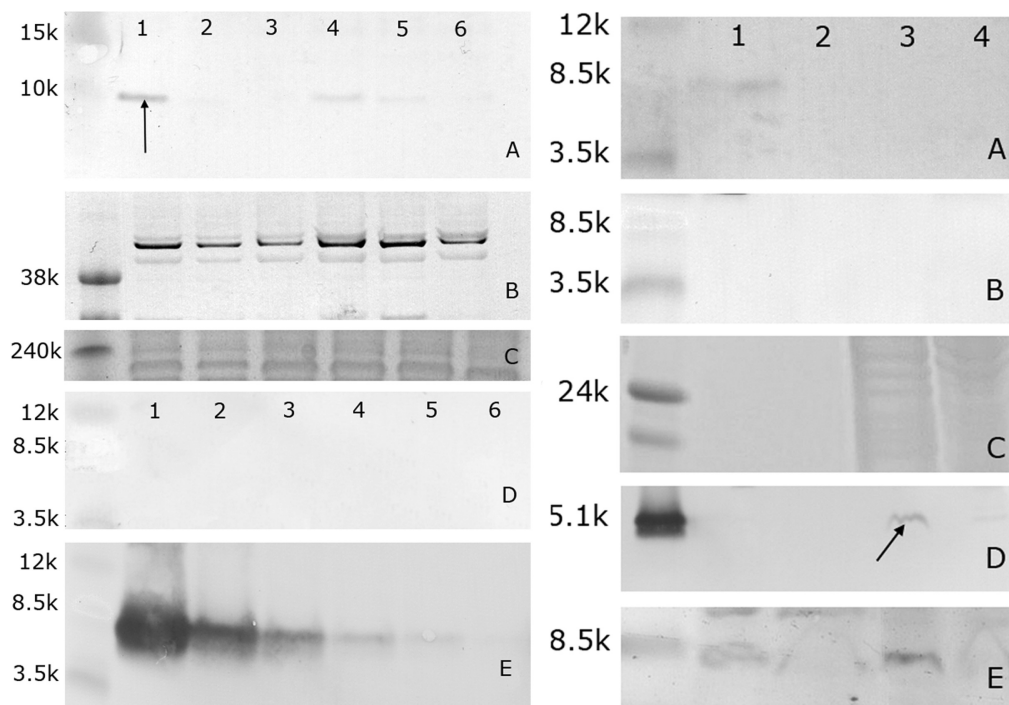


Figure 5.1: Western blots of hBD3

Western blots were performed on whole AM extract to detect hBD3 (left). **A** Extract from fresh AM (lanes 1 and 2), v-d AM (3 and 4) and f-t AM (5 and 6). 30 μ g of protein was added to each well under reducing conditions. A rabbit polyclonal antibody to hBD3, ab19270, was used as a primary antibody. A low molecular weight protein was identified at ~9 kDa (black arrow). **B** A β actin loading control was run to ascertain equivalent loading. **C** SimplyBlue™ SafeStain was used to demonstrate protein in the gels. **D** Western blotting was repeated with 40 μ g of extract from 5 donors (and 1 repeat). **E** Recombinant hBD3 was loaded in halving doses from 250 ng (lane 1) to 7.8 ng (lane 6). Right: **A** A western blot with recombinant hBD3 in lanes 1 (15.6 ng) and 2 (7.8 ng) is shown. AM samples were run in lanes 3 and 4. **B** Fractionated AM samples (to remove proteins >30 kDa) were run in lanes 1 and 2. Fractionated whole placental samples were run in lanes 3 and 4. **C** A gel was run with fractionated AM extract in lanes 1 and 2 and unfractionated samples in lanes 3 and 4. This was stained with SimplyBlue™ SafeStain. **D** Two AM extracts were loaded in lanes 1 and 2 (40 μ g per lane). In lane 3, 25 μ g of an AM sample that was obtained separately was loaded; a band is shown at 5 kDa (black arrow). In lane 4, the AM was purified by high performance liquid chromatography. **E** 30 μ g of extract from each of 2 AM samples were loaded into a Tricine gel. In lanes 1 and 3, the sample was reduced. In lanes 2 and 4, the sample was non-reduced.

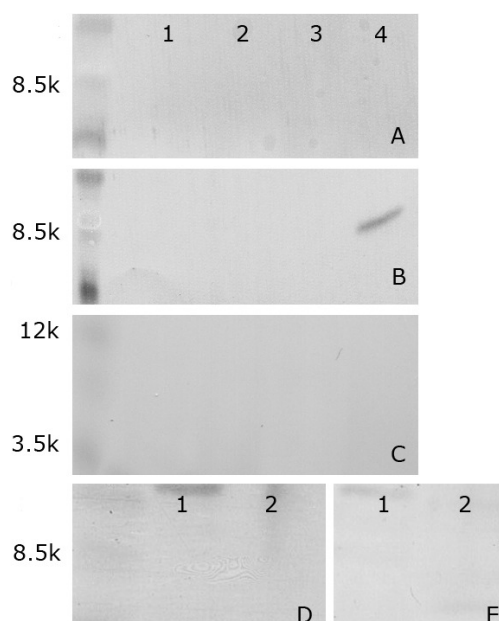


Figure 5.2: Western blots of hBD1 and LL-37

Two western blots were performed to detect hBD1 and LL-37. The first blot (A-C) was performed on fractionated samples. HBD1 (A) and LL-37 (B) are negative. A band representing recombinant LL-37 (1 ng) is shown in lane 4 (B). The gel was stained with SimplyBlue™ SafeStain, demonstrating protein loss (C). In the second blot (D-E), unfractionated samples (lane 1) were run alongside tonsil controls (lane 2). These were negative for hBD1 (D) and LL-37 (E).

identified by MS are members of the S100 family (table 5.7), which are localised in the cytoplasm and/or nucleus of a wide range of cells, and are involved in the regulation of a number of cellular processes such as cell cycle progression and differentiation. S100 genes include at least 13 members located as a cluster on chromosome 1q21.

Table 5.7: Mascot Peptide Summary Report

Protein	M _r	Protein	Score	Matches	% coverage
S100A4	11721	Calcium-binding protein A4	131	4	19
S100A11	11733	Calcium-binding protein A11	59	1	8
S100A10	11064	Chain A, P11, Ligand of Annexin Ii	56	2	17

Table 5.8: LL-37 levels in AM

Incubation period	2 hrs				4h			
	10%		20%		10%		20%	
1° ab concentration	Mean	Md	Mean	Md	Mean	Md	Mean	Md
Blank 1	240	235	158	159	302	279	107	107
Fresh AM 1	186	172	118	109	184	161	118	118
Fresh AM 2	172	124	126	119	186	170	120	116
F-t AM 1	161	179	117	118	200	217	142	139
F-t AM 2	186	175	132	121	241	229	125	126
V-d AM 1	184	162	120	120	213	204	125	121
V-d AM 2	172	153	119	113	169	174	192	190

Md, median; *ab*, antibody; *MFI*, mean fluorescence intensity

5.4.1.2 Cytometric bead analysis

The functional beads that were coated with a mouse monoclonal capture antibody to LL-37, and the negative control, underwent flow cytometry. The MFI measured by the PE channel was 145 for the control sample and 26336 for the antibody-coated beads. Measured via the APC channel, the MFI readings were 2380 for the controls and 2370 for the test sample. This indicated that the covalent linking of the functional beads with the capture antibody had been successful. The initial concentration of the rabbit polyclonal detection antibody was 428 $\mu\text{g}/\text{mg}$. The samples were incubated with a 10% and 20% concentration of detection antibody for 2 hrs and 4 hrs. Plots of the MFI (mean and median) of the control and test samples are shown in figure 5.3. The data are shown in table 5.8. In the samples incubated for 2 hrs (10% and 20% antibody concentration) and 4 hrs (10% concentration), the blank samples had a higher MFI than the test samples. In the samples incubated for 4 hrs at 20% antibody concentration, no significant difference was observed between MFI of the AM supernatants and negative controls.

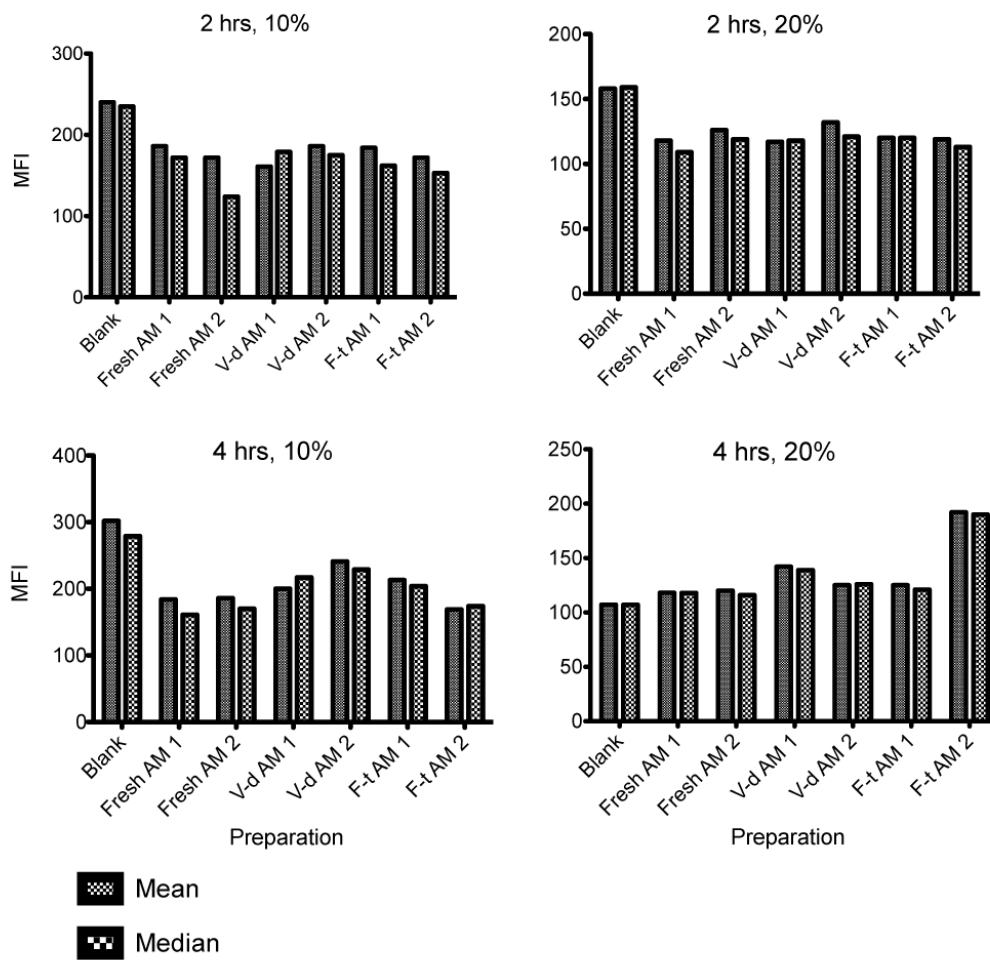


Figure 5.3: CBA assay for LL-37

CBA assay of supernatants of fresh, v-d and f-t AM extracts were performed in duplicate. The samples were incubated with 10% and 20% concentrations of primary antibody for 2 hrs and 4 hrs. The negative control is labelled blank.

Table 5.9: AMP fluorescence per AM

EXPT 1	EXPT 2	EXPT 3	EXPT 4
Psoriasis (m), -ve	Psoriasis (m), 9.0%	Psoriasis (m), -ve	Psoriasis(m), 61.8%
LEAP-2 (r), 14.7%	LEAP-2 (r), 54.3%	LEAP-2 (r), -ve	LEAP-2 (r), 91.3%
hBD2 (m), -ve	hBD2 (m), -ve	hBD2 (m), -ve	
hBD3 (m), -ve	hBD3 (m), 3.8%	hBD3 (m), -ve	
		hBD3 (r) 53.5%	hBD3 (r), 84.8%
RNAse-7 (r), 3.7%	RNAse-7 (r), 81.4%		RNAse-7 (r), 88.1%
		LL-37 (r), 37.5%	LL-37 (r, PE), 98.6%

M, mouse; r, rabbit; PE, phycoerythrin-conjugated

5.4.1.3 Flow cytometry

Optimisation step A single cell suspension of AEC was stained with rabbit polyclonal anti-hBD3 antibody. Positivity was obtained for hBD3 expression in cells that were either permeabilised and fixed in 3% FA (row A, 96.6%) or permeabilised and fixed in 0.5% FA (row C, 97.9%) (figure 5.4). Cells that were non-permeabilised and fixed in 0.5% FA exhibited less intense staining (row B, 53.8%).

Antimicrobial peptide detection The dot plots of flow cytometry analyses of permeabilised AEC from four AMs (flow cytometry 1 to 4). Flow cytometry 1 and 2 are shown in figure 5.5 and 3 and 4 are shown in figure 5.6. The percentages of fluorescent cells compared to the negative control for each sample are listed in table 5.9, with figures of less than 1% listed as negative. In flow cytometry 1, rabbit polyclonal antibodies detected LEAP-2 (14.7%) and RNAse-7 (3.7%) in AEC (figure 5.5). Using mouse monoclonal antibodies, hBD2, hBD3 and psoriasis were not detected. In flow cytometry 2 there was positivity for hBD3 (3.8%) and psoriasis (9.0%) using mouse monoclonal antibodies and LEAP-2 (54.3%) and RNAse-7 (81.4%) using rabbit polyclonals. HBD2 (mouse) was negative. In flow cytometry 3, hBD3 (53.5%) and LL-37 (37.5%), both raised in rabbit, were positive (figure 5.6), whereas LEAP-2 (rabbit) and psoriasis, hBD2 and hBD3 (mouse) were all

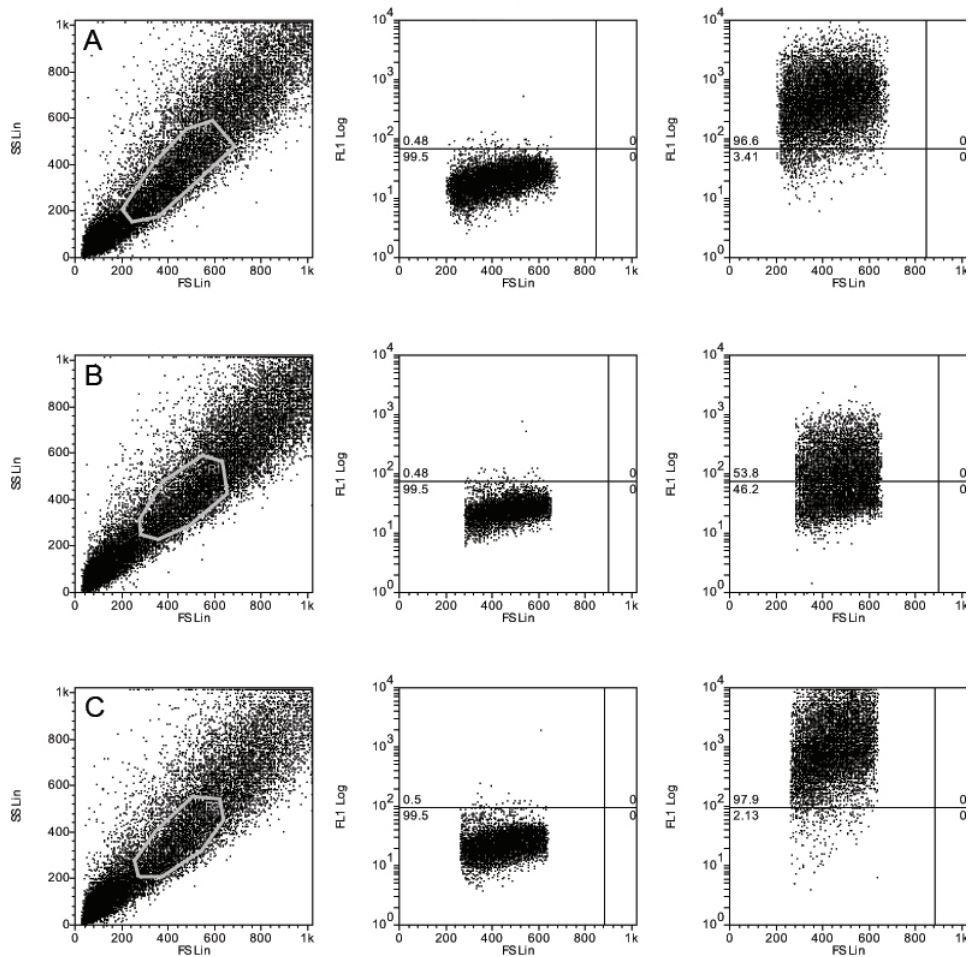


Figure 5.4: Flow cytometry optimisation

Dot plots of AEC are shown in 3 rows and columns. In the left hand column, the cells are sorted by linear side scatter (SSLin, Y axis) and linear forward scatter (FSLin, X axis). A central polygonal shape (gate) has been drawn around a population of cells to capture cells of average size and shape. Cells incubated with rabbit polyclonal anti-hBD3 antibodies are shown in the dot plots on the right. The antibodies were labelled with fluorescein isothiocyanate (FITC), which was detected on the FL1 channel (Y axis). The plots of A and C were obtained after permeabilising the epithelial cells and fixing them in 3% FA and 0.5% FA respectively. The cells in row B were not permeabilised. Negative controls are shown in the central column.

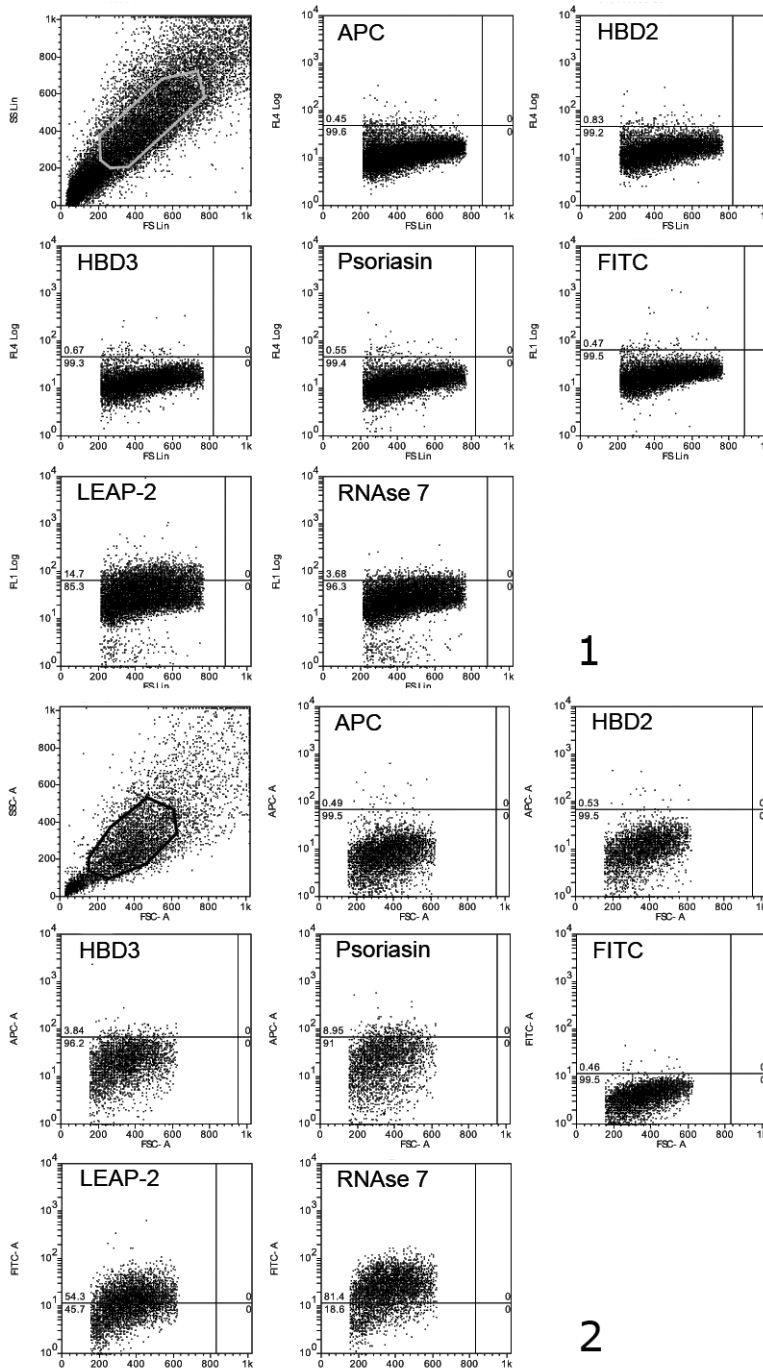


Figure 5.5: Flow cytometry for AMPs (1)

1 Flow cytometry was conducted on AEC to detect an array of AMPs. Cells were sorted by linear side scatter and forward scatter and gated. Fluorescence is shown on a logarithmic scale for APC (channel FL4) and FITC (FL1). Negative controls (no primary antibody) are labelled as APC and FITC. Positivity was obtained for LEAP-2 (14.7%) and RNase 7 (3.7%). **2** Positivity was obtained for LEAP-2 (54.3%) and RNase 7 (81.4%), psoriasin (9.0%) and hBD3 (3.8%), but not for hBD2. APC, allophycocyanin; FITC, fluorescein isothiocyanate.

negative. In flow cytometry 4, the AEC were incubated overnight at 4°C with primary antibody. There was strong positivity for psoriasin (mouse, 61.8%), LEAP-2 (rabbit, 91.3%), hBD3 (rabbit, 84.8%), RNase-7 (rabbit, 88.1%) and LL-37 (rabbit, 98.6%).

5.4.2 Antimicrobial assays

Concentrated extracts of v-d AM were incubated with Gram positive and Gram negative bacterial strains in 96-well plates. The MIC for the amnion extracts could not be determined due to the absence of antimicrobial activity. Bacterial growth was observed at each concentration of extract and with each of the bacterial strains tested. In agreement with the MIC tests, no antibacterial activity was observed in concentrated AM extract or in AM squares incubated on LB agar. Each of the bacterial strains populated the outer edges of the chromatography discs saturated with AM extract and zones of inhibition could not be identified. Only AM samples saturated in antibiotic solution displayed antimicrobial activity.

5.4.3 Protein microarray

Protein microarrays of four different AM preparations were performed to compare MMP/TIMP levels and to determine their localisation. These results are taken from a total of four AMs, normalised by total protein concentration in extraction medium and expressed in pg/mg. Median normalised levels of MMP/TIMP analytes are shown in table 5.10. MMP-13 was not detected. The median levels of TIMPs in fresh AM were significantly higher than levels of MMPs (Kruskal-Wallis, $p < 0.001$) (figure 5.7). The compartmentalisation of MMPs is indicated by the respective concentrations (figure 5.8). The concentration of MMP-1 was significantly higher in de-epithelialised than in fresh AM ($p < .05$). The concentrations of MMP-3 and TIMP-1 were significantly higher in fresh than in de-epithelialised AM (p

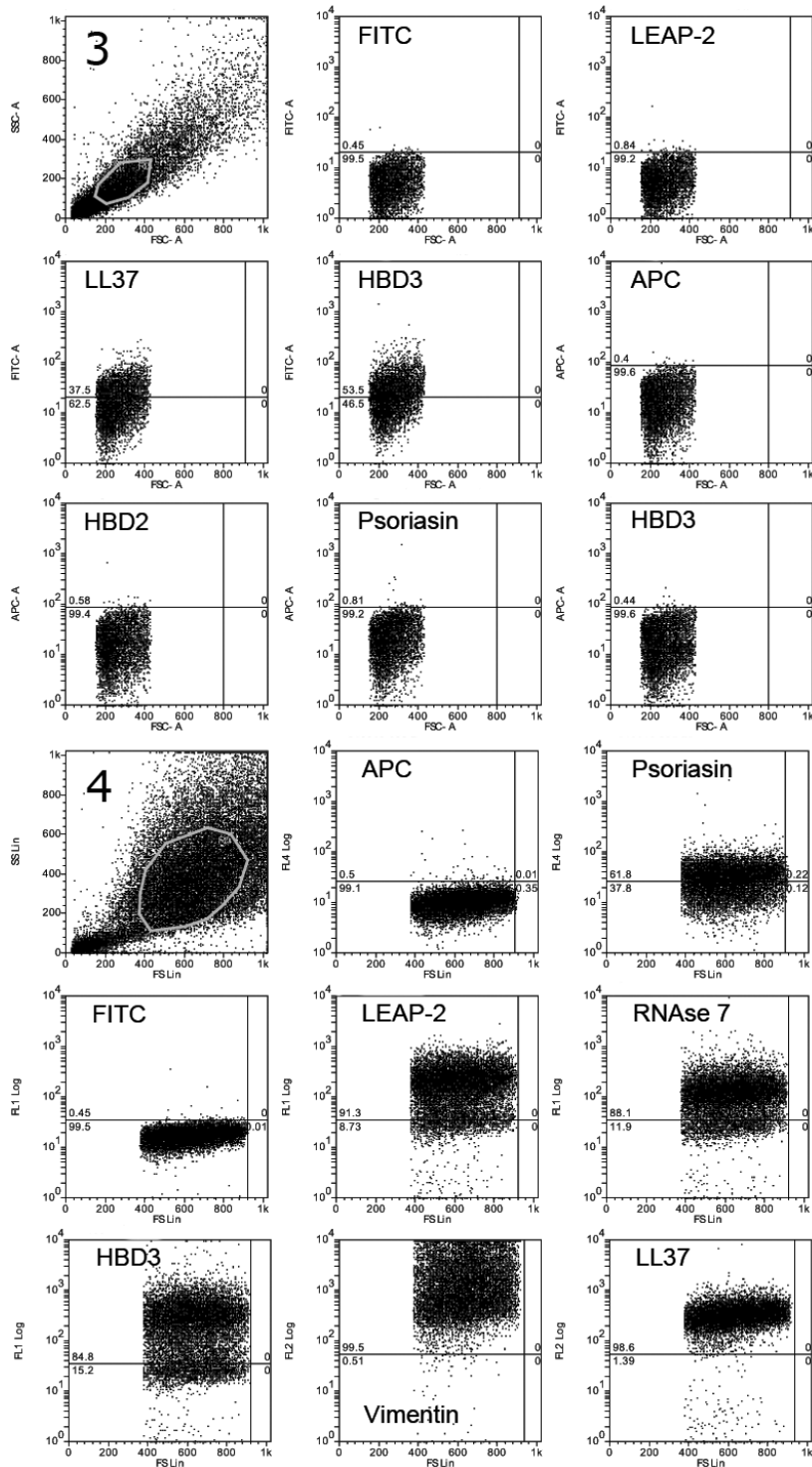


Figure 5.6: Flow cytometry (2)

3 Flow cytometry dot plots were conducted on AEC to detect AMPs. Positivity was obtained for LL-37 (rabbit, 37.5%) and hBD3 (rabbit, 53.5%), while LEAP-2, psoriasis, mouse hBD3 and hBD2 were negative. Negative controls are labelled as APC and FITC. Fluorescence is shown on a logarithmic scale. **4** Positivity was obtained for LEAP-2 (91.3%), RNase 7 (88.1%), psoriasis (61.8%), hBD3 (84.8%) and rabbit LL-37 (98.6%). A positive vimentin control was labelled with PE (channel FL2). APC, allophycocyanin; FITC, fluorescein isothiocyanate; PE, phycoerythrin.

Table 5.10: Median levels of MMPs and TIMPs

AM preparation	MMP-1	MMP-2	MMP-3	MMP-7	MMP-8	MMP-9	MMP-10	TIMP-1	TIMP-2
Fresh	215.0	9512.0	287.0	372.0	381.5	1572.5	1026.0	97562.0	32673.0
De-epithelialised	4996.0	12049.5	0	173.5	183.5	1238.5	2020.0	11625.0	23798.0
Freeze-thawed	422.0	12968.5	76.50	754.5	1259.0	1399.5	1520.5	82051.5	25956.5
Vacuum-dried	944.0	13213.0	435.5	669.5	780.0	4277.0	2370.0	136987.0	55299.5

Protein microarrays were carried out on the homogenates of four AM preparations. Levels of MMPs and TIMPs are expressed as pg of analyte per mg of homogenised tissue.

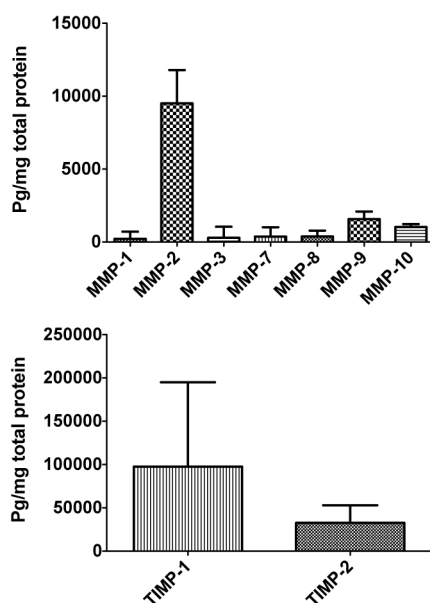


Figure 5.7: MMPs and TIMPs in fresh AM

MMPs and TIMPs in fresh AM were measured in quadruplicate by protein microarray and expressed as pg per mg of total protein. Median values are shown, with error bars representing the ranges.

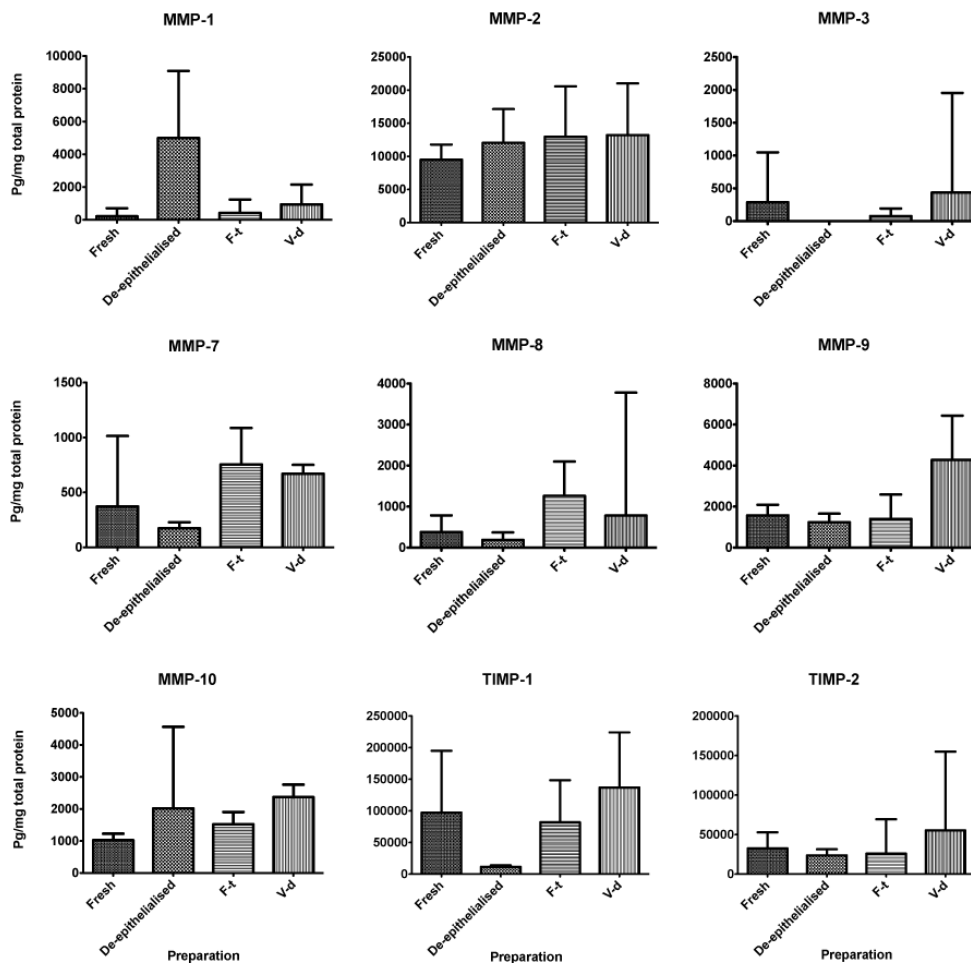


Figure 5.8: Protein microarrays of MMPs and TIMPs

Protein microarrays were performed in quadruplicate on four different AM preparations (fresh, de-epithelialised, v-d and f-t AM), demonstrating the compartmentalisation of MMPs and TIMPs in AM. MMP-1, MMP-2, MMP-3, MMP-7, MMP-8, MMP-9, MMP-10, TIMP-1 and TIMP-2 were analysed and TIMP-1. The analyte levels are expressed as pg / mg of total protein.

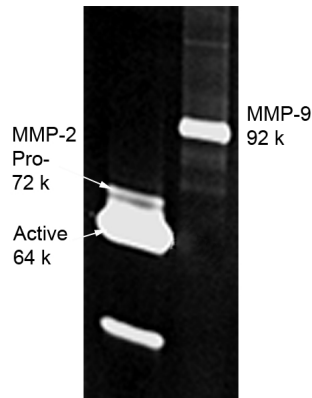


Figure 5.9: MMP-2 and MMP-9 zymography markers

Zymographic markers are shown for MMP-2 and MMP-9. Separate bands are seen for the MMP-2 pro-enzyme (72 kDa), active MMP-2 (64 kDa) and MMP-9 pro-enzyme (92 kDa).

< .05). The concentrations of MMP-2, MMP-9, TIMP-1 and TIMP-2 were higher in v-d AM than in f-t AM and fresh AM. In all preparations, MMP-2 was significantly higher than all other MMPs ($p < .05$).

5.4.3.1 Matrix metalloprotease elution

The MMP-2 marker reveals separate bands for the inactive pro-enzyme (72 kDa) and the active enzyme (64 kDa) (figure 5.9). The pro-enzyme of MMP-9 exhibits a distinct band at 92 kDa. A low molecular weight cleavage product of MMP-2, of no significance, is also visible (unmarked).

Elution at 24h Zymography was performed in two experiments on homogenates and supernatants of fresh, f-t and v-d AM preparations at baseline and 24 hrs. Triplicate measurements were taken for each sample of AM as well as the f-t AM wash medium ('wash') and storage medium ('medium'). Zymograms from one representative sample are shown in figure 5.10. Protein levels were not normalised for this experiment. Pro-MMP-2 is present in the supernatant and homogenate at 0h (gels 1 and 2). The MMP-2 pro-enzyme is also present in the f-t AM wash and storage media (gels 2 and 3) and in both the supernatants and homogenates after 24 hrs (gels 3 and 4). No

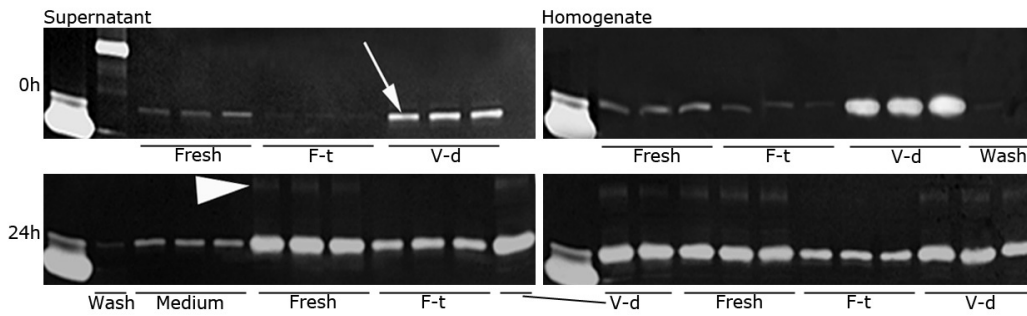


Figure 5.10: Zymography of fresh, v-d and f-t AM

Zymography was performed on fresh, f-t and v-d AM supernatants and homogenates at 0h and 24h. F-t AM storage ('medium') and wash media ('wash') were also sampled. Protein levels were not normalised. MMP-2 pro-enzyme bands are seen at baseline (small white arrow) and after 24 hrs. Faint MMP-9 bands are seen after 24 hrs (large white arrowhead). This represents one of two replicate experiments.

MMP-9 is detected at baseline. There is faint expression of MMP-9 after 24 hrs in fresh and v-d AM supernatants and homogenates.

Elution at 48h Zymography was performed on a total of six AMs in two experiments to detect MMP-2 and MMP-9 at baseline and at 48 hrs. Each measurement was made in triplicate. Homogenised samples were taken at baseline, while supernatants were taken at 48h. Samples were obtained from samples of AM at 0h and 48h and from f-t AM storage medium at 0h. A total of 1.5 µg of protein was dispensed into each well. Representative zymograms for three AMs are shown (figure 5.11). At 0h, there are bands of MMP-2 pro-enzyme in all preparations. MMP-9 is not present in AM extracted at baseline. After 48 hrs, MMP-2 pro-enzyme is present in all preparations. MMP-9 bands were detected in the fresh AM supernatants (white arrow) and in the supernatant of one f-t AM sample (large white arrowhead).

Band intensity measurements were pooled for both experiments. The median intensity values, which do not take a unit, are shown in table 5.11. One of the zymograms, for fresh AM at 48h, was damaged and did not return any data. A statistically significant increase in normalised values of MMP-2 pro-enzyme intensity was found between baseline and after 48 hrs for fresh

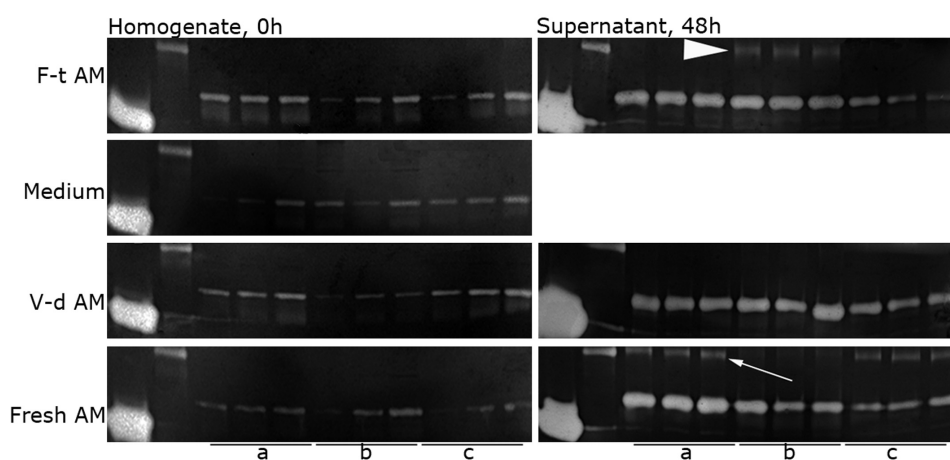


Figure 5.11: Elution of MMP-2 and MMP-9

Zymography was performed on fresh, *f-t* and *v-d* AM after processing for use (0h), on *f-t* AM storage medium at baseline (0h) and after 48 hrs incubation. A total of 1.5 µg was dispensed into each well. MMP-2 and MMP-9 were analysed in triplicate in homogenates at 0h and supernatants at 48h of three AMs (a, b and c). This represents one of two replicate experiments. The white arrowhead and white arrow show MMP-9 bands in *f-t* AM and fresh AM respectively.

Table 5.11: Intensity values, MMP-2

Zymogram	AM	0h			48h		
		Fresh	F-t	V-d	Fresh	F-t	V-d
1	a	117.1	86.9	84.0	125.7	176.3	172.3
	b	90.7	76.6	119.2	112.7	116.3	78.7
	c	73.2	34.2	87.7	126.0	151.3	168.0
2	a	88.9	71.8	94.4	-	91.1	137.0
	b	85.8	129.5	79.2	-	125.8	156.7
	c	65.0	122.7	69.6	-	106.2	60.6
Median		87.3	81.8	85.9	121.1	125.7	146.9

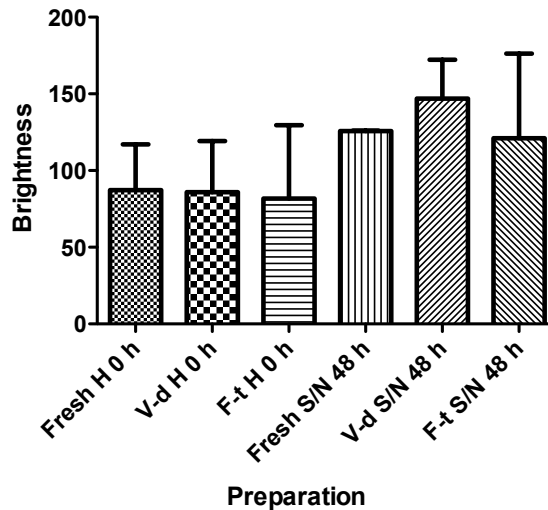


Figure 5.12: MMP-2 band intensity

Zymography was performed on a total of six AMs to compare the intensity of MMP-2 and MMP-9 at baseline and after incubation for 48 hrs. The intensity of the bands was normalised against MMP markers in each zymogram gel. There is an increase in the intensity of MMP-2 after 48 hrs. Median values are shown with error bars representing range.

and f-t AM ($p = 0.024$ and 0.047 respectively; Mann Whitney) (figure 5.12). The increase in intensity between v-d AM at 0h (Md 85.9) and at 48h (Md 146.9) was non-significant.

5.4.4 Macrophage assays

Six optimising steps and one triplicate macrophage assay were performed. Fresh uncoagulated whole blood samples resulted in an insufficient yield of macrophages. This technique was abandoned in favour of using buffy coats. Flow cytometry results from one representative sample of cells cultured by this method are shown in figure 5.13. The events (cells) were positive for CD14 (76.7%), HLA-DR (86.8%), mannose receptor (93.3%), CD11b (94.2%) and CD16 (69.0%), and negative for CD3. This was taken as evidence of activated macrophages.

In Assay 2, 3-mm f-t and v-d AM discs were incubated with macrophages from two buffy coats cultured in Teflon bottles. The macrophages were stimulated with 1 - 10 $\mu\text{g/mL}$ of FPL or 25 - 100 ng/mL of LPS. The negative

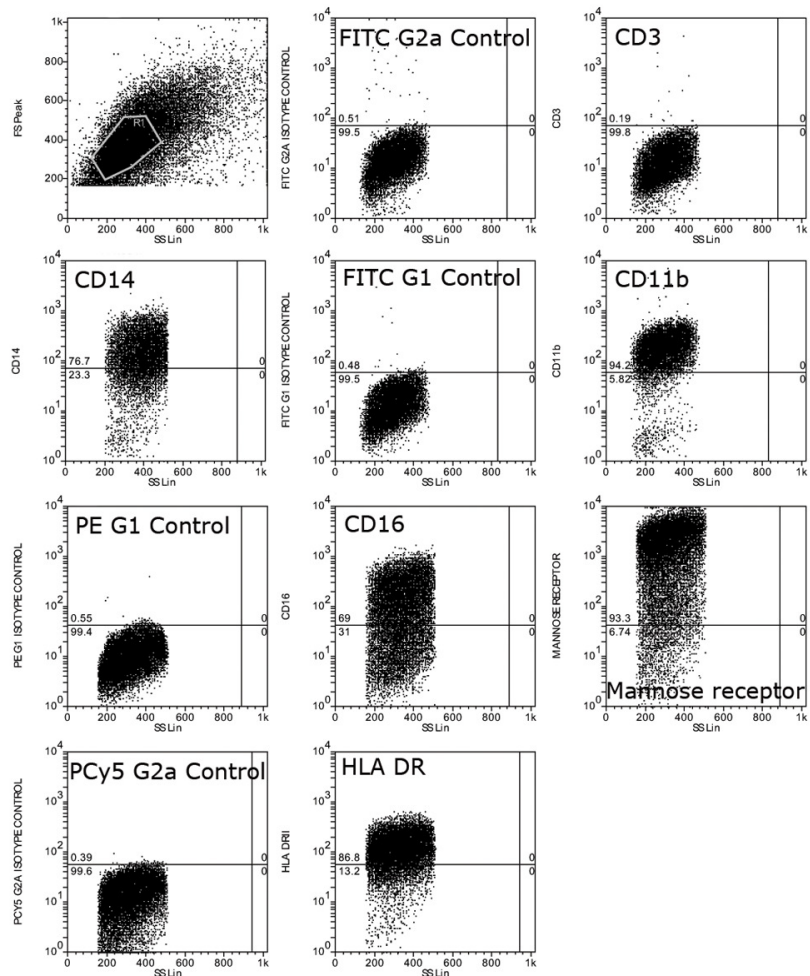


Figure 5.13: Activated macrophage markers

CD14⁺ cells extracted from buffy coats were cultured for 7 days. After 7 days, the cells were labelled with IgG1 and IgG2a monoclonal antibodies to CD16, CD14, CD11b, CD3, HLA-DR and mannose receptor with isotype controls. Flow cytometry was performed (representative sample shown).

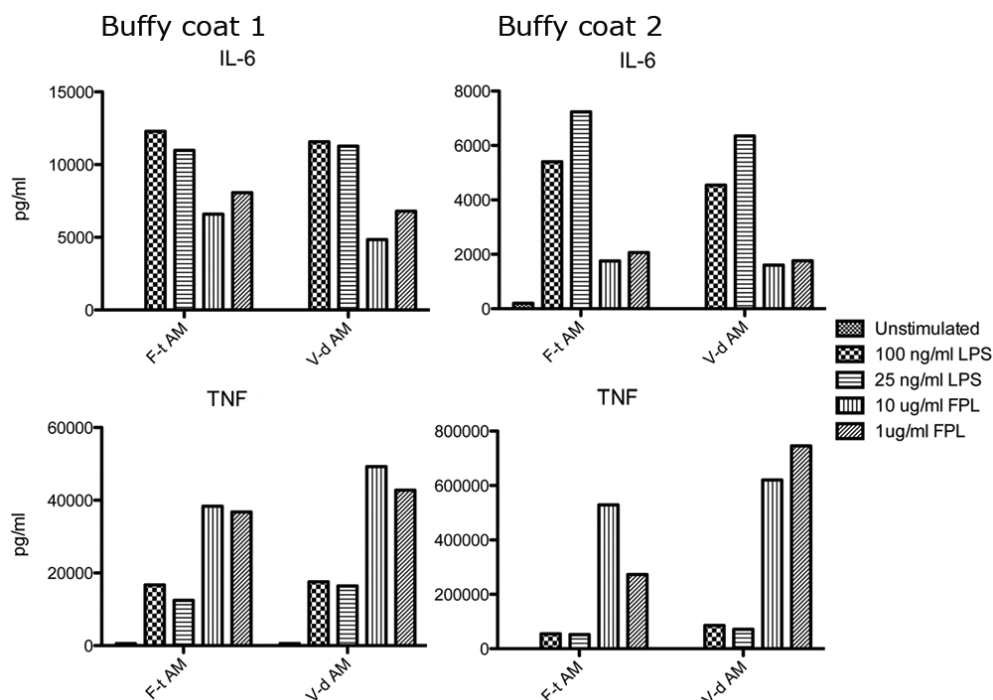


Figure 5.14: Macrophage Assay 2

LPS, lipopolysaccharide; *FPL*, French press lysate (*pseudomonas antigen*); *IL-6*, interleukin 6; *IL-8*, interleukin 8; *TNF*, tumour necrosis factor, *alpha*

controls and several of the test samples were irretrievably damaged during cytokine analysis, and it was not possible to analyse the levels of IL-8 or IL-10. Following stimulation by LPS and FPL, IL-4, and IL-13 were undetectable. The levels of IL-6 and TNF are shown in figure 5.14. Levels of FPL-stimulated TNF, and LPS-stimulated TNF in one set of macrophages (buffy coat 2), were considerably higher than the recommended detection limit of 20 000 pg/mL covered by the standard curve. The IL-6 responses of LPS-stimulated macrophages cultured with f-t AM and v-d AM were similar, while there was variability between macrophage donors across both levels of LPS stimulation (100 ng/mL, $p = .006$; 25 ng/mL, $p = .09$). The values are shown in table 5.12.

In Assay 3, 4-mm f-t and v-d AM discs were incubated with macrophages from two buffy coats. The macrophages were stimulated with 1 μ g/mL of FPL or 25 ng/mL of LPS. The data for IL-6, IL-8, IL-10 and TNF are shown in table 5.13, and plots of IL-6, IL-8, and TNF levels for each buffy coat are

Table 5.12: Cytokine levels, Assay 2

Stimulant	Analyte	AM	-	LPS (ng/mL)		FPL (μ g/mL)	
			0	100	25	10	1
Buffy coat 1	IL-6	F-t	0	12296	10985	6591	8064
		V-d	0	11569	11264	4840	6792
	TNF	F-t	564	16735	12461	38365	36759
		V-d	588	17560	16431	49257	42756
Buffy coat 2	IL-6	F-t	200	5402	7238	1759	2064
		V-d	0	4545	6349	1605	1765
	TNF	F-t	0	54782	52390	529122	272946
		V-d	0	85873	71910	620556	745971

LPS, lipopolysaccharide; *FPL*, French press lysate; *IL*, interleukin; *TNF*, tumour necrosis factor.

shown in figure 5.15.

Levels of TNF produced by LPS- and FPL- stimulated macrophages were over the recommended detection limit. The levels of IL-8 in unstimulated macrophages were significantly higher than in macrophages stimulated with LPS ($p < .0001$) and FPL ($p < .0001$). A trend is suggested from the IL-6 levels of the LPS-stimulated macrophages of buffy coat 1, which are lowest for the control and highest for f-t AM. Conversely, TNF, which is only marginally outside the standard, is highest for control AM and lowest for f-t AM.

In Assay 4, 6-mm AM discs were incubated with macrophages from two buffy coats. There were five preparations of AM, including fresh, f-t, 0% v-d, 10% v-d and thermolysin-denuded AM (figure 5.14, table 5.16).

Several measurements of IL-6 were beyond the limits of the standard curve. The levels of IL-8 were higher in unstimulated macrophages were higher than in macrophages stimulated with LPS and FPL (beyond standard limits). There were minimal levels of IL-10. The macrophages incubated with no AM (negative control) produced levels of TNF that were beyond the standard limit. The levels are higher than those produced by macrophages incubated with AM from each preparation, except for one value

Table 5.13: Cytokine levels, Assay 3

Analyte	Stimulant	Buffy coat 1			Buffy coat 2		
		-	LPS	FPL	-	LPS	FPL
		AM	25 (ng/mL)	1 (µg/mL)	AM	25 (ng/mL)	1 (µg/mL)
IL-6	F-t	74	20307	8518	198	7446	1839
	V-d	48	13378	8287	586	7548	1667
	Control	51	12161	6927	39	7232	1718
IL-8	F-t	5842	3024	2241	4783	2072	1398
	V-d	5187	3300	2327	4482	2194	1417
	Control	5492	3111	2383	5014	2160	1456
IL-10	F-t	0	0	31	0	39	928
	V-d	0	0	26	0	20	999
	Control	0	0	25	0	10	620
TNF	F-t	595	19321	42102	55	51583	464653
	V-d	510	23382	48219	70	57271	651916
	Control	807	27251	55618	49	62151	95681

LPS, lipopolysaccharide; FPL, French press lysate; IL, interleukin; TNF, tumour necrosis factor.

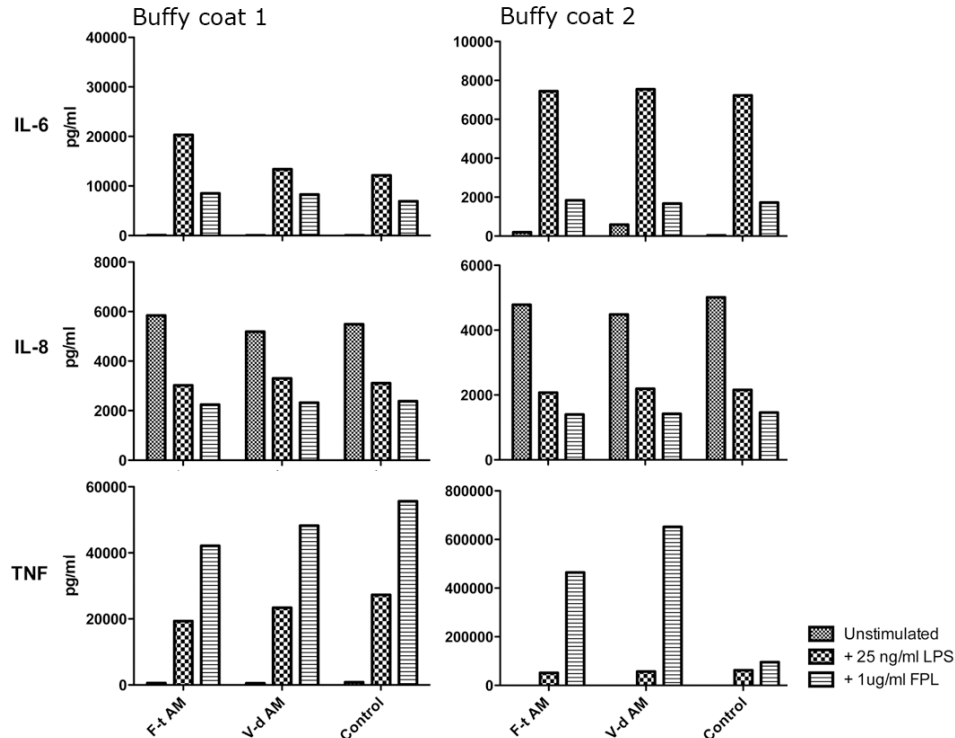


Figure 5.15: Macrophage Assay 3

LPS, lipopolysaccharide; FPL, French press lysate (pseudomonas antigen); f-t AM, freeze-thawed amniotic membrane; v-d AM, vacuum-dried amniotic membrane; IL-6, interleukin 6; IL-8, interleukin 8; TNF, tumour necrosis factor, alpha

Table 5.14: Cytokine levels, Assay 4

Analyte	Stimulant AM	Buffy coat 1			Buffy coat 2		
		-	LPS 10 (ng/mL)	FPL 0.01 (µg/mL)	-	LPS 10 (ng/mL)	FPL 0.01 (µg/mL)
IL-6	F-t	134	26813	27978	50	39432	68186
	V-d	125	27145	23234	61	27912	16521
	Control	1	20821	18596	21	39726	31484
	Fresh	106	21516	18383	37	36481	19899
	Denuded	25	37005	-	88	95626	42834
	10% v-d	31	20256	16186	63	27428	15392
IL-8	F-t	11950	6192	5372	16708	7817	5721
	V-d	12607	6230	4939	16390	7813	4626
	Control	11527	5895	4907	18572	7479	5690
	Fresh	10775	4908	5341	16721	6791	4853
	Denuded	12984	7011	-	17627	8912	5713
	10% v-d	8072	5480	4356	17267	7547	4479
IL-10	F-t	0	54	53	0	2	33
	V-d	0	45	74	1	8	61
	Control	0	80	46	10	8	11
	Fresh	0	0	-	5	5	39
	Denuded	0	38	-	0	0	34
	10% v-d	0	61	-	0	0	62
TNF	F-t	42	7931	3593	119	7249	20867
	V-d	51	7296	3150	143	2357	40374
	Control	1	27206	29405	138	14977	41577
	Fresh	50	6600	5486	124	4543	37872
	Denuded	10	7277	-	108	3021	18226
	10% v-d	23	4720	12789	78	3436	43367

LPS, lipopolysaccharide; *FPL*, French press lysate; *IL*, interleukin; *TNF*, tumour necrosis factor.

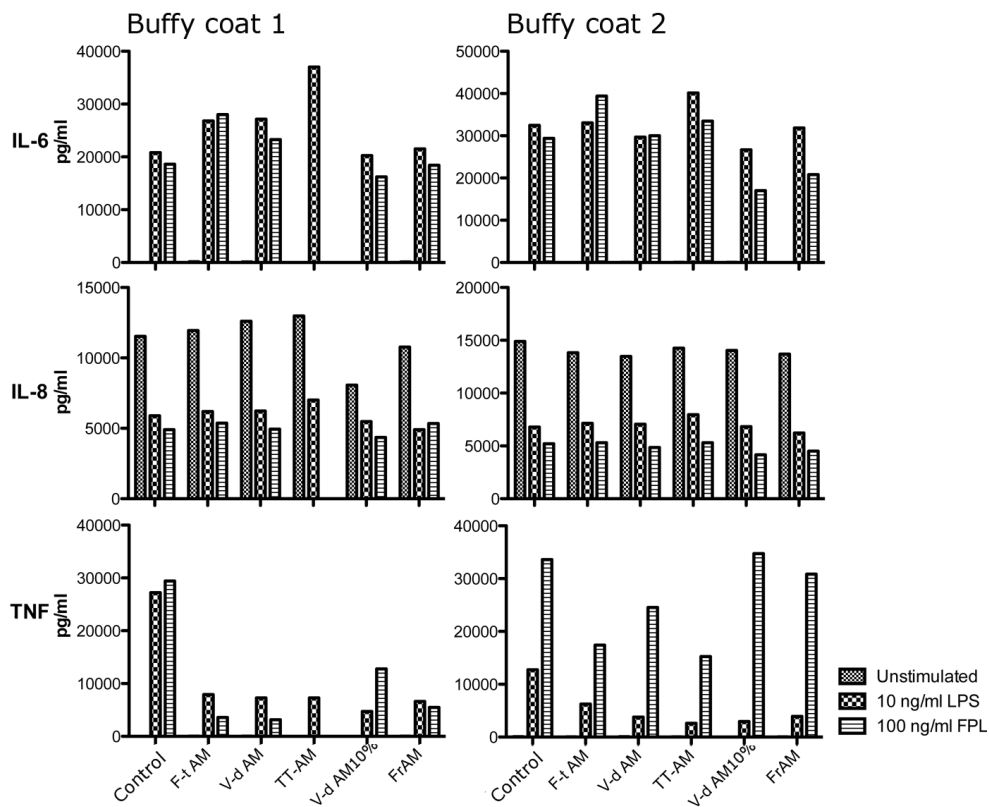


Figure 5.16: Macrophage Assay 4

LPS, lipopolysaccharide; *FPL*, French press lysate (*pseudomonas antigen*); *TT-AM*, thermolysin-denuded AM; *FrAM*, fresh AM; *V-d AM10%*, trehalose-treated AM; *IL-6*, interleukin 6; *IL-8*, interleukin 8; *TNF*, tumour necrosis factor, alpha

Table 5.15: Cytokine levels, Assay 6

Stimulant		-	LPS	FPL
Analyte	AM		100 ng/mL	70 ng/mL
IL-6	F-t	222	36610	26607
	V-d	130	38049	-
	Control	135	38607	16006
	10% v-d	1234	36094	23521
IL-8	F-t	2686	5482	7904
	V-d	3690	5478	-
	Control	2520	5570	8962
	10% v-d	8353	5392	7823
IL-10	F-t	30	12	12
	V-d	36	-	-
	Control	1	16	16
	10% v-d	0	36	36
TNF	F-t	98	9003	5079
	V-d	27	14144	-
	Control	0	21633	4014
	10% v-d	0	8882	2577

LPS, lipopolysaccharide; *FPL*, French press lysate; *IL*, interleukin; *TNF*, tumour necrosis factor.

of v-d AM (donor 2).

A fifth assay resulted in a yield of macrophages that was too low to proceed. This prompted a switch to the ultra-low adherence flasks.

In Assay 6, AM discs of 6 mm were incubated with macrophages from one buffy coat cultured in ultra-low adherence flasks. AM preparations included f-t, v-d and 10% v-d AM. These were stimulated with 100 ng/mL of LPS and 70 ng/mL of FPL. The data are shown in table 5.15 with plots in figure 5.17.

The levels of IL-6 were beyond the standard curve. IL-8 is higher in the stimulated preparations (non-significant). The level of TNF is higher in the negative control than in the three AM preparations.

In Assay 7, the format of the experiment was changed to include three different AMs. F-t, v-d and 10% v-d AM discs of 8 mm were incubated with

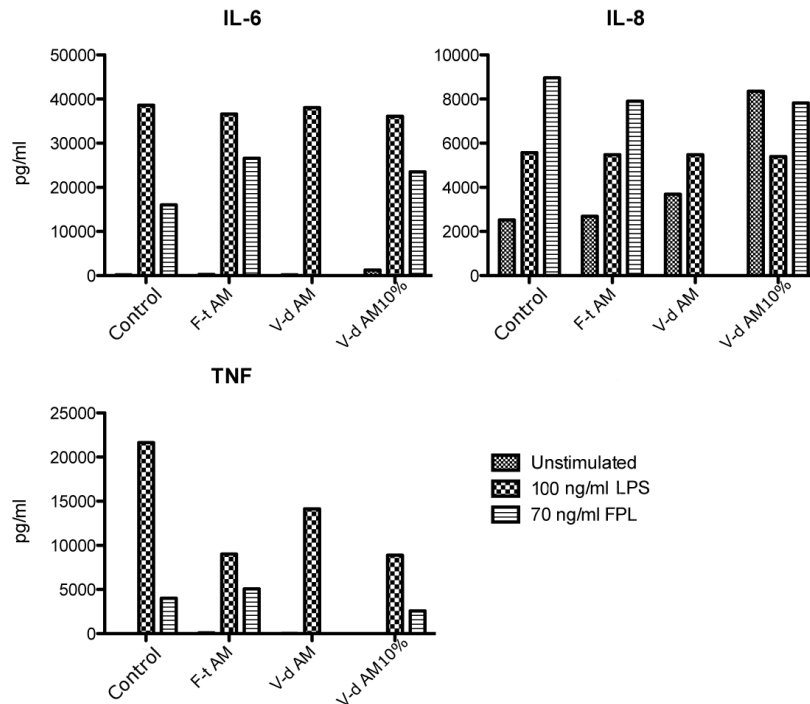


Figure 5.17: Macrophage Assay 6

LPS, lipopolysaccharide; *FPL*, French press lysate (*pseudomonas antigen*); *V-d AM10%*, trehalose-treated *v-d AM*; *IL-6*, interleukin 6; *IL-8*, interleukin 8; *TNF*, tumour necrosis factor, alpha

macrophages from one buffy coat. The supernatants were diluted 1:10 in RPMI-1640 for cytokine analysis. The data are shown in table 5.16. IL-8 measurements were beyond the detection limits. Plots are shown of the mean values of IL-6 and TNF across the three AMs with error bars representing *SD* values. (figure 5.18). The mean values of the cytokines (*SD*) are shown in table 5.17. In the supernatants of both LPS- and FPL-stimulated macrophages, IL-6 levels were higher in f-t AM and v-d AM than in negative controls (non-significant). In LPS-stimulated macrophages, TNF levels were higher in controls than either f-t AM or v-d AM. There was a significant difference in TNF levels between LPS-stimulated macrophages incubated with f-t AM and negative controls ($p = .026$, paired *t* test).

Table 5.16: Cytokine levels, Assay 7

Stimulant	-	LPS	FPL	-	LPS	FPL	
Analyte	AM	10 ng/mL	100 ng/mL	10 ng/mL	100 ng/mL	100 ng/mL	
		AM 1			AM 2		
IL-6	F-t	6	21870	13904	0	13714	10016
	V-d	125	20900	20300	0	20861	10287
	Control	0	16419	6637	6	14631	5793
IL-8	F-t	1041	16406	16408	1101	27677	30302
	V-d	2881	25160	14727	3303	13552	16270
	Control	2388	15750	31852	2183	28658	36239
TNF	F-t	0	4023	5168	0	3266	2707
	V-d	0	5001	4020	0	4569	3369
	Control	0	6019	3480	0	5224	2924
		AM 3					
IL-6	F-t	214	21256	7938			
	V-d	6	15341	9191			
	Control	3	15525	6215			
IL-8	F-t	2444	15892	13464			
	V-d	1297	25669	11456			
	Control	2286	22204	34045			
TNF	F-t	17	2484	1950			
	V-d	0	3246	2724			
	Control	0	5622	3202			

LPS, lipopolysaccharide; FPL, French press lysate; IL, interleukin; TNF, tumour necrosis factor.

Table 5.17: Mean cytokine levels, Assay 7

Stimulant	LPS		FPL	
AM	IL-6	TNF	IL-6	TNF
F-t	18 947 (4542)	3258 (770)	10 619 (3029)	3275 (1682)
V-d	19 034 (3198)	4272 (914)	13 259 (6122)	3371 (648)
Control	15 525 (894)	5622 (398)	6215 (422)	3202 (398)

Mean values are shown (SD) in pg/mL.

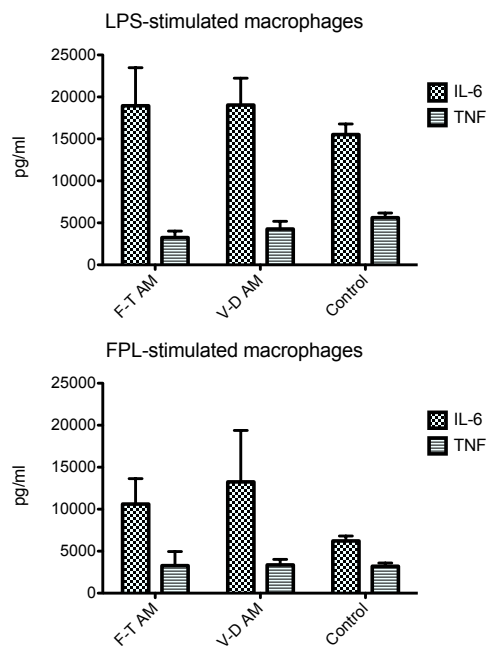


Figure 5.18: Macrophage Assay 7

Macrophages were stimulated with LPS and FPL in co-culture with three different *f-t* and *v-d* AM samples and negative controls. IL-6 and TNF in the supernatants were measured in pg/mL. Plots of mean values with error bars representing standard deviation are shown. LPS, lipopolysaccharide; FPL, French press lysate; IL, interleukin; TNF, tumour necrosis factor.

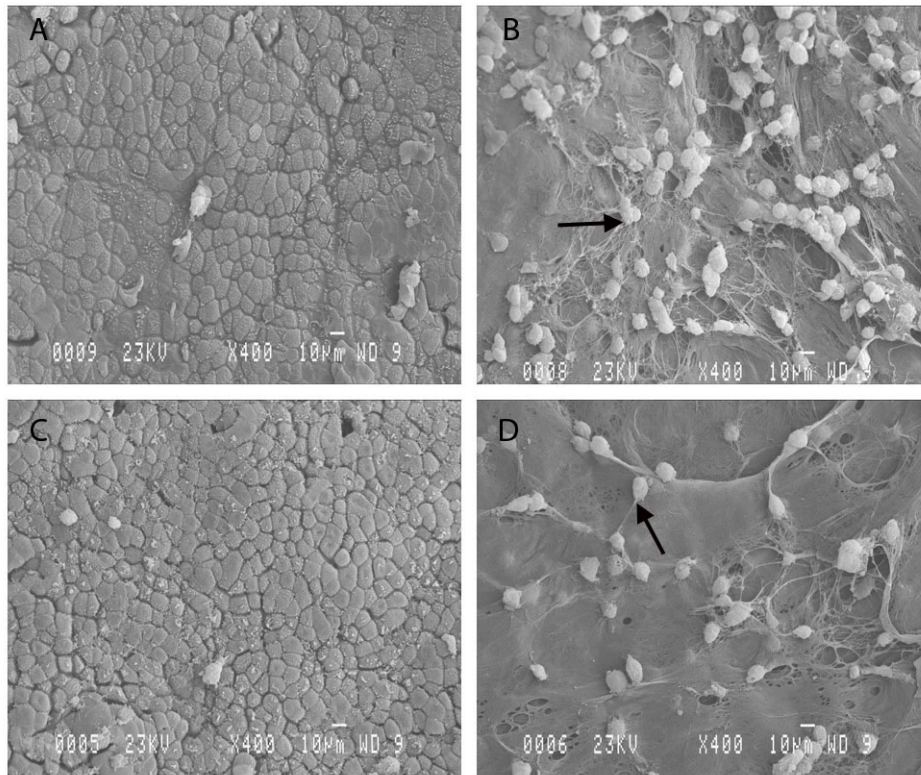


Figure 5.19: Macrophage adherence

Macrophages were co-cultured with AM discs and stimulated with LPS or FPL. The samples were lyophilised and SEM images taken of both epithelial and stromal aspects. Macrophages are shown to adhere to spongy layer remnants (black arrows). Representative images are shown for fresh AM (A and B) and v-d AM (C and D). LPS, lipopolysaccharide; FPL, French press lysate.

5.4.5 Scanning electron microscopy

SEM images of the epithelial and stromal sides of fresh AM (A and B) and v-d AM (C and D) are shown in figure 5.19 shows that the macrophages adhere preferentially to the network of residual spongy layer on the stromal aspect. Fewer macrophages can be seen on the epithelial aspect of the same AM samples.

5.5 Discussion

5.5.1 Antimicrobial activity

The expression of hBD3 in AEC is well-known (Buhimschi et al., 2004; Stock et al., 2007; King et al., 2007b), and psoriasin has been detected in AEC by PCR (Porre et al., 2005). The documentation of AM-derived AMPs is important, as it suggests a potentially useful therapeutic avenue. In this study, the detection of AM-derived AMPs by western blotting proved difficult. The repeated negative findings were obtained despite concentrating the proteins and using using different antibodies. Fractionation of proteins was also tried, although protein loss occurred. The western blots were conducted on whole tissue and AEC extracts. Low molecular weight bands were detected in one sample extracted in TBST_x overnight and in two reduced samples on a Tricine gel (figure 5.2). These could represent hBD3. hBD1 and LL-37 were not detected. The technique of western blotting is suitable for detecting AMPs. Strong bands of psoriasin were detected in a western blot of ocular surface epithelial cells (Garreis et al., 2011), and the presence of α -defensins in amniotic fluid has been shown by western blotting (Akinbi et al., 2004). Sørensen et al. (2003) were able to demonstrate the presence of hCAP-18 in keratinocyte medium on SDS-polyacrylamide gel electrophoresis (PAGE) followed by immunoblotting. The most likely explanation for the inconsistent expression of hBD3 may be that it can only be detected by western blotting in stimulated AM. HBD3 can be present in in unstimulated AEC, yet it is upregulated by inflammatory stimuli (Buhimschi et al., 2004). hBD3 can be upregulated in other tissues. HBD3 and hBD9 were found to be constitutively expressed on the ocular surface, becoming up-regulated in bacterial keratitis (Otri et al., 2012). Similarly, 10-fold expression in hBD3 was found in corneal epithelial cells exposed to *Acanthamoeba castellanii* (Otri et al., 2010). Sørensen et al. (2003) found no basal expression of hBD3

in keratinocytes, but were able to demonstrate its presence in keratinocyte medium following stimulation with TGF- α . Several other AMPs are similarly inducible. Ikeda et al. (2005) found constitutive expression of HNP 1 - 3 and hBD1 on the ocular surface, yet the detection of hBD2 was contingent upon the stage of ocular surface disease. In the same study, RNase-7 was consistently up-regulated, whereas hBD1 was downgraded Otri et al. (2010).

The failure of the CBA assay to detect hCAP-18/LL-37 in the AM is not likely to reflect the choice of antibodies. The capture antibody used (ab80895) is specific to the N-terminal pro-region of the hCAP-18 molecule, and not the microbicidal C-terminus, LL-37. Since intracellular hCAP-18 remains uncleaved until exocytosis (Sørensen et al., 2001), it may be expressed in AEC. The detection antibody (G-075-06) also recognises the uncleaved molecule (Heilborn et al., 2003). The next stage of the CBA would have been to quantitate the protein against a known quantity of recombinant LL-37, but in the absence of any detection of the peptide, this stage was deferred. Although CBA is a more sensitive tool than western blotting, the failure to detect LL-37 could have been due to insufficient titration of the detection antibody.

For flow cytometry experiments, single cell suspensions of AEC was gated in the central portion of the cells sorted by side scatter and linear scatter to reduce the proportion of non-viable cells, which can give rise to non-specific staining. Permeabilisation was useful in obtaining increased positivity for hBD3, suggesting a predominantly intracellular localisation (figure 5.4). An inspection of the results shows that the rabbit polyclonal antibodies produced higher rates of positive results than the mouse monoclonals (table 5.9). In the first three flow cytometry experiments after the optimisation step, only one test out of seven using rabbit polyclonals returned a negative result. Of the rest, frequent high values were reported for positivity (e.g.,

81.4% for RNase-7, 54.3% for LEAP-2, 53.5% for hBD3). In contrast, the experiments using mouse monoclonals returned negative values in seven out of nine tests. The two positives were low (9.0% for psoriasin, 3.8% for hBD3). In the final flow cytometry experiment, the incubation with primary antibody was overnight at 4°C. Strong positives were returned for all the antibodies (one mouse, four rabbit). Of these, the mouse antibody had the least positivity (psoriasin, 61.8%), whereas the four rabbit antibodies returned positivities of between 84.8% and 98.6%. Therefore, the possibility of non-specific binding must be considered.

Polyclonal antibodies can recognise a variety of epitopes, and therefore have an increased propensity for non-specific binding. In addition, the polyclonal antibodies used were not validated specifically for intracellular staining. In the case of psoriasin it is interesting to note that the likelihood of non-specific binding has been noted in previous studies (Porre et al., 2005). This is because psoriasin contains a calcium-binding region which is homologous with that of other members of the S100 family of calcium-binding proteins. Non-specific binding is unpredictable, even for fluorochrome-conjugated monoclonal antibodies (Keeney et al., 1998). For this reason, non-specific binding sites are blocked by pre-incubating the cells in serum. In the current study, the cells were blocked in NGS. It has been suggested that the serum should be the same species as the primary antibodies (Stewart and Stewart, 1994), which, in this study, were produced in rabbit and mouse. In addition to adequate blocking, flow cytometry usually necessitates a negative control. For monoclonal reagents, isotype-matched controls are recommended to generate background fluorescence as a reference point for optimising the experiment (O’Gorman and Thomas, 1999). There are alternatives to isotype-matched controls, such as blocking the antibody-binding portion of the antibody to allow visualisation of the extent of non-specific binding (Keeney et al., 1998). In the current study, both monoclonal

and polyclonal antibodies were used, for which isotype controls may not have been suitable as they contain more than one IgG subclass. Therefore, the negative controls consisted of secondary antibody with no primary. While this may be flawed, since the goat secondaries will have different non-specific binding sites to the rabbit and mouse primaries, it provided a gross estimate of background non-specific binding. In order to increase confidence in the positive findings, directly conjugated monoclonal antibodies with isotype-matched controls are recommended for future testing.

The antimicrobial assays returned an absence of antimicrobial activity in fresh and therapeutic AM against common Gram positive and Gram negative pathogens. This is in contrast with the findings of Talmi et al. (1991) and Kjaergaard et al. (2001). The latter study demonstrated marked inhibition of *S. aureus*, *S. saprophyticus* and group A streptococci. The authors noted that direct contact was not mandatory for the effect, suggesting it might be due to the presence of defensins. The relevance of detecting AMPs in fresh AM was lessened by the inability to reproduce these findings. No definitive evidence was found for AM-derived AMPs by any technique.

5.5.2 The elution of metalloproteases

In protein microarrays, higher levels of TIMPs than MMPs were found in fresh and processed AM (figure 5.10). As an illustration, the median level of TIMP-1 in fresh AM was 97 562 pg per mg of tissue extract, which when compared to 9512 pg of constitutively-expressed MMP-2 gives a ratio of 10:1. Since TIMP molecules inhibit MMP molecules stoichiometrically (Zucker and Cao, 2006; Ardi et al., 2009), this suggests that AM-derived TIMPs prevents MMPs from degrading collagens. By far the most abundant MMP was MMP-2, which was significantly higher than all other MMPs in all preparations. MMP-9 was second. These were compartmentalised in both epithelial and stromal layers. While MMP-2 is constitutively expressed, gestational

timing and individual variation can influence the expression of MMP-9. Indeed, Fortunato et al. (1997) were only able to detect MMP-9 in membranes from women with intra-amniotic infections. In an organ culture model, inflammatory mediators such as LPS, TNF and IL-1 β stimulated the production of MMP-9 pro-enzyme from AM (Arechavaleta-Velasco et al., 2002).

Analytes with concentrations higher in de-epithelialised tissue than in fresh tissue have a stromal compartmentalisation, while the converse suggests an epithelial compartmentalisation. Statistically significant examples include MMP-1, which was predominantly retained in the stroma, while MMP-3 and TIMP-1 were compartmentalised in the epithelium. Retention of the analytes in f-t AM (compared to fresh) may indicate low water solubility, as the factors would otherwise have been eluted in the storage medium and washes. This is most evident for MMP-7 and MMP-8 (non-significant). The higher levels of MMP-2, MMP9, TIMP-1 and TIMP-2 in v-d AM suggest a higher concentration of protein was present in the v-d AM samples. This is a concentration effect, since the wet preparations all lose protein during processing, whereas in v-d AM water soluble proteins are highly concentrated.

MMP-2 pro-enzyme was detected in supernatants and homogenates at baseline and after incubating for 24 hours (figure 5.10) and 48 hours (figure 5.11). Higher concentrations of protein were obtained by homogenising the samples at baseline, while sufficient protein levels in the supernatant were available after incubation. MMP-2 pro-enzyme was detected in AM supernatants after incubation, indicating its elution. The intensity of MMP-2 in supernatants after incubation for 48 hours was higher than in homogenates at baseline. Although the protein levels were normalised across the wells, the technique of zymography is difficult and can lead to variable results. The increased in MMP-2 intensity after incubation for 48 hrs may have occurred by chance alone. However, an inspection of the zymograms suggests

that the MMP-2 levels are indeed higher after incubation in all preparations. As is the case for other soluble molecules (Hopkinson et al., 2006b), f-t AM loses soluble MMP-2 into the storage and washing media during freezing and preparation for use. MMP-9 expression can occur after incubation of fresh tissue. It can also be detected in preserved, devitalised tissue after incubation, suggesting its expression prior to preservation. MMP-9 was not detected in baseline homogenates.

It is not clear why MMP-2 and MMP-9 were detected in preserved AM after incubation, since the tissue is devitalised. The possibilities include that they were not completely extracted at baseline. However, the protein microarrays indicate that MMP-9 is present in the preserved tissues. An alternative explanation is that the latent pro-enzymes may be undetectable by zymography at baseline, undergoing conformational change during incubation to become detectable. An unlikely explanation is that residual living cells are expressing these enzymes.

The significance of elution of inactive MMP-2 and MMP-9 is unclear. As they are highly regulated, they may remain largely inactive. Since MMP-9 is normally bound to TIMP-1 (Goldberg et al., 1992), it is unlikely that it would affect the ocular surface in the same way as neutrophil-derived MMP-9, which is TIMP-free (Ardi et al., 2007). However, Arechavaleta-Velasco et al. (2002) indicate that the pro-enzyme may become activated by MMP-2 and MMP-3, suggesting that MMP-9 activation may occur on the inflamed ocular surface.

Taken together, these data indicate that MMPs are a factor to be considered when applying AM therapeutically, for example in patients with corneal melting (Hossain, 2012). The clinical effects of these enzymes on the ocular surface are incompletely understood, reflecting the complex interaction between MMPs and their inhibitors.

5.5.3 Macrophage suppression

Macrophages that were cultured with GM-CSF were identified by their expression of a range of markers, including CD14, CD16, mannose receptor, CD11b and HLA-DR (figure 5.13). These were co-cultured with various preparations of AM and stimulated with LPS or FPL. This was optimised over a series of assays. The technique was difficult, and subject to high levels of variability between the responses of macrophages from different sources (e.g., Assay 2, figure 5.14), between the methods of culture (i.e., Teflon bottles versus ultra-low adherence flasks) and even in cytokine levels across similar preparations. The latter could be due to variations in technique, which may have resulted in occasional incidences of missed data and spurious measurements (e.g., TNF levels in FPL-stimulated macrophages in Assay 3, table 5.15). In addition, while buffy coats generally gave sufficient yields of PBMCs, their supply was dependent on availability, which was a limiting factor in this study. Future researchers may consider using whole-blood leukoreduction filters, which provide a safely and convenient source of white blood cells from donated blood (Néron et al., 2007). Two assays did not yield sufficient PBMCs.

Despite the variability, a pattern was observed in Assay 3 (buffy coat 1, figure 5.15) which suggested TNF suppression in the supernatants of macrophages co-cultured with AM, and, paradoxically, concomitant elevation of IL-6. IL-8 levels were unchanged. However, the data for TNF were beyond the standard curves, so could not be used. As these were single measurements, statistical analysis was not performed. In Assay 4 (buffy coat 1 and buffy coat 2, figure 5.16), the suppression of LPS-stimulated macrophage TNF (and also FPL-stimulated macrophages from buffy coat 1) was marked across all preparations of AM. There was high variability across the IL-6 levels, whereas IL-8 levels remained consistent. Suppression of TNF was again noted in Assay 6 (LPS-stimulated; figure 5.17). A

further assay using triplicate AMs demonstrated TNF suppression and IL-6 elevation in LPS-stimulated macrophages (Assay 7, figure 5.18). An elevated IL-6 response by FPL-stimulated macrophages co-cultured with AM was also seen. Thus, the suppression of TNF and elevation of IL-6 expressed by macrophages was demonstrated on different occasions using different buffy coats and different AMs. IL-10 expression was negligible, whereas IL-8 expression did not show any clear trends. This suggests complex interaction effects between the macrophages and AM. There was no evidence of a difference in the effects across the different preparations of AM was found.

The activation of macrophages is of key importance in acute inflammation and wound healing (Alber et al., 2012). Depending on their stimulation, macrophages can give rise to pro-inflammatory, anti-inflammatory or regulatory subtypes. Activation of macrophages triggers an intracellular signalling cascade leading to NF- κ B-mediated production of cytokines, including IL-1 α , IL-6, IL-10, TNF and GM-CSF and chemokines such as monocyte chemoattractant protein-1 (MCP-1), macrophage inflammatory protein (MIP) -1a and -1b and RANTES (regulated upon activation, normal T-cell expressed and secreted) (Zhou et al., 2012). Macrophages may also up-regulate MMP-9 and vascular endothelial growth factor (VEGF), key promoters of neovascularisation (Li et al., 2012). The NF- κ B pathway is one of the principal intracellular pathways by which LPS, a major component of the outer membrane of the cell-wall of Gram negative bacteria, is able to stimulate a pro-inflammatory cytokine response (Dos Santos et al., 2007). While pro-inflammatory macrophages are classically stimulated by IFN- γ and LPS, activation can also be initiated by key regulators of corneal epithelial healing such as IL-1 (Scheel et al., 2006) and TNF (Saika, 2007). As CD11b⁺ macrophages mediate angiogenesis in the inflamed cornea (Maruyama et al., 2005), their modulation by AM is highly relevant. TNF, which is produced primarily by macrophages, is a major pro-

inflammatory cytokine (Ming et al., 1987). In addition, while IL-6 can have pro-inflammatory effects, it can also suppress inflammation by inhibiting TNF production by LPS-stimulated human monocytes (Aderka et al., 1989) and murine macrophages *in vivo* (Di Santo et al., 1997), suggesting an auto-regulatory role. Therefore, the apparent modulation of TNF and IL-6 levels by AM may be clinically significant.

It is not clear from the SEM images whether the macrophages in the current study became apoptotic, as implied by previous reports (He et al., 2008; Li et al., 2006a). However, the possible elevation of IL-6 levels suggests that the cells may remain viable. Clinical reports have indicated that inflammatory cells, including monocytes, are entrapped by the AM stroma (Shimmura et al., 2001). However, EM images from the current study show that the component of AM to which the cells adhere is the spongy layer (figure 5.19). In this study, the spongy layer was routinely removed, leaving residual strands behind. It may be that removing the spongy layer also removes an important anti-inflammatory component of AM.

The specific intracellular pathways of AM-induced immune suppression are of great interest, and may help determine whether AM can suppress inflammation over and above topical corticosteroids. Expression of the gene encoding TNF is suppressed by phosphorylation of NF- κ B (Wall et al., 2009). This pathway has been implicated in macrophage apoptosis induced by AM-derived factors (He et al., 2008; Li et al., 2006a). The reduced expression of corneal epithelial IL-1 α and IL-1 β has also been linked to the suppression of NF- κ B cytokine pathways by matriceal hyaluronans (Solomon et al., 2001). These nonsulphated glycosaminoglycans are abundant structural components of AM, and are predominantly located in the spongy layer (Meinert et al., 2001). Therefore, the adherence of macrophages to spongy layer remnants implicates hyaluronans. High molecular weight hyaluronans have a marked anti-inflammatory effect, inhibiting inflammatory cell chemotaxis

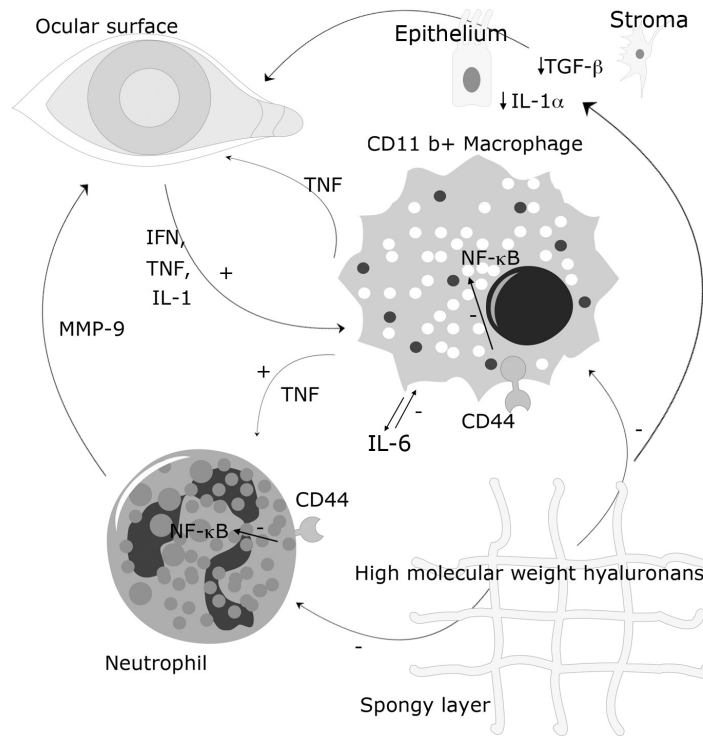


Figure 5.20: Suppression of inflammation by AM

Simplified schema representing the putative mechanisms of suppression of inflammation by AM. High molecular weight hyaluronans in the spongy layer may suppress TNF-mediated $NF-\kappa B$ pathways in activated macrophages and neutrophils via the CD44 receptor, as well as directly suppressing $TGF-\beta$ and $IL-1\alpha$ production on the ocular surface. This would result in suppression of neovascularisation (MMP-9), inflammation (TNF) and scarring (TGF). Macrophage IL-6 may have an auto-regulatory function.

and phagocytosis (Tamoto et al., 1994). They can inhibit $NF-\kappa B$ -induced inflammatory cytokine up-regulation in macrophages via the CD44 receptor (Neumann et al., 1999). This receptor is known to mediate adhesion between lymphocytes and the stromal aspect of AM (Higa et al., 2005). In a study by He et al. (2009), high molecular weight hyaluronans isolated from AM extract suppressed TGF transcription in corneal stromal cells and induced macrophage apoptosis. The authors suggest that these hyaluronans constitute the principal active component in AM to cause clinically observed suppression of scarring and inflammation. These interactions are summarised in figure 5.20.

These findings suggest that some of the principal biological mediators of AM may be relatively insoluble structural components of the ECM, rather

than soluble factors derived from the epithelium, such as IL-10, as previously suggested (Tseng et al., 2004). This is consistent with the finding that a proteoglycan present in AM stroma, lumican, can promote epithelial wound healing in the cornea (Yeh et al., 2005). This has significant implications on AM processing, since it suggests that the epithelium can be removed with no adverse consequences and that the spongy layer may be a useful therapeutic adjunct and a valuable component of AM. It also indicates that f-t and v-d AM might retain the anti-inflammatory properties of the fresh tissue, since, unlike soluble factors, the high molecular weight hyaluronans may not be easily eluted.

5.6 Conclusion

Questions remain as to whether AM-derived factors such as AMPs and MMPs can have any activity on the ocular surface and contribute towards wanted or unwanted effects. However, the interaction of the macrophages with the spongy layer remnants suggests that suppression occurs as a consequence of direct contact, rather than through soluble factors. This may be the most significant of the biological properties of therapeutic AM. The two hypotheses are not mutually exclusive, illustrating the complexity of the tissue as a therapeutic modality. To resolve these questions, *in vitro* models or animal models of eye injury will be important in establishing whether this laboratory finding has a clinical parallel.

Chapter 6

CONCLUSION

6.1 Discussion

This study of the use of dried AM in the treatment of acute ocular surface injuries brings together seemingly unrelated study domains, including evidence based medicine, materials science and biology, and makes a number of original contributions. These include an investigation of the evidence for AMT in acute ocular surface burns. In addition, a novel framework was devised for the optimisation of dried AM using methods usually available to food scientists, pharmacists and polymer engineers. Mechanical tests and a novel mathematical model indicated that dried AM is weaker than fresh or frozen preparations. This led to an unsuccessful attempt to strengthen the tissue by cross-linking the collagen matrix. Finally, a human macrophage assay was performed in which the suppression of TNF was shown, possibly as a result of direct contact with the AM spongy layer.

6.1.1 Significance of this study

6.1.1.1 Clinical trials

As a biological treatment, AM is unique, being the only allogeneic tissue to be transplanted with no expectation of permanence and usually not for

reasons of organ failure, and often without clear evidence to support its use. While a systematic review can be effective in highlighting the need for high-quality RCTs, ocular burns are sufficiently uncommon, in many parts of the world, to make this a challenging proposition. These injuries are more common in geographical areas in which medical services are not equipped to manage them comprehensively (Adepoju et al., 2007), making it even harder to organise a RCT. The emergence of RCTs from India (Tamhane et al., 2005; Tandon et al., 2011) is encouraging, combining high rates of presentation with modern treatment and academic attention. The review emphasises the need for more RCTs. In turn, this should encourage clear objectives in AM treatment, with objective criteria for success and failure in outcome reporting.

6.1.1.2 Optimisation of AM

The tissue moisture sorption, thermal and surface characteristics are highly relevant to its stability. Since the end moisture content of dried AM is directly linked to its A_w , these are mandatory parameters in optimisation. In addition, AM can be in a glassy phase at ambient temperature, depending on the moisture content. As it is highly hygroscopic, it may rapidly absorb ambient humidity, indicating a need for drying and sealing to be performed in a closed system. Trehalose increased the enthalpy of moisture sorption, stabilising the tissue. On the other hand, the trehalose excipient was not in a glassy state, prompting a need for further drying. The vitrification of trehalose/PBS mixtures can be optimised using thermoanalytical methods such as DVS in conjunction with mathematical models (Sitaula and Bhowmick, 2006). Since crystallisation of trehalose may harm the stability of the tissue by releasing water, it is important for it be vitrified (Costantino et al., 1998a), and the same is likely to apply to any excipient sugar. The further characterisation of polymorphs will be useful in this regard, as the

causes of excipient crystallisation on v-d AM are not fully understood.

6.1.1.3 Cross-linking of AM

The cross-linking of dried AM remains an important goal. Extensive mechanical testing showed that, while v-d AM may be sufficiently robust for clinical use, it is weaker than fresh and f-t AM. This was further indicated by a novel approach using mathematical modelling, which promises to be a useful technique in characterising different preparations of AM. Although cross-linking protocols, such as the one described by Ma et al. (2010), have already been shown to be effective at cross-linking AM, the clinical worth of dried cross-linked AM is just beginning to emerge Kitagawa et al. (2011). The effectiveness of alternative chemical means of cross-linking AM, such as the transglutaminase method (Chau et al., 2012), has not been demonstrated conclusively.

6.1.1.4 Biological activity of AM

Evidence of AMP expression in therapeutic AM was scant, while separate testing revealed no evidence of anti-microbial activity. However, the increasingly well-known reservoir effect of AM suggests that it may have genuine usefulness in treating infections (Gicquel et al., 2007). On the other hand, the possibility that inactive MMPs may become activated on the ocular surface prompts questions as to whether these enzymes can cause enzymatic degradation of corneal collagens or facilitate neovascularisation. This might be investigated by degradation assays using *in vitro* models of AM treatment on cadaveric human eyes. While the effects of MMPs are unclear, AM-induced TNF suppression could represent a significant contributor towards the clinical action of AM. Macrophage assays produced variable results, suggesting a need for further refinement. However, if the anti-inflammatory activity of AM is mediated principally by high molecular weight hyaluronans

in the spongy layer, the retention of epithelial soluble factors such as IL-10 would become less relevant, and the epithelium could be removed with no loss of function. It also suggests that purified spongy layer hyaluronans may have therapeutic potential.

6.1.2 Further work

6.1.2.1 Future RCTs

Although the lack of suitable RCTs of AMT for acute ocular burns precluded a meta-analysis, it is clear that well-designed RCTs are preferable to uncontrolled case series. Since the injury is relatively rare, a multicentre RCT can be considered to ensure sufficient numbers of cases. This could be made easier by introducing an anonymised worldwide web-based registry of ocular burns, enabling ocular burns and their treatment to be recorded in an accessible way, and has been proposed in a new grant application recently submitted by the University of Nottingham. In relatively uncommon and complex diseases, RCTs can be very difficult. Professor Radhika Tandon, of the Rajendra Prasad Eye Institute, has suggested that a stepwise sequential treatment trial with stratified randomisation would be a useful model to determine best practice.

For more precise classification, the Dua grading system is recommended for future studies. It is important that the treatment be performed in the acute phase (by day 7) in order to clearly demarcate the timing of the intervention. Since the timing of AMT is variable, this will improve confidence in the findings of an RCT by increasing the homogeneity of the patient base. The length of treatment can also be temporary (e.g., patch removed at 21 days post-injury). This would facilitate a masked assessment of epithelial recovery and avoid the problem of attempting to measure the rate of epithelial healing through an opaque membrane. Temporary patching may also reduce the risk of adverse outcomes, such as fungal keratitis, which often

take several weeks to develop. It is unlikely that an AM patch will continue to have any effect after this period. The inclusion of patients with a narrow grade of burn will increase confidence in the study findings, as it may help to equalise the baseline characteristics between treatment and control arms. The grade of burn should be severe enough to warrant treatment, but not so severe as to carry a high likelihood of secondary procedures or dismal prognosis. Furthermore, inclusion criteria should specify a single category of causative agent, since it is possible that burns from different causes will respond differently to treatment.

Clear outcome measures are of great importance in RCTs, and should answer clinically meaningful questions. For example, does AMT in the acute phase of a grade III alkaline burn result in a higher likelihood of complete epithelial healing by the end of the early reparative phase, compared to an untreated control? Many studies compare the daily epithelial healing rate, which fails to answer this fundamental question. This could be addressed by assessing epithelial healing at a fixed time point (i.e., day 21 post-injury), rather than by measuring the epithelial healing rate. A statistically significant difference in the size of a PED between treated and untreated groups by day 21 would constitute a clinically meaningful outcome, and would be simple to measure. In contrast, epithelial healing rates are highly dependent on case-by-case factors, such as timing of presentation and depth of burn. In addition, they are difficult to measure and subject to observer biases. The epithelial defect on day 21 could be measured with the AMT removed to minimise assessor bias.

Similarly, an assessment of visual outcomes should be performed after a fixed interval, rather than across a range of different time-points, as this is imprecise and can introduce bias. It is important to specify previously identified visual loss among study participants, and whether visual acuities were measured with or without correction. A comparison between the visual

outcomes of treatment and control groups can be misleading; a comparison of the improvement in visual acuity before and after treatment is more helpful. Separate studies could address the prevention of symblepharon, helping to direct treatment with AMT in increasingly specific ways. For example, in symblepharon prevention studies, AMT would be reserved for cases in which there was forniceal involvement, which would tend to be more severe. Simple grading systems for pain and neovascularisation are useful. An assessment of pain relief could include visual analogue pain rating scales before and after treatment. Convincing evidence of improved comfort alone could justify treatment of acute burns with AMT, but even this is currently lacking.

6.1.2.2 Animal model

A protocol for an animal model for AM treatment of chemical eye burns has been prepared as part of the wider project and is currently proceeding. The ARRIVE guidelines of the National Centre for the Replacement, Refinement and Reduction of Animals in Research were followed in the protocol design. A summary is provided below. The primary objective of the study is to compare the rate of corneal epithelialisation following patching of an acute chemical injury with either f-t AM or v-d AM. Ethical review permission has been sought and relevant licences applied for under the Animals (Scientific Procedures) Act 1986. The study was designed as a randomised control trial, with random sequence generation of the animals, random allocation of treatment and masked participants.

To facilitate statistical analysis, and to maximise the yield of information, the fellow eye was designated as a control (Murdoch et al., 1998). A power analysis was performed to determine the number of animals that would be required. Assuming a level of 10% increased epithelial healing in the treatment group to be clinically significant and a standard deviation of

10% in the epithelial healing rate, for a study with 90% power, this returned the number of eyes for each treatment and control arm as 21, giving the total number of rabbits as 42. The primary outcome to be assessed is corneal epithelial healing. This can be calculated as the percentage of recovered epithelium by subtracting the residual defect size from the original defect size, returning a continuous variable.

The entire experiment can be performed in the biomedical sciences unit animal facility laboratory of the University of Nottingham, where female and male New Zealand white rabbits can be kept anaesthetised for the entire duration of the experiment, and euthanised at the end for eye retrieval. A method of chemical injury was proposed to cause minimal damage to the ocular surface of the white rabbit by placing a corneal ring, similar to the rings used for alcohol delamination in human eyes, on the rabbit ocular surface. A volume of alkali or acid can be placed inside the ring for a predetermined period of time, and then removed with a Weck-cell sponge. The strength, volume and duration can be determined by prior *in vitro* testing of animal eyes. Both eyes will receive medical therapy, including irrigation with phosphate-free isotonic media (until pH neutrality is achieved), and antibiotics and steroids four times a day. The surgeon will be masked to the treatment (f-t or v-d), which can be applied to the rabbit ocular surface by using a PMMA ring with fibrin glue (Liu et al., 2008). Following AMT, both eyes can be closed with tape, and the animal monitored until the end of the experiment. After a specified period, the AM can be removed, the eyes stained with fluorescein dye and photographed and the digital images assessed by a masked observer. The size of the epithelial defect can be measured using computer software to compare the AM-treated injuries to the untreated controls.

6.1.2.3 Tissue engineering

The cultivation of oral and corneal stem cell sheets is technically demanding and there is a lag period between the patient presenting and the sheet being ready for transplantation (Kinoshita et al., 2004). A readily transplantable construct of stable, non-immunogenic stem cells could circumvent the limitations encountered with expanded cell sheets. Researchers have used mesenchymal stem cell sheets to treat acute ocular surface burns in experimental animal models (Ye et al., 2006). These cells have anti-inflammatory and anti-angiogenic properties (Oh et al., 2008), and have the capacity to differentiate into corneal epithelial cells (Gu et al., 2009), making them attractive propositions for treating acute ocular chemical injuries. As mesenchymal sheets do not need to be cultivated on AM, the possibility of combining a multilayered mesenchymal stem cell network supported by a synthetic tissue engineered scaffold is attractive, and constitutes a potential research avenue. A synthetic construct in place of AM will circumvent the key issues of supply, variability and risks associated with AM. The artificial constructs must be biocompatible and robust enough to resist the ocular inflammatory response, while helping to prevent inflammation and promoting LSC survival in the early repair phase.

6.2 Conclusion

This thesis contributes original research to the body of knowledge available to ophthalmic surgeons about the properties and usefulness of AM as a biomaterial. In its dried form, it can constitute a part of the overall treatment armamentarium for ophthalmologists at the battlefield. While the lack of conclusive evidence for its use in acute burns highlights the limitations of AM treatment, it remains useful as a biocompatible material with added biological functionality. Dried AM can contribute to the treatment of eye in-

juries sustained on the battlefield only once a full assessment has been carried out by a military ophthalmologist, and where it can be demonstrated that the benefits of treatment outweigh the potential risks.

Word count: 99 995

References

- Abbotts R, Harrison SE, Cooper GL (2007) Primary blast injuries to the eye: a review of the evidence. *J R Army Med Corps* 153:119–123.
- Abdullah N, Nawawi A, Othman I (2000) Fungal spoilage of starch-based foods in relation to its water activity (Aw). *Journal of Stored Products Research* 36:47 – 54.
- Acker J, Fowler A, Lauman B, Cheley S, Toner M (2002) Survival of desiccated mammalian cells: Beneficial effects of isotonic media. *Cell Preservation Technology* 1:129–140.
- Adams G (2007) Principles of freeze-drying. In Day JG, Stacey GN, editors, *Cryopreservation and freeze-drying protocols*, Methods in Molecular Biology, chapter 2, pp. 15–38. Humana Press, Totowa, NJ, 2nd edition.
- Adams GD (1995) The preservation of inocula. In Brown M, Gilbert P, editors, *Microbiological quality assurance: a guide towards relevance and reproducibility of inocula*, chapter 2.1, pp. 89–119. CRC Press, Boca Raton, FL.
- Adds PJ, Hunt C, Hartley S (2001a) Bacterial contamination of amniotic membrane. *Br J Ophthalmol* 85:228–230.
- Adds PJ, Hunt CJ, Dart JK (2001b) Amniotic membrane grafts, "fresh" or frozen? a clinical and in vitro comparison. *Br J Ophthalmol* 85:905–907.

- Adepoju FG, Adeboye A, Adigun IA (2007) Chemical eye injuries: presentation and management difficulties. *Ann Afr Med* 6:7–11.
- Aderka D, Le JM, Vilcek J (1989) IL-6 inhibits lipopolysaccharide-induced tumor necrosis factor production in cultured human monocytes, U937 cells, and in mice. *J Immunol* 143:3517–23.
- Ahearne M, Yang Y, Then KY, Liu KK (2008) Non-destructive mechanical characterisation of uva/riboflavin crosslinked collagen hydrogels. *Br J Ophthalmol* 92:268–271.
- Akao K, Okubo Y, Asakawa N, Inoue Y, Sakurai M (2001) Infrared spectroscopic study on the properties of the anhydrous form II of trehalose. implications for the functional mechanism of trehalose as a biostabilizer. *Carbohydr Res* 334:233–41.
- Akao KI, Okubo Y, Ikeda T, Inoue Y, Sakurai M (1998) Infrared spectroscopic study on the structural property of a trehalose-water complex. *Chem. Lett.* 8:759–760.
- Akinbi HT, Narendran V, Pass AK, Markart P, Hoath SB (2004) Host defense proteins in vernix caseosa and amniotic fluid. *American Journal of Obstetrics and Gynecology* 191:2090 – 2096.
- Alber A, Howie SEM, Wallace WAH, Hirani N (2012) The role of macrophages in healing the wounded lung. *Int J Exp Pathol* 93:243–51.
- Alberth B, Kettesy A (1971) [Surgical treatment of caustic eye injuries]. *Buch Augenarzt* 57:1–119.
- Altman DG (1998) Confidence intervals for the number needed to treat. *Br Med J* 317:1309–12.
- Anderson DF, Ellies P, Pires RT, Tseng SC (2001) Amniotic membrane

- transplantation for partial limbal stem cell deficiency. *Br J Ophthalmol* 85:567–575.
- Aplin JD, Campbell S, Allen TD (1985) The extracellular matrix of human amniotic epithelium: ultrastructure, composition and deposition. *J Cell Sci* 79:119–136.
- Ardi VC, Kupriyanova TA, Deryugina EI, Quigley JP (2007) Human neutrophils uniquely release TIMP-free MMP-9 to provide a potent catalytic stimulator of angiogenesis. *Proc Natl Acad Sci USA* 104:20262–20267.
- Ardi VC, Van den Steen PE, Opdenakker G, Schweighofer B, Deryugina EI, Quigley JP (2009) Neutrophil MMP-9 proenzyme, unencumbered by TIMP-1, undergoes efficient activation in vivo and catalytically induces angiogenesis via a basic fibroblast growth factor (FGF-2)/FGFR-2 pathway. *J Biol Chem* 284:25854–25866.
- Arechavaleta-Velasco F, Ogando D, Parry S, Vadillo-Ortega F (2002) Production of matrix metalloproteinase-9 in lipopolysaccharide-stimulated human amnion occurs through an autocrine and paracrine proinflammatory cytokine-dependent system. *Biol Reprod* 67:1952–1958.
- Ari A (2006) Eye injuries on the battlefields of Iraq and Afghanistan: public health implications. *Optometry* 77:329–339.
- Arora R, Mehta D, Jain V (2005) Amniotic membrane transplantation in acute chemical burns. *Eye* 19:273–278.
- Artal R, Sokol R, Neuman M, Burstein A, Stojkov J (1976) The mechanical properties of prematurely and non-prematurely ruptured membranes. methods and preliminary results. *Am J Obstet Gynecol* 125:655–659.
- Ashby MF, Jones DR (2012) The elastic moduli. In Ashby MF, Jones DR, editors, *Engineering materials*, Vol. 1, chapter 3, pp. 29–54. Butterworth-Heinemann, Oxford, 4th edition.

- Azuara-Blanco A, Pillai CT, Dua HS (1999) Amniotic membrane transplantation for ocular surface reconstruction. *Br J Ophthalmol* 83:399–402.
- Bagley D, Casterton P, Dressler W, Edelhauser H, Kruszewski F, McCulley J, Nussenblatt R, Osborne R, Rothenstein A, Stitzel K, Thomas K, Ward S (2006) Proposed new classification scheme for chemical injury to the human eye. *Regul Toxicol Pharmacol* 45:206–213.
- Baharvand H, Heidari M, Ebrahimi M, Valadbeigi T, Salekdeh GH (2007) Proteomic analysis of epithelium-denuded human amniotic membrane as a limbal stem cell niche. *Mol Vis* 13:1711–1721.
- Bailey AJ, Rhodes DN, Cater CW (1964) Irradiation-induced crosslinking of collagen. *Radiat Res* 22:606–21.
- Ballen PH (1964) Treatment of chemical burns of the eye. *Eye Ear Nose Throat Mon* 43:57–61.
- Baradaran-Raffiee A (2008) The role of amniotic membrane transplantation in ocular chemical burns <http://clinicaltrials.gov/ct2/show/NCT00370812>.
- Barbaro V, Di IE, Ferrari S, Bisceglia L, Ruzza A, De LM, Pellegrini G (2006) Expression of VSX1 in human corneal keratocytes during differentiation into myofibroblasts in response to wound healing. *Invest Ophthalmol Vis Sci* 47:5243–5250.
- Barequet IS, Habot-Wilner Z, Keller N, Smollan G, Ziv H, Belkin M, Rosner M (2008) Effect of amniotic membrane transplantation on the healing of bacterial keratitis. *Invest Ophthalmol Vis Sci* 49:163–7.
- Battle J, Perdomo F (1993) Placental membranes as a conjunctival substitute. *Ophthalmology* 100:107(abstract 9A).
- Batmanov I, Egorova K, Kolesnikova L (1990) [Use of fresh amnion in the treatment of corneal diseases]. *Vestn Oftalmol* 106:17–19.

- Baum J (2002) Thygeson lecture. amniotic membrane transplantation: why is it effective? *Cornea* 21:339–341.
- Beattie GM, Crowe JH, Lopez AD, Cirulli V, Ricordi C, Hayek A (1997) Trehalose: a cryoprotectant that enhances recovery and preserves function of human pancreatic islets after long-term storage. *Diabetes* 46:519–523.
- Benson-Martin J, Zammaretti P, Bilic G, Schweizer T, Portmann-Lanz B, Burkhardt T, Zimmermann R, Ochsenbein-Kölbl N (2006) The Young's modulus of fetal preterm and term amniotic membranes. *Eur J Obstet Gynecol Reprod Biol* 128:103–107.
- Bhatia M, Pereira M, Rana H, Stout B, Lewis C, Abramson S, Labazzo K, Ray C, Liu Q, Hofgartner W, Hariri R (2007) The mechanism of cell interaction and response on decellularized human amniotic membrane: implications in wound healing. *Wounds* 19:201–217.
- Bhattacharya S, Hom G, Fernandez C, Hom L (2007) Ocular effects of exposure to industrial chemicals: clinical management and proteomic approaches to damage assessment. *Cutan Ocul Toxicol* 26:203–225.
- Blanch R, Bindra M, Jacks A, Scott R (2011) Ophthalmic injuries in British Armed Forces in Iraq and Afghanistan. *Eye (Lond)* 25:218–223.
- Blanch R, Scott R (2009) Military ocular injury: presentation, assessment and management. *J R Army Med Corps* 155:279–284.
- Boone KD, Boone DE, Lewis RW, Kealey GP (1998) A retrospective study of the incidence and prevalence of thermal corneal injury in patients with burns. *J Burn Care Rehabil* 19:216–218.
- Borderie V (2004) [Clinical aspects of corneal burns]. *J Fr Ophtalmol* 27:1170–1174.

- Bottom R (2008) Thermogravimetric analysis. In Gabbott P, editor, *Principles and applications of thermal analysis*, chapter 3, pp. 87–118. Blackwell Publishing Ltd., Oxford.
- Bouchard C, John T (2004) Amniotic membrane transplantation in the management of severe ocular surface disease: indications and outcomes. *Ocul Surf* 2:201–211.
- Bourne G (1960) The microscopic anatomy of the human amnion and chorion. *Am J Obstet Gynecol* 79:1070–1073.
- Bourne G (1966) The anatomy of the human amnion and chorion. *Proc R Soc Med* 59:1127–1128.
- Bravo-Osuna I, Ferrero C, Jiménez-Castellanos MR (2005) Water sorption-desorption behaviour of methyl methacrylate-starch copolymers: effect of hydrophobic graft and drying method. *Eur J Pharm Biopharm* 59:537–48.
- Brinkman WT, Nagapudi K, Thomas BS, Chaikof EL (2003) Photocross-linking of type I collagen gels in the presence of smooth muscle cells: mechanical properties, cell viability, and function. *Biomacromolecules* 4:890–5.
- Brown A (1941) Lime burns of the eye: use of rabbit peritoneum to prevent severe delayed effects. *Arch Ophthalmol* 26:754–769.
- Bryant-Greenwood G (1998) The extracellular matrix of the human fetal membranes: structure and function. *Placenta* 19:1–11.
- Bucki R, Leszczyńska K, Namiot A, Sokołowski W (2010) Cathelicidin LL-37: a multitask antimicrobial peptide. *Arch Immunol Ther Exp (Warsz)* 58:15–25.

- Budenz DL, Barton K, Tseng SC (2000) Amniotic membrane transplantation for repair of leaking glaucoma filtering blebs. *Am J Ophthalmol* 130:580–588.
- Buhimschi IA, Jabr M, Buhimschi CS, Petkova AP, Weiner CP, Saed GM (2004) The novel antimicrobial peptide beta 3-defensin is produced by the amnion: a possible role of the fetal membranes in innate immunity of the amniotic cavity. *Am J Obstet Gynecol* 191:1678–1687.
- Calvin SE, Oyen ML (2007) Microstructure and mechanics of the chorioamnion membrane with an emphasis on fracture properties. *Ann N Y Acad Sci* 1101:166–185.
- Cameron G, Alberts I, Laing J, Wess T (2002) Structure of type I and type III heterotypic collagen fibrils: An X-ray diffraction study. *Journal of Structural Biology* 137:15–22.
- Carpenter JF, Arakawa T, Crowe JH (1992) Interactions of stabilizing additives with proteins during freeze-thawing and freeze-drying. *Dev Biol Stand* 74:225–38; discussion 238–9.
- Carrington LM, Albon J, Anderson I, Kamma C, Boulton M (2006) Differential regulation of key stages in early corneal wound healing by TGF-beta isoforms and their inhibitors. *Invest Ophthalmol Vis Sci* 47:1886–94.
- Casey M, MacDonald P (1996) Interstitial collagen synthesis and processing in human amnion: a property of the mesenchymal cells. *Biol Reprod* 55:1253–1260.
- Castro-Combs J, Noguera G, Cano M, Yew M, Gehlbach PL, Palmer J, Behrens A (2008) Corneal wound healing is modulated by topical application of amniotic fluid in an ex vivo organ culture model. *Exp Eye Res* 87:56–63.

- Cauchi PA, Ang GS, Azuara-Blanco A, Burr JM (2008) A systematic literature review of surgical interventions for limbal stem cell deficiency in humans. *Am J Ophthalmol* 146:251–259.
- Chae SW, Lee SH, Cho JH, Lee HM, Choi G, Hwang SJ (2001) Expression of human beta defensin-1 mRNA in human palatine tonsil. *Acta Otolaryngol* 121:414–418.
- Challis JR, Lockwood CJ, Myatt L, Norman JE, Strauss r JF, Petraglia F (2009) Inflammation and pregnancy. *Reprod Sci* 16:206–15.
- Champion H, Holcomb J, Young L (2009) Injuries from explosions: physics, biophysics, pathology, and required research focus. *J Trauma* 66:1468–1477.
- Chang C, Green C, McGhee C, Sherwin T (2008) Acute wound healing in the human central corneal epithelium appears to be independent of limbal stem cell influence. *Invest Ophthalmol Vis Sci* 49:5279–5286.
- Chao YC, Humphreys S, Penfield W (1940) A new method of preventing adhesions: The use of amnioplastin after craniotomy. *Br Med J* pp. 517–520.
- Chau DYS, Brown SV, Mather ML, Hutter V, Tint NL, Dua HS, Rose FRAJ, Ghaemmaghami AM (2012) Tissue transglutaminase (TG-2) modified amniotic membrane: a novel scaffold for biomedical applications. *Biomed Mater* 7:045011.
- Chen H, Jhanji V (2012) Survey of systematic reviews and meta-analyses published in ophthalmology. *Br J Ophthalmol* 96:896–9.
- Chen J, Zhou S, Huang T, Liu Z, Chen L, Lin Y (2000) [A clinical study on fresh amniotic membrane transplantation for treatment of severe ocular surface disorders at acute inflammatory and cicatricial stage]. *Zhonghua Yan Ke Za Zhi* 36:13–7, 1.

- Chen T, Acker J, Eroglu A, Cheley S, Bayley H, Fowler A, Toner M (2001) Beneficial effect of intracellular trehalose on the membrane integrity of dried mammalian cells. *Cryobiology* 43:168–181.
- Chen T, Fowler A, Toner M (2000) Literature review: supplemented phase diagram of the trehalose-water binary mixture. *Cryobiology* 40:277–282.
- Cheng C, Sun C, Yu W, Hsieh H, Ma D, Pang J, Yang C (2009) Novel laminin 5 gamma 2-chain fragments potentiating the limbal epithelial cell outgrowth on amniotic membrane. *Invest Ophthalmol Vis Sci* 50:4631–4639.
- Chew HF (2011) Amniotic membrane transplantation as an adjunct to medical therapy in acute ocular burns. *Evidence-based Ophthalmology* 12:152–153.
- Chiang PPC, Keeffe JE, Mesurier RTL, Taylor HR (2006) Global burden of disease and visual impairment. *Lancet* 368:365.
- Choi YS, Kim JY, Wee WR, Lee JH (1998) Effect of the application of human amniotic membrane on rabbit corneal wound healing after excimer laser photorefractive keratectomy. *Cornea* 17:389–95.
- Christensen D, Kirby D, Foged C, Agger EM, Andersen P, Perrie Y, Nielsen HM (2008) Alpha, alpha'-trehalose 6,6'-dibehenate in non-phospholipid-based liposomes enables direct interaction with trehalose, offering stability during freeze-drying. *Biochim Biophys Acta* 1778:1365–1373.
- Chuck RS, Graff JM, Bryant MR, Sweet PM (2004) Biomechanical characterization of human amniotic membrane preparations for ocular surface reconstruction. *Ophthalmic Res* 36:341–348.
- Clare G, Suleman H, Bunce C, Dua H (2011) Amniotic membrane transplantation for acute ocular burns. In *Cochrane Database of Systematic Reviews*, number 10. John Wiley and Sons, Ltd.

- Cohen J (1988) The analysis of variance and covariance. In *Statistical power analysis for the behavioral sciences*, chapter 8, pp. 273–406. Lawrence Erlbaum Associates, Hillsdale, NJ, 2nd edition.
- Connon CJ, Douth J, Chen B, Hopkinson A, Mehta JS, Nakamura T, Kinoshita S, Meek KM (2010) The variation in transparency of amniotic membrane used in ocular surface regeneration. *Br J Ophthalmol* 94:1057–1061.
- Connon C, Nakamura T, Hopkinson A, Quantock A, Yagi N, Douth J, Meek K (2007) The biomechanics of amnion rupture: an x-ray diffraction study. *PLoS ONE* 2:e1147.
- Cooper LJ, Kinoshita S, German M, Koizumi N, Nakamura T, Fullwood NJ (2005) An investigation into the composition of amniotic membrane used for ocular surface reconstruction. *Cornea* 24:722–729.
- Cordeiro MF, Mead A, Ali RR, Alexander RA, Murray S, Chen C, York-Defalco C, Dean NM, Schultz GS, Khaw PT (2003) Novel antisense oligonucleotides targeting tgf-beta inhibit in vivo scarring and improve surgical outcome. *Gene Ther* 10:59–71.
- Costantino HR, Carrasquillo KG, Cordero RA, Mumenthaler M, Hsu CC, Griebenow K (1998a) Effect of excipients on the stability and structure of lyophilized recombinant human growth hormone. *J Pharm Sci* 87:1412–20.
- Costantino HR, Curley JG, Wu S, Hsu CC (1998b) Water sorption behavior of lyophilized protein-sugar systems and implications for solid-state interactions. *International Journal of Pharmaceutics* 166:211 – 221.
- Croll M, Croll LJ (1952) Egg membrane for chemical injuries of the eye; a new adjuvant treatment. *Am J Ophthalmol* 35:1585–1596.

- Crowe JH, Carpenter JF, Crowe LM (1998) The role of vitrification in anhydrobiosis. *Annu Rev Physiol* 60:73–103.
- Crowe J, Crowe L, Chapman D (1984) Infrared spectroscopic studies on interactions of water and carbohydrates with a biological membrane. *Arch Biochem Biophys* 232:400–407.
- Crowe JH (2007) Trehalose as a "chemical chaperone": Fact and fantasy. In Csermely P, Vigh L, editors, *Molecular aspects of the stress response: chaperones, membranes and networks*, Vol. 594 of *Advances in experimental medicine and biology*, chapter 13, pp. 143–158. Springer, New York.
- Crowe JH, Tablin F, Wolkers WF, Gousset K, Tsvetkova NM, Ricker J (2003) Stabilization of membranes in human platelets freeze-dried with trehalose. *Chem Phys Lipids* 122:41–52.
- Crowe LM, Reid DS, Crowe JH (1996) Is trehalose special for preserving dry biomaterials? *Biophys J* 71:2087–2093.
- da Silva Ricardo JR, de Barros SL, dos Santos MS, de Souza LB, Gomes JAP (2009) [Amniotic membrane transplantation for severe acute cases of chemical ocular burn and Stevens-Johnson syndrome]. *Arq Bras Oftalmol* 72:215–220.
- Daly M, Tuft SJ, Munro PMG (2005) Acute corneal calcification following chemical injury. *Cornea* 24:761–5.
- Dansey-Browning C (1949) On the use of amniotic membrane. *Br J Ophthalmol* 33:518–520.
- Das S, Ramamurthy B, Sangwan V (2009) Fungal keratitis following amniotic membrane transplantation. *Int Ophthalmol* 29:49–51.
- Davis J (1910) Skin transplantation. With a review of 550 cases at the Johns Hopkins Hospital. *Johns Hopkins Hospital Reports* 15:307–396.

- Daya SM, Watson A, Sharpe JR, Giledi O, Rowe A, Martin R, James SE (2005) Outcomes and DNA analysis of ex vivo expanded stem cell allograft for ocular surface reconstruction. *Ophthalmology* 112:470–477.
- de Rötth A (1940) Plastic repair of conjunctival defects with fetal membranes. *Arch Ophthalmol* 23:522–525.
- De Sousa JL, Daya S, Malhotra R (2009) Adnexal surgery in patients undergoing ocular surface stem cell transplantation. *Ophthalmology* 116:235–242.
- Dell SJ, Hovanesian JA, Raizman MB, Crandall AS, Doane J, Snyder M, Masket S, Lane S, Fram N (2011) Randomized comparison of postoperative use of hydrogel ocular bandage and collagen corneal shield for wound protection and patient tolerability after cataract surgery. *Journal of Cataract and Refractive Surgery* 37:113 – 121.
- Demir-Weusten AY, Seval Y, Kaufmann P, Demir R, Yucel G, Huppertz B (2007) Matrix metalloproteinases-2, -3 and -9 in human term placenta. *Acta Histochem* 109:403 –412.
- Denig R (1912) [A surgical treatment for alkali burns of the eye.]. *München Med Wochenschr* 1:579–590.
- Deocarís C, Abad L (2005) Radiolytic damage to freeze-dried human amniotic membrane. *Philippine Journal of Science* 134:45–50.
- Derjaguin B, Muller V, Toporov Y (1975) Effect of contact deformations on the adhesion of particles. *Journal of Colloid and Interface Science* 53:314 – 326.
- D'Este F, Tomasinsig L, Skerlavaj B, Zanetti M (2012) Modulation of cytokine gene expression by cathelicidin BMAP-28 in LPS-stimulated and -unstimulated macrophages. *Immunobiology* 217:962–71.

- Di Santo E, Alonzi T, Poli V, Fattori E, Toniatti C, Sironi M, Ricciardi-Castagnoli P, Ghezzi P (1997) Differential effects of IL-6 on systemic and central production of TNF: a study with IL-6-deficient mice. *Cytokine* 9:300–6.
- Dietrich T, Schlotzer-Schrehardt U, Hofmann-Rummelt C, Seitz B, Kruse F (2005) Comparative analysis of basement membrane composition of the human limbal and amniotic membrane epithelia. *Invest Ophthalmol Vis Sci* 46:2093.
- Dietrich-Ntoukas T, Hofmann-Rummelt C, Kruse FE, Schlötzer-Schrehardt U (2012) Comparative analysis of the basement membrane composition of the human limbus epithelium and amniotic membrane epithelium. *Cornea* 31:564–9.
- Dobrev MP, Pereira PNG, Deprest J, Zwijsen A (2010) On the origin of amniotic stem cells: of mice and men. *Int J Dev Biol* 54:761–777.
- Dos Santos S, Delattre AI, De Longueville F, Bult H, Raes M (2007) Gene expression profiling of LPS-stimulated murine macrophages and role of the NF-kappaB and PI3K/mTOR signaling pathways. *Ann N Y Acad Sci* 1096:70–7.
- Du Y, Carlson E, Funderburgh M, Birk D, Pearlman E, Guo N, Kao W, Funderburgh J (2009) Stem cell therapy restores transparency to defective murine corneas. *Stem Cells* 27:1635–1642.
- Du Y, Funderburgh M, Mann M, Sundarraj N, Funderburgh J (2005) Multipotent stem cells in human corneal stroma. *Stem Cells* 23:1266–1275.
- Du Y, Sundarraj N, Funderburgh M, Harvey S, Birk D, Funderburgh J (2007) Secretion and organization of a cornea-like tissue in vitro by stem cells from human corneal stroma. *Invest Ophthalmol Vis Sci* 48:5038–5045.

- Dua HS, Rahman I, Miri A, Said DG (2010) Variations in amniotic membrane: relevance for clinical applications. *Br J Ophthalmol* 94:963–964.
- Dua HS, Gomes JAP, King AJ, Maharajan VS (2004) The amniotic membrane in ophthalmology. *Surv Ophthalmol* 49:51–77.
- Dua H, King A, Joseph A (2001) A new classification of ocular surface burns. *Br J Ophthalmol* 85:1379–1383.
- Dua H, Shanmuganathan V, Powell-Richards A, Tighe P, Joseph A (2005) Limbal epithelial crypts: a novel anatomical structure and a putative limbal stem cell niche. *Br J Ophthalmol* 89:529–532.
- Duchesne B, Tahiri H, Galand A (2001) Use of human fibrin glue and amniotic membrane transplant in corneal perforation. *Cornea* 20:230–232.
- Duncan J (2008) Principles and applications of mechanical thermal analysis. In Gabbott P, editor, *Principles and applications of thermal analysis*, chapter 4, pp. 120–163. Blackwell Publishing Ltd., Oxford, 1st edition.
- Dwivedi PC, Raizada JK, Saini VK, Mittal PC (1985) Ocular lesions following methyl isocyanate contamination: the Bhopal experience. *Arch Ophthalmol* 103:1627.
- El Khwad M, Pandey V, Stetzer B, Mercer B, Kumar D, Moore R, Fox J, Redline R, Mansour J, Moore J (2006) Fetal membranes from term vaginal deliveries have a zone of weakness exhibiting characteristics of apoptosis and remodeling. *J.Soc.Gynecol.Investig.* 13:191–195.
- El Khwad M, Stetzer B, Moore R, Kumar D, Mercer B, Arikat S, Redline R, Mansour J, Moore J (2005) Term human fetal membranes have a weak zone overlying the lower uterine pole and cervix before onset of labor. *Biol Reprod* 72:720–726.

- Ellenberg D, Azar DT, Hallak JA, Tobaigy F, Han KY, Jain S, Zhou Z, Chang JH (2010) Novel aspects of corneal angiogenic and lymphangiogenic privilege. *Prog Retin Eye Res* 29:208–48.
- Enders AC, Schlafke S, Hendrickx AG (1986) Differentiation of the embryonic disc, amnion, and yolk sac in the rhesus monkey. *Am J Anat* 177:161–185.
- Endo K, Nakamura T, Kawasaki S, Kinoshita S (2004) Human amniotic membrane, like corneal epithelial basement membrane, manifests the alpha 5 chain of type IV collagen. *Invest Ophthalmol Vis Sci* 45:1771–1774.
- Espinoza J, Chaiworapongsa T, Romero R, Edwin S, Rathnasabapathy C, Gomez R, Bujold E, Camacho N, Kim YM, Hassan S, Blackwell S, Whitty J, Berman S, Redman M, Yoon BH, Sorokin Y (2003) Antimicrobial peptides in amniotic fluid: defensins, calprotectin and bacterial/permeability-increasing protein in patients with microbial invasion of the amniotic cavity, intra-amniotic inflammation, preterm labor and premature rupture of membranes. *J Matern Fetal Neonatal Med* 13:2 –21.
- Evans P, Cindrova-Davies T, Muttukrishna S, Burton GJ, Porter J, Jauniaux E (2011) Heparin and iron species distribution inside the first-trimester human gestational sac. *Mol Hum Reprod* 17:227–32.
- Eyre DR, Weis MA, Wu JJ (2008) Advances in collagen cross-link analysis. *Methods* 45:65–74.
- Fawthrop R, Ockleford C (1994) Cryofracture of human term amniochorion. *Cell Tissue Res* 277:315–323.
- Fini ME, Girard MT, Matsubara M (1992) Collagenolytic/gelatinolytic enzymes in corneal wound healing. *Acta Ophthalmol Suppl* pp. 26–33.
- Fini M (1999) Keratocyte and fibroblast phenotypes in the repairing cornea. *Prog Retin Eye Res* 18:529–551.

- Fini M, Cook J, Mohan R (1998) Proteolytic mechanisms in corneal ulceration and repair. *Arch Dermatol Res* 290 Suppl:S12–S23.
- Fini M, Stramer B (2005) How the cornea heals: cornea-specific repair mechanisms affecting surgical outcomes. *Cornea* 24:S2–S11.
- Fortunato SJ, Menon R, Lombardi SJ (1997) Collagenolytic enzymes (gelatinases) and their inhibitors in human amniochorionic membrane. *Am J Obstet Gynecol* 177:731–741.
- Frasca L, Lande R (2012) Role of defensins and cathelicidin LL37 in autoimmune and auto-inflammatory diseases. *Curr Pharm Biotechnol* .
- Frick K, Gower E, Kempen J, Wolff J (2007) Economic impact of visual impairment and blindness in the United States. *Arch Ophthalmol* 125:544–550.
- Fujisato T, Tomihata K, Tabata Y, Iwamoto Y, Burczak K, Ikada Y (1999) Cross-linking of amniotic membranes. *J Biomater Sci Polym Ed* 10:1171–1181.
- Fuller BJ, Paynter SJ (2007) Cryopreservation of mammalian embryos. In Day JG, Stacey GN, editors, *Cryopreservation and freeze-drying protocols*, Methods in Molecular Biology, chapter 23, pp. 325–339. Humana Press, New York, 2nd edition.
- Funderburgh M, Du Y, Mann M, Sundarraj N, Funderburgh J (2005) PAX6 expression identifies progenitor cells for corneal keratocytes. *FASEB J*. 19:1371–1373.
- Fung YC (1984) Structure and stress-strain relationship of soft tissues. *American Zoologist* 24:13–22.

- Fung YC (1993) Bioviscoelastic solids. In *Biomechanics: mechanical properties of living tissues*, chapter 7, pp. 269–277. Springer-Verlag, New York, 2nd edition.
- Gabbott P (2008) A practical introduction to differential scanning calorimetry. In Gabbott P, editor, *Principles and Applications of Thermal Analysis*, chapter 1, pp. 1–50. Blackwell Publishing Ltd., Oxford.
- Gabler B, Lohmann CP (2000) Hypopyon after repeated transplantation of human amniotic membrane onto the corneal surface. *Ophthalmology* 107:1344–6.
- Gajiwala K, Gajiwala AL (2004) Evaluation of lyophilised, gamma-irradiated amnion as a biological dressing. *Cell Tissue Bank* 5:73–80.
- Garreis F, Gottschalt M, Paulsen FP (2010) Antimicrobial peptides as a major part of the innate immune defense at the ocular surface. *Dev Ophthalmol* 45:16–22.
- Garreis F, Gottschalt M, Schlorf T, Gläser R, Harder J, Worlitzsch D, Paulsen FP (2011) Expression and regulation of antimicrobial peptide psoriasin (S100A7) at the ocular surface and in the lacrimal apparatus. *Invest Ophthalmol Vis Sci* 52:4914–22.
- Gicquel JJ, Bejjani RA, Ellies P, Mercière M, Dighiero P (2007) Amniotic membrane transplantation in severe bacterial keratitis. *Cornea* 26:27–33.
- Gicquel JJ, Dua HS, Brodie A, Mohammed I, Suleman H, Lazutina E, James DK, Hopkinson A (2009) Epidermal growth factor variations in amniotic membrane used for ex vivo tissue constructs. *Tissue Eng Part A* 15:1919–1927.
- Gil A, Belton P, Felix V (1996) Spectroscopic studies of solid alpha-alpha trehalose. *Spectrochimica Acta Part A: Molecular and Biomolecular Spectroscopy* 52:1649 – 1659.

- Gillaux C, Méhats C, Vaiman D, Cabrol D, Breuiller-Fouché M (2011) Functional screening of TLRs in human amniotic epithelial cells. *J Immunol* 187:2766–74.
- Goldberg GI, Strongin A, Collier IE, Genrich LT, Marmer BL (1992) Interaction of 92-kda type IV collagenase with the tissue inhibitor of metalloproteinases prevents dimerization, complex formation with interstitial collagenase, and activation of the proenzyme with stromelysin. *J Biol Chem* 267:4583–91.
- Goodall EA, Moore J, Moore T (2009) The estimation of approximate sample size requirements necessary for clinical and epidemiological studies in vision sciences. *Eye (Lond)* 23:1589–1597.
- Goodeve CF, Kitchener JA (1938) The mechanism of photosensitisation by solids. *Trans. Faraday Soc.* 34:902–908.
- Gould GW (1996) Methods for preservation and extension of shelf life. *International Journal of Food Microbiology* 33:51 – 64.
- GRADE Working Group (2004) Grading quality of evidence and strength of recommendations. *Br Med J* 328:1490.
- GRADEpro (Jan Brozek, Andrew Oxman, Holger Schünemann, 2008) [Computer program] Version 3.2 for Windows.
- Grant RA, Cox RW, Kent CM (1973) The effects of gamma irradiation on the structure and reactivity of native and cross-linked collagen fibres. *J Anat* 115:29–43.
- Gregory DG (2008) The ophthalmologic management of acute Stevens-Johnson syndrome. *Ocul Surf* 6:87–95.
- Gris O, del Campo Z, Wolley-Dod C, Güell JL, Bruix A, Calatayud M, Adán

- A (2002) Amniotic membrane implantation as a therapeutic contact lens for the treatment of epithelial disorders. *Cornea* 21:22–27.
- Gross JH (2004) Fragmentation of organic ions and interpretation of EI mass spectra. In *Mass spectrometry: a textbook*, chapter 6, pp. 223–320. Springer, Berlin-Heidelberg-New York.
- Grueterich M, Espana EM, Touhami A, Ti SE, Tseng SCG (2002) Phenotypic study of a case with successful transplantation of ex vivo expanded human limbal epithelium for unilateral total limbal stem cell deficiency. *Ophthalmology* 109:1547–1552.
- Grueterich M, Espana EM, Tseng SCG (2003) Ex vivo expansion of limbal epithelial stem cells: amniotic membrane serving as a stem cell niche. *Surv Ophthalmol* 48:631–46.
- Grueterich M, Tseng SCG (2002) Human limbal progenitor cells expanded on intact amniotic membrane ex vivo. *Arch Ophthalmol* 120:783–790.
- Gu S, Xing C, Han J, Tso MOM, Hong J (2009) Differentiation of rabbit bone marrow mesenchymal stem cells into corneal epithelial cells in vivo and ex vivo. *Mol Vis* 15:99–107.
- Gupta N, Kalaivani M, Tandon R (2011) Comparison of prognostic value of Roper Hall and Dua classification systems in acute ocular burns. *Br J Ophthalmol* 95:194–198.
- Hackett JM, Lagali N, Merrett K, Edelhauser H, Sun Y, Gan L, Griffith M, Fagerholm P (2011) Biosynthetic corneal implants for replacement of pathologic corneal tissue: performance in a controlled rabbit alkali burn model. *Invest Ophthalmol Vis Sci* 52:651–657.
- Halaburt JT, Uldbjerg N, Helmig R, Ohlsson K (1989) The concentration of collagen and the collagenolytic activity in the amnion and the chorion. *Eur J Obstet Gynecol Reprod Biol* 31:75–82.

- Hanada K, Shimazaki J, Shimmura S, Tsubota K (2001) Multilayered amniotic membrane transplantation for severe ulceration of the cornea and sclera. *Am J Ophthalmol* 131:324–331.
- Hancock B, Zografi G (1997) Characteristics and significance of the amorphous state in pharmaceutical systems. *J. Pharm. Sci.* 86:1–12.
- Hao Y, Ma DH, Hwang DG, Kim WS, Zhang F (2000) Identification of anti-angiogenic and antiinflammatory proteins in human amniotic membrane. *Cornea* 19:348–352.
- Hayashi S, Ishimoto S, Wu G, Wee W, Rao N, McDonnell P (1997) Oxygen free radical damage in the cornea after excimer laser therapy. *Br J Ophthalmol* 81:141–144.
- Haynes RJ, Tighe PJ, Dua HS (1999) Antimicrobial defensin peptides of the human ocular surface. *Br J Ophthalmol* 83:737–41.
- He H, Li W, Chen SY, Zhang S, Chen YT, Hayashida Y, Zhu YT, Tseng SCG (2008) Suppression of activation and induction of apoptosis in RAW264.7 cells by amniotic membrane extract. *Invest Ophthalmol Vis Sci* 49:4468–4475.
- He H, Li W, Tseng DY, Zhang S, Chen SY, Day AJ, Tseng SCG (2009) Biochemical characterization and function of complexes formed by hyaluronan and the heavy chains of inter-alpha-inhibitor (HC*HA) purified from extracts of human amniotic membrane. *J Biol Chem* 284:20136–46.
- Heilborn JD, Nilsson MF, Kratz G, Weber G, Sorensen O, Borregaard N, Stahle-Backdahl M (2003) The cathelicidin anti-microbial peptide LL-37 is involved in re-epithelialization of human skin wounds and is lacking in chronic ulcer epithelium. *J Investig Dermatol* 120:379–389.

- Heiligenhaus A, Li HF, Yang Y, Wasmuth S, Steuhl KP, Bauer D (2005) Transplantation of amniotic membrane in murine herpes stromal keratitis modulates matrix metalloproteinases in the cornea. *Invest Ophthalmol Vis Sci* 46:4079–85.
- Hennerbichler S, Reichl B, Pleiner D, Gabriel C, Eibl J, Redl H (2007) The influence of various storage conditions on cell viability in amniotic membrane. *Cell Tissue Bank* 8:1–8.
- Henriques ST, Tan CC, Craik DJ, Clark RJ (2010) Structural and functional analysis of human liver-expressed antimicrobial peptide 2. *Chem-biochem* 11:2148–2157.
- Hermans PH, Weidinger A (1948) Quantitative X-ray investigations on the crystallinity of cellulose fibers. a background analysis. *Journal of Applied Physics* 19:491–506.
- Hick S, Demers PE, Brunette I, La C, Mabon M, Duchesne B (2005) Amniotic membrane transplantation and fibrin glue in the management of corneal ulcers and perforations: a review of 33 cases. *Cornea* 24:369–377.
- Higa K, Shimmura S, Shimazaki J, Tsubota K (2005) Hyaluronic acid-CD44 interaction mediates the adhesion of lymphocytes by amniotic membrane stroma. *Cornea* 24:206–12.
- Higgins J, Green S (2011) Assessing risk of bias in included studies. In Higgins J, Green S, editors, *Cochrane handbook for systematic reviews of interventions, version 5.1.6*, chapter 8. The Cochrane Collaboration.
- Hopkinson A, McIntosh RS, Shanmuganathan V, Tighe PJ, Dua HS (2006a) Proteomic analysis of amniotic membrane prepared for human transplantation: characterization of proteins and clinical implications. *J Proteome Res* 5:2226–35.

- Hopkinson A, McIntosh RS, Tighe PJ, James DK, Dua HS (2006b) Amniotic membrane for ocular surface reconstruction: donor variations and the effect of handling on TGF-beta content. *Invest Ophthalmol Vis Sci* 47:4316–4322.
- Hopkinson A, Shanmuganathan VA, Gray T, Yeung AM, Lowe J, James DK, Dua HS (2008) Optimization of amniotic membrane (AM) denuding for tissue engineering. *Tissue Eng Part C Methods* 14:371–381.
- Hori J, Wang M, Kamiya K, Takahashi H, Sakuragawa N (2006) Immunological characteristics of amniotic epithelium. *Cornea* 25:S53–S58.
- Hossain P (2012) The corneal melting point. *Eye* 26:1029–30.
- Hughes J WF (1946) Alkali burns of the eye; clinical and pathologic course. *Arch Ophthalmol* 36:189–214.
- Huis in 't Veld JH (1996) Microbial and biochemical spoilage of foods: an overview. *Int J Food Microbiol* 33:1–18.
- Hunter NE, Frampton CS, Craig DQM, Belton PS (2010) The use of dynamic vapour sorption methods for the characterisation of water uptake in amorphous trehalose. *Carbohydr Res* 345:1938–44.
- Ikeda A, Sakimoto T, Shoji J, Sawa M (2005) Expression of alpha- and beta-defensins in human ocular surface tissue. *Jpn J Ophthalmol* 49:73–8.
- Inatomi T, Nakamura T, Koizumi N, Sotozono C, Yokoi N, Kinoshita S (2006) Midterm results on ocular surface reconstruction using cultivated autologous oral mucosal epithelial transplantation. *American Journal of Ophthalmology* 141:267–275.
- ISO 6721-11 (2012) *Part 11: Plastics – Determination of Dynamic Mechanical Properties – Glass transition temperature*. International Organization for Standardization, Geneva, Switzerland.

- Itoh Y, Seiki M (2006) MT1-MMP: a potent modifier of pericellular microenvironment. *J Cell Physiol* 206:1–8.
- Jabareen M, Mallik AS, Bilic G, Zisch AH, Mazza E (2009) Relation between mechanical properties and microstructure of human fetal membranes: an attempt towards a quantitative analysis. *Eur J Obstet Gynecol Reprod Biol* 144 Suppl 1:S134–S141.
- Jain NK, Roy I (2009) Effect of trehalose on protein structure. *Protein Sci* 18:24–36.
- Jakoby B, Vellekoop MJ (1998) Viscosity sensing using a Love-wave device. *Sensors and Actuators A: Physical* 68:275–281.
- Jester J, Huang J, Petroll W, Cavanagh H (2002) TGF-beta induced myofibroblast differentiation of rabbit keratocytes requires synergistic TGF-beta, PDGF and integrin signaling. *Exp Eye Res*. 75:645–657.
- Jiang A, Li C, Gao Y, Zhang M, Hu J, Kuang W, Hao S, Yang W, Xu C, Gao G, Wang Z, Liu Z (2006) In vivo and in vitro inhibitory effect of amniotic extraction on neovascularization. *Cornea* 25:S36–40.
- Joseph A, Dua HS, King AJ (2001) Failure of amniotic membrane transplantation in the treatment of acute ocular burns. *Br J Ophthalmol* 85:1065–1069.
- Joyce E, Moore J, Sacks M (2009) Biomechanics of the fetal membrane prior to mechanical failure: review and implications. *Eur J Obstet Gynecol Reprod Biol* 144 Suppl 1:S121–S127.
- Jüni P, Altman DG, Egger M (2001) Systematic reviews in health care: Assessing the quality of controlled clinical trials. *Br Med J* 323:42–6.
- Kadar T, Dachir S, Cohen L, Sahar R, Fishbine E, Cohen M, Turetz J, Gutman H, Buch H, Brandeis R, Horwitz V, Solomon A, Amir A (2009) Ocular

- injuries following sulfur mustard exposure—pathological mechanism and potential therapy. *Toxicology* 263:59–69.
- Kamiya K, Wang M, Uchida S, Amano S, Oshika T, Sakuragawa N, Hori J (2005) Topical application of culture supernatant from human amniotic epithelial cells suppresses inflammatory reactions in cornea. *Experimental Eye Research* 80:671 – 679.
- Kao W (2006) Ocular surface tissue morphogenesis in normal and disease states revealed by genetically modified mice. *Cornea* 25:S7–S19.
- Kaplan DG, Furtek AB, Aklonis JJ (1987) Crosslinking in collagen (rat tail tendon). *J Soc Cosmet Chem* 82:163–169.
- Katz S, Hukkanen M, Lounatmaa K, Rousselle P, Tervo T, Virtanen I (2006) Cooperation of isoforms of laminin-332 and tenascin-CL during early adhesion and spreading of immortalized human corneal epithelial cells. *Exp Eye Res* 83:1412–1422.
- Kaushik JK, Bhat R (2003) Why is trehalose an exceptional protein stabilizer? An analysis of the thermal stability of proteins in the presence of the compatible osmolyte trehalose. *J Biol Chem* 278:26458–26465.
- Keeffe J, Chou S, Lamoureux E (2009) The cost of care for people with impaired vision in Australia. *Arch Ophthalmol* 127:1377–1381.
- Keelan JA, Sato T, Mitchell MD (1997) Interleukin IL-6 and IL-8 production by human amnion: regulation by cytokines, growth factors, glucocorticoids, phorbol esters, and bacterial lipopolysaccharide. *Biol Reprod* 57:1438 –1444.
- Keeney M, Gratama JW, Chin-Yee IH, Sutherland DR (1998) Isotype controls in the analysis of lymphocytes and CD34+ stem and progenitor cells by flow cytometry—time to let go! *Cytometry* 34:280–3.

- Keros V, Xella S, Hultenby K, Pettersson K, Sheikhi M, Volpe A, Hreinsson J, Hovatta O (2009) Vitrification versus controlled-rate freezing in cryopreservation of human ovarian tissue. *Hum Reprod* 24:1670–1683.
- Khankari RK, Grant DJ (1995) Pharmaceutical hydrates. *Thermochimica Acta* 248:61 – 79.
- Kheirkhah A, Johnson DA, Paranjpe DR, Raju VK, Casas V, Tseng SCG (2008) Temporary sutureless amniotic membrane patch for acute alkaline burns. *Arch Ophthalmol* 126:1059–1066.
- Kim HS, Luo L, Pflugfelder SC, Li DQ (2005) Doxycycline inhibits TGF-beta 1-induced MMP-9 via Smad and MAPK pathways in human corneal epithelial cells. *Invest Ophthalmol Vis Sci* 46:840–848.
- Kim JC, Tseng SC (1995a) The effects on inhibition of corneal neovascularization after human amniotic membrane transplantation in severely damaged rabbit corneas. *Korean J Ophthalmol* 9:32–46.
- Kim JC, Tseng SC (1995b) Transplantation of preserved human amniotic membrane for surface reconstruction in severely damaged rabbit corneas. *Cornea* 14:473–484.
- Kim JS, Kim JC, Na BK, Jeong JM, Song CY (2000) Amniotic membrane patching promotes healing and inhibits proteinase activity on wound healing following acute corneal alkali burn. *Exp Eye Res* 70:329–337.
- Kim JY, Choi YM, Jeong SW, Williams DL (2009) Effect of bovine freeze-dried amniotic membrane (Amnisite-BA) on uncomplicated canine corneal erosion. *Vet Ophthalmol* 12:36–42.
- King AE, Kelly RW, Sallenave JM, Bocking AD, Challis JRG (2007a) Innate immune defences in the human uterus during pregnancy. *Placenta* 28:1099–106.

- King AE, Paltoo A, Kelly RW, Sallenave JM, Bocking AD, Challis JRG (2007b) Expression of natural antimicrobials by human placenta and fetal membranes. *Placenta* 28:161–9.
- Kinoshita S, Koizumi N, Sotozono C, Yamada J, Nakamura T, Inatomi T (2004) Concept and clinical application of cultivated epithelial transplantation for ocular surface disorders. *Ocul Surf* 2:21–33.
- Kinoshita S, Nakamura T (2004) Development of cultivated mucosal epithelial sheet transplantation for ocular surface reconstruction. *Artif Organs* 28:22–27.
- Kitagawa K, Okabe M, Yanagisawa S, Zhang XY, Nikaido T, Hayashi A (2011) Use of a hyperdried cross-linked amniotic membrane as initial therapy for corneal perforations. *Jpn J Ophthalmol* 55:16–21.
- Kitagawa K, Yanagisawa S, Watanabe K, Yunoki T, Hayashi A, Okabe M, Nikaido T (2009) A hyperdry amniotic membrane patch using a tissue adhesive for corneal perforations and bleb leaks. *Am J Ophthalmol* 148:383–389.
- Kjaergaard N, Hein M, Hyttel L, Helmig RB, Schønheyder HC, Uldbjerg N, Madsen H (2001) Antibacterial properties of human amnion and chorion in vitro. *Eur J Obstet Gynecol Reprod Biol* 94:224–9.
- Knox F, Chan W, Jackson A, Foot B, Sharkey J, McGinnity F (2008) A British ophthalmological surveillance unit study on serious ocular injuries from fireworks in the UK. *Eye (Lond)* 22:944–947.
- Kobayashi A, Shirao Y, Yoshita T, Yagami K, Segawa Y, Kawasaki K, Shozu M, Tseng SCG (2003) Temporary amniotic membrane patching for acute chemical burns. *Eye (Lond)* 17:149–158.
- Kochevar IE (2010) Corneal protection for burn patients. Technical report, Massachusetts General Hospital, Boston.

- Koczulla A, Bals R (2003) Antimicrobial peptides: Current status and therapeutic potential. *Drugs* 63:389–406.
- Koh JW, Shin YJ, Oh JY, Kim MK, Ko JH, Hwang JM, Wee WR, Lee JH (2007) The expression of TIMPs in cryo-preserved and freeze-dried amniotic membrane. *Curr Eye Res* 32:611–616.
- Koizumi N, Inatomi T, Quantock A, Fullwood N, Dota A, Kinoshita S (2000b) Amniotic membrane as a substrate for cultivating limbal corneal epithelial cells for autologous transplantation in rabbits. *Cornea* 19:65–71.
- Koizumi N, Inatomi T, Suzuki T, Sotozono C, Kinoshita S (2001a) Cultivated corneal epithelial stem cell transplantation in ocular surface disorders. *Ophthalmology* 108:1569–1574.
- Koizumi N, Inatomi T, Suzuki T, Sotozono C, Kinoshita S (2001b) Cultivated corneal epithelial transplantation for ocular surface reconstruction in acute phase of Stevens-Johnson syndrome. *Arch.Ophthalmol.* 119:298–300.
- Koizumi NJ, Inatomi TJ, Sotozono CJ, Fullwood NJ, Quantock AJ, Kinoshita S (2000) Growth factor mRNA and protein in preserved human amniotic membrane. *Curr Eye Res* 20:173–177.
- Koizumi N, Rigby H, Fullwood NJ, Kawasaki S, Tanioka H, Koizumi K, Kociok N, Jousseaume AM, Kinoshita S (2007) Comparison of intact and denuded amniotic membrane as a substrate for cell-suspension culture of human limbal epithelial cells. *Graefes Arch Clin Exp Ophthalmol* 245:123–134.
- Kolli S, Lako M, Figueiredo F, Mudhar H, Ahmad S (2008) Loss of corneal epithelial stem cell properties in outgrowths from human limbal explants cultured on intact amniotic membrane. *Regen Med* 3:329–342.

- Korossis SA, Booth C, Wilcox HE, Watterson KG, Kearney JN, Fisher J, Ingham E (2002) Tissue engineering of cardiac valve prostheses II: biomechanical characterization of decellularized porcine aortic heart valves. *J Heart Valve Dis* 11:463–71.
- Kovacs G, Vellekoop M, Haueis R, Lubking G, Venema A (1994) A love wave sensor for (bio)chemical sensing in liquids. *Sensors and Actuators A: Physical* 43:38 – 43.
- Kruse FE, Jousseaume AM, Rohrschneider K, You L, Sinn B, Baumann J, Völcker HE (2000) Cryopreserved human amniotic membrane for ocular surface reconstruction. *Graefes Arch Clin Exp Ophthalmol* 238:68–75.
- Kruse FE, Rohrschneider K, Völcker HE (1999) Multilayer amniotic membrane transplantation for reconstruction of deep corneal ulcers. *Ophthalmology* 106:1504–10; discussion 1511.
- Kubo M, Sonoda Y, Muramatsu R, Usui M (2001) Immunogenicity of human amniotic membrane in experimental xenotransplantation. *Invest Ophthalmol Vis Sci* 42:1539–1546.
- Kuckelkorn R, Kottek A, Schrage N, Reim M (1995b) Poor prognosis of severe chemical and thermal eye burns: the need for adequate emergency care and primary prevention. *Int Arch Occup Environ Health* 67:281–284.
- Kuckelkorn R, Schrage N, Redbrake C, Kottek A, Reim M (1996) Autologous transplantation of nasal mucosa after severe chemical and thermal eye burns. *Acta Ophthalmol Scand* 74:442–448.
- Kuckelkorn R, Schrage N, Reim M (1995) Treatment of severe eye burns by tenonplasty. *Lancet* 345:657–8.
- Kuhn F, Maisiak R, Mann L, Mester V, Morris R, Witherspoon C (2002) The ocular trauma score (OTS). *Ophthalmol Clin North Am* 15:163–5, vi.

- Kuhn F, Morris R, Witherspoon C (2002) Birmingham eye trauma terminology (BETT): terminology and classification of mechanical eye injuries. *Ophthalmol Clin North Am* 15:139–43, v.
- Kumar D, Moore RM, Elkhwad M, Silver RJ, Moore JJ (2004) Vitamin c exacerbates hydrogen peroxide induced apoptosis and concomitant PGE2 release in amnion epithelial and mesenchymal cells, and in intact amnion. *Placenta* 25:573–9.
- Kumar TR, Shanmugasundaram N, Babu M (2003) Biocompatible collagen scaffolds from a human amniotic membrane: physicochemical and in vitro culture characteristics. *J Biomater Sci Polym Ed* 14:689–706.
- Lan W, Petznick A, Heryati S, Rifada M, Tong L (2012) Nuclear factor-kappab: Central regulator in ocular surface inflammation and diseases. *Ocul Surf* 10:137–48.
- Länge K, Rapp BE, Rapp M (2008) Surface acoustic wave biosensors: a review. *Anal Bioanal Chem* 391:1509–19.
- Lasagabaster A, Abad MJ, Barral L, Ares A (2006) FTIR study on the nature of water sorbed in polypropylene (PP)/ethylene alcohol vinyl (EVOH) films. *European Polymer Journal* 42:3121 – 3132.
- Lavery F (1946) Lime burn of conjunctiva and cornea treated with amnioplastin graft. *Trans Ophthalmol Soc UK* 66:668.
- Lavery J, Miller C (1977) The viscoelastic nature of chorioamniotic membranes. *Obstet Gynecol* 50:467–472.
- Lavery J, Miller C (1979) Deformation and creep in the human chorioamniotic sac. *Am J Obstet Gynecol* 134:366–375.
- Lazutina E, Suleman H, Dua HS, Tint NL, James D, Hopkinson A (2008)

- The effect of spongy layer (SL) isolated from amniotic membrane on ocular cells growth. *Acta Ophthalmologica* 86:S243.
- Lee CR, Grodzinsky AJ, Spector M (2001) The effects of cross-linking of collagen-glycosaminoglycan scaffolds on compressive stiffness, chondrocyte-mediated contraction, proliferation and biosynthesis. *Biomaterials* 22:3145–3154.
- Lee JLS, Gilmore IS (2009) The application of multivariate data analysis techniques in surface analysis. In Vickerman JC, Gilmore IS, editors, *Surface analysis: the principal techniques*, chapter 10, pp. 563–612. John Wiley and Sons, Ltd., Hoboken, NJ, 2nd edition.
- Lee SB, Li DQ, Tan DT, Meller DC, Tseng SC (2000) Suppression of TGF-beta signaling in both normal conjunctival fibroblasts and pterygial body fibroblasts by amniotic membrane. *Curr Eye Res* 20:325 –334.
- Lee SH, Tseng SC (1997) Amniotic membrane transplantation for persistent epithelial defects with ulceration. *Am J Ophthalmol* 123:303–312.
- Lei H, Furth EE, Kalluri R, Chiou T, Tilly KI, Tilly JL, Elkon KB, Jeffrey JJ, Strauss JF (1996) A program of cell death and extracellular matrix degradation is activated in the amnion before the onset of labor. *J Clin Invest* 98:1971–8.
- Letko E, Stechschulte SU, Kenyon KR, Sadeq N, Romero TR, Samson CM, Nguyen QD, Harper SL, Primack JD, Azar DT, Gruterich M, Dohlman CH, Baltatzis S, Foster CS (2001) Amniotic membrane inlay and overlay grafting for corneal epithelial defects and stromal ulcers. *Arch Ophthalmol* 119:659–663.
- Levinson R, Paterson C, Pfister R (1976) Ascorbic acid prevents corneal ulceration and perforation following experimental alkali burns. *Invest Ophthalmol* 15:986–993.

- Levy O (2007) Innate immunity of the newborn: basic mechanisms and clinical correlates. *Nat Rev Immunol* 7:379–90.
- Li H, Niederkorn JY, Neelam S, Mayhew E, Word RA, McCulley JP, Alizadeh H (2005) Immunosuppressive factors secreted by human amniotic epithelial cells. *Invest Ophthalmol Vis Sci* 46:900–907.
- Li R, Ackerman I WE, Summerfield TL, Yu L, Gulati P, Zhang J, Huang K, Romero R, Kniss DA (2011) Inflammatory gene regulatory networks in amnion cells following cytokine stimulation: Translational systems approach to modeling human parturition. *PLoS ONE* 6:e20560.
- Li ST (2000) Biologic biomaterials: Tissue-derived biomaterials (collagen). In Bronzino JD, editor, *The biomedical engineering handbook*, Vol. II, chapter 42, pp. 42.1–42.4. CRC Press, Boca Raton, FL, 2nd edition.
- Li W, He H, Kawakita T, Espana EM, Tseng SCG (2006a) Amniotic membrane induces apoptosis of interferon-gamma activated macrophages in vitro. *Exp Eye Res* 82:282–92.
- Li W, He H, Kuo CL, Gao Y, Kawakita T, Tseng SCG (2006b) Basement membrane dissolution and reassembly by limbal corneal epithelial cells expanded on amniotic membrane. *Invest Ophthalmol Vis Sci* 47:2381–2389.
- Li ZR, Li YP, Lin ML, Su WR, Zhang WX, Zhang Y, Yao L, Liang D (2012) Activated macrophages induce neovascularization through upregulation of MMP-9 and VEGF in rat corneas. *Cornea* 31:1028–35.
- Libera RD, de Melo GB, de Souza Lima A, Haapalainen EF, Cristovam P, Gomes JAP (2008) Assessment of the use of cryopreserved vs freeze-dried amniotic membrane (AM) for reconstruction of ocular surface in rabbit model. *Arq Bras Oftalmol* 71:669–673.

- Lillie MA, Gosline JM (1990) The effects of hydration on the dynamic mechanical properties of elastin. *Biopolymers* 29:1147–60.
- Lim L, Poh R, Riau A, Beuerman R, Tan D, Mehta J (2010) Biological and ultrastructural properties of Acelagraft, a freeze-dried gamma-irradiated human amniotic membrane. *Arch Ophthalmol* 128:1303–1310.
- Lim M, Goldstein M, Tuli S, Schultz G (2003) Growth factor, cytokine and protease interactions during corneal wound healing. *Ocul Surf* 1:53–65.
- Linnala A, Balza E, Zardi L, Virtanen I (1993) Human amnion epithelial cells assemble tenascins and three fibronectin isoforms in the extracellular matrix. *FEBS Lett* 317:74–8.
- Liu BC, Harrell R, Davis RH, Dresden MH, Spira M (1989) The effect of gamma irradiation on injectable human amnion collagen. *J Biomed Mater Res* 23:833–44.
- Liu BQ, Wang ZC, Liu LM, Liu JB, Li NY, Wang LN, Ma P, Jiang RZ, Ge J (2008) Sutureless fixation of amniotic membrane patch as a therapeutic contact lens by using a polymethyl methacrylate ring and fibrin sealant in a rabbit model. *Cornea* 27:74–79.
- Loon SC, Tay WT, Saw SM, Wang JJ, Wong TY (2009) Prevalence and risk factors of ocular trauma in an urban south-east Asian population: the Singapore Malay Eye Study. *Clin Experiment Ophthalmol* 37:362–367.
- López-García JS, Rivas L, García-Lozano I, Murube J (2006) Analysis of corneal surface evolution after moderate alkaline burns by using impression cytology. *Cornea* 25:908–913.
- López-García JS, Jara LR, García-Lozano I, Murube J (2007) Histopathologic limbus evolution after alkaline burns. *Cornea* 26:1043–1048.

- Lu L, Reinach P, Kao W (2001) Corneal epithelial wound healing. *Exp Biol Med* 226:653–664.
- Ma DHK, Kuo MT, Tsai YJ, Chen HCJ, Chen XL, Wang SF, Li L, Hsiao CH, Lin KK (2009) Transplantation of cultivated oral mucosal epithelial cells for severe corneal burn. *Eye (Lond)* 23:1442–50.
- Ma DHK, Lai JY, Cheng HY, Tsai CC, Yeh LK (2010) Carbodiimide cross-linked amniotic membranes for cultivation of limbal epithelial cells. *Biomaterials* 31:6647–6658.
- Ma DHK, Wang SF, Su WY, Tsai RJF (2002) Amniotic membrane graft for the management of scleral melting and corneal perforation in recalcitrant infectious scleral and corneoscleral ulcers. *Cornea* 21:275–83.
- Ma X, Li J (2005) Corneal neovascularization suppressed by TIMP2 released from human amniotic membranes. *Yan Ke Xue Bao* 21:56–61.
- MacDermott RI, Landon CR (2000) The hydroxyproline content of amnion and prelabour rupture of the membranes. *Eur J Obstet Gynecol Reprod Biol* 92:217–221.
- MacNaughtan B, Farhat IA (2008) Thermal methods in the study of food and food ingredients. In Gabbott P, editor, *Principles and applications of thermal analysis*, chapter 9, pp. 331–409. Blackwell Publishing Ltd., Oxford.
- Mader T, Carroll R, Slade C, George R, Ritchey J, Neville S (2006) Ocular war injuries of the Iraqi insurgency. *Ophthalmology* 113:97–104.
- Maharajan VS, Shanmuganathan V, Currie A, Hopkinson A, Powell-Richards A, Dua HS (2007) Amniotic membrane transplantation for ocular surface reconstruction: indications and outcomes. *Clin Experiment Ophthalmol* 35:140–147.

- Majo F, Rochat A, Nicolas M, Jaoude G, Barrandon Y (2008) Oligopotent stem cells are distributed throughout the mammalian ocular surface. *Nature* 456:250–254.
- Makeeva G (1983) [Use of the amnion and dura mater for barrier plastic operations in the surgical treatment of pterygium]. *Oftalmol Zh* 38:104–106.
- Malak TM, Bell SC (1994) Structural characteristics of term human fetal membranes: a novel zone of extreme morphological alteration within the rupture site. *Br J Obstet Gynaecol* 101:375–386.
- Malak TM, Ockleford CD, Bell SC, Dalglish R, Bright N, Macvicar J (1993) Confocal immunofluorescence localization of collagen types I, III, IV, V and VI and their ultrastructural organization in term human fetal membranes. *Placenta* 14:385–406.
- Malhotra R, Sheikh I, Dheansa B (2009) The management of eyelid burns. *Surv Ophthalmol* 54:356–371.
- Maruyama K, Ii M, Cursiefen C, Jackson DG, Keino H, Tomita M, Van Rooijen N, Takenaka H, D'Amore PA, Stein-Streilein J, Losordo DW, Streilein JW (2005) Inflammation-induced lymphangiogenesis in the cornea arises from CD11b-positive macrophages. *J Clin Invest* 115:2363–72.
- Matejtschuk P, Phillips P (2007) Product stability and accelerated degradation studies. In Stacey G, Davis J, editors, *Medicines from animal cell culture*, chapter 27, pp. 503–522. John Wiley and Sons, Ltd., Hoboken, NJ.
- Mattice JM, Lau AG, Oyen ML, Kent RW (2006) Spherical indentation load-relaxation of soft biological tissues. *Journal of Materials Research* 21:2003–2010.

- McCulley JP, Whiting DW, Petitt MG, Lauber SE (1983) Hydrofluoric acid burns of the eye. *J Occup Med* 25:447–450.
- McCulley J (1987) Chemical injuries. In Smolin G, Thoft RA, editors, *The cornea: scientific foundation and clinical practice*, chapter 11, pp. 527–542. Little, Brown and Co., Boston, 2nd edition.
- McDermott AM (2004) Defensins and other antimicrobial peptides at the ocular surface. *Ocul Surf* 2:229–47.
- McIntosh RS, Cade JE, Al-Abed M, Shanmuganathan V, Gupta R, Bhan A, Tighe PJ, Dua HS (2005) The spectrum of antimicrobial peptide expression at the ocular surface. *Invest Ophthalmol Vis Sci* 46:1379–85.
- McLaren J, Malak TM, Bell SC (1999) Structural characteristics of term human fetal membranes prior to labour: identification of an area of altered morphology overlying the cervix. *Hum Reprod* 14:237–241.
- Meinert M, Eriksen GV, Petersen AC, Helmig RB, Laurent C, Uldbjerg N, Malmström A (2001) Proteoglycans and hyaluronan in human fetal membranes. *Am J Obstet Gynecol* 184:679–685.
- Mejía LF, Acosta C, Santamaría JP (2000) Use of nonpreserved human amniotic membrane for the reconstruction of the ocular surface. *Cornea* 19:288–291.
- Meller D, Pires RT, Mack RJ, Figueiredo F, Heiligenhaus A, Park WC, Prabhasawat P, John T, McLeod SD, Steuhl KP, Tseng SC (2000) Amniotic membrane transplantation for acute chemical or thermal burns. *Ophthalmology* 107:980–9; discussion 990.
- Mencucci R, Menchini U, Dei R (2006) Antimicrobial activity of antibiotic-treated amniotic membrane: An in vitro study. *Cornea* 25:428–31.

- Menon R, Fortunato SJ (2007) Infection and the role of inflammation in preterm premature rupture of the membranes. *Best Pract Res Clin Obstet Gynaecol* 21:467–478.
- Merle H, Gérard M, Schrage N (2008) [Ocular burns]. *J Fr Ophthalmol* 31:723–734.
- Ming WJ, Bersani L, Mantovani A (1987) Tumor necrosis factor is chemotactic for monocytes and polymorphonuclear leukocytes. *The Journal of Immunology* 138:1469–74.
- Møbjerg N, Halberg KA, Jørgensen A, Persson D, Bjørn M, Ramløv H, Kristensen RM (2011) Survival in extreme environments – on the current knowledge of adaptations in tardigrades. *Acta Physiologica* 202:409–420.
- Modesti A, Scarpa S, D’Orazi G, Simonelli L, Caramia FG (1989) Localization of type IV and V collagens in the stroma of human amnion. *Prog Clin Biol Res* 296:459–463.
- Mohammed I, Yeung A, Abedin A, Hopkinson A, Dua HS (2011) Signalling pathways involved in ribonuclease-7 expression. *Cell Mol Life Sci* 68:1941–52.
- Moller-Pedersen T, Cavanagh H, Petroll W, Jester J (1998) Neutralizing antibody to TGF-beta modulates stromal fibrosis but not regression of photoblastic effect following PRK. *Curr Eye Res* 17:736–747.
- Moore RM, Mansour JM, Redline RW, Mercer BM, Moore JJ (2006) The physiology of fetal membrane rupture: insight gained from the determination of physical properties. *Placenta* 27:1037–1051.
- Moore RM, Silver RJ, Moore JJ (2003) Physiological apoptotic agents have different effects upon human amnion epithelial and mesenchymal cells. *Placenta* 24:173–80.

- Morawetz H (1985) The impact of X-ray crystallography. In *Polymers: the growth and origins of a science*, chapter 9, pp. 83–85. John Wiley and Sons, Ltd., Hoboken, NJ.
- Morley MG, Nguyen JK, Heier JS, Shingleton BJ, Pasternak JF, Bower KS (2010) Blast eye injuries: a review for first responders. *Disaster Med Public Health Prep* 4:154–60.
- Movasaghi Z, Rehman S, Rehman I (2008) Fourier transform infrared (FTIR) spectroscopy of biological tissues. *Applied Spectroscopy Reviews* 43:134–179.
- Muraine M, Descargues G, Franck O, Villeroy F, Toubreau D, Menguy E, Martin J, Brasseur G (2001) [Amniotic membrane graft in ocular surface disease. Prospective study with 31 cases]. *J Fr Ophthalmol* 24:798–812.
- Murdoch IE, Morris SS, Cousens SN (1998) People and eyes: statistical approaches in ophthalmology. *Br J Ophthalmol* 82:971–3.
- Nagase H, Visse R, Murphy G (2006) Structure and function of matrix metalloproteinases and timp. *Cardiovasc Res* 69:562–573.
- Nagase H, Endo T, Ueda H, Nakagaki M (2002) An anhydrous polymorphic form of trehalose. *Carbohydrate Research* 337:167–173.
- Nakamura T, Inatomi T, Sotozono C, Amemiya T, Kanamura N, Kinoshita S (2004) Transplantation of cultivated autologous oral mucosal epithelial cells in patients with severe ocular surface disorders. *Br J Ophthalmol* 88:1280–1284.
- Nakamura T, Ishikawa F, Sonoda K, Hisatomi T, Qiao H, Yamada J, Fukata M, Ishibashi T, Harada M, Kinoshita S (2005) Characterization and distribution of bone marrow-derived cells in mouse cornea. *Invest Ophthalmol Vis Sci* 46:497–503.

- Nakamura T, Kinoshita S (2003) Ocular surface reconstruction using cultivated mucosal epithelial stem cells. *Cornea* 22:S75–S80.
- Nakamura T, Koizumi N, Tsuzuki M, Inoki K, Sano Y, Sotozono C, Kinoshita S (2003) Successful regrafting of cultivated corneal epithelium using amniotic membrane as a carrier in severe ocular surface disease. *Cornea* 22:70–71.
- Nakamura T, Sekiyama E, Takaoka M, Bentley AJ, Yokoi N, Fullwood NJ, Kinoshita S (2008) The use of trehalose-treated freeze-dried amniotic membrane for ocular surface reconstruction. *Biomaterials* 29:3729–3737.
- Nakamura T, Yoshitani M, Rigby H, Fullwood NJ, Ito W, Inatomi T, Sotozono C, Nakamura T, Shimizu Y, Kinoshita S (2004) Sterilized, freeze-dried amniotic membrane: a useful substrate for ocular surface reconstruction. *Invest Ophthalmol Vis Sci* 45:93–99.
- Négrel AD, Thylefors B (1998) The global impact of eye injuries. *Ophthalmic Epidemiol* 5:143–169.
- Néron S, Thibault L, Dussault N, Côté G, Ducas E, Pineault N, Roy A (2007) Characterization of mononuclear cells remaining in the leukoreduction system chambers of apheresis instruments after routine platelet collection: a new source of viable human blood cells. *Transfusion* 47:1042–9.
- Neumann A, Schinzel R, Palm D, Riederer P, Münch G (1999) High molecular weight hyaluronic acid inhibits advanced glycation endproduct-induced NF-kappaB activation and cytokine expression. *FEBS Lett* 453:283–7.
- Newcombe RG (1998) Interval estimation for the difference between independent proportions: comparison of eleven methods. *Stat Med* 17:873–90.
- Ntim M, Bembey A, Ferguson V, Bushby A (2006) Hydration effects on the viscoelastic properties of collagen. *MRS Proc* 898E:L05–02.

- Nubile M, Dua HS, Lanzini M, Ciancaglini M, Calienno R, Said DG, Pocabelli A, Mastropasqua R, Carpineto P (2011) In vivo analysis of stromal integration of multilayer amniotic membrane transplantation in corneal ulcers. *Am J Ophthalmol* 151:809–822.
- O’Gorman MRG, Thomas J (1999) Isotype controls—time to let go? *Cytometry* 38:78–80.
- Oh JY, Kim MK, Shin MS, Lee HJ, Ko JH, Wee WR, Lee JH (2008) The anti-inflammatory and anti-angiogenic role of mesenchymal stem cells in corneal wound healing following chemical injury. *Stem Cells* 26:1047–55.
- Oliver WC, Pharr GM (1992) An improved technique for determining hardness and elastic modulus using load and displacement sensing indentation experiments. *Journal of Materials Research* 7:1564–1583.
- Otri AM, Mohammed I, Abedin A, Cao Z, Hopkinson A, Panjwani N, Dua HS (2010) Antimicrobial peptides expression by ocular surface cells in response to *Acanthamoeba castellanii*: an *in vitro* study. *Br J Ophthalmol* 94:1523–7.
- Otri AM, Mohammed I, Al-Aqaba MA, Fares U, Peng C, Hopkinson A, Dua HS (2012) Variable expression of human beta defensins 3 and 9 at the human ocular surface in infectious keratitis. *Invest Ophthalmol Vis Sci* 53:757–61.
- Oxlund H, Helmig R, Halaburt J, Uldbjerg N (1990) Biomechanical analysis of human chorioamniotic membranes. *Eur J Obstet Gynecol Reprod Biol* 34:247–255.
- Oyen ML, Calvin SE, Cook RF (2004) Uniaxial stress-relaxation and stress-strain responses of human amnion. *J Mater Sci Mater Med* 15:619–624.

- Oyen ML, Calvin SE, Landers DV (2006) Premature rupture of the fetal membranes: is the amnion the major determinant? *Am J Obstet Gynecol* 195:510–5.
- Oyen ML, Cook RF (2009) A practical guide for analysis of nanoindentation data. *J Mech Behav Biomed Mater* 2:396–407.
- Pager CK, McCluskey PJ, Retsas C (2004) Cataract surgery in australia: a profile of patient-centred outcomes. *Clin Experiment Ophthalmol* 32:388–92.
- Pallant J (2007) *SPSS Survival Manual A Step by Step Guide to Data Analysis using SPSS for Windows*. McGraw-Hill Open University Press, New York, 3rd edition.
- Panda A, Nainiwal SK, Sudan R (2002) Failure of amniotic membrane transplantation in the treatment of acute ocular burns. *Br J Ophthalmol* 86:831.
- Park CY, Kohanim S, Zhu L, Gehlbach PL, Chuck RS (2009) Immunosuppressive property of dried human amniotic membrane. *Ophthalmic Res* 41:112–3.
- Park J, Lakes R (1992) Structure-property relationships of biological materials. In *Biomaterials: an introduction*, chapter 9, pp. 185–222. Plenum Press, New York, 2nd edition.
- Park W, Tseng S (2000) Modulation of acute inflammation and keratocyte death by suturing, blood, and amniotic membrane in PRK. *Invest Ophthalmol Vis Sci* 41:2906–2914.
- Parot P, Dufrêne YF, Hinterdorfer P, Le Grimellec C, Navajas D, Pellequer JL, Scheuring S (2007) Past, present and future of atomic force microscopy in life sciences and medicine. *J Mol Recognit* 20:418–31.

- Parry S, Strauss J (1998) Premature rupture of the fetal membranes. *N Engl J Med* 338:663–670.
- Pashley DH, Agee KA, Carvalho RM, Lee KW, Tay FR, Callison TE (2003) Effects of water and water-free polar solvents on the tensile properties of demineralized dentin. *Dent Mater* 19:347–52.
- Patist A, Zoerb H (2005) Preservation mechanisms of trehalose in food and biosystems. *Colloids and Surfaces B: Biointerfaces* 40:107 – 113.
- Pegg DE (2007) Principles of cryopreservation. In Day JG, Stacey GN, editors, *Cryopreservation and freeze-drying protocols*, Methods in Molecular Biology, chapter 3, pp. 39–57. Humana Press, New York, 2nd edition.
- Perkins DN, Pappin DJ, Creasy DM, Cottrell JS (1999) Probability-based protein identification by searching sequence databases using mass spectrometry data. *Electrophoresis* 20:3551–67.
- Perrella G, Brusini P, Spelat R, Hossain P, Hopkinson A, Dua HS (2007) Expression of haematopoietic stem cell markers, CD133 and CD34 on human corneal keratocytes. *Br J Ophthalmol* 91:94–99.
- Pfister RR, Haddox JL, Sommers CI (1997) Effect of synthetic metalloproteinase inhibitor or citrate on neutrophil chemotaxis and the respiratory burst. *Invest Ophthalmol Vis Sci* 38:1340–1349.
- Pfister R, Koski J (1982) Alkali burns of the eye: pathophysiology and treatment. *South Med J* 75:417–422.
- Porre S, Heinonen S, Mäntyjärvi R, Rytkönen-Nissinen M, Perola O, Rautainen J, Virtanen T (2005) Psoriasin, a calcium-binding protein with chemotactic properties is present in the third trimester amniotic fluid. *Mol Hum Reprod* 11:87–92.

- Portmann-Lanz CB, Ochsenbein-Kölble N, Marquardt K, Lithi U, Zisch A, Zimmermann R (2007) Manufacture of a cell-free amnion matrix scaffold that supports amnion cell outgrowth in vitro. *Placenta* 28:6–13.
- Prabhasawat P, Barton K, Burkett G, Tseng SC (1997) Comparison of conjunctival autografts, amniotic membrane grafts, and primary closure for pterygium excision. *Ophthalmology* 104:974–985.
- Prabhasawat P, Tesavibul N, Prakairungthong N, Booranapong W (2007) Efficacy of amniotic membrane patching for acute chemical and thermal ocular burns. *J Med Assoc Thai* 90:319–326.
- Pratoomsot C, Tanioka H, Hori K, Kawasaki S, Kinoshita S, Tighe PJ, Dua H, Shakesheff KM, Rose FRAJ (2008) A thermoreversible hydrogel as a biosynthetic bandage for corneal wound repair. *Biomaterials* 29:272–281.
- Prévost TP (2006) Biomechanics of the human chorioamnion. Master's thesis, Massachusetts Institute Of Technology.
- Psolka M, Bower K, Brooks D, Donnelly S, Iglesias M, Rimm W, Ward T (2007) Ocular diseases and nonbattle injuries seen at a tertiary care medical center during the Global War on Terrorism. *Mil Med* 172:491–497.
- Quirijns EJ (2006) Modelling and dynamic optimisation of quality indicator profiles during drying. Ph.D. diss., Wageningen University.
- Rahman I, Said DG, Maharajan VS, Dua HS (2009) Amniotic membrane in ophthalmology: indications and limitations. *Eye* 23:1954–1961.
- Raimbault V, Rebiere D, Dejous C, Guirardel M, Pistre J, Lachaud J (2010) High frequency microrheological measurements of PDMS fluids using saw microfluidic system. *Sensors and Actuators B: Chemical* 144:467–471.
- Rama P, Giannini R, Bruni A, Gatto C, Tiso R, Ponzin D (2001) Further

- evaluation of amniotic membrane banking for transplantation in ocular surface diseases. *Cell Tissue Bank* 2:155–163.
- Rama P, Matuska S, Paganoni G, Spinelli A, Luca MD, Pellegrini G (2010) Limbal stem-cell therapy and long-term corneal regeneration. *N Engl J Med* 363:147–155.
- Ramasamy A, Harrisson S, Lasrado I, Stewart M (2009) A review of casualties during the Iraqi insurgency 2006—a British field hospital experience. *Injury* 40:493–497.
- Reim M, Overkämping B, Kuckelkorn R (1992) [2 years experiences with tenon-plasty]. *Ophthalmologe* 89:524–530.
- Rejzek A, Weyer F, Eichberger R, Gebhart W (2001) Physical changes of amniotic membranes through glycerolization for the use as an epidermal substitute. light and electron microscopic studies. *Cell Tissue Bank* 2:95–102.
- Resch M, Schlotzer-Schrehardt U, Hofmann-Rummelt C, Sauer R, Cursiefen C, Kruse F, Beckmann M, Seitz B (2006) Adhesion structures of amniotic membranes integrated into human corneas. *Invest Ophthalmol Vis Sci* 47:1853–1861.
- Resch MD, Resch BE, Csizmazia E, Imre L, Németh J, Szabó-Révész P, Csányi E (2011) Drug reservoir function of human amniotic membrane. *J Ocul Pharmacol Ther* 27:323–6.
- Riau AK, Beuerman RW, Lim LS, Mehta JS (2010) Preservation, sterilization and de-epithelialization of human amniotic membrane for use in ocular surface reconstruction. *Biomaterials* 31:216–225.
- Rigal-Sastourné JC, Tixier JM, Renard JP, Maurin JF, Pouliquen Y, Legeais JM (2002) [Corneal burns and matrix metalloproteinases (MMP-2 and -9): the effects of human amniotic membrane transplantation]. *J Fr Ophtalmol* 25:685–693.

- Rodríguez-Ares MT, López-Valladares MJ, Touriño R, Vieites B, Gude F, Silva MT, Couceiro J (2009) Effects of lyophilization on human amniotic membrane. *Acta Ophthalmol* 87:396–403.
- Rohini G, Murugeswari P, Prajna NV, Lalitha P, Muthukkaruppan V (2007) Matrix metalloproteinases (MMP-8, MMP-9) and the tissue inhibitors of metalloproteinases (TIMP-1, TIMP-2) in patients with fungal keratitis. *Cornea* 26:207–11.
- Roorda WE, Bouwstra JA, de Vries MA, Junginger HE (1988) Thermal behavior of poly hydroxy ethyl methacrylate (pHEMA) hydrogels. *Pharm Res* 5:722–5.
- Roper-Hall M (1965) Thermal and chemical burns. *Trans Ophthalmol Soc UK* 85:631–653.
- Rubin MB, Bodner SR (2002) A three-dimensional nonlinear model for dissipative response of soft tissue. *International J Solids Struct* 39:5081–99.
- Sabella N (1913) Use of fetal membranes in skin grafting. *Med Rec NY* 83:478.
- Safarinejad M, Moosavi S, Montazeri B (2001) Ocular injuries caused by mustard gas: diagnosis, treatment, and medical defense. *Mil Med* 166:67–70.
- Said DG, Nubile M, Alomar T, Hopkinson A, Gray T, Lowe J, Dua HS (2009) Histologic features of transplanted amniotic membrane: implications for corneal wound healing. *Ophthalmology* 116:1287–1295.
- Saika S (2007) Yin and yang in cytokine regulation of corneal wound healing: roles of TNF-alpha. *Cornea* 26:S70–4.
- Salomao M, Wilson S (2009) Corneal molecular and cellular biology update for the refractive surgeon. *J Refract Surg* 25:459–466.

- Sangwan VS, Vemuganti GK, Iftexhar G, Bansal AK, Rao GN (2003) Use of autologous cultured limbal and conjunctival epithelium in a patient with severe bilateral ocular surface disease induced by acid injury: a case report of unique application. *Cornea* 22:478–481.
- Santagapita P, Buera MP (2008) Electrolyte effects on amorphous and supercooled sugar systems. *Journal of Non-Crystalline Solids* 354:1760–1767.
- Sasaki N, Odajima S (1996) Stress-strain curve and Young's modulus of a collagen molecule as determined by the X-ray diffraction technique. *J Biomech* 29:655–658.
- Satpathy GR, Török Z, Bali R, Dwyre DM, Little E, Walker NJ, Tablin F, Crowe JH, Tsvetkova NM (2004) Loading red blood cells with trehalose: a step towards biostabilization. *Cryobiology* 49:123–136.
- Saunders M (2008) Thermal analysis of pharmaceuticals. In Gabbott P, editor, *Principles and Applications of Thermal Analysis*, chapter 8, pp. 287–329. Blackwell.
- Saw VPJ, Minassian D, Dart JKG, Ramsay A, Henderson H, Poniatowski S, Warwick RM, Cabral S, Group AMTU (2007) Amniotic membrane transplantation for ocular disease: a review of the first 233 cases from the UK user group. *Br J Ophthalmol* 91:1042–1047.
- Schebor C, Burin L, del Pilar Buera M, Chirife J (1999) Stability to hydrolysis and browning of trehalose, sucrose and raffinose in low-moisture systems in relation to their use as protectants of dry biomaterials. *LWT - Food Science and Technology* 32:481 – 485.
- Schechter BA, Rand WJ, Nagler RS, Estrin I, Arnold SS, Villate N, Velazquez GE (2005) Corneal melt after amniotic membrane transplant. *Cornea* 24:106–107.

- Scheel O, Papavlassopoulos M, Blunck R, Gebert A, Hartung T, Zähringer U, Seydel U, Schromm AB (2006) Cell activation by ligands of the toll-like receptor and interleukin-1 receptor family depends on the function of the large-conductance potassium channel MaxiK in human macrophages. *Infect Immun* 74:4354–6.
- Schick C (2009) Differential scanning calorimetry (DSC) of semicrystalline polymers. *Anal Bioanal Chem* 395:1589–611.
- Schrage NF, Reim M, Burchard WG (1990) Particulate matter contamination in the corneal stroma of severe eye burns in humans. *Lens Eye Toxic Res* 7:427–444.
- Schrage N, Langefeld S, Zschocke J, Kuckelkorn R, Redbrake C, Reim M (2000) Eye burns: an emergency and continuing problem. *Burns* 26:689–699.
- Sekiyama E, Nakamura T, Kurihara E, Cooper LJ, Fullwood NJ, Takaoka M, Hamuro J, Kinoshita S (2007) Novel sutureless transplantation of bioadhesive-coated, freeze-dried amniotic membrane for ocular surface reconstruction. *Invest Ophthalmol Vis Sci* 48:1528–1534.
- Shafto C (1950) A simple method of inserting amniotic membrane grafts into the conjunctival sac. *Br J Ophthalmol* 34:445–446.
- Shahriari HA, Tokhmehchi F, Reza M, Hashemi NF (2008) Comparison of the effect of amniotic membrane suspension and autologous serum on alkaline corneal epithelial wound healing in the rabbit model. *Cornea* 27:1148–50.
- Shao C, Sima J, Zhang SX, Jin J, Reinach P, Wang Z, Ma JX (2004) Suppression of corneal neovascularization by PEDF release from human amniotic membranes. *Invest Ophthalmol Vis Sci* 45:1758–1762.

- Shapiro H (2003) Overture. In *Practical flow cytometry*, chapter 1, pp. 38–39. John Wiley and Sons, Ltd., Hoboken, NJ, 4th edition.
- Sharma N, Goel M, Velpandian T, Titiyal JS, Tandon R, Vajpayee RB (2011) Evaluation of umbilical cord serum therapy in acute ocular chemical burns. *Invest Ophthalmol Vis Sci* 52:1087–1092.
- Shay E, Khadem JJ, Tseng SCG (2010) Efficacy and limitation of sutureless amniotic membrane transplantation for acute toxic epidermal necrolysis. *Cornea* 29:359–61.
- Shimazaki J, Konomi K, Shimmura S, Tsubota K (2006) Ocular surface reconstruction for thermal burns caused by fireworks. *Cornea* 25:139–145.
- Shimazaki J, Yang HY, Tsubota K (1997) Amniotic membrane transplantation for ocular surface reconstruction in patients with chemical and thermal burns. *Ophthalmology* 104:2068–2076.
- Shimazaki J, Aiba M, Goto E, Kato N, Shimmura S, Tsubota K (2002) Transplantation of human limbal epithelium cultivated on amniotic membrane for the treatment of severe ocular surface disorders. *Ophthalmology* 109:1285–1290.
- Shimmura S, Shimazaki J, Ohashi Y, Tsubota K (2001) Antiinflammatory effects of amniotic membrane transplantation in ocular surface disorders. *Cornea* 20:408–413.
- Shimmura S, Tsubota K (2008) Surgical treatment of limbal stem cell deficiency: are we really transplanting stem cells? *Am J Ophthalmol* 146:154–155.
- Shortt AJ, Secker GA, Lomas RJ, Wilshaw SP, Kearney JN, Tuft SJ, Daniels JT (2009) The effect of amniotic membrane preparation method on its ability to serve as a substrate for the ex-vivo expansion of limbal epithelial cells. *Biomaterials* 30:1056–1065.

- Shukla I (1962) Amniotic membrane grafts in corneal ulcer. *J All India Ophthalmol Soc* 10:55–60.
- Singh R, Gupta P, Kumar P, Kumar A, Chacharkar MP (2003) Properties of air dried radiation processed amniotic membranes under different storage conditions. *Cell Tissue Bank* 4:95–100.
- Singh R, Purohit S, Chacharkar MP (2007) Effect of high doses of gamma radiation on the functional characteristics of amniotic membrane. *Radiation physics and chemistry* 76:1026–1030.
- Singh R, Purohit S, Chacharkar MP, Bhandari PS, Bath AS (2007b) Microbiological safety and clinical efficacy of radiation sterilized amniotic membranes for treatment of second-degree burns. *Burns* 33:505–510.
- Sinha S (2008) Pattern of trauma to anterior segment of eyes in a tertiary eye care centre of jharkhand. *J Indian Med Assoc* 106:289–290.
- Sitaula R, Bhowmick S (2006) Moisture sorption characteristics and thermophysical properties of trehalose-pbs mixtures. *Cryobiology* 52:369–85.
- Smieja Z, Zakar T, Walton JC, Olson DM (1993) Prostaglandin endoperoxide synthase kinetics in human amnion before and after labor at term and following preterm labor. *Placenta* 14:163 –175.
- Smith VA, Cook SD (2004) Doxycycline-a role in ocular surface repair. *Br J Ophthalmol* 88:619–25.
- Smith VA, Hoh HB, Easty DL (1999) Role of ocular matrix metalloproteinases in peripheral ulcerative keratitis. *Br J Ophthalmol* 83:1376–83.
- Solomon A, Rosenblatt M, Monroy D, Ji Z, Pflugfelder SC, Tseng SC (2001) Suppression of interleukin 1 alpha and interleukin 1 beta in human limbal epithelial cells cultured on the amniotic membrane stromal matrix. *Br J Ophthalmol* 85:444–9.

- Solomon A, Wajngarten M, Alviano F, Anteby I, Elchalal U, Pe'er J, Levi-Schaffer F (2005) Suppression of inflammatory and fibrotic responses in allergic inflammation by the amniotic membrane stromal matrix. *Clin Exp Allergy* 35:941–8.
- Solomon A, Espana EM, Tseng SCG (2003) Amniotic membrane transplantation for reconstruction of the conjunctival fornices. *Ophthalmology* 110:93–100.
- Son J, Coffee T, Yowler C, Steinemann T (2011) A cohort analysis and prevalence study of the therapeutic uses of amniotic membrane for acute ocular injuries. *Journal of Burn Care and Research* 32:56.
- Song JJ, Hwang KS, Woo JS, Chae SW, Cho JG, Kang HJ, Hwang SJ, Lee HM (2006) Expression of cathelicidin in recurrent throat infection. *Int J Pediatr Otorhinolaryngol* 70:487–492.
- Sørensen OE, Borregaard N, Cole AM (2008) Antimicrobial peptides in innate immune responses. *Contrib Microbiol* 15:61–77.
- Sørensen OE, Follin P, Johnsen AH, Calafat J, Tjabringa GS, Hiemstra PS, Borregaard N (2001) Human cathelicidin, hCAP-18, is processed to the antimicrobial peptide LL-37 by extracellular cleavage with proteinase 3. *Blood* 97:3951–3959.
- Sørensen OE (2005) The human cathelicidin hCAP-18. *Dan Med Bull* 52:1–10.
- Sørensen OE, Cowland JB, Theilgaard-Mönch K, Liu L, Ganz T, Borregaard N (2003) Wound healing and expression of antimicrobial peptides/polypeptides in human keratinocytes, a consequence of common growth factors. *J Immunol* 170:5583–9.

- Sorsby A, Haythorne J, Reed H (1947) Further experience with amniotic membrane grafts in caustic burns of the eye. *Br J Ophthalmol* 31:409–418.
- Sorsby A, Symons H (1946) Amniotic membrane grafts in caustic burns of the eye (burns of the second degree). *Br J Ophthalmol* 30:337–345.
- Spencer JD, Schwaderer AL, Dirosario JD, McHugh KM, McGillivary G, Justice SS, Carpenter AR, Baker PB, Harder J, Hains DS (2011) Ribonuclease 7 is a potent antimicrobial peptide within the human urinary tract. *Kidney Int* 80:174–80.
- Spira M, Liu B, Xu Z, Harrell R, Chahadeh H (1994) Human amnion collagen for soft tissue augmentation—biochemical characterizations and animal observations. *J Biomed Mater Res* 28:91–6.
- Spoerl E, Huhle M, Seiler T (1998) Induction of cross-links in corneal tissue. *Experimental Eye Research* 66:97–103.
- Spoerl E, Wollensak G, Reber F, Pillunat L (2004) Cross-linking of human amniotic membrane by glutaraldehyde. *Ophthalmic Res* 36:71–77.
- Spoerl E, Wollensak G, Seiler T (2004) Increased resistance of crosslinked cornea against enzymatic digestion. *Curr Eye Res* 29:35–40.
- Sridhar MS, Bansal AK, Sangwan VS, Rao GN (2000) Amniotic membrane transplantation in acute chemical and thermal injury. *Am J Ophthalmol* 130:134–137.
- Srinivasan R, T SS, Gupta A, Kaliaperumal S (2007) Hypopyon iritis after primary fresh amniotic membrane transplantation. *Cornea* 26:1275–6.
- Starner TD, Agerberth B, Gudmundsson GH, McCray PB (2005) Expression and activity of beta-defensins and LL-37 in the developing human lung. *The Journal of Immunology* 174:1608–1615.

- Stegeman H, Stalder K (1967) Determination of hydroxyproline. *Clinica Chemica Acta* 18:267–273.
- Stern M (1913) The grafting of preserved amniotic membranes to burned and ulcerated surfaces substituting skin grafts. *JAMA* 60:973.
- Stewart CC, Stewart SJ (1994) Cell preparation for the identification of leukocytes. In Zbigniew Darzynkiewicz JPR, Crissman HA, editors, *Flow Cytometry Second Edition, Part A*, Vol. 41 of *Methods in Cell Biology*, chapter 3, pp. 39 – 60. Academic Press, San Diego, CA.
- Stock SJ, Kelly RW, Riley SC, Calder AA (2007) Natural antimicrobial production by the amnion. *Am J Obstet Gynecol* 196:255 –256.
- Stoenchev S (1953) [Plastic surgery of the conjunctiva with amnion.]. *Khirurgiia (Sofia)* 6:608–612.
- Su CY, Lin CP (2000) Combined use of an amniotic membrane and tissue adhesive in treating corneal perforation: a case report. *Ophthalmic Surg Lasers* 31:151–154.
- Surana R, Pyne A, Suryanarayanan R (2004a) Effect of aging on the physical properties of amorphous trehalose. *Pharm Res* 21:867–74.
- Surana R, Pyne A, Suryanarayanan R (2004b) Effect of preparation method on physical properties of amorphous trehalose. *Pharm Res* 21:1167–76.
- Sussich F, Skopec C, Brady J, Cesàro A (2001) Reversible dehydration of trehalose and anhydrobiosis: from solution state to an exotic crystal? *Carbohydr Res* 334:165–76.
- Szukiewicz D, Szewczyk G, Pyzlak M, Klimkiewicz J, Maslinska D (2008) Increased production of beta-defensin 3 (hBD-3) by human amniotic epithelial cells (HAEC) after activation of toll-like receptor 4 in chorioamnionitis. *Inflamm.Res.* 57 Suppl 1:S67 –S68.

- Takahashi H, Igarashi T, Fujimoto C, Ozaki N, Ishizaki M (2007) Immunohistochemical observation of amniotic membrane patching on a corneal alkali burn in vivo. *Jpn J Ophthalmol* 51:3–9.
- Takaoka M, Nakamura T, Sugai H, Bentley AJ, Nakajima N, Fullwood NJ, Yokoi N, Hyon SH, Kinoshita S (2008) Sutureless amniotic membrane transplantation for ocular surface reconstruction with a chemically defined bioadhesive. *Biomaterials* 29:2923 – 2931.
- Takashima S, Yasuo M, Sanzen N, Sekiguchi K, Okabe M, Yoshida T, Toda A, Nikaido T (2008) Characterization of laminin isoforms in human amnion. *Tissue Cell* 40:75–81.
- Talmi YP, Finkelstein Y, Zohar Y (1990) Use of human amniotic membrane as a biologic dressing. *European Journal Of Plastic Surgery* 13:160–162.
- Talmi YP, Sigler L, Inge E, Finkelstein Y, Zohar Y (1991) Antibacterial properties of human amniotic membranes. *Placenta* 12:285–8.
- Tamhane A, Vajpayee RB, Biswas NR, Pandey RM, Sharma N, Titiyal JS, Tandon R (2005) Evaluation of amniotic membrane transplantation as an adjunct to medical therapy as compared with medical therapy alone in acute ocular burns. *Ophthalmology* 112:1963–1969.
- Tamoto K, Nochi H, Tada M, Shimada S, Mori Y, Kataoka S, Suzuki Y, Nakamura T (1994) High-molecular-weight hyaluronic acids inhibit chemotaxis and phagocytosis but not lysosomal enzyme release induced by receptor-mediated stimulations in guinea pig phagocytes. *Microbiol Immunol* 38:73–80.
- Tandon R, Gupta N, Kalaivani M, Sharma N, Titiyal JS, Vajpayee RB (2011) Amniotic membrane transplantation as an adjunct to medical therapy in acute ocular burns. *Br J Ophthalmol* 95:199–204.

- Tejwani S, Kolari RS, Sangwan VS, Rao GN (2007) Role of amniotic membrane graft for ocular chemical and thermal injuries. *Cornea* 26:21–26.
- Thoft RA (1977) Conjunctival transplantation. *Arch Ophthalmol* 95:1425–7.
- Tindall BJ (2007) Vacuum-drying and cryopreservation of prokaryotes. In Day JG, Stacey GN, editors, *Cryopreservation and freeze-drying protocols*, Methods in Molecular Biology, chapter 5, pp. 73–98. Humana Press, New York, 2nd edition.
- Toda A, Okabe M, Yoshida T, Nikaido T (2007) The potential of amniotic membrane/amnion-derived cells for regeneration of various tissues. *J Pharmacol Sci* 105:215–28.
- Tollin M, Jägerbrink T, Haraldsson A, Agerberth B, Jörnvall H (2006) Proteome analysis of vernix caseosa. *Pediatr Res* 60:430–4.
- Toth M, Chvyrkova I, Bernardo MM, Hernandez-Barrantes S, Fridman R (2003) Pro-MMP-9 activation by the MT1-MMP/MMP-2 axis and MMP-3: role of TIMP-2 and plasma membranes. *Biochem Biophys Res Commun* 308:386–95.
- Trelford J, Trelford-Sauder M (1979) The amnion in surgery, past and present. *Am J Obstet Gynecol* 134:833–845.
- Tsai RJ, Li LM, Chen JK (2000) Reconstruction of damaged corneas by transplantation of autologous limbal epithelial cells. *N Engl J Med* 343:86–93.
- Tsai RJ, Tseng SC (1995) Effect of stromal inflammation on the outcome of limbal transplantation for corneal surface reconstruction. *Cornea* 14:439–449.
- Tseng SC, Li DQ, Ma X (1999) Suppression of TGF-beta isoforms, TGF-beta receptor type II, and myofibroblast differentiation in cultured hu-

- man corneal and limbal fibroblasts by amniotic membrane matrix. *J Cell Physiol* 179:325–335.
- Tseng S, Espana E, Kawakita T, Di Pascuale M, Li W, He H, Liu T, Cho T, Gao Y, Yeh L, Liu C (2004) How does amniotic membrane work? *Ocul Surf* 2:177–187.
- Tsubota K, Satake Y, Ohyama M, Toda I, Takano Y, Ono M, Shinozaki N, Shimazaki J (1996) Surgical reconstruction of the ocular surface in advanced ocular cicatricial pemphigoid and Stevens-Johnson syndrome. *Am J Ophthalmol* 122:38–52.
- Tuft SJ, Shortt AJ (2009) Surgical rehabilitation following severe ocular burns. *Eye* 23:1966–1971.
- Turi EA, editor (1997) *Thermal characterization of polymeric materials.*, Vol. I Academic Press, San Diego, CA, 2nd edition.
- Uçakhan OO, Köklü G, Firat E (2002) Nonpreserved human amniotic membrane transplantation in acute and chronic chemical eye injuries. *Cornea* 21:169–172.
- Uchida S, Inanaga Y, Kobayashi M, Hurukawa S, Araie M, Sakuragawa N (2000) Neurotrophic function of conditioned medium from human amniotic epithelial cells. *J Neurosci Res* 62:585–90.
- Ueta M, Kweon MN, Sano Y, Sotozono C, Yamada J, Koizumi N, Kiyono H, Kinoshita S (2002) Immunosuppressive properties of human amniotic membrane for mixed lymphocyte reaction. *Clin Exp Immunol* 129:464–70.
- Uglova T, Goleminova R (1957) [Amnion in caustic injuries of the eye.]. *Khirurgiia (Sofia)* 10:444–451.

- Vajpayee RB, Gupta NK, Angra SK, Chhabra VK, Sandramouli S, Kishore K (1991) Contact thermal burns of the cornea. *Can J Ophthalmol* 26:215–218.
- von Versen-Hoeynck F, Steinfeld AP, Becker J, Hermel M, Rath W, Hesselbarth U (2008) Sterilization and preservation influence the biophysical properties of human amnion grafts. *Biologicals* 36:248–255.
- von Versen-Höynck F, Syring C, Bachmann S, Müller DE (2004) The influence of different preservation and sterilisation steps on the histological properties of amnion allografts—light and scanning electron microscopic studies. *Cell Tissue Bank* 5:45–56.
- Vu H, Keeffe J, McCarty C, Taylor H (2005) Impact of unilateral and bilateral vision loss on quality of life. *Br J Ophthalmol* 89:360–363.
- Wagner MS, Castner DG (2001) Characterization of adsorbed protein films by Time-of-Flight Secondary Ion Mass Spectrometry with Principal Component Analysis. *Langmuir* 17:4649–4660.
- Wagner M, Graham D, Ratner B, Castner DG (2004) Maximizing information obtained from secondary ion mass spectra of organic thin films using multivariate analysis. *Surface Science* 570:78 – 97.
- Wagoner MD (1997) Chemical injuries of the eye: current concepts in pathophysiology and therapy. *Surv Ophthalmol* 41:275–313.
- Wall EA, Zavzavadjian JR, Chang MS, Randhawa B, Zhu X, Hsueh RC, Liu J, Driver A, Bao XR, Sternweis PC, Simon MI, Fraser IDC (2009) Suppression of LPS-induced TNF-alpha production in macrophages by cAMP is mediated by PKA-AKAp95-p105. *Sci Signal* 2:ra28.
- Wang G, editor (2010) *Antimicrobial Peptides: Discovery, Design and Novel Therapeutic Strategies*. Number 18 in Advances in molecular and cellular microbiology. CAB International, Oxford.

- Wang M, Yoshida A, Kawashima H, Ishizaki M, Takahashi H, Hori J (2006) Immunogenicity and antigenicity of allogeneic amniotic epithelial transplants grafted to the cornea, conjunctiva, and anterior chamber. *Invest Ophthalmol Vis Sci* 47:1522–1532.
- Wang MX, Gray TB, Park WC, Prabhasawat P, Culbertson W, Forster R, Hanna K, Tseng SC (2001) Reduction in corneal haze and apoptosis by amniotic membrane matrix in excimer laser photoablation in rabbits. *J Cataract Refract Surg* 27:310–319.
- Weichel E, Colyer M, Ludlow S, Bower K, Eiseman A (2008) Combat ocular trauma visual outcomes during Operations Iraqi and Enduring Freedom. *Ophthalmology* 115:2235–2245.
- Weichel ED, Colyer MH (2008) Combat ocular trauma and systemic injury. *Curr Opin Ophthalmol* 19:519–525.
- West-Mays JA, Strissel KJ, Sadow PM, Fini ME (1995) Competence for collagenase gene expression by tissue fibroblasts requires activation of an interleukin 1 alpha autocrine loop. *Proc Natl Acad Sci U S A* 92:6768–72.
- West-Mays J, Dwivedi D (2006) The keratocyte: corneal stromal cell with variable repair phenotypes. *Int J Biochem Cell Biol* 38:1625–1631.
- Whitcher JP, Srinivasan M, Upadhyay MP (2001) Corneal blindness: a global perspective. *Bull World Health Organ* 79:214–221.
- Whittle WL, Gibb W, Challis JR (2000) The characterization of human amnion epithelial and mesenchymal cells: the cellular expression, activity and glucocorticoid regulation of prostaglandin output. *Placenta* 21:394–401.
- Wilshaw SP, Kearney J, Fisher J, Ingham E (2008) Biocompatibility and potential of acellular human amniotic membrane to support the attachment and proliferation of allogeneic cells. *Tissue Eng Part A* 14:463–72.

- Wilshaw SP, Kearney JN, Fisher J, Ingham E (2006) Production of an acellular amniotic membrane matrix for use in tissue engineering. *Tissue Eng* 12:2117–2129.
- Wilson SE, Liu JJ, Mohan RR (1999) Stromal-epithelial interactions in the cornea. *Prog Retin Eye Res* 18:293–309.
- Wilson S, Netto M, Ambrosio R J (2003) Corneal cells: chatty in development, homeostasis, wound healing, and disease. *Am J Ophthalmol* 136:530–536.
- Wolbank S, Hildner F, Redl H, van Griensven M, Gabriel C, Hennerbichler S (2009) Impact of human amniotic membrane preparation on release of angiogenic factors. *J Tissue Eng Regen Med* 3:651–654.
- Wolkers WF, Walker NJ, Tablin F, Crowe JH (2001) Human platelets loaded with trehalose survive freeze-drying. *Cryobiology* 42:79–87.
- Wolkers WF, Oldenhof H, Glasmacher B (2010) Dehydrating phospholipid vesicles measured in real-time using ATR Fourier transform infrared spectroscopy. *Cryobiology* 61:108–114.
- Wolkers WF, Oliver AE, Tablin F, Crowe JH (2004) A fourier-transform infrared spectroscopy study of sugar glasses. *Carbohydrate Research* 339:1077 – 1085.
- Wolkers WF, Tablin F, Crowe JH (2002) From anhydrobiosis to freeze-drying of eukaryotic cells. *Comp Biochem Physiol A Mol Integr Physiol* 131:535–543.
- Wollensak G, Redl B (2008) Gel electrophoretic analysis of corneal collagen after photodynamic cross-linking treatment. *Cornea* 27:353–356.
- Wollensak G, Spoerl E, Seiler T (2003) Riboflavin/ultraviolet-A-induced

- collagen crosslinking for the treatment of keratoconus. *Am J Ophthalmol* 135:620–627.
- Wollensak G, Wilsch M, Spoerl E, Seiler T (2004) Collagen fiber diameter in the rabbit cornea after collagen crosslinking by riboflavin/UVA. *Cornea* 23:503–7.
- Wolsztyn J (1951) [Results of the tissue therapy with the conserved amnion in the same diseases of the eye.]. *Ann.Univ Mariae.Curie Sklodowska Med.* 6:131–151.
- Wong EYH, Chou SL, Lamoureux EL, Keeffe JE (2008) Personal costs of visual impairment by different eye diseases and severity of visual loss. *Ophthalmic Epidemiol* 15:339–344.
- Wong TY, Klein BE, Klein R (2000) The prevalence and 5-year incidence of ocular trauma. the Beaver Dam Eye Study. *Ophthalmology* 107:2196–2202.
- Woo HM, Kim MS, Kweon OK, Kim DY, Nam TC, Kim JH (2001) Effects of amniotic membrane on epithelial wound healing and stromal remodeling after excimer laser keratectomy in rabbit cornea. *Br J Ophthalmol* 85:345–349.
- Woods EJ, Benson JD, Agca Y, Critser JK (2004) Fundamental cryobiology of reproductive cells and tissues. *Cryobiology* 48:146–156.
- Xia N, May C, McArthur S, Castner D (2002) Time-of-flight secondary ion mass spectrometry analysis of conformational changes in adsorbed protein films. *Langmuir* 18:4090–4097.
- Xu P, Alfaidy N, Challis JRG (2002) Expression of matrix metalloproteinase MMP-2 and MMP-9 in human placenta and fetal membranes in relation to preterm and term labor. *J Clin Endocrinol Metab* 87:1353–61.

- Yang L, Lua YY, Jiang G, Tyler BJ, Linford MR (2005) Multivariate analysis of tof-sims spectra of monolayers on scribed silicon. *Anal Chem* 77:4654–61.
- Ye HQ, Azar DT (1998) Expression of gelatinases A and B, and TIMPs 1 and 2 during corneal wound healing. *Invest Ophthalmol Vis Sci* 39:913–21.
- Ye J, Lee S, Kook K, Yao K (2008) Bone marrow-derived progenitor cells promote corneal wound healing following alkali injury. *Graefes Arch Clin Exp Ophthalmol* 246:217–222.
- Ye J, Yao K, Kim JC (2006) Mesenchymal stem cell transplantation in a rabbit corneal alkali burn model: engraftment and involvement in wound healing. *Eye (Lond)* 20:482–490.
- Yeh LK, Chen WL, Li W, Espana EM, Ouyang J, Kawakita T, Kao WWY, Tseng SCG, Liu CY (2005) Soluble lumican glycoprotein purified from human amniotic membrane promotes corneal epithelial wound healing. *Invest Ophthalmol Vis Sci* 46:479–486.
- Yiu S, Thomas P, Nguyen P (2007) Ocular surface reconstruction: recent advances and future outlook. *Curr Opin Ophthalmol* 18:509–514.
- Yoshio H, Lagercrantz H, Gudmundsson GH, Agerberth B (2004) First line of defense in early human life. *Semin Perinatol* 28:304–11.
- Yoshio H, Tollin M, Gudmundsson GH, Lagercrantz H, Jornvall H, Marchini G, Agerberth B (2003) Antimicrobial polypeptides of human vernix caseosa and amniotic fluid: implications for newborn innate defense. *Pediatr Res* 53:211–6.
- Young J, Nelson G (1967) Research of hysteresis between sorption and desorption isotherms of wheat. *Trans Am Soc Agric Eng* 10:756–761.

- Zankiewicz A (1960) [Results of the treatment of diseases of the anterior chamber of the eye by means of subconjunctival implantation of preserved amnion.]. *Pol Tyg Lek* 15:1499–1501.
- Zhang J, Zografi G (2000) The relationship between "BET" and "free volume"-derived parameters for water vapor absorption into amorphous solids. *J Pharm Sci* 89:1063–72.
- Zhang Q, Andrew Chan KL, Zhang G, Gillece T, Senak L, Moore DJ, Mendelsohn R, Flach CR (2011) Raman microspectroscopic and dynamic vapor sorption characterization of hydration in collagen and dermal tissue. *Biopolymers* 95:607–15.
- Zhong Q, Inniss D, Kjoller K, Elings V (1993) Fractured polymer/silica fiber surface studied by tapping mode atomic force microscopy. *Surface Science Letters* 290:L688 – L692.
- Zhou H, Zhao K, Li W, Yang N, Liu Y, Chen C, Wei T (2012) The interactions between pristine graphene and macrophages and the production of cytokines/chemokines via TLR- and NF-kappa B-related signaling pathways. *Biomaterials* 33:6933–42.
- Zhou SY, Chen JQ, Liu ZG, Huang T, Chen LS (2004) [A clinical study of amniotic membrane transplantation for severe eye burns at the acute stage]. *Zhonghua Yan Ke Za Zhi* 40:97–100.
- Zucker S, Cao J (2006) Detection of activated, TIMP-free MMPs. *Chem Biol* 13:347–9.

1 CENTRAL search strategy

#1 MeSH descriptor Eye Burns

#2 (eye* or ocular) near/6 (burn*)

#3 (#1 OR #2)

#4 MeSH descriptor Amnion

#5 amniotic near/3 membrane*

#6 AMT

#7 (#4 OR #5 OR #6)

#8 (#3 AND #7)

2 MEDLINE (OVID) search strategy

1. Eye burns/

2. ((eye\$ or ocular) adj6 burn\$).tw.

3. or/1-2

4. exp Amnion/

5. (amniotic adj3 membrane\$).tw.

6. AMT.tw.

7. or/4-6

8. 3 and 7

3 EMBASE (OVID) search strategy

1. Eye burn/

2. Cornea burn/

3. ((eye\$ or ocular) adj6 burn\$).tw.

4. or/1-3

5. exp Amnion/

6. (amniotic adj3 membrane\$).tw.

7. AMT.tw.

8. or/5-7

9. 4 and 8

4 LILACS search strategy

amniotic and eye or ocular burn\$

5 metaRegister of Controlled Trials search strategy

amniotic and ocular burn

6 ClinicalTrials.gov search strategy

amniotic AND ocular burn